Universität Hamburg

Optimisation of Searches for Supersymmetry with the ATLAS Detector

Master-Arbeit

vorgelegt von

Milan Zvolský

Dezember 2011

Fachbereich Physik
Universität Hamburg

Gutachter der Masterarbeit	:	Dr. P. Bechtle Prof. Dr. P. Schleper
Vorsitzender des Prüfungsausschusses	:	Prof. Dr. W. Hansen
Fachbereichsleiterin	:	Prof. Dr. D. Pfannkuche

'Darin besteht das Wesen der Wissenschaft. Zuerst denkt man an etwas, das wahr sein könnte. Dann sieht man nach, ob es der Fall ist und im Allgemeinen ist es nicht der Fall.'

Bertrand Russell (1872-1970)

Abstract

The ATLAS experiment is one of the four large experiments at the Large Hadron Collider which is specifically designed to search for the Higgs boson and physics beyond the Standard Model. The aim of this thesis is the optimisation of searches for Supersymmetry in decays with two leptons and missing transverse energy in the final state. Two different optimisation studies have been performed for two important analysis aspects: The final signal region selection and the choice of the trigger selection. In the first part of the analysis, a cut-based optimisation of signal regions is performed, maximising the signal for a minimal background contamination. By this, the signal yield can in parts be more than doubled. The second approach is to introduce di-lepton triggers which allow to lower the lepton transverse momentum threshold, thus enhancing the number of selected signal events significantly. The signal region optimisation was considered for the choice of the final event selection in the ATLAS di-lepton analyses [1, 2]. The trigger study contributed to the incorporation of di-lepton triggers to the ATLAS trigger menu.

Zusammenfassung

ATLAS ist eines der vier großen Experimente am Large Hadron Collider und speziell für die Suche nach dem Higgs-Boson und Physik jenseits des Standardmodells konzipiert. Das Ziel dieser Arbeit ist die Optimierung der Suche nach Supersymmetrie in Zerfällen mit zwei Leptonen und fehlender transversaler Energie im Endzustand. Hierzu wurden zwei Optimierungen für zwei wichtige Aspekte der Analyse durchgeführt: Die Selektion der finalen Signalregionen und die Wahl der Triggerselektion. Im ersten Teil der Analyse wird eine Schnitt-basierte Optimierung durchgeführt, welche das Signal bei minimaler Untergrundkontamination maximiert. Dadurch kann die Signalausbeute teilweise mehr als verdoppelt werden. Der zweite Ansatz ist die Einführung von Zwei-Lepton-Triggern, welche es erlauben, die Schwelle für den Transversalimpuls des Leptons zu reduzieren und somit die Zahl der selektierten Signalereignisse signifikant zu erhöhen. Die Optimierung der Signalregionen wurde für die Wahl der finalen Ereignisselektion der ATLAS-Zwei-Lepton-Analyse [1, 2] verwendet. Die Triggerstudien trugen zur Aufnahme von Zwei-Lepton-Triggern in das ATLAS-Trigger-Menü bei.

Contents

Chapter 1

Introduction

CERN's Large Hadron Collider (LHC) is a proton-proton collider with obtained center-of-mass energies of 7 TeV (14 TeV design center-of-mass energy). The ATLAS experiment is one of the four large experiments at the LHC. It is a multi-purpose detector that is especially designed to search for the Higgs boson and physics beyond the Standard Model.

The analyses presented in this thesis optimise the searches for Supersymmetry with the ATLAS detector using final states with two leptons and missing transverse momentum.

Supersymmetry (SUSY) is a very promising model for solving several open issues of the Standard Model of particle physics. It assigns a fermionic particle to each boson and vice versa, thereby introducing a supersymmetric particle for each Standard Model particle differing in spin by 1/2. These SUSY particles are presumed to have masses of the order of 1 TeV in order to be able to solve the Hierarchy problem. Thus, if existing, they should be accessible with the Large Hadron Collider (LHC).

Most SUSY scenarios exhibit an extremely low cross-section compared to the Standard Model background so that one is literally looking for the needle in the haystack. Therefore, it is crucial to optimise the search strategy and thereby maximise the probability of finding SUSY.

In this thesis, the optimisation of the search strategy is approached from two different directions. The first approach is to optimise the purity and efficiency of signal regions, striving after separating supersymmetric signal signatures from SM background in the best possible way. This is realised by imposing cuts on different variables with the aim of maximising the signal-to-background ratio, leading to purer signals and thus a higher probability of finding supersymmetric particles if they exist.

The second approach is to optimise the search by means of optimising the trigger selection. With the constant increase of the instantaneous luminosity and the constraints on the throughputs of the ATLAS trigger system, the trigger selections need to be tightened to keep the rates below the limit. As an alternative to higher trigger thresholds, di-lepton triggers can be introduced. These have the advantage of lower transverse momentum thresholds as the rate of di-lepton events is much lower than that of single-lepton

events. While new triggers are necessary, it is desired to establish triggers which are able to improve the event yield.

The thesis is organised as follows: The second chapter begins with an introduction to the theory of the Standard Model of particle physics. An emphasis is laid on the concept of symmetry from which most attributes of the Standard Model can be derived. This concept, as the name implies, is also the basic module of Supersymmetry, revealed in Sec. 2.2. After an introduction to the fundamental properties, Supersymmetry breaking and the mSUGRA model are presented, followed by some implications on the search for Supersymmetry at the LHC. The subsequent chapter is devoted to the LHC collider and the main components of the ATLAS detector. In some more detail, the ATLAS trigger system is introduced which is a prerequisite for the understanding of the trigger optimisation. Chapter 4 depicts the ATLAS data taking, i.e. the reconstruction and identification of particles, as well as the event simulation with Monte Carlo generators. Chapter 5 presents the configuration of the di-lepton analysis which is the baseline for the studies performed in the successive chapters. That is, the Monte Carlo and data samples, the object reconstruction and event selection as well as the main Standard Model background contributions and the treatment of systematic uncertainties are summarised. Chapters 6 and 7 are devoted to this thesis' studies. In chapter 6, the optimisation of signal region cuts for the mSUGRA model is portrayed. First, some basic optimisation techniques are described, followed by the presentation of the cut optimisation performed on different regions of the mSUGRA parameter space for two different search channels: the opposite-sign (OS) and the opposite-sign same-flavour (OSSF) channel. The study of di-lepton triggers is exhibited in chapter 7. First, the yield of several emulated di-lepton triggers with respect to the current trigger selection is determined for different supersymmetric models. In the subsequent section, the techniques and results of the determination of trigger efficiencies is presented, on both Monte Carlo and data. The thesis closes with a summary of the results and a conclusion in chapter 8.

Chapter 2

Theory

'Miracle of miracles, some concepts in mathematics turn out to provide the fundamental structures that govern the physical universe!'
Chen N. Yang [3]

One of the 'fundamental structures' that C. N. Yang refers to in the quote above is that of symmetries. The consideration of symmetry principles marks the most fundamental concept in particle physics. By requiring the invariance of a Lagrangian under a certain symmetry or (gauge) transformation, most of the properties of the interactions between particles can be deduced.

Symmetries can be described concisely by means of group theory. Noether's theorem states that the invariance of a Lagrangian $\mathscr{L}$ under a symmetry transformation (described by an unitary group) results in a set of conserved charges Q^i [4]. These charges are the electromagnetic charge for Quantum Electrodynamics (Sec. 2.1.1), the colour for Quantum Chromodynamics (Sec. 2.1.2) and the hypercharge for the Glashow-Salam-Weinberg model of electroweak interactions (Sec. 2.1.3). Supersymmetry introduces charges which transform as spinors. The consequences of that concept are far-reaching and shall be introduced in Sec. 2.2.

2.1 The Standard Model

In the following sections the building blocks of the Standard Model (SM), namely the electroweak theory (including QED and the Higgs mechanism) and QCD are introduced. First, QED is taken as an example to demonstrate the implications of gauge invariance. In the subsequent sections, QCD, the theory of the strong interactions is introduced, followed by the Glashow-Salam-Weinberg model of electroweak interactions. After that, the Higgs mechanism which is necessary to produce massive particles, is presented. The section is closed by naming some shortcomings of the Standard Model and thus motivating Supersymmetry.

2.1.1 Quantum Electrodynamics (QED)

Quantum electrodynamics (QED) is the theory of electromagnetism [5, 6, 7]. It describes the interaction of charged fermions with the electromagnetic field which is mediated by the photon.
In the following, the deviation of the QED Lagrangian by means of symmetry considerations is shown exemplarily. The requirement of invariance under a special symmetry postulates the existence of the photon field and generates the interaction of the fermion current to the photon. The calculations for QCD and the electroweak theory follow a similar procedure.
Consider the Lagrangian of a single free fermion with mass m,

$$\mathscr{L}(x) = \overline{\psi}(x)(i\gamma^\mu\partial_\mu - m)\psi(x) \tag{2.1}$$

of a 4-component Dirac spinor $\psi(x)$ which obeys the Dirac equation due to the principle of smallest action

$$(i\gamma^\mu\partial_\mu - m)\psi(x) = 0. \tag{2.2}$$

$\mathscr{L}$ is invariant under the global symmetry transformation

$$\psi \to \psi' = e^{-i\theta}\psi = U\psi \tag{2.3}$$

which is a complex phase transformation. The symmetry group associated with this *abelian* transformation is U(1) [8].
Under the local U(1) gauge transformation $\psi \to \psi' = e^{i\theta(x)}\psi(x)$ the Lagrangian is not invariant:

$$\mathscr{L} \to \mathscr{L}' = \mathscr{L} + \overline{\psi}\gamma^\mu\psi\partial_\mu\theta(x) \tag{2.4}$$

with the term $\overline{\psi}\gamma^\mu\psi$ being the conserved Noether current j^μ. The Lagrangian can be adapted to fulfill the symmetry requirements by replacing the derivative ∂_μ with the covariant derivative $\mathscr{D}_\mu \equiv \partial_\mu - ieA_\mu$ with the auxiliary field A_μ transforming as

$$A_\mu \to A'_\mu = A_\mu - \frac{1}{e}\partial_\mu\theta(x). \tag{2.5}$$

It turns out that the arbitrary constant e is the coupling constant of the theory (the elementary charge of QED) [4, 8].
In order to promote A_μ to a propagating field one needs to add a kinetic term which is invariant under the given U(1) symmetry:

$$\mathscr{L}_{\text{kin}} = -\frac{1}{4}F_{\mu\nu}F^{\mu\nu}, \quad \text{with } F_{\mu\nu} = \partial_\mu A_\nu - \partial_\nu A_\mu \tag{2.6}$$

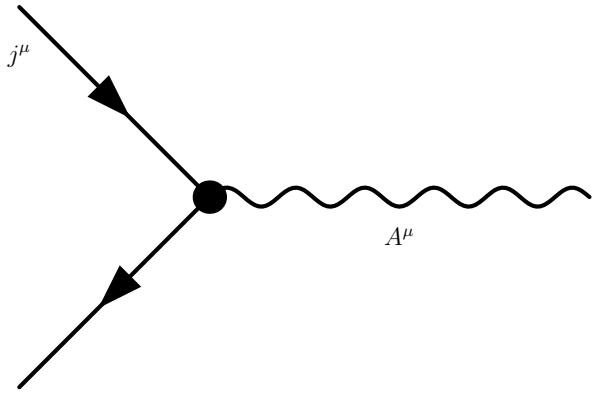

Figure 2.1: Feynman diagram of the QED vertex: Coupling of the Noether current j^μ to the photon field A^μ which occurs e.g. in the annihilation $e^+e^- \to \gamma$. All Feynman diagrams are produced with the help of the FeynEdit package [10].

By the above transformations the complete QED Lagrangian reads as ([8])

$$\begin{aligned}\mathscr{L}_{\text{QED}} &= \overline{\psi}(x)(i\gamma^\mu \mathscr{D}_\mu - m)\psi(x) - \frac{1}{4}F_{\mu\nu}F^{\mu\nu} \\ &= \overline{\psi}(i\gamma^\mu\partial_\mu - m)\psi + \underbrace{e\overline{\psi}\gamma^\mu\psi A_\mu}_{=ej^\mu(x)A_\mu} + \mathscr{L}_{\text{kin}}. \end{aligned} \tag{2.7}$$

As one can see from the Lagrangian (2.7), the gauge principle has generated an interaction between the fermion current $j^\mu = \overline{\psi}\gamma^\mu\psi$ and the massless[1] gauge field A_μ which is associated with the photon. The term $ej^\mu A_\mu$ describes the coupling of the fermion current to the photon field with the coupling constant e. The annihilation $e^+e^- \to \gamma$ for instance is exactly represented by this (QED) vertex [9] (cf. Fig. 2.1).

2.1.2 Quantum Chromodynamics (QCD)

The strong interactions are described by Quantum Chromodynamics (QCD) [11], mediated by eight SU(3) gauge bosons. There are $3^2 - 1 = 8$ generators[2] which are associated with the gauge bosons of the theory, the gluons. They are denoted by G^a_μ, $a = 1, \ldots, 8$.. The quarks, the building blocks of hadrons (baryons and mesons) are fermions and transform under the fundamental three-dimensional representation of SU(3). This group is non-abelian which has some strong implications. The SU(3) quantum number is called colour and in this nomenclature the quarks form a colour-triplet. Experimentally one observes six quarks which are colour triplets so that the quarks are denoted by

$$q^I_i,\ i = 1, \ldots, 3,\ I = u, d, c, s, t, b \tag{2.8}$$

[1] It is noteworthy that gauge invariance forbids an additional mass term for the photon field; the photon stays massless as required from experiment.

[2] In general, the group SU(n) has $n^2 - 1$ generators.

where q_i^J is a Dirac spinor with i and J being the colour and flavour index, respectively. The quarks are grouped into three families according to their SU(2) doublet structure (Tab. 2.1).

Table 2.1: Overview of the six quarks and their charge

Family	Quark	charge	Quark	charge
1	u (up)	2/3	d (down)	-1/3
2	c (charme)	2/3	s (strange)	-1/3
3	t (top)	2/3	b (bottom)	-1/3

The complete QCD Lagrangian can be deduced from the same symmetry principles which were sketched for the case of QED. It reads as

$$\begin{aligned}\mathscr{L}_{\mathrm{QCD}} = & -\frac{1}{4}\left(\partial^\mu G_a^\nu - \partial^\nu G_a^\mu\right)\left(\partial_\mu G_\nu^a - \partial_\nu G_\mu^a\right) \\ & + \sum_f \overline{q}_f^\alpha \Big(i\gamma^\mu \mathscr{D}_\mu - m_f\Big) q_f^\alpha \\ & + \alpha_s G_a^\mu \sum_f \overline{q}_f^\alpha \gamma_\mu \Big(\frac{\lambda^a}{2}\Big)_{\alpha\beta} q_f^\beta \\ & - \frac{\alpha_s}{2} f^{abc}\left(\partial^\mu G_a^\nu - \partial^\nu G_a^\mu\right) G_\mu^b G_\nu^c - \frac{\alpha_s^2}{4} f^{abc} f_{ade} G_b^\mu G_c^\nu G_\mu^d G_\nu^e \end{aligned} \tag{2.9}$$

with the covariant derivative

$$\mathscr{D}_\mu q_i^I = \partial_\mu q_i^I - i\alpha_s \sum_a \sum_j G_\mu^a t_{ij}^a q_j^I. \tag{2.10}$$

The t_{ij}^a are the generators of SU(3), f^{abc} are the structure constants of the group and α_s is the strong coupling constant. The first two lines give the kinetic terms for the gluon fields as well as the propagators for the quark fields. The third line describes the quark-gluon interaction (gluon-quark-quark vertex). Finally, the fourth line of the Lagrangian gives the gluon self-interactions, both three-gluon and four-gluon vertex. The self-gluon interaction is automatically included in the QCD theory by the mere fact that SU(3) is a non-abelian symmetry group (in contrast to the abelian QED U(1) symmetry). It is emphasised that solely the requirement of local gauge invariance under SU(3) transformations has created the Lagrangian which correctly describes the interactions [4]. The QCD vertices are shown in Fig. 2.2. The first experimental evidence of the existence of gluons was obtained at PETRA (DESY) in 1979 through the observation of three-jet events [12].

The non-abelian character of QCD leads to another crucial property of QCD, the so-called confinement. QCD is an asymptotically free theory which is weakly coupling at high energy scales and strongly at low energy scales [13] (see Fig. 2.3). At high energies it is possible to use perturbation theory in α_s. For low energies other methods such as lattice gauge theory are necessary. The scale at which QCD becomes strongly coupling

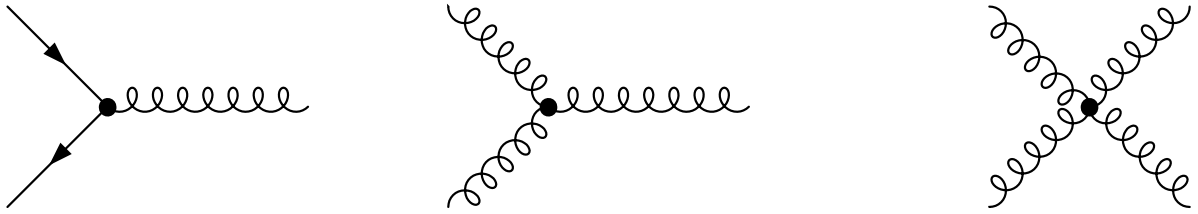

Figure 2.2: Feynman diagram of the QCD vertices: Coupling of the quark fields to the gluon fields (left) as well as three-gluon and four-gluon self-interaction (middle and right).

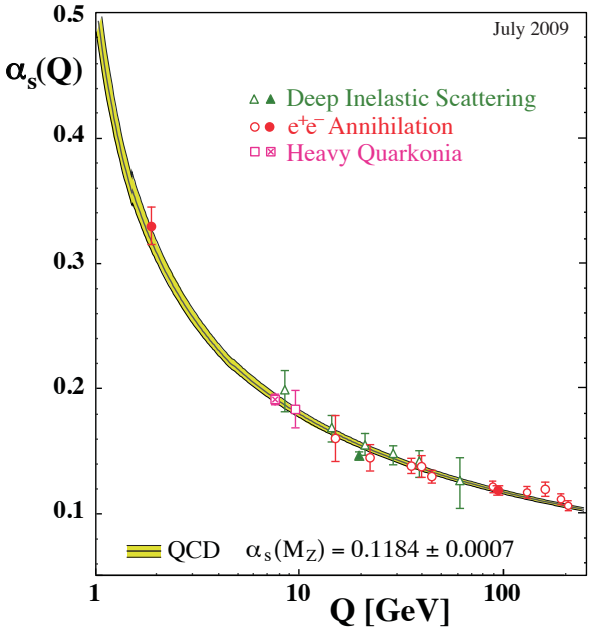

Figure 2.3: Summary of measurements of the QCD coupling constant α_S as a function of the respective energy scale Q. Taken from [14], cf. [15].

can be estimated from theory to be $\Lambda_{\mathrm{QCD}} \approx 200$ MeV. The fact that the coupling constant of QCD diverges for small momentum transfers Q^2 (large distances r) leads to the non-observability of free quarks; at low energies the quarks and gluons are *confined* to SU(3) colour singlets called hadrons which are bound states of the quarks:

$$\text{Mesons: } M^{IJ} = \sum_i \overline{q}_i^I q_i^I, \tag{2.11}$$

$$\text{Baryons: } B^{IJK} = \sum_{ijk} \epsilon_{ijk} q_i^I q_j^J q_k^K \tag{2.12}$$

with i, j, k being the colour index. So, mesons are quark-antiquark systems while baryons consist of three quarks. Due to the confinement hypothesis every free particle has to be colour neutral so that baryons need to consist of three differently charged quarks (red, green, blue). Confinement is the reason why quarks hadronise and can only be observed as *jets*. An exception is the top quark which decays before hadronising due to its high mass of 172.9 GeV [15].

2.1.3 Glashow-Salam-Weinberg Model

The weak interactions are mediated by the $W^{\pm}$ and Z^0 bosons, just like QED is mediated by the photon (Sec. 2.1.1) and QCD by the gluons (Sec. 2.1.2). The unification of the weak and the electromagnetic (EM) interactions to the electroweak theory was established by Glashow, Salam and Weinberg [16, 17, 18] (GSW model). The particles that couple to the gauge bosons of the electroweak theory are the electron, the muon and the tau lepton and their corresponding neutrinos as well as the quarks. They can be grouped into three generations, respectively:

$$\begin{pmatrix} \nu_e \\ e \end{pmatrix}, \begin{pmatrix} \nu_\mu \\ \mu \end{pmatrix}, \begin{pmatrix} \nu_\tau \\ \tau \end{pmatrix}, \tag{2.13}$$

$$\begin{pmatrix} u \\ d \end{pmatrix}, \begin{pmatrix} c \\ s \end{pmatrix}, \begin{pmatrix} t \\ b \end{pmatrix}. \tag{2.14}$$

The first step towards the GSW model is to introduce the concept of *helicity* and *chirality*. The helicity is defined as the projection of the spin onto the direction of the momentum. The helicity of a particle is called 'left-handed' if the direction of the spin vector is opposite to the direction of motion and 'right-handed' if their directions are identical. The chirality is the eigenvalue of γ^5 which is the product of all γ matrices[3]. Positive and negative eigenvalues of the chirality are denoted by right-handed and left-handed as well, even though these are not helicity eigenstates. The helicity is only identical to the chirality for massless particles. The two γ^5 eigenstates can be constructed from the original spinor by the chirality projection operators $P_{R,L} = 1/2(1 \pm \gamma^5)$. With this, a $\mathrm{SU}(2)_L$ doublet of a left-handed electron and left-handed neutrino can be constructed by

$$L \equiv \begin{pmatrix} \nu \\ e \end{pmatrix}_L = \frac{1}{2}(1-\gamma^5)\begin{pmatrix} \nu \\ e \end{pmatrix} \tag{2.15}$$

while the right-handed electron is a singlet since massless neutrinos only occur left-handed [8, 9],

$$R \equiv e_R = \frac{1}{2}(1+\gamma^5)e. \tag{2.16}$$

This distinction is necessary as the weak interactions violate parity conservation. The separation into left- and right-handed spinors is possible because in general every four-component Dirac spinor ψ_D can be decomposed into two two-component Weyl spinors $\psi_{L,R}$ via[4]

$$\psi_D = \begin{pmatrix} \psi_L \\ \psi_R \end{pmatrix}, \quad \overline{\psi}_D = \psi^\dagger\gamma^0 = (\overline{\psi}_R, \overline{\psi}_L). \tag{2.17}$$

[3]The matrix γ^5 is the product of all γ matrices: $\gamma^5 = i\gamma^0\gamma^1\gamma^2\gamma^3$.
[4]This decomposition is important for SUSY as well (Sec. 2.2).

The fermionic Lagrangian decomposes correspondingly into a left-handed and a right-handed part [8]. The left-handed and right-handed spinors have in general different transformation properties. Gauge theories in which ψ_L and ψ_R transform in different representations of the gauge group are called chiral gauge theories.

In addition, the different transformation properties of left- and right-handed fermions can be accounted for with the *hypercharge* Y which is $-1/2$ for left-handed fermions and -1 for right-handed ones. Analogously to the concept of the isospin, the quantum numbers hypercharge Y and the third component of the isospin I^3 are introduced which are related to the electric charge Q by

$$Q = I^3 + \frac{1}{2}Y. \tag{2.18}$$

The weak hypercharge current [9]

$$j_\mu^Y = 2j_\mu^{\mathrm{EM}} - 2j_\mu^3 = -2\overline{e}_R\gamma_\mu e_R - \overline{e}_L\gamma_\mu e_L - \overline{\nu}_L\gamma_\mu\nu_L \tag{2.19}$$

is invariant under the unified symmetry group $\mathrm{SU}(2)_L \times \mathrm{U}(1)_Y$ where $\mathrm{SU}(2)_L$ refers to the weak isospin with the index L indicating that its transformations only act on left-handed fermions and $\mathrm{U}(1)_Y$ refers to the weak hypercharge involving both chiralities.

In order to achieve invariance under the local $\mathrm{SU}(2)_L \times \mathrm{U}(1)_Y$ symmetry one needs to add a triplet $W_\mu^{1,2,3}$ for $\mathrm{SU}(2)_L$ and a vector field B^μ for $\mathrm{U}(1)$. The three weak isospin currents couple with strength g to a weak isotriplet of vector bosons W_μ, whereas the weak hypercharge current couples with strength g' to an isosinglet B_μ. The physical $W^\pm$ fields are constructed as

$$W_\mu^\pm = \frac{1}{\sqrt{2}}(W_\mu^1 \mp iW_\mu^2). \tag{2.20}$$

The two neutral states W_μ^3 and B_μ mix to the physical photon field A_μ and an orthogonal linear combination, the Z_μ^0. The photon and Z boson fields are given by:

$$\begin{pmatrix} A_\mu \\ Z_\mu^0 \end{pmatrix} = \begin{pmatrix} \cos\theta_W & \sin\theta_W \\ -\sin\theta_W & \cos\theta_W \end{pmatrix} \begin{pmatrix} B^\mu \\ W^{3\mu} \end{pmatrix} \tag{2.21}$$

with the weak or Weinberg angle

$$\sin\theta_W = \frac{g'}{\sqrt{g^2 + g'^2}}. \tag{2.22}$$

The Lagrangian for the GSW model is given for the first generation by

$$\begin{aligned} \mathscr{L} = {} & \overline{E}_L i\partial\!\!\!/ E_L + \overline{e}_R i\partial\!\!\!/ e_R + \text{ quark terms} \\ & + g\big(W_\mu^+ J_W^{\mu+} + W_\mu^- J_W^{\mu-} + Z_\mu^0 J_Z^\mu\big) + eA_\mu J_{\mathrm{EM}}^\mu. \end{aligned} \tag{2.23}$$

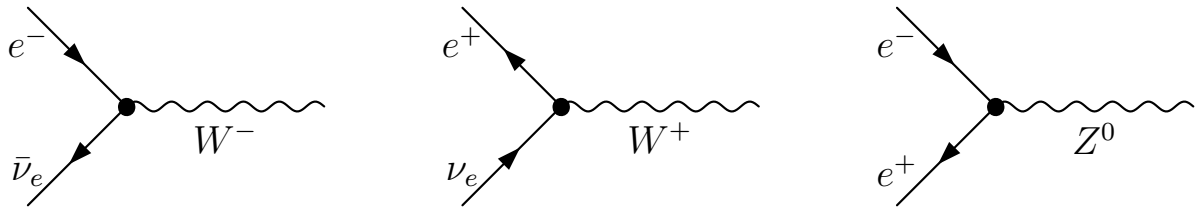

Figure 2.4: Feynman diagrams of the electroweak charged current vertices (coupling to the $W^\pm$ bosons, left and middle diagram) and of the neutral current vertex (coupling to the Z^0 boson, right diagram), shown exemplarily for the first lepton generation.

J^μ_{EM} turns out to be exactly the electromagnetic current j^μ from Sec. 2.1.1. The neutral current J^μ_Z is a rather complex linear combination of all involved fermion-antifermion currents (cf. [8]) and $J^{\mu\pm}_W$ and J^μ_Z are the charged and neutral currents, respectively, given by

$$J^{\mu+}_W = \frac{1}{\sqrt{2}}\left(\overline{\nu}_L \gamma^\mu e_L + \overline{u}_L \gamma^\mu d_L\right) \tag{2.24}$$

and

$$J^{\mu-}_W = \frac{1}{\sqrt{2}}\left(\overline{e}_L \gamma^\mu \nu_L + \overline{d}_L \gamma^\mu u_L\right). \tag{2.25}$$

The vertices for the coupling of the lepton current to the $W^\pm$ bosons are shown exemplarily in Fig. 2.4 ($e^- + \overline{\nu}_e \rightarrow W^-$ and $e^+ + \nu_e \rightarrow W^+$) and the particle content of the GSW model is summarised in Tab. 2.2.

Table 2.2: Particle spectrum of the GSW model including the values for the weak hypercharge Y and the charge Q.

Name	Symbol	Y	Q
Gauge bosons	$W^{a=1,2,3}_\mu$	0	$0, \pm 1$
	B_μ	0	0
Weyl fermions	$E^{i=1,2}_L = \begin{pmatrix} \nu_e \\ e \end{pmatrix}_L$	$-1/2$	$\begin{pmatrix} 0 \\ -1 \end{pmatrix}$
	e^-_R	-1	-1
Higgs boson	$\phi^i = \begin{pmatrix} \phi^+ \\ \phi^0 \end{pmatrix}$	$1/2$	$\begin{pmatrix} 0 \\ 1 \end{pmatrix}$

Because left- and right-handed fermions transforming differently, the chiral Lagrangian is only invariant if $m = 0$: chiral gauge theories forbid fermionic mass terms. Moreover, the gauge bosons of the electroweak theory are massless, despite the fact that the $W^\pm$ and Z^0 gauge bosons do have a mass. So, the theory has to produce massive $W^\pm$ and Z^0 bosons while leaving the photon massless. These fermionic and bosonic masses are generated by the Higgs mechanism.

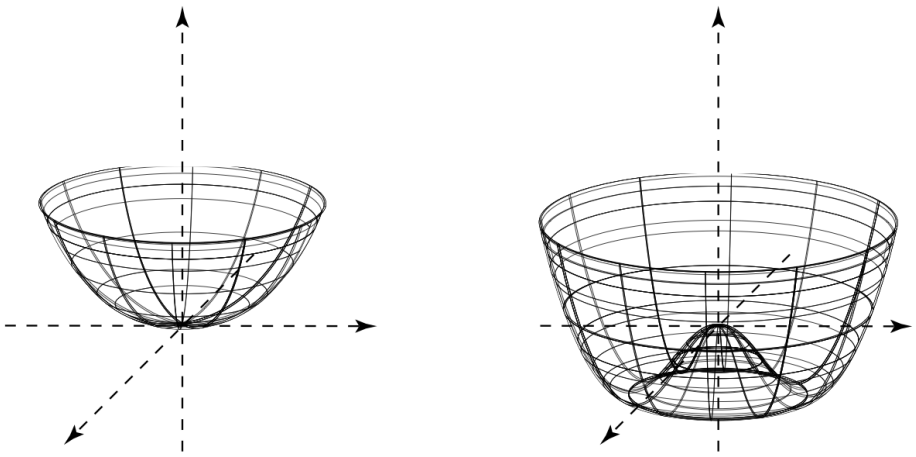

Figure 2.5: The ϕ^4 Higgs potential without spontaneous symmetry breaking ($\mu^2 \geq 0$,left) and with spontaneous symmetry breaking ($\mu^2 < 0$, right)

2.1.4 Spontaneous Symmetry Breaking and the Higgs Mechanism

The SM, which combines the electroweak theory with QCD is a consistent theory for massless particles. However, one observes massive particles (the W and Z bosons, the gauge fields of the electroweak theory, the fermions and the quarks) [8, 19]. The Higgs mechanism provides a way to add mass terms. This mechanism adds an additional scalar field to the Lagrangian which breaks the underlying symmetry spontaneously and thus assigns masses to the fermions and gauge bosons.
In order to illustrate the basic concept of spontaneous symmetry breaking, first an unphysical toy model is presented where the breaking of U(1) is shown which gives mass to the photon in QED by the Higgs mechanism. Consider the U(1) Lagrangian

$$\mathscr{L} = -\frac{1}{4}F_{\mu\nu}F^{\mu\nu} + \mathscr{D}^{\mu}\phi^{*}\mathscr{D}_{\mu}\phi - V(\phi,\phi^{*}) \tag{2.26}$$

with

$$\mathscr{D}_{\mu}\phi = \partial_{\mu}\phi - igA_{\mu}\phi, \tag{2.27}$$

the potential

$$V(\phi,\phi^{*}) = -\mu^2\phi\phi^{*} + \frac{1}{2}\lambda(\phi\phi^{*})^2,\ \mu^2,\ \lambda > 0 \tag{2.28}$$

and the complex scalar field

$$\phi = \phi_1 + i\phi_2. \tag{2.29}$$

The minimum of V is not at zero but at $\phi|_{\min} = \phi^{*}|_{\min} = \frac{\mu^2}{\lambda} = \frac{1}{\sqrt{2}}v$ which is the equation of a circle. The form of the Higgs potential is shown in Fig. 2.5. The Lagrangian is

invariant under local U(1) symmetry

$$\phi \rightarrow \phi^{'} = e^{i\alpha(x)}\phi \tag{2.30}$$

with the gauge field transforming as in Eq. (2.5). The Lagrangian at its minimum $\phi\phi^* = \mu^2/\lambda$ does not have this symmetry. The ground state of the Higgs field populates an arbitrary point in the minimum and breaks the symmetry of the vacuum. Spontaneous symmetry breaking occurs if the theory has a symmetry which is not shared by its ground state.
It is convenient to introduce a parametrisation $(\phi, \phi^*) \rightarrow (h, \beta)$ of the form

$$\phi(x) = \frac{1}{\sqrt{2}}\big(v + h(x)\big)e^{i\beta(x)}. \tag{2.31}$$

The *Goldstone theorem* tells that for every spontaneously broken continuous symmetry there exists a real massless scalar field $\beta(x)$ called *Goldstone boson*. $h(x)$ is the physical *Higgs boson*. The Goldstone boson β can be removed from the Lagrangian by a (unitary) gauge transformation. Thus, the Goldstone boson does not appear as a physical particle. The gauge boson A_μ gets a mass term $m_A = g^2v^2$ via the interaction between A_μ and the Higgs field $h(x)$:

$$\mathscr{L} = -\frac{1}{4}F_{\mu\nu}F^{\mu\nu} + \frac{1}{2}\partial^\mu h \partial_\mu \phi - V(h) + \frac{1}{2}m_A^2 A_\mu A^\mu + (g^2vh + \frac{1}{2}g^2h^2)A_\mu A^\mu. \tag{2.32}$$

The Goldstone boson plays the role of the longitudinal degree of freedom of the now massive A_μ [8, 9, 19].
The previous example illustrates the concept of the Higgs mechanism within a toy theory but is unphysical since U(1) is an unbroken symmetry within the SM (the photon is massless).

The electroweak symmetry group $\mathrm{SU}(2)_L \times \mathrm{U}(1)_Y$ is spontaneously broken to $\mathrm{U}(1)_{\mathrm{EM}}$ which is the symmetry group of the massless gauge boson of the theory, i.e. the photon. The field ϕ is now a weak isospin doublet of two complex scalar fields,

$$\phi = \begin{pmatrix} \phi^+ \\ \phi^0 \end{pmatrix} = \begin{pmatrix} \phi_1 + i\phi_2 \\ \phi_3 + i\phi_4 \end{pmatrix}. \tag{2.33}$$

The vacuum expectation value (VEV) is chosen to be at

$$\phi_0 = \frac{1}{\sqrt{2}}\begin{pmatrix} 0 \\ v \end{pmatrix} \tag{2.34}$$

and the field is expanded around this minimum as in Eq. (2.31). Inserting this into $\mathscr{L}$ it can be derived that the spontaneous symmetry breaking generates the heavy $W_\mu^\pm$ and

Z_μ^0 bosons while leaving the photon massless [8, 19]. The masses of the gauge bosons are given by

$$m_W = \frac{1}{2}gv \ , \ m_Z = \frac{1}{2}v\sqrt{g^2 + g'^2} \ , \ m_\gamma = 0 \tag{2.35}$$

where g and g' are the coupling constants of the weak and electromagnetic theory, respectively. Note that the W and Z masses are not independent but connected by the relation (cf. Eq. (2.22))

$$m_W = m_Z \cos\theta_W. \tag{2.36}$$

Fermion masses can be generated by the Higgs mechanism as well via a Yukawa coupling (a coupling between a scalar field and a Dirac field)[8]. The masses of the charged fermions are proportional to their coupling to the Higgs boson. Due to the Higgs boson's coupling being proportional to the mass of the charged fermion it couples to, the Higgs boson dominantly decays into the heavy quarks and leptons.

The electroweak model (including the Higgs mechanism) is an extremely predictive model. The weak neutral currents were confirmed in 1974 in a neutrino experiment at the Gargamelle experiment at CERN [20]. The heavy gauge bosons $W_\mu^\pm$ and Z_μ^0 with a mass relation as in Eq. (2.36) were both observed at the UA1 and UA2 collaborations of the SPS $\mathrm{p\overline{p}}$ accelerator at CERN in 1983 [21, 22, 23, 24]. The actual world averages of the W and Z masses are determined to be $m_W = (80.399 \pm 0.023)$ GeV and $m_Z = 91.1876 \pm 0.0021$ GeV [15]. The GSW model also requires the existence of at least one Higgs boson with a free mass m_H. The Higgs boson is the last unobserved parameter of the Standard Model. The Higgs boson with a mass between 141 GeV and 476 GeV is excluded at 95% confidence level (CL) by ATLAS and CMS [25]. Furthermore, a lower bound of 114.4 GeV at 95% CL can be set on the SM Higgs boson mass, obtained from combined LEP searches [26]. Figure 2.6 shows the ATLAS and CMS combined upper limit on the SM Higgs boson cross section over the SM expectation as a function of its mass. Also shown are the limits from LEP and the Tevatron.

Recent ATLAS results [27] provide a possible evidence for the existence of the Higgs boson with a mass of $m_H \approx 126$ GeV. The maximum local significance of this excess amounts 3.6σ above the expected SM background, cf. Fig. A.1.

2.1.5 Current Status of the Standard Model

All elementary particles of the SM have been introduced now. The Standard Model is the combination of QCD and the electroweak theory. The gauge group is therefore $\mathrm{SU(3)} \times \mathrm{SU(2)}_L \times \mathrm{U(1)}_Y$ which is spontaneously broken by the Higgs mechanism to $\mathrm{SU(3)} \times \mathrm{U(1)}_{\mathrm{EM}}$. The leptons $(e, \nu_e, \mu, \nu_\mu, \tau, \nu_\tau)$ and the quarks (u, d, c, s, t, b) interact with the photon γ as well as with the $W^\pm$ and Z^0 bosons whereas the quarks also interact strongly with the gluons g. The Higgs boson H couples to all massive fermions and gauge

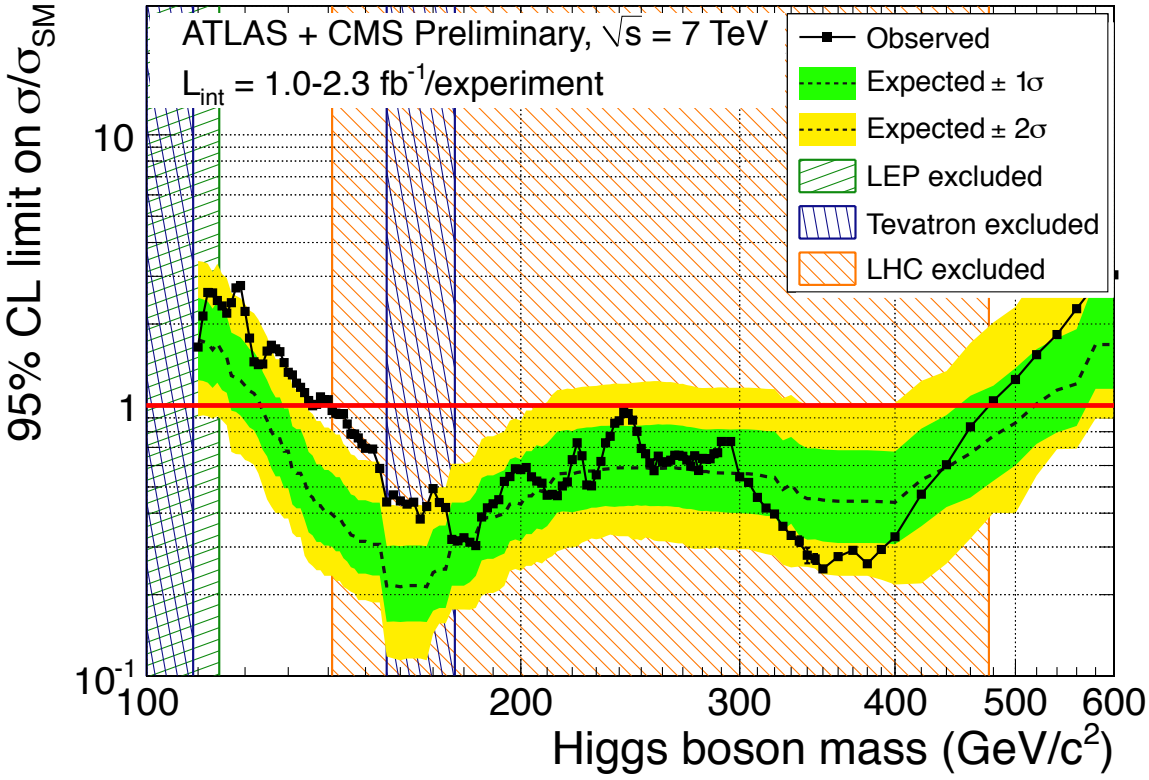

Figure 2.6: The combined 95% C.L. upper limits on the ratio $\sigma/\sigma_{\mathrm{SM}}$, obtained with the CL_s method, as a function of the SM Higgs boson mass in the range $110 - 600$ GeV. The solid points show the observed limits from the combined ATLAS and CMS searches for an integrated luminosity of $1.0 - 2.3\,\mathrm{fb}^{-1}$ per experiment. The dashed line indicates the median expected 95% value for the background-only hypothesis, while the green (yellow) bands indicate the ranges expected to contain 68% (95%) of all observed limit excursions from the median. The SM Higgs boson mass range excluded by the ATLAS and CMS combination is depicted by the hatched orange area. Also shown are the SM Higgs boson mass ranges excluded by LEP (green hatched) and by the Tevatron (blue hatched) [25].

bosons. Additionally, there exist self-interactions of the gluons and the Higgs boson. This is illustrated in Fig. 2.7.

The free parameters of the SM are:

- Three gauge couplings g, g', α_s
- Two parameters of the Higgs potential, namely the Higgs vacuum expectation value v and a linear independent parameter of the Higgs potential (λ or μ),
- six quark masses and three charged lepton masses,
- four parameters of the CKM mixing matrix.

A priori, the neutrinos stay massless. Measurements of neutrino oscillations prove that neutrinos do have a (tiny) mass, though [15, 28]. Massive neutrinos can be added to

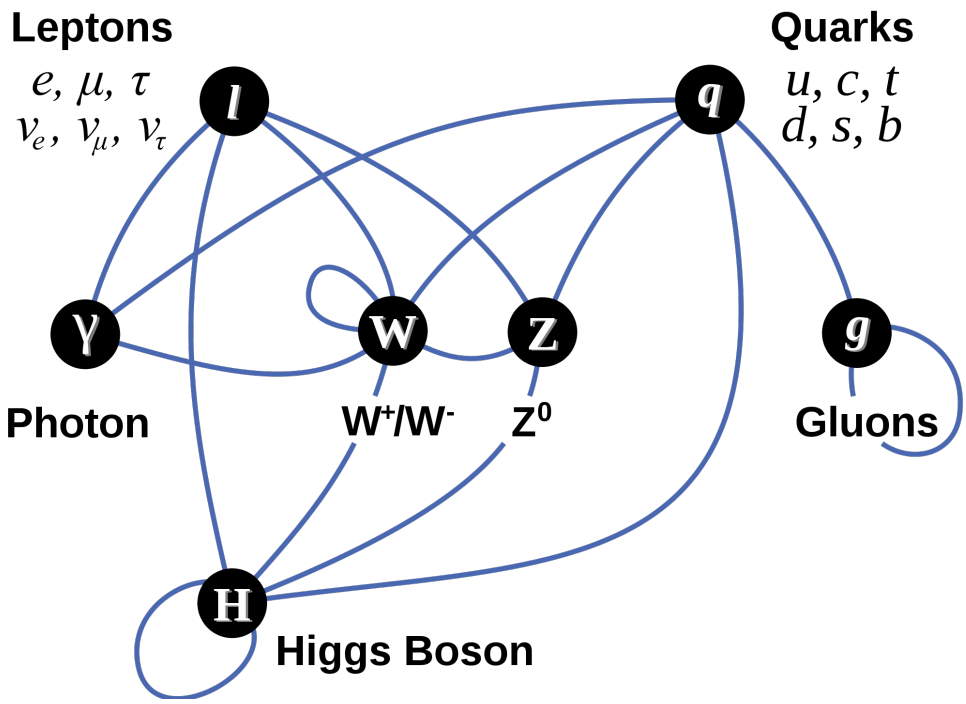

Figure 2.7: The particle content of the Standard Model. The blue lines indicate the couplings of the particles. The leptons and the quarks interact with the photon as well as with the $W^{\pm}$ and Z^0 bosons whereas the quarks also interact strongly with the gluons. The Higgs boson couples to all massive fermions and gauge bosons. Additionally, there exist self-interactions of the gluon, the W boson and the Higgs boson.

the theory, cf. [8, 29]. However, in the SM and supersymmetric extensions, the neutrinos are generally assumed to be massless.
So far, only one complex scalar Higgs field has been considered. However, there is no fundamental reason why all fermions should couple to the same Higgs field. It will be shown in Sec. 2.2 that supersymmetric theories require at least two Higgs doublets. In addition, supersymmetry imposes constraints on the Higgs boson mass (see Ch. 2.2).

The Standard Model provides an extremely successful description of the known phenomena of particle physics. It is a renormalisable theory [30] which means that finite results are obtained for all higher-order (loop) corrections, i.e. the theory is well-defined and calculable. The frontier of high energy experiments has approached the TeV scale and except for the Higgs boson, which has not been found yet, there is an extremely good agreement between the SM predictions and the experiment and so far no sign of physics beyond the SM has emerged. However, there are several unsolved problems which suggest that an extension of the SM is necessary.

2.1.6 Problems of the SM/ Motivation for SUSY

Gauge Hierarchy Problem/ Fine-tuning

There inevitably must be some kind of new physics at the energy scale where quantum gravitational effects become important, i.e. at the scale indicated by the Planck mass

$$M_P \approx 1.2 \times 10^{19} \text{ GeV}. \tag{2.37}$$

This implies that loop integrals need to be *cut-off* at the Planck scale Λ. The four-Higgs-boson self-interaction of Eq. (2.28) has, at one-loop order, a contribution proportional to $\lambda\Lambda\phi^*\phi$ to the $\mu^2\phi^*\phi$ term in the Higgs potential (2.28). The coefficient μ^2 therefore has to be corrected to

$$\mu^2_{\text{phys}} = \mu^2 - \lambda\Lambda. \tag{2.38}$$

The numerical value for $v = 2\mu/\lambda$ has been determined experimentally to $v \approx 246$ GeV which implies

$$\mu_{\text{phys}} \approx \sqrt{\lambda}\, 123 \text{ GeV}. \tag{2.39}$$

In order to treat λ perturbatively it should be of the order of 1 so that μ_{phys} should be of order 100 GeV. But if the cut-off scale Λ is of the order of 10^{19} GeV then μ_{phys} should be significantly larger than 100 GeV. To get the desired value of ~ 100 GeV, a remarkably exact cancellation, or *fine-tuning* would be necessary to get from 10^{19} GeV down to 10^2 GeV. This unnatural fine-tuning involves the Higgs mass $m_H = \sqrt{2}\mu_{\text{phys}}$ as well as all the other masses of the SM which depend on v and thus on μ_{phys}.

If each of the quarks and leptons would be accompanied by complex scalars S with a spin differing by 1/2 but all other quantum numbers being the same, as it is in SUSY theories, the loop corrections of both are identical in its absolute value but with different sign. Thus, the corrections would add to zero. The Λ contributions of Fig. 2.8 to μ_{phys} would cancel.

As SUSY needs to be a broken theory, the divergent contributions do not cancel exactly anymore. However, the quadratically divergent terms cancel and only logarithmically divergent terms remain. In order for those divergences not to be too large, the masses of the newly introduced particles need to be at a scale much smaller that M_P, at best within one order of magnitude of the weak scale (defined by v), so no higher than a few TeV.

Coupling Constants

The three coupling constants of the SM tend to unify at a high $Q^2 \approx (10^{16} \text{ GeV})^2$, but they do not meet exactly, which is quite an unsatisfactory behaviour since the electromagnetic and weak interactions can be unified into the electroweak theory at the scale given by

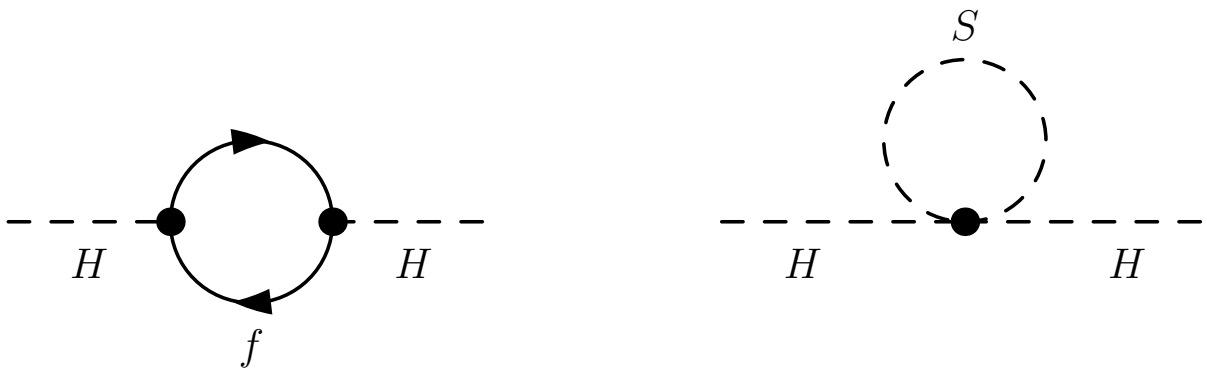

Figure 2.8: One-loop corrections to the Higgs boson mass parameter due to a Dirac fermion f (left). The quadratic divergence of the fermion loop would be compensated by the one-loop correction due to a scalar particle S (right).

$v \approx 246$ GeV. Within the minimal supersymmetric standard model (MSSM) the coupling constants meet exactly at a single unification scale of $10^{16.0\pm0.3}$ GeV (see Fig. 2.9) if the SUSY masses are within 100 GeV $-$ 10 TeV [31] [5]. The MSSM together with the unification requirement additionally provides a prediction for the Weinberg angle ($\sin^2\theta_W$, cf. Eq. (2.22)) which is in perfect agreement with LEP measurements [33]:

$$\sin^2\theta_W^{\text{Exp.}}(M_Z) = 0.2334 \pm 0.0008\,,\ \sin^2\theta_W^{\text{MSSM}}(M_Z) = 0.2333 \pm 0.0008. \tag{2.40}$$

Dark Matter

The SM describes the building blocks of matter. However, this matter only accounts for 4% of the energy density content of the universe. Around 76% is made of dark energy[6] while around 20% is made of dark matter (DM). The measurement of galactic rotation curves which cannot be explained by gravitational interaction of its visible components is a strong indication for the existence of DM. The structure formation in the universe as well as the structure of the microwave background radiation suggest that most DM should be 'cold'. Thus, DM is expected to consist of weakly interacting massive particles (WIMPs). There is no standard model particle that fulfills the necessary requirements for such a WIMP. Certain (R-parity conserving) supersymmetric scenarios would provide a candidate for this, the lightest supersymmetric particle (LSP) [15].

2.2 Supersymmetry in a Nutshell

As already suggested in the last section, Supersymmetry (SUSY) is able to solve several problems of the SM. SUSY is a theory which relates bosonic and fermionic degrees of

[5] Besides, unification can only be achieved with the minimal SUSY model with two Higgs doublets. Including more Higgs doublets would not be compatible with the proton lifetime [31].

[6] Nobel prize in physics 2011 for S. Perlmutter, P. Schmitt and A. Riess for the discovery of the accelerated expansion of the universe through observations of distant supernovae [34].

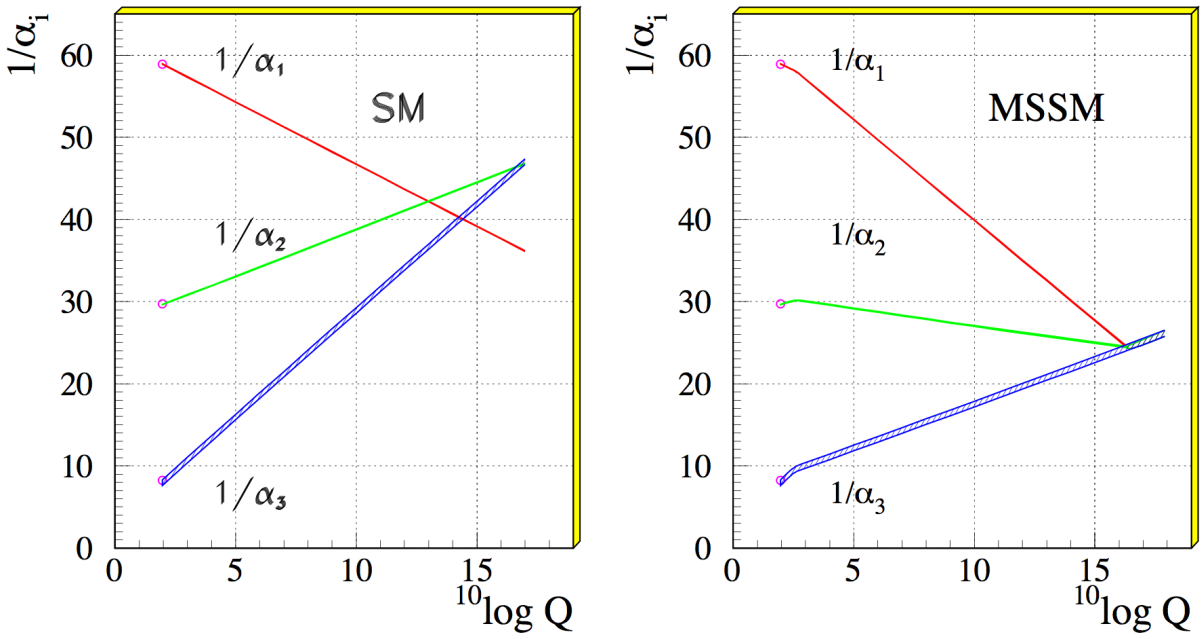

Figure 2.9: Evolution of the inverse coupling constants in the SM (left) and the MSSM (right). The SUSY particles are assumed to contribute only above the effective SUSY scale of about 1 TeV, which causes a change in the slope in the evolution of couplings. The thickness of the lines represents the uncertainty in the coupling constants.[32].

freedom, i.e. a fermionic particle is assigned to each bosonic particle and vice versa. So, there exists a SUSY generator Q with

$$Q|\text{fermion}\rangle = |\text{boson}\rangle. \tag{2.41}$$

Supersymmetry is a technically rather complicated theory, which cannot be reviewed in all its detail here. However, in order to motivate the search for SUSY particles, a glimpse into the basic ideas of the theory and its phenomenological consequences shall be provided in this chapter [35, 36].

After an introduction to the basic concepts of SUSY, the minimal supersymmetric extension of the SM (MSSM) is presented. It is the simplest SUSY theory consistent with the SM observations. In the subsequent section, the basic principle of SUSY breaking and the special scenario *mSUGRA* [37] is introduced. At the end of this chapter, some phenomenological consequences for the LHC SUSY searches are shown.

2.2.1 Basic Concept

It was motivated in the previous section (Sec. 2.1) that most of the attributes of the interactions between elementary particles can be gained from symmetry principles. One may therefore ask whether the SM exploits all symmetries which could exist (consistent with Lorentz invariance) or whether there may be others that could suit an extension of the

SM. In fact, it is possible to introduce 'charges' which transform under Lorentz transformation as *spinors*. Such a spinorial charge operator Q_a must fulfill an anti-commutation relation of the form [35]

$$\{Q_a, Q_b^\dagger\} \sim P_\mu \tag{2.42}$$

with P_μ being the 4-momentum operator[7]. This relation already shows a remarkable new feature of SUSY: The anti-commutator of two SUSY transformations, when applied to a field, gives back the derivative of the original field. So, Q is proportional to the square root of a space-time operator. This enlarges the concept of space-time to further fermionic dimensions (*superspace*) [35, 36].
In general, a symmetry is characterised by the requirement of the invariance of a Lagrangian under a certain infinitesimal transformation of the form

$$\delta_\xi \psi_r = -i\xi\lambda_{rs}\psi_s \tag{2.43}$$

where ξ is an infinitesimal parameter and λ_{rs} are certain coefficients. As already suggested by Eq. (2.41) the SUSY transformations will transform bosonic fields ϕ into fermionic fields χ, explicitly

$$\delta_\xi \phi = \xi^T(-i\sigma_2)\chi \equiv \xi \cdot \chi \tag{2.44}$$

and

$$\delta_\xi \chi_a = -[i\sigma^\mu(i\sigma_2\xi^*)]_a \partial_\mu \phi. \tag{2.45}$$

and similar for the hermitian conjugates of the fields. For this to be valid, the infinitesimal parameter ξ has to be a spinor. Here, χ is a two-component Weyl fermion[8].
The simplest supersymmetric Lagrangian (invariant under the above transformations) consists of a free complex spin-0 field ϕ and a free left-handed (L-type) spinor field χ, both being massless. The free Lagrangian is given by

$$\mathscr{L}_{\text{free}} = \partial_\mu \phi^\dagger \partial^\mu \phi + \chi^\dagger i\bar{\sigma}^\mu \partial_\mu \chi. \tag{2.46}$$

The Wess-Zumino Model of Interactions

Interactions can be added to the theory by the Wess-Zumino model [39, 40]. The most general Lagrangian involving interactions is given by

$$\mathscr{L}_{\text{WZ}} = \mathscr{L}_{\text{free}} - |W_i|^2 - \frac{1}{2}\big(W_{ij}\chi \cdot \chi + \text{h.c.}\big) \tag{2.47}$$

[7] Eq. (2.42) is of cause not correct because there is an uncontracted Lorentz index μ but gives a first gist of the correct SUSY algebra. The SUSY algebra turns out to be $\{Q_a, Q_b^\dagger\} = (\sigma^\mu)_{ab}P_\mu$, $\{Q_a, Q_b\} = 0 = \{Q_a^\dagger, Q_b^\dagger\}$ and $[Q_a, P_\mu] = 0 = [Q_a^\dagger, P_\mu]$ with $\sigma_\mu \equiv (1, \vec{\sigma})$, $\bar{\sigma}_\mu \equiv (1, -\vec{\sigma})$. The last equality comes from the fact that Q_a is assumed to be x-independent, i.e., only global symmetries are considered. Making SUSY local leads to *supergravity* [35, 38] which is discussed in Sec. 2.2.3.

[8] One can decompose a Dirac spinor Ψ into two two-component Weyl spinors ψ and χ. ψ can be expressen in terms of χ and vice versa by hermitian conjugation. In this notation, the Dirac Lagrangian from Eq. 2.1 can be written as $\mathscr{L}_{\text{Dirac}} = i\xi^\dagger\bar{\sigma}^\mu\partial_\mu\xi + i\chi^\dagger\bar{\sigma}^\mu\partial_\mu\chi - m(\xi\chi + \xi^\dagger\chi^\dagger)$.

where W_i and W_{ij} are given by the *superpotential* W which encodes all the allowed interactions:

$$W = \frac{1}{2}M\phi^2 + \frac{1}{6}\lambda\phi^3 \tag{2.48}$$

via

$$W_i = \frac{\partial W}{\partial \phi} = M\phi + \frac{1}{2}\lambda\phi^2 \ , \quad W_{ij} = \frac{\partial^2 W}{\partial \phi^2} = M + \lambda\phi. \tag{2.49}$$

So, the interaction terms of the Lagrangian (2.47) are given by

$$-\underbrace{|M|^2\phi^\dagger\phi - \frac{1}{2}M\chi\chi}_{\text{quadratic int.}} - \underbrace{\frac{1}{2}(M\lambda^*\phi\phi^{\dagger 2} + M^*\lambda\phi^2\phi^\dagger)}_{\text{cubic int.}} - \underbrace{\frac{1}{4}|\lambda|^2\phi^2\phi^{\dagger 2}}_{\text{quartic int.}} - \underbrace{\frac{1}{2}(\lambda\phi\chi\chi)}_{\text{Yukawa int.}}. \tag{2.50}$$

M is the mass matrix for the fermions and λ is the usual Yukawa coupling of a scalar ϕ and two fermions $\psi\psi$ [36]. The quadratic terms in Eq. 2.50 describe free spin-0 and spin-1/2 fields which are degenerate and have mass $|M|$. So, the existence of massive SUSY particles is possible, in contrast to the SM where fermion masses are forbidden in an unbroken chiral gauge theory. There are three interactions allowed in the Wess-Zumino model, namely interaction terms cubic and quartic in ϕ as well as Yukawa-type couplings between ϕ and χ fields. As one can see from Eq. (2.50), the quartic coupling constant is the square of the Yukawa coupling. This is exactly what is required for the cancellation of quadratic divergences in the bosonic self-energy [36, 35].

2.2.2 The MSSM

The minimal supersymmetric extension of the Standard Model (MSSM) is the most general SUSY model which is minimal in terms of its particle content and is based on the SM Lagrangian.

Particle Content of the MSSM

The particles of the MSSM reside in *supermultiplets* where each supermultiplet contains both fermions and bosons which are *superpartners* of each other. Eq. (2.46) contains one massless complex scalar field and one massless Weyl fermion field. Such fields form a *chiral supermultiplett*. In addition to this, *gauge* or *vector* supermultiplets occur in the MSSM, where a massless spin-1 field is partnered with a massless Weyl fermion field. The squared-mass operator $-P^2$ commutes with Q, $Q^\dagger$ and with all spacetime rotations and translations. Therefore, the particles in a supermultiplet must have the same eigenvalue of $-P^2$ and thus must be degenerate in mass. If the superpartners had the same mass as the SM particles, one would have already observed them. This is why SUSY must be a broken theory (see Sec. 2.2.3). Moreover, the SUSY transformations leave the $\mathrm{SU}(3)_c \times \mathrm{SU}(2)_L \times \mathrm{U}(1)_Y$ symmetry invariant (cf. Sec. 2.1.5). This implies that each SM field and its partner in a supermultiplet must have the same quantum numbers (electric charge,

weak isospin and colour degrees of freedom).
There are no particles in the SM that could be partnered in such a way. The gluon, for example, transforms under the eight-dimensional representation of SU(3) and is a flavour singlet. None of the SM fermions has these quantum numbers, so that a new superpartner of the gluon has to be postulated. The same holds for all the other SM particles. Thus, a new particle for each SM particle needs to be introduced.
SM particles and their superpartners share the same symbol, but with a tilde being assigned to the SUSY particles. The partners of the gauge bosons are called *gauginos* and get a '*-ino*' appended to their name. The superpartners of the SM fermions are called *squarks* and *sleptons*. The names of the superpartners of the SM fermions receive a '*s-*' prepended (*selectrons, smuons, staus* and their *sneutrinos*, etc.).
The superpartner of the gluon is called *gluino* $\tilde{g}$ which is a Weyl fermion and resides in a SU(3) octet. Similarily to the gluinos, a $\mathrm{SU}(2)_L$ triplet of Weyl fermions, called *winos* ($\tilde{W}^{\pm}$, $\tilde{W}^0$) and a $\mathrm{U}(1)_Y$ *bino* ($\tilde{B}$) need to be introduced as partners for the gauge bosons of electroweak interactions. After electroweak symmetry breaking, the gauge eigenstates mix to give mass eigenstates Z^0 and γ whose superpartners are called *zino* $\tilde{Z}^0$ and *photino* $\tilde{\gamma}$. The $\mathrm{SU}(2)_L$ doublet of electron and electron-neutrino must be partnered with a doublet of spin-0 bosons with the same quantum numbers,

$$\begin{pmatrix} \nu_{eL} \\ e_L \end{pmatrix} \text{ partnered by } \begin{pmatrix} \tilde{\nu}_{eL} \\ \tilde{e}_L \end{pmatrix} \tag{2.51}$$

and similarily for the other lepton families as well as for the quarks. Since the left-handed and right-handed components of the quarks and leptons transform differently under the corresponding gauge symmetry, each component needs its own complex scalar partner. These are all chiral supermultiplets, $S\mathrm{U}(2)_L$ doublets and carry the same lepton numbers as their SM partners (although being bosons). The gauge interactions of the squarks and sleptons are the same as for their SM fields, namely the left-handed squarks $\tilde{u}_L$ and $\tilde{d}_L$ couple to the W bosons while the right-handed squarks $\tilde{u}_R$ and $\tilde{d}_R$ do not. The handedness does not refer to the helicity of the sfermions since they are spin-0 bosons but to that of their superpartners. It is emphasised that there are two physical superpartners for each of the charged leptons and quarks, one for the left-handed and one for the right-handed polarisation.

An important consequence of imposing supersymmetry on the SM is that two separate Higgs doublets are required. The reason is that in the SM, Yukawa interactions involving the Higgs field $\phi = (\phi^+, \phi^0)$ give masses to the $Y = -1/2$ component of the fermion doublets when ϕ^0 aquires a vacuum expectation value. The masses for the $Y = +1/2$ components are generated via interactions with the charge-conjugated field $\phi_c = i\sigma_2\phi^{\dagger T}$. Now, the hermitian conjugate of a left-handed superfield is right-handed and vice versa. But

in the MSSM, only left- or right-handed superfields are allowed to enter the Lagrangian so that the coupling to a hermitian conjugate Higgs superfield is forbidden[9]. Thus one arrives at two chiral Higgs supermultiplets, one with $Y = 1/2$, denoted with H_u for the up-type quarks (u,c,t) and one with $Y = -1/2$ (H_d) for the down-type quarks (d,s,b) and the charged leptons:

$$H_u : \begin{pmatrix} H_u^+ \\ H_u^0 \end{pmatrix} , \begin{pmatrix} \tilde{H}_u^+ \\ \tilde{H}_u^0 \end{pmatrix} \tag{2.52}$$

and

$$H_d : \begin{pmatrix} H_d^0 \\ H_d^- \end{pmatrix} , \begin{pmatrix} \tilde{H}_d^0 \\ \tilde{H}_d^- \end{pmatrix} . \tag{2.53}$$

The superpotential for the MSSM which includes all allowed interactions is given by

$$W_{\text{MSSM}} = \bar{u}\mathbf{y_u}QH_u - \bar{d}\mathbf{y_d}QH_d - \bar{e}\mathbf{y_e}LH_d + \mu H_u H_d \tag{2.54}$$

where H_u, H_d, Q, L, $\bar{u}$, $\bar{d}$, $\bar{e}$ are chiral superfields. $\mathbf{y_u}$, $\mathbf{y_d}$ and $\mathbf{y_e}$ are the 3×3 dimensionless Yukawa coupling matrices. The μ term is the supersymmetric version of the Higgs boson mass in the SM.

The particle content of the MSSM is summarised in Tab. 2.3 for the chiral supermultiplets and Tab. 2.4 for the gauge supermultiplets.

Table 2.3: Chiral supermultiplets in the MSSM. The spin-0 fields are complex scalars and the spin-1/2 fields are left-handed two-component Weyl fermions.

Names		spin 0	spin 1/2
squarks, quarks	Q	$(\tilde{u}_L, \tilde{d}_L)$	(u_L, d_L)
	$\bar{u}$	$\tilde{\bar{u}}_L = \tilde{u}_R^\dagger$	$\bar{u}_L$
	$\bar{d}$	$\tilde{\bar{d}}_L = \tilde{d}_R^\dagger$	$\bar{d}_L$
sleptons, leptons	L	$(\tilde{\nu}_{eL}, \tilde{e}_L)$	$\bar{e}_L$
	$\bar{e}$	$\tilde{\bar{e}}_L = \tilde{e}_R^\dagger$	$\bar{e}_L$
Higgs, Higgsinos	H_u	(H_u^+, H_u^0)	$(\tilde{H}_u^+, \tilde{H}_u^0)$
	H_d	(H_d^0, H_d^-)	$(\tilde{H}_d^0, \tilde{H}_d^-)$

Table 2.4: Gauge or vector supermultiplets in the MSSM. The spin-1 fields are complex scalars and the spin-1/2 fields are left-handed two-componment Weyl fermions.

Names	spin 1/2	spin 1
gluinos, gluons	$\tilde{g}$	g
winos, W bosons	$\tilde{W}^\pm, \tilde{W}^0$	$W^\pm, W^0$
bino, B bosons	$\tilde{B}$	B

[9] Moreover, one single Higgs chiral supermultiplet would lead to gauge anomalies in the electroweak gauge symmetry, cf. [36, 8].

Mass Eigenstates

The sparticle fields from Tab. 2.3 and 2.4 are not necessarily mass eigenstates. The mass matrices in gauge eigenstates can be diagonalised by a unitary transformation to obtain the mass eigenstates.
Just like in the SM, the electroweak symmetry breaking of the MSSM leads to the absorption of three degrees of freedom of the Higgs fields (Goldstone bosons) by the gauge bosons. The existence of two Higgs supermultiplets leads to five physical Higgs fields, the relatively light neutral scalar Higgs boson h^0, the heavy scalar H^0, the heavy pseudoscalar A^0 and two charged Higgs fields $H^{\pm}$. In the framework of the MSSM, an upper bound on the mass of the lightest neutral Higgs boson h^0 can be found to be [36]

$$m_{h^0} \lesssim 135 \text{ GeV} \tag{2.55}$$

This assumes that the masses of all sparticles contributing to the loop corrections of m_{h^0} do not exceed 1 TeV. Without this constraint there still is an upper limit of ~ 150 GeV on the mass of the light Higgs boson [41, 42, 36]. Hence, a light Higgs boson as it is favoured by the electroweak data is natural in SUSY. On the other hand, most MSSM models are unfeasible if the existence of the Higgs boson is excluded experimentally up to the masses stated above.

The winos ($\tilde{W}$) and binos ($\tilde{B}$) are not mass eigenstates because of splitting and mixing due to electroweak symmetry breaking [36]. The electrically charged winos and the charged Higgsinos mix to produce the *charginos* $\tilde{\chi}_1^{\pm}$ and $\tilde{\chi}_2^{\pm}$. The electrically neutral wino, the bino and the two neutral parts of the Higgsinos mix to the *neutralinos* $\tilde{\chi}_i^0, i = 1, ...4$. After electroweak symmetry breaking, particles with identical spin and charges can mix arbitrarily, depending on the choice of the free parameters. Especially for the mass eigenstates of the heavy stop and sbottom there is a significant mixing of the left- and right-handed squarks [43, 36]. The gauge eigenstates and the corresponding mass eigenstates are summarised in Tab. 2.5.

R-Parity

A priori, the most general MSSM Lagrangian allows the proton to decay via e.g.
$p \to \pi^0 + e^+$ (see Fig. 2.10).

If the coupling constants λ' and λ'' are assumed to be of order 1 and the squark mass $m_{\tilde{q}} \sim 1$ TeV, then the lifetime of the proton would be much smaller than 1 s. This is certainly not the case; the proton is stable, or at least has a half-life larger that $\sim 10^{34}$ years [44]. This problem can be solved by imposing a new symmetry, called R-parity [36, 35]. It is a multiplicative quantum number which is defined by

$$R = (-1)^{3B+L+2s} \tag{2.56}$$

Table 2.5: Gauge and mass eigenstates for the unobserved particles of the MSSM. P_R denotes the value of the R-parity quantum number. The squark and slepton mixing is assumed to be negligible for the first two families [36].

Names	Spin	P_R	Gauge eigenstates	Mass eigenstates
Higgs bosons	0	+1	$H_u^0, H_d^0, H_u^+, H_d^-$	$h^0, H^0, A^0, H^\pm$
Squarks	0	-1	$\tilde{u}_L, \tilde{u}_R, \tilde{d}_L, \tilde{d}_R$	(same)
			$\tilde{s}_L, \tilde{s}_R, \tilde{c}_L, \tilde{c}_R$	(same)
			$\tilde{t}_L, \tilde{t}_R, \tilde{b}_L, \tilde{b}_R$	$\tilde{t}_1, \tilde{t}_2, \tilde{b}_1, \tilde{b}_2$
Sleptons	0	-1	$\tilde{e}_L, \tilde{e}_R, \tilde{\nu}_e$	(same)
			$\tilde{\mu}_L, \tilde{\mu}_R, \tilde{\nu}_\mu$	(same)
			$\tilde{\tau}_L, \tilde{\tau}_R, \tilde{\nu}_\tau$	$\tilde{\tau}_1, \tilde{\tau}_2, \tilde{\nu}_\tau$
Neutralinos	1/2	-1	$\tilde{B}^0, \tilde{W}^0, \tilde{H}_u^0, \tilde{H}_d^0$	$\tilde{\chi}_1^0, \tilde{\chi}_2^0, \tilde{\chi}_3^0, \tilde{\chi}_4^0$
Charginos	1/2	-1	$\tilde{W}^\pm, \tilde{H}_u^+, \tilde{H}_d^-$	$\tilde{\chi}_1^\pm, \tilde{\chi}_2^\pm$
Gluino	1/2	-1	$\tilde{g}$	(same)
Goldstino	1/2	-1	$\tilde{G}$	(same)
(Gravitino)	(3/2)	-1	?	(same)

where B, L and s denote baryon number, lepton number and spin, respectively. The definition of R implies $R = +1$ for all SM particles and $R = -1$ for all sparticles. If R-parity is conserved (then R has to be $+1$ at each vertex), this has some very important consequences:

- Vertices have an even number of superpartners. Thus the proton decay is forbidden.
- At collider experiments, sparticles can only be produced in pairs.
- Each sparticle decays into another sparticle and a SM particle.
- Thus, there exists a lightest supersymmetric particle (LSP) which is stable.

If the LSP is neutral and a SU(3) singlet (colourless), then the LSP is only interacting weakly and a candidate for the Dark Matter (WIMP).

2.2.3 SUSY Breaking

As already stated above, SUSY must be a broken symmetry because otherwise the particles in a supermultiplet (consisting of a SM particle an its corresponding superpartner) would need to be degenerate in mass. If that would be the case, SUSY particles would have already been observed.
Broken SUSY can still provide a solution to the SM fine-tuning problem. The radiative

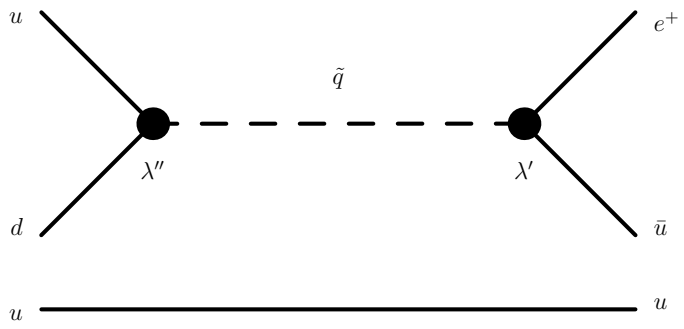

Figure 2.10: The decay of the proton in the MSSM: The u and d quarks from the proton (uud) couple via a coupling λ'' to the squark $\tilde{q}$ which decays via a coupling λ' to a positron and a $\bar{u}$ quark. This results in the decay $p \to \pi^0 + e^+$.

corrections do not cancel exactly anymore, but SUSY is able to *stabilise* the hierarchy $m_H \ll M_P$ in the sense that radiative corrections will not drag m_H up to the high scale Λ. For the desired stabilisation to occur, the sparticle masses need to be of the order of 1 TeV.

In general, there are two ways how a symmetry can be broken. The first is spontaneous symmetry breaking which was introduced for the SM in Sec. 2.1.4. Within the SM this is the only way of symmetry breaking without spoiling renormalizability. The second one is to introduce explicit SUSY-breaking terms in the Lagrangian which decouples the origin of supersymmetry breaking (spontaneous symmetry breaking in another sector) from its phenomenological low-energy consequences. The explicit SUSY breaking is generally favoured as the exact SUSY breaking mechanism is unknown [35]. Such SUSY-breaking terms need to be *soft* which means that the effective Lagrangian can be written as

$$\mathscr{L} = \mathscr{L}_{\text{SUSY}} + \mathscr{L}_{\text{soft}} \tag{2.57}$$

where the first part contains all gauge and Yukawa couplings and is SUSY invariant whereas the second (SUSY-breaking) term only contains mass terms and coupling parameters with *positive* mass dimension [36]. Divorcing the spontaneous supersymmetry breaking from the supersymmetric Standard Model leads to the notion of mediated supersymmetry breaking. Such a model maintains the cancellation of quadratically divergent terms in the radiative corrections of all scalar masses to all orders in perturbation theory. Thus, SUSY can still provide a solution for the fine-tuning problem. This only holds if the masses of at least the lightest SUSY particles amount at most about 1 TeV in order for the MSSM scalar potential to provide a Higgs VEV resulting in the known W and Z boson masses without miraculous cancellation. This is the main reason why SUSY particles, if existing, are expected to be discovered at the LHC.
The most general soft SUSY-breaking Lagrangian which is compatible with gauge invari-

ance and R-parity conservation in the MSSM is given by

$$\begin{aligned}\mathscr{L}_{\text{soft}}^{\text{MSSM}} = &-\frac{1}{2}\left(M_3\tilde{g}\tilde{g} + M_2\tilde{W}\tilde{W} + M_1\tilde{B}\tilde{B} + \text{c.c.}\right)\\ &-\left(\tilde{u}\mathbf{a_u}\tilde{Q}H_u - \tilde{\bar{d}}\mathbf{a_d}\tilde{Q}H_d - \tilde{e}\mathbf{a_e}\tilde{L}H_d + \text{c.c.}\right)\\ &-\tilde{Q}^\dagger\mathbf{m_Q^2}\tilde{Q} - \tilde{L}^\dagger\mathbf{m_L^2}\tilde{L} - \tilde{u}\mathbf{m_{\bar{u}}^2}\tilde{u}^\dagger - \tilde{\bar{d}}\mathbf{m_{\bar{d}}^2}\tilde{\bar{d}}^\dagger - \tilde{e}\mathbf{m_{\bar{e}}^2}\tilde{e}^\dagger\\ &-m_{H_u}^2H_u^*H_u - m_{H_d}^2H_d^*H_d - (bH_uH_d + \text{c.c.}).\end{aligned} \tag{2.58}$$

M_3, M_2 and M_1 are the gluino, wino and bino masses, respectively. So the first line of Eq. (2.58) gives the mass terms for gluino, wino and bino. The second line contains the (scalar)^3 couplings and the third line represents the squark and slepton mass terms. The last line shows the SUSY-breaking contributions to the Higgs potential. The $\mathbf{a}$'s are complex 3×3 matrices in family space and correspond to the Yukawa couplings of the superpotential of Eq. (2.54). The $\mathbf{m^2}$'s are hermitian 3×3 matrices in family space. It is expected that the mass parameters lie in roughly the same order of magnitude,

$$M_1, M_2, M_3, \mathbf{a_u}, \mathbf{a_d}, \mathbf{a_e} \sim m_{\text{soft}}\,, \tag{2.59}$$

$$\mathbf{m_Q^2}, \mathbf{m_L^2}, \mathbf{m_{\bar{u}}^2}, \mathbf{m_{\bar{d}}^2}, \mathbf{m_{\bar{e}}^2}, m_{H_u}^2, m_{H_d}^2, b \sim m_{\text{soft}}^2 \tag{2.60}$$

with a mass scale m_{soft} of the order of 1 TeV.

Unfortunately, the most general MSSM model with soft supersymmetry breaking terms re-introduces over 100 new parameters, namely 30 masses, 9 for fermions and 21 for scalars, 39 mixing angles as well as 40 phases [45] which leads to an immense arbitrariness in the Lagrangian [36].

In order to be able to make any prediction of the free parameters and to define search channels for the LHC SUSY searches, it is vital to impose some strong constraints and thus simplify the model. A prominent example of a mediated SUSY breaking with much less free parameters is the *minimal supergravity* model or mSUGRA (also known as *constrained MSSM* (CMSSM)).

mSUGRA

SUSY breaking is assumed to occur in a 'hidden sector' (at a very high energy scale) of particles that have only very small direct coupling to the 'visible sector' (the energy sector which is accessible for experiment) of the MSSM. By this coupling the SUSY breaking is *mediated* from the hidden to the visible sector, resulting in the soft terms in the MSSM Lagrangian. One of the most regarded theories is the *gravity-mediated* or *Planck-scale-mediated* supersymmetry breaking.

Spontaneous global SUSY breaking implies the existence of the *goldstino* which is a massless Weyl fermion. When taking gravity into account, SUSY must be a *local* symmetry

and is then called *supergravity*. The particle content of the MSSM is then extended by a supermultiplet of a spin-2 graviton and a spin-3/2 gravitino. The latter is the gauge field of local SUSY transformations. By spontaneous SUSY breaking, the gravitinos aquire a mass by absorbing the goldstino (cf. Sec. 2.1.4). This is called the *super-Higgs* mechanism. However, the gravitino will not play any role in collider experiments as the interactions of the gravitino will only be of gravitational strength.
The mSUGRA (minimal SUper GRAvity) model is an appealing and intensively investigated model as it reduces the number of free parameters to five. In terms of these, the parameters appearing in Eq. (2.58) take a particularly simple form at the GUT scale:

$$M_3 = M_2 = M_1 = m_{1/2}, \tag{2.61}$$

$$\mathbf{m_Q^2}, \mathbf{m_L^2}, \mathbf{m_{\bar{u}}^2}, \mathbf{m_{\bar{d}}^2}, \mathbf{m_{\bar{e}}^2} = m_0^2\mathbf{1},\ m_{H_u}^2, m_{H_d}^2 = m_0^2 \tag{2.62}$$

$$\mathbf{a_u} = A_0\mathbf{y_u}, \mathbf{a_d} = A_0\mathbf{y_d}, \mathbf{a_e} = A_0\mathbf{y_e}. \tag{2.63}$$

m_0 and $m_{1/2}$ are the scalar mass and the gaugino mass at the GUT scale, respectively. So at the GUT scale, all squarks and sleptons are degenerate in mass and thus squarks and sleptons with the same electroweak quantum numbers can transform into each other by unitary transformations. A_0 is the trilinear scalar coupling constant. All mixings apart from this one can be eliminated [35]. The evolution of the soft parameters down to the electroweak scale allows the prediction of the entire MSSM spectrum in terms of just five parameters, $m_{1/2}, m_0, A_0$ as well as $\tan\beta$, the ratio of the vacuum expectation values of the Higgs fields and the sign of μ, the sign of the Higgsino mass term (plus the already measured gauge and Yukawa couplings) [36]. Fig. 2.11 shows the mass spectrum of a benchmark point in the mSUGRA parameter space, called SU4, with $m_0 = 200$ GeV, $m_{1/2} = 160$ GeV, $A_0 = -400$ GeV, $\tan\beta = 10$ and $\mu > 0$ (see also Fig. 2.20).

2.2.4 SUSY Signatures at the LHC

It is for the experiment to decide whether SUSY is realised in nature or not. Due to the large number of free parameters of the MSSM, there is a tremendous number of a priori allowed production and decay channels which require different analyses. This makes the quest for SUSY so difficult.
At hadron colliders such as the LHC, sparticles are mainly produced in pairs from collisions of QCD strength, namely

$$gg \to \tilde{g}\tilde{g},\ \tilde{q}_i\tilde{q}_j^*, \tag{2.64}$$

$$gq \to \tilde{g}\tilde{q}_i, \tag{2.65}$$

$$q\bar{q} \to \tilde{g}\tilde{g},\ \tilde{q}_i\tilde{q}_j^*, \tag{2.66}$$

$$qq \to \tilde{q}_i\tilde{q}_j \tag{2.67}$$

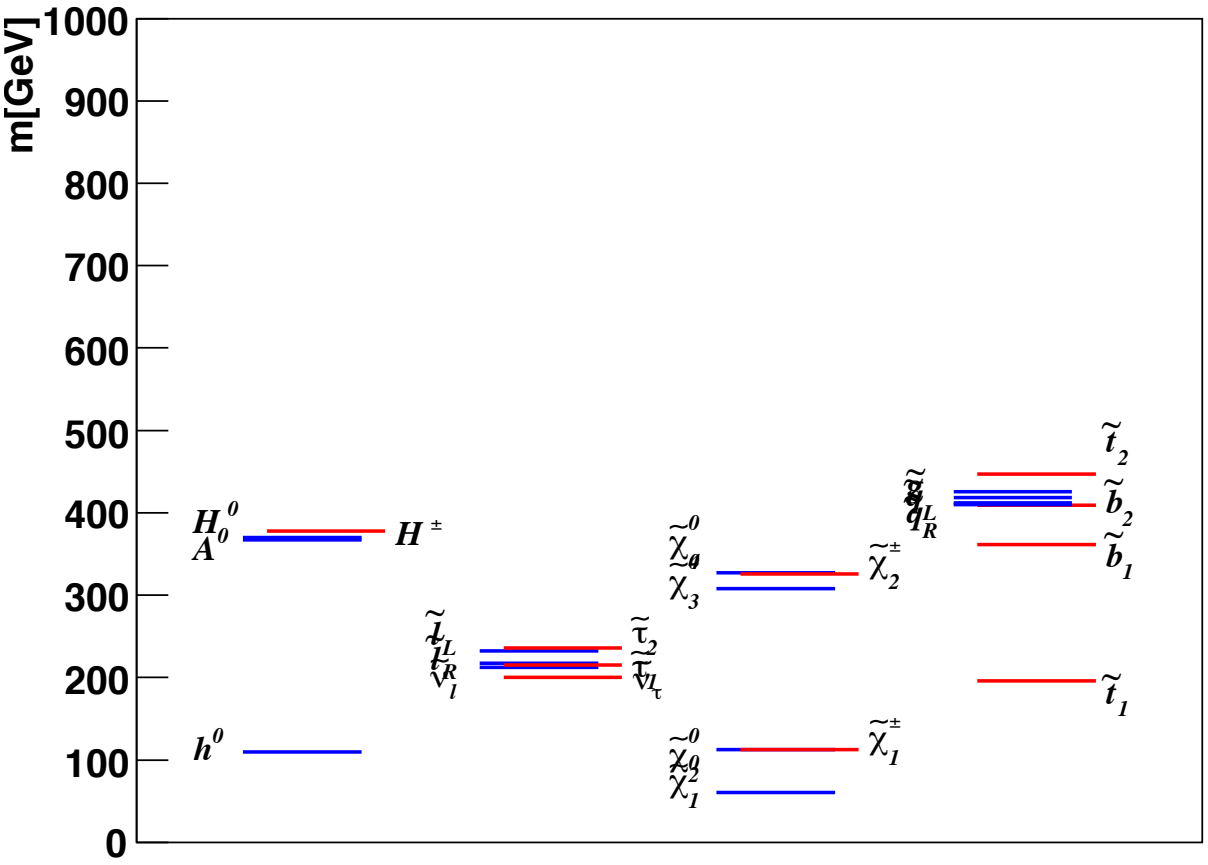

Figure 2.11: Mass spectrum for the mSUGRA SU4 point ($m_0 = 200$ GeV, $m_{1/2} = 160$ GeV, $A_0 = -400$ GeV, $\tan\beta = 10$ and $\mu > 0$). The mass hierarchy is calculated with the program ISAJET [46].

as shown in Fig. 2.12 and 2.13. Sparticle production of electroweak strength such as

$$q\bar{q} \to \tilde{\chi}_i^+ \tilde{\chi}_j^-,\ \tilde{\chi}_i^0 \tilde{\chi}_j^0, \quad u\bar{d} \to \tilde{\chi}_i^+ \tilde{\chi}_j^0, \quad d\bar{u} \to \tilde{\chi}_i^- \tilde{\chi}_j^0, \tag{2.68}$$

$$q\bar{q} \to \tilde{\ell}_i^+ \tilde{\ell}_j^-,\ \tilde{\nu}_\ell \tilde{\nu}_\ell^*, \quad u\bar{d} \to \tilde{\ell}_L^+ \tilde{\nu}_\ell, \quad d\bar{u} \to \tilde{\ell}_L^- \tilde{\nu}_\ell^* \tag{2.69}$$

as shown in Fig. 2.14 are strongly suppressed. They may be relevant anyhow because charginos and neutralinos are produced directly.

Sparticle Decays

There are various decay modes of the sparticles. In this study, a search channel with exactly two oppositely charged leptons is chosen. A decay into two leptons in the final state is phenomenologically important because of the resulting clean signal. Thus, an emphasis is laid here on decays relevant for the dilepton analysis.

The neutralinos and charginos have an admixture of electroweak gauginos $\tilde{B}$, $\tilde{W}^0$ or $\tilde{W}^\pm$. Therefore, a neutralino or chargino can decay into lepton+slepton or quark+squark, if the sleptons or squarks are sufficiently light. As sleptons are assumed to be lighter

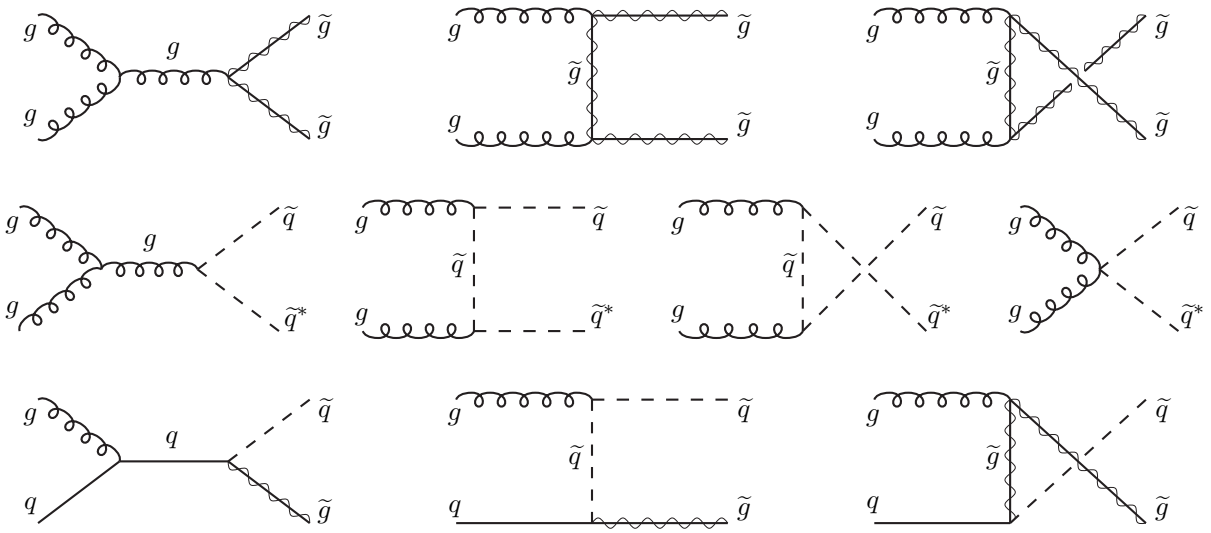

Figure 2.12: Feynman diagrams for squark and gluino production at hadron colliders from gluon-gluon and gluon-quark fusion [36].

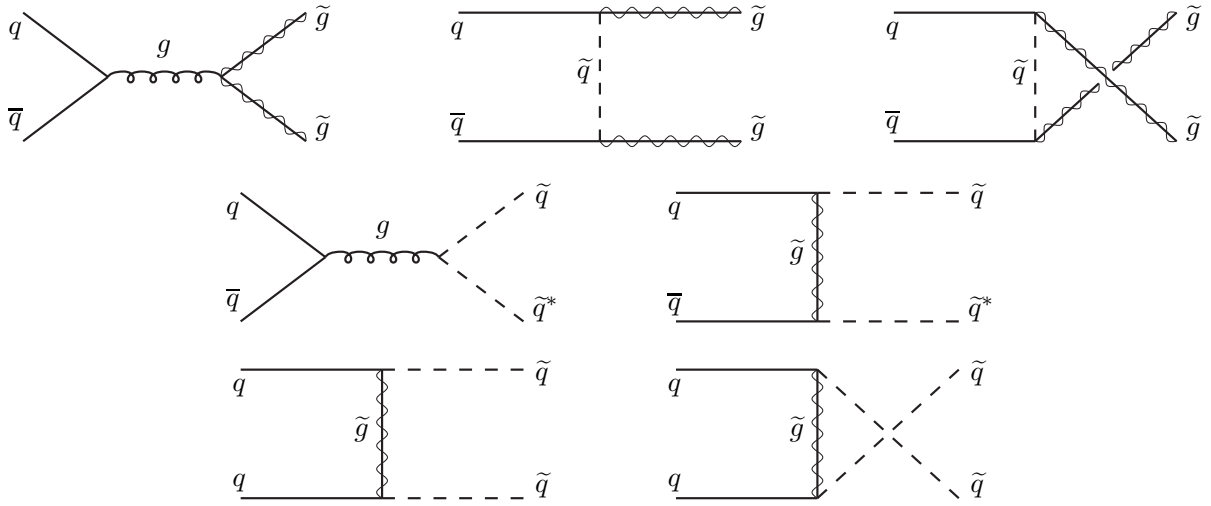

Figure 2.13: Feynman diagrams for squark and gluino production at hadron colliders from strong quark-antiquark annihilation and quark-quark scattering [36].

than squarks [36], the lepton+slepton decay is favoured. If these two-body decays are kinematically forbidden, it is possible that the neutralinos and charginos decay via an off-shell slepton (three-body decay). Sleptons have a gaugino admixture and thus can decay into a lepton and a chargino or neutralino,

$$\tilde{\ell} \to \ell \tilde{\chi}_i^0, \quad \tilde{\ell} \to \ell \tilde{\chi}_i^{\pm}. \tag{2.70}$$

The neutralino and chargino decays into the LSP and two leptons are shown in Fig. 2.15. The main SUSY decays involving leptons in the final state are (omitting the intermediate

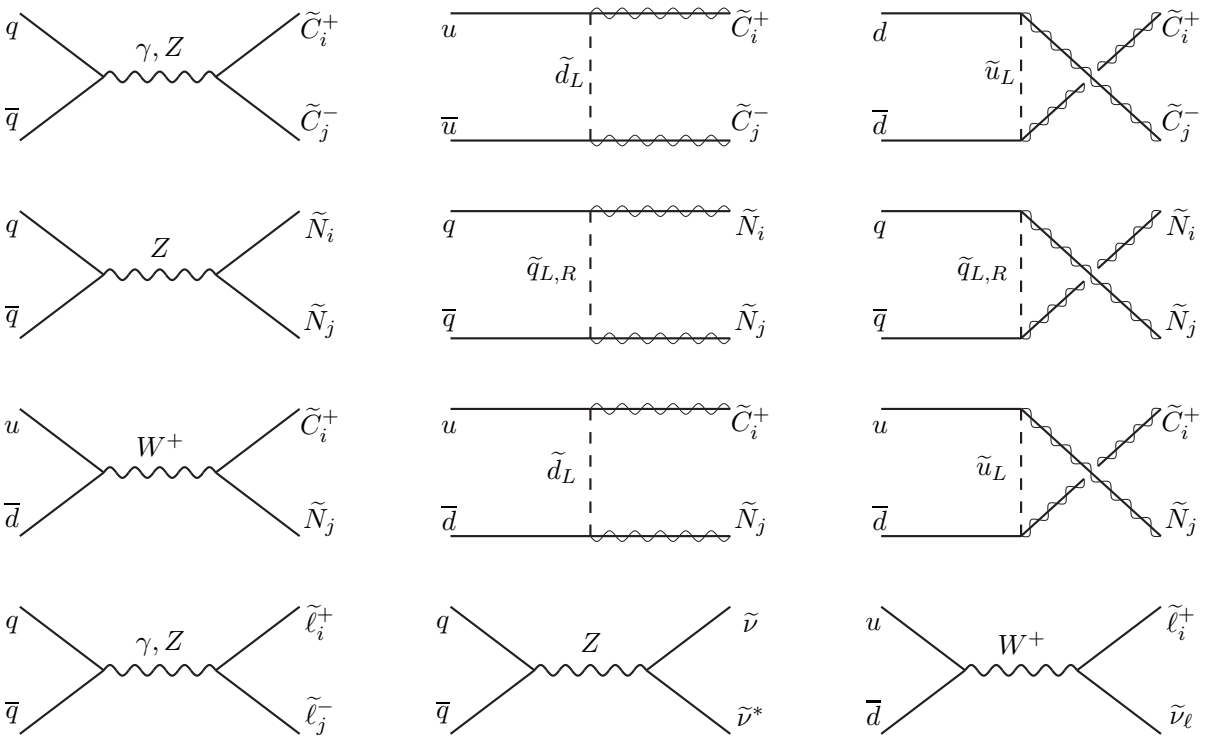

Figure 2.14: Feynman diagrams for electroweak sparticle production at hadron colliders from quark-antiquark annihilation. The naming convention differs compared to the text such that $\tilde{C}_i^+$ indicates a chargino ($\tilde{\chi}_i^+$) and $\tilde{N}_i$ indicates a neutralino ($\tilde{\chi}_i^0$) [36].

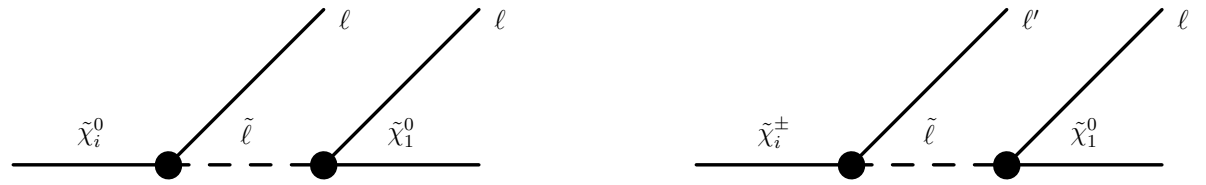

Figure 2.15: Neutralino and chargino decay with the LSP $\tilde{\chi}_1^0$ and two leptons in the final state. The intermediate scalar can be either on-shell or off-shell.

sleptons)

$$\tilde{\chi}_i^0 \to \ell^\pm \nu \tilde{\chi}_j^\mp \tag{2.71}$$

$$\tilde{\chi}_i^\pm \to \ell^\pm \nu \tilde{\chi}_j^0 \tag{2.72}$$

$$\tilde{\chi}_i^0 \to \ell^\pm \ell^\mp \tilde{\chi}_j^0 \tag{2.73}$$

$$\tilde{\chi}_i^\pm \to \ell^\pm \ell^\mp \tilde{\chi}_j^\pm. \tag{2.74}$$

If R-parity is conserved (what is assumed in the following), sparticles are produced in pairs, each of which cascades to the LSP. Therefore, the first two decays, if being involved in each of the two decay chains, produce two leptons in the final state, either having opposite or same sign. The latter two decays produce exactly two opposite-sign leptons. A typical decay chain of the gluino involving two leptons is shown in Fig. 2.16. Fig. A.5

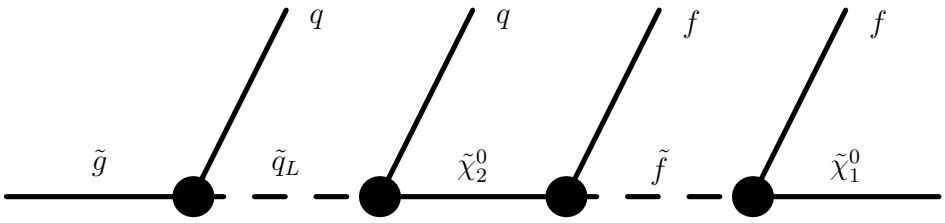

Figure 2.16: One of the possible gluino decay cascades ending with the LSP as well as two leptons (f) in the final state. The squarks in this diagram are allowed to be either on-shell or off-shell, depending on the mass spectrum of the theory.

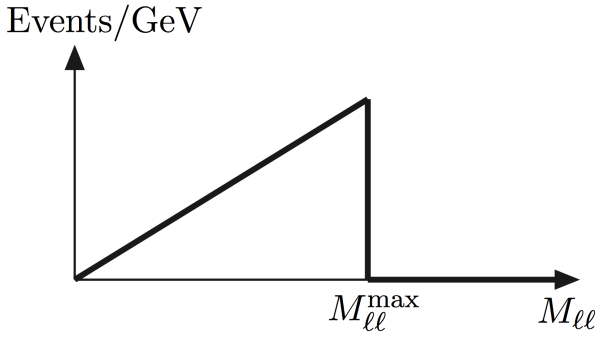

Figure 2.17: Sketch of the expected shape of the dilepton invariant mass distribution from a decay of the form $\tilde{\chi}_2^0 \to \ell\tilde{\ell} \to \ell^+\ell^-\tilde{\chi}_1^0$ [36].

depicts the complete Feynman diagram of a typical SUSY production and decay chain that results in two OSSF leptons.

Once SUSY is observed, the LHC data can be used to measure sparticle masses with the help of the kinematics of the decays [36]. Since the LSP only interacts weakly and escapes the detector, no mass peaks (as it is the case for e.g. the Z resonance) can be reconstructed. However, kinematic edges can be measured from which mass differences of the particles can be extracted. The dilepton channel suits well the reconstruction of mass edges. For example, consider the decay of the next-to-lightest neutralino (cf. Fig. 2.15),

$$\tilde{\chi}_2^0 \to \ell\tilde{\ell} \to \ell^+\ell^-\tilde{\chi}_1^0. \tag{2.75}$$

The resulting dilepton invariant mass distribution features a sharp edge (see Fig. 2.17) from which the mass difference between $\tilde{\chi}_2^0$, $\tilde{\chi}_1^0$ and $\tilde{\ell}$ can be determined [47] via

$$m_{\ell\ell,max}^2 = \frac{(m_{\tilde{\chi}_2^0}^2 - m_{\tilde{\ell}}^2)(m_{\tilde{\ell}}^2 - m_{\tilde{\chi}_1^0}^2)}{m_{\tilde{\ell}}^2}. \tag{2.76}$$

Constraining SUSY Models

It is interesting to consider the implications for SUSY from an assumed absence of any signal in the first period of LHC data taking. This was studied with the program *Fittino* [48, 49]. Fig. 2.19 (left) shows the mSUGRA parameter region in m_0 and $m_{1/2}$ compatible with low-energy observables, collider data from LEP, SLC and the Tevatron and the Dark Matter relic density without taking current LHC exclusion limits into account. Assuming an LHC exclusion for 1fb^{-1} (r.h.s. of Fig. 2.19) pushes the best fit point (indicated by the cross) to higher values of m_0 and $m_{1/2}$. It is noteworthy that the global fit allows areas in the mSUGRA parameter space that are located in the region of 95% CL exclusion of the LHC. An LHC exclusion is mainly sensitive to the squark and gluino masses. Already with 1fb^{-1}, the LHC exclusion would push the lower limit of the squark and gluino masses to above 1 TeV (Fig. 2.20). The only parameter that is nearly insensitive to the experimental input is the mass of the light scalar Higgs boson h^0. The only possibility to exclude mSUGRA and most other MSSM models is thus by excluding SM-like Higgs bosons up to a mass of 135 GeV (cf. Sec. 2.2.2) [49, 48].

Fig. 2.18 exhibits the exclusion plot of the OS di-lepton analysis in the mSUGRA $m_0 - m_{1/2}$ plane. An exclusion plot obtained from the 0-Lepton analysis for $\mathcal{L} = 1.04\,\text{fb}^{-1}$ is appended in Fig. A.2. Fig. A.3 shows the lower limits on several sparticle masses obtained from different ATLAS analyses.

Simplified Models

It is a common procedure to construct simplified models which are driven by phenomenology rather than theoretical considerations. In the Monte-Carlo production of such models, some parameters that are not expected to have a high influence on the decay topology are manually set to some value while only few parameters are regarded as free. The phase space of such models is referred to as *grid*.

Direct Gaugino:

The free parameters of this model are M_1 and M_2, the bino and wino mass parameters which enter the soft SUSY-breaking Lagrangian (Eq. (2.58)) as well as the Higgs/Higgsino mass parameter μ from the unbroken superpotential (2.54). In general, these mass terms do not correspond to the mass eigenstates of the sparticles but enter the mass matrix. The squark masses are assumed to be so high that squarks are only produced in negligible amount. The neutralinos and charginos will then be dominantly produced. Their masses and properties are governed mainly by M_1, M_2 and μ (as well as $\tan\beta$) [46]. In this model, only right-handed sleptons are included, and their mass is set to lie midway between the two lightest neutralinos. This choice is arbitrary but prevents the re-introduction of further degrees of freedom.

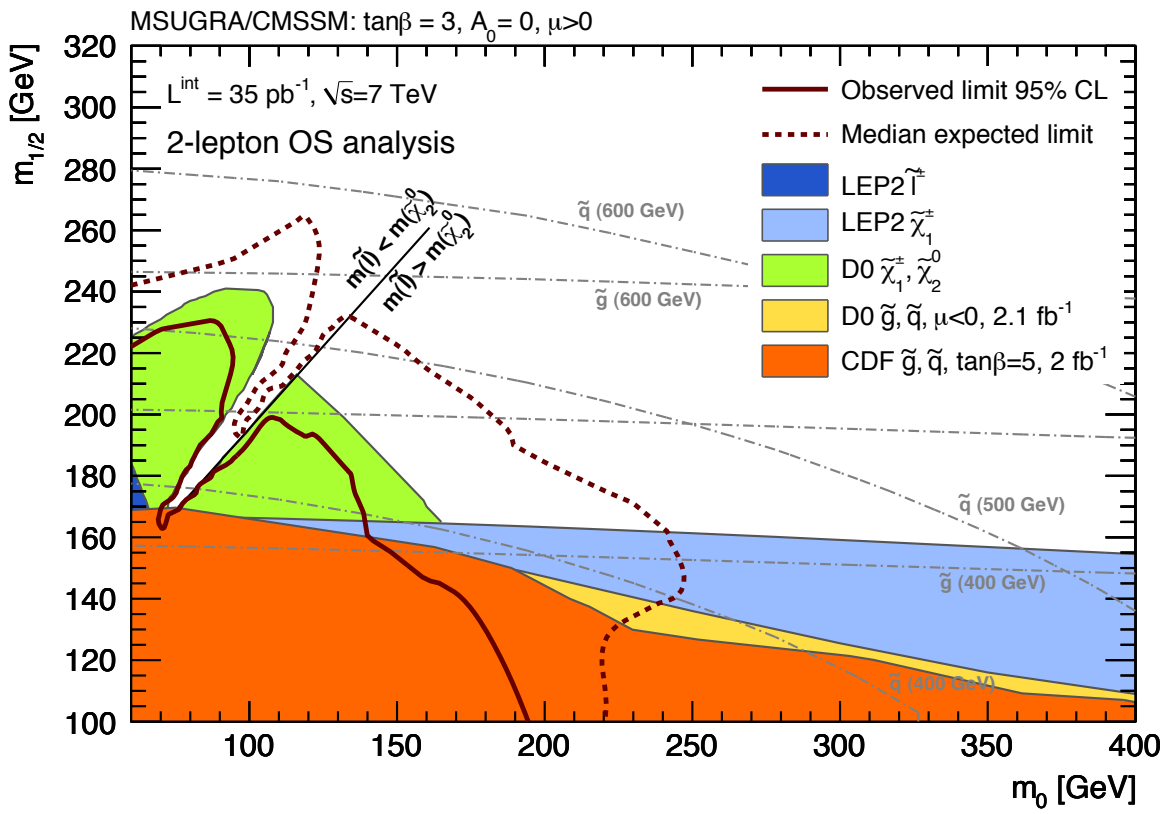

Figure 2.18: Expected (dashed line) and observed (solid line) exclusion limits for mSUGRA in the $m_0 - m_{1/2}$ plane. The limit is obtained using the 2-lepton OS analysis with a signal region defined by $E_{\mathrm{T}}^{\mathrm{miss}} > 100$ GeV for an integrated luminosity of $35\,\mathrm{pb}^{-1}$ [50]. Limits are computed using the profile likelihood method. The coloured areas depict the areas in the parameter space which were excluded by LEP and TeVatron experiments. The dashed grey curves exhibit the 'isobars' of constant gluino and squark mass.

PhenoGrid:

There are special grids that explicitly produce leptons in the final states. The PhenoGrid constructs the initial sparticles to be two gluinos, two squarks or a gluino and a squark (cf. Fig. 2.12 and 2.13). These sparticles then mostly decay into each other and either the lightest chargino $\tilde{\chi}_1^{\pm}$ or one of the two lightest neutralinos $\tilde{\chi}_1^0$ and $\tilde{\chi}_2^0$. With a slepton positioned between these charginos and neutralinos, the final decay down to $\tilde{\chi}_1^0$ (LSP) often produces leptons. In mSUGRA this particular decay is strongly constrained, especially at higher m_0 and $m_{1/2}$. The PhenoGrid is a less constrained physics model for showing the reach and setting limits in lepton channels. The free parameters of that grid are the squark and gluino mass, $m_{\tilde{q}}$ and $m_{\tilde{g}}$. $m_{\tilde{q}}$ corresponds to the mass of the squarks of the first and second generation which are degenerate. The squarks of the third generation are set to 3 TeV. The mass of the LSP is set to $m_{\tilde{\chi}_1^0} = 100$ GeV [51, 46]. Tab. 2.6 lists the masses for a specific benchmark point. The large mass differences between $\tilde{\chi}_2^0$, $\tilde{\ell}$ and $\tilde{\chi}_1^0$ imply that the resulting leptons are very hard. The Next-to-leading order (NLO) cross sections σ for the PhenoGrid in the $m_{\tilde{g}} - m_{\tilde{q}}$) plane is depicted in Fig. A.4.

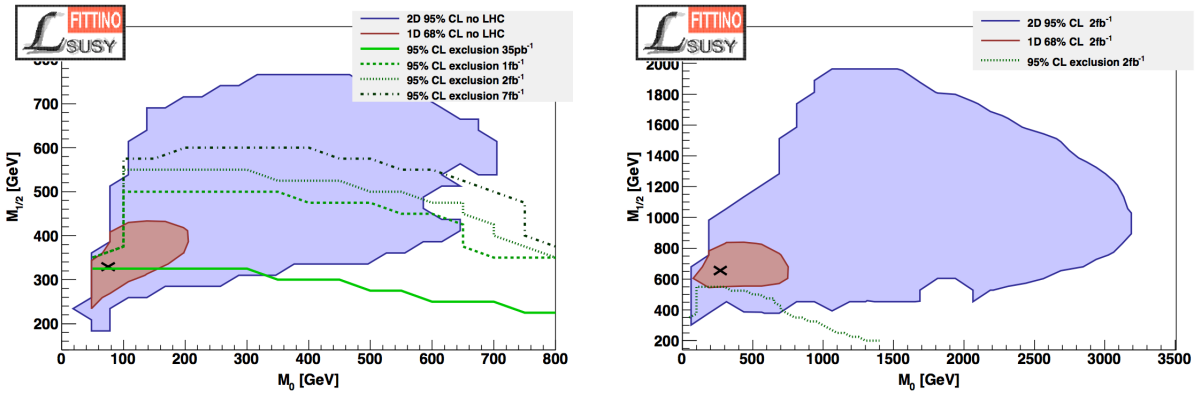

Figure 2.19: The mSUGRA parameter region in m_0 and $m_{1/2}$ compatible with low-energy observables, collider data from LEP, SLC and the Tevatron, and the Dark Matter relic density. Shown are the two-dimensional 95% (blue area) and one-dimensional 68% (red area) confidence levels (CL) exclusion limits in the four-jets, zero-lepton and $E_{\mathrm{T}}^{\mathrm{miss}}$ channel for different integrated luminosities. The best fit point is indicated by the cross. The left plot does not take into account current LHC exclusion limits while the right plot considers a potential LHC exclusion limit in the four-jet, zero-lepton and $E_{\mathrm{T}}^{\mathrm{miss}}$ channel for 1 fb^{-1} of integrated luminosity. The left plot also shows the estimate of the potential 95% CL exclusion limits in this channel for different integrated luminosities (blue and green lines). The dashed line on the right-hand side shows the potential LHC 95% exclusion limit [49].

Table 2.6: Example of a mass spectrum of a benchmark point in the PhenoGrid (Light LSP mode). The light neutralino grid has a fixed neutralino mass of $m_{\tilde{\chi}_1^0} = 100$ GeV. The other masses are determined by the squark and gluino masses.

$m_{\tilde{g}}$ [GeV]	$m_{\tilde{q}}$ [GeV]	$m_{\tilde{\chi}_2^0}$ [GeV]	$m_{\tilde{\ell}}$ [GeV]	$m_{\tilde{\chi}_1^0}$ [GeV]
-	-	$\min(m_{\tilde{g}}, m_{\tilde{q}}) - 100$ GeV	$(m_{\tilde{\chi}_2^0} + m_{\tilde{\chi}_1^0})/2$	100
600	610	500	300	100

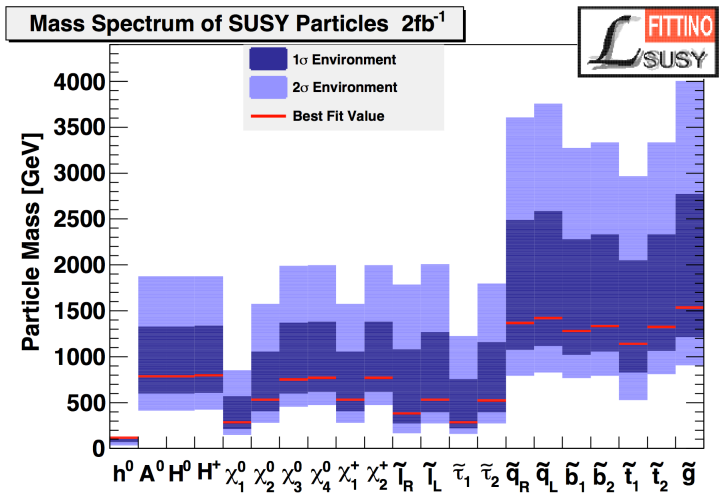

Figure 2.20: SUSY mass spectrum as predicted by a combined mSUGRA fit of low-energy observables, collider data from LEP, SLC and the Tevatron, the Dark Matter relic density and a potential LHC exclusion limit in the four-jet, zero-lepton and $E_{\mathrm{T}}^{\mathrm{miss}}$ channel for 2 fb^{-1} integrated luminosity [49].

Chapter 3

The LHC and the ATLAS Experiment

'It does not make any difference how beautiful your guess is. (...) - If it disagrees with experiment it is wrong. That is all there is to it.'
RICHARD P. FEYNMAN [52]

In this section, the basic principles of the Large Hadron Collider (LHC) as well as the most important properties of the ATLAS detetector and the ATLAS trigger system are presented.

3.1 The LHC

The LHC is a proton-proton[1] storage ring with a circumference of 26.7 km. With its center-of-mass energy $\sqrt{s}$ of up to 14 TeV at a frequency of 40 MHz and a design instantaneous luminosity of $\mathcal{L} = 10^{34}$ cm^{-2}s^{-1} [53] the LHC is able to produce very rare decay products with significant statistics. Up to now the LHC operates with $\sqrt{s} = 7$ TeV.
In order to achieve such high energies, the protons are first pre-accelerated by a linear accelerator to an energy of 50 MeV before they are accelerated to 450 GeV via the 'proton synchrotron' (PS) and the 'super proton synchrotron' (SPS) [54]. Then, the proton bunches are injected into the main LHC tunnel (Fig. 3.1).

In the LHC tunnel, the protons are accelerated by superconducting cavities. The LHC has eight arcs and eight straight sections. Each of the straight sections is approximately 530 m long, hosting the experiments ATLAS, CMS, LHCb and ALICE as well as beam dump insertion and collimation systems.

Two beam pipes host the proton bunches. 9300 superconducting magnets are responsible for focussing and bending the beams. There are 1232 dipole magnets with a length of 15 m and a field of 8.3 T which force the beam onto its circular trajectory. In order

[1] There is also a heavy ion mode with lead-lead collisions with which the ALICE detector as well as ATLAS and CMS aim to detect -amongst others- the quark-gluon plasma.

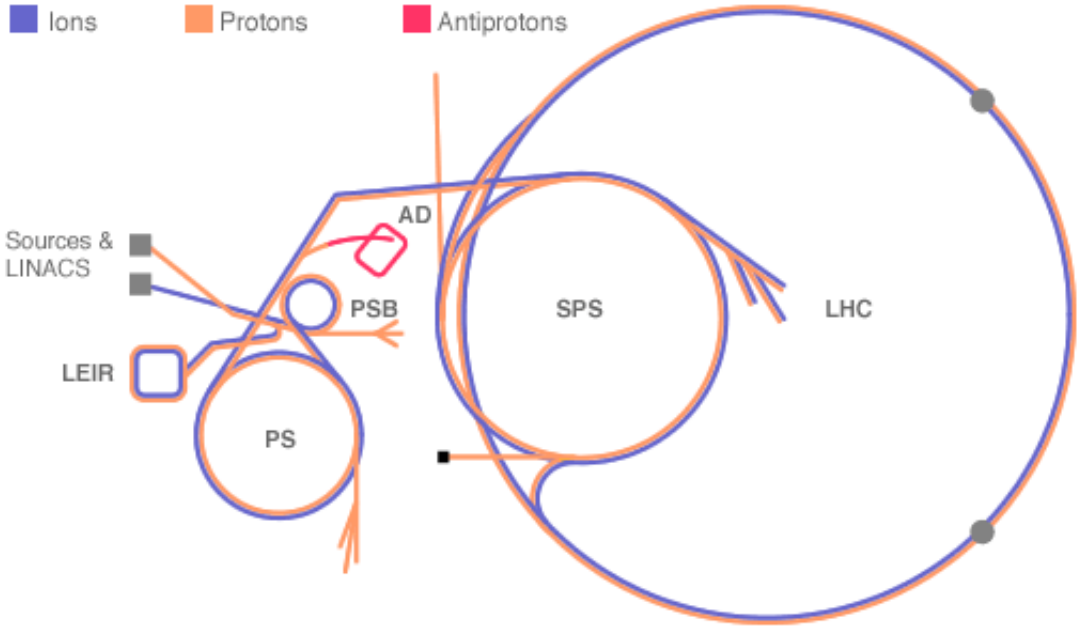

Figure 3.1: Sketch of the LHC ring and its preamplifiers [55]. Two sources and linear colliders (LINACS) generate and pre-accelerate low energy protons (orange) and Pb ions (blue). The ions are then accelerated by the Low Energy Ion Ring (LEIR) whereas the Proton Synchrotron Booster (PSB) accelerates the protons. The Proton Synchrotron (PS) and the Super-Proton Synchrotron (SPS) accelerate the protons and ions to an energy of 450 GeV which are then injected into the LHC ring. Besides, the Antiproton Decelerator (AD) is shown which provides low-energy antiprotons (pink) for studies of antimatter. The black rectangle symbolises the CNGS (*CERN Neutrinos to Gran Sasso*) experiment where proton beams from the SPS are hit on a target to produce muon neutrinos which travel to the OPERA experiment at the Gran Sasso laboratory [56].

to produce such a high magnetic field the magnets need to be superconducting, beeing cooled down to 1.7 K by superfluid helium. 392 quadrupole magnets with lenghts between 5 m and 7 m focus the beams. A quadrupole magnet is able to focus either vertically or horizontally. Therefore, the quadrupole magnets are aligned in a so-called FODO lattice structure. It is a periodic sequence of focusing ('F') and defocusing ('D') quadupole magnets, with dipole magnets or drift spaces- denoted by 'O'- between them [57]. At the four interaction points where the two proton beams meet, the FODO structure is dropped and a triplet quadrupole assembly aims to get a minimal β function value. The β function is the envelope of the trajectories of the particles circulating in the FODO lattice. Moreover, sextupole magnets are used to account for instabilities arising from the β function dependence of the momentum (chromaticity) [58, 57] as well as octupole magnets that damp the coherent oscillations caused by collective effects inside a bunch [54, 53].

The number of events that are created at a collision is given by the product of the

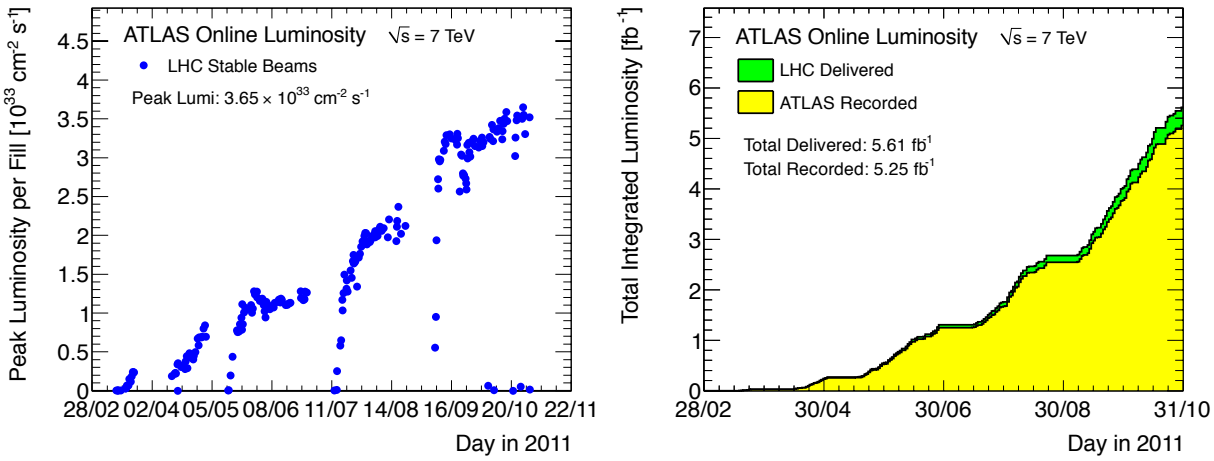

Figure 3.2: **Left:** Peak instantaneous luminosity as a function of the day in 2011. Only stable beams which were delivered to ATLAS are recorded. The drops and new rise in the luminosity are due to down-times of the ATLAS detector. **Right:** Integrated luminosity versus day delivered to (green), and recorded by ATLAS (yellow) during stable pp beams at 7 TeV centre-of-mass energy in 2011. A total integrated luminosity of $5.25\,\mathrm{fb}^{-1}$ has been recorded during the 2011 data taking. [59]

instantaneous luminosity L and the cross section for the process under study,

$$N = L\sigma \tag{3.1}$$

where the luminosity is completely determined by machine parameters. Assuming a Gaussian beam distribution and equal parameters for each beam, it is given by [54]

$$L = \frac{N_b^2 n_b f_{\mathrm{rev}} \gamma_r}{4\pi\epsilon_n \beta^*} F \tag{3.2}$$

whereN_b is the number of particles per bunch, n_b the number of bunches per beam, f_{rev} the revolution frequency, γ_r the (relativistic) gamma factor, β^* the beta function at the collision point, ϵ_n the transverse beam emittance[2] and F the so-called geometric luminosity reduction factor which accounts for the reduction in luminosity due to the crossing angle at the interaction point [54].

At the moment, there are 1380 bunches per fill with a bunch spacing of 50 ns and approximately 1.1×10^{11} protons per bunch. The value of β^* is 1 m and the emittance is about 2 μm rad [59]. These values lead to an instantaneous luminosity of $\sim 3 \times 10^{33}$ cm^{-2} s^{-1} which is the highest luminosity ever achieved at a collider. Fig. 3.2 shows the peak luminosity per fill (left plot) and the integrated luminosity (right) as a function of the day in 2011. The constant growth in luminosity can be achieved by an increase of the number of bunches per beam and the reduction of the bunch-spacing.

[2]The emittance is the area of the phase-space ellipse of a particle bunch. When the particles are accelerated, the emittance decreases inversely proportional to the momentum [57].

3.2 The ATLAS Detector

In this section, the nomenclature of the ATLAS coordinate system, which will be used throughout this thesis, is introduced. Following, the design of the main components and attributes of the ATLAS detector, namely the Inner Detector, the Calorimeter and the Muon spectrometer are presented. The descriptions closely follow [60].

3.2.1 The ATLAS Coordinate System

The origin of the right-handed coordinate system is defined as the interaction point. The beam line lies in the direction of the z axis and the positive x axis points towards the centre of the LHC ring. In a spherical coordinate system, the polar angle θ is the angle between some vector $\vec{r}$ and the z axis and the azimuthal angle ϕ is the angle between the projection of $\vec{r}$ onto the x-y plane and the x axis. Instead of the polar angle, a more convenient quantity, the *pseudo-rapidity*

$$\eta = -\ln\tan(\theta/2) \tag{3.3}$$

is used as it is Lorentz invariant under longitudinal boosts [61]. An azimuthal angle of $\theta = 0°$ thus correspons to $\eta = \infty$ while $\theta = 90°$ corresponds to $\eta = 0$. An often used quantity is the opening angle between two objects in the η-ϕ plane [60],

$$\Delta R = \sqrt{\Delta\eta^2 + \Delta\phi^2}. \tag{3.4}$$

At hadron colliders, only the momentum/energy components transverse to the colliding beams is detectable. The transverse momentum p_T is defined as the momentum perpendicular to the LHC beam, $p_T = p\sin\theta$.

3.2.2 Overview and Physics Requirements

In the LHC, bunches of 10^{11} protons collide at a rate of 40 MHz [54], so that a very powerful detector system is needed in order to be able to separate and identify all the particles created in the collisions with the best available precision as well as an extremely fast readout and trigger system with as less dead-time as possible. The different particles created at a proton-proton collision interact differently with matter so that the detector system needs to fulfill several requirements: First of all, the particle type needs to be identified, e.g. a pion needs to be separable from an electron. Quarks, except for the top quark, cannot be detected directly since they hadronise. The resulting hadron showers can be measured as jets whose direction is dominated by the initial state quark. Neutrinos escape the detector as they only interact weakly. The same holds for the lightest supersymmetric particle (LSP) which in certain SUSY scenarios is the last particle in a

SUSY decay chain [36]. While not being able to detect these particles directly, the sum of the overall missing (transverse) energy can be determined from all the other involved particles' energies due to energy conservation. For this method to give reasonable results, a complete coverage of the detector material in all space directions as well as a minimal amount of dead material (cables, support structures, etc.) is crucial. Moreover, muons need to be measured. Due to their high mass, their interaction length is much higher than that of electrons so that special detectors are needed for the identification and measurement of the muons. Besides the energy measurement, the tracks of the particles need to be reconstructed in oder to reproduce the kinematics of the decays.

The ATLAS detector aims at fulfilling all these requirements [60]. Its main building blocks are presented in the following. Fig. 3.3 depicts a cut-away view of the ATLAS detector. The Inner Detector is immersed into a 2 T magnetic field created by a thin superconducting solenoid[3]. The Calorimeter is located around the Inner Detector. Three large superconducting toroids (barrel and endcaps) are located azymuthally around the calorimeters. The outermost part of the detector is the muon system.

3.2.3 Inner Detector

The Inner Detector consists of high-resolution semiconductor [15] pixel and strip detectors (SCT) surrounded by straw-tube tracking detectors. Its main purpose is to reconstruct the tracks of charged particles, that the magnetic system bend in the R-ϕ plane, by registrating the hits of the particles in the different detector components. As less energy of the particles as possible should be deposited in the Inner Detector because the energy determination is performed by the calorimeter system. By reconstructing the sagitta[4] of the charged particles, their momentum and charge can be measured. The combination of different tracks originating from the same point allows the determination of primary and secondary vertices. The outer tracking detectors are furthermore able to detect transition radiation. The silicon strip detector and the pixel detector form the precision tracking detectors and are arranged in the barrel region in concentric cylinders around the beam axis and in the end-caps on disks perpendicular to the beam axis. SCT and pixels cover an η region of $|\eta| < 2.5$ [60]. The Inner Detector components can be seen in Fig. 3.4.

The **pixel detector** is the innermost part of the Inner Detector and has an extremely high granularity. A pixel sensor is a 16×60 mm^2 silicon wafer segmented in $R - \phi$ and z into over 46000 pixels with an approximate pixel size of $50 \times 400\,\mu$m^2 [60]. The pixel detector system consists of 1500 modules for the barrel and 1000 disk modules for the end-caps. In the barrel region (length of 1.3 m), three pixel layers are arranged close to

[3] A solenoid is a cylindrically wounded coil.

[4] Measuring the sagitta, the deviation of a track from a straight line, instead of the curvature radius itself has the advantage that the sagitta follows a Gaussian distribution.

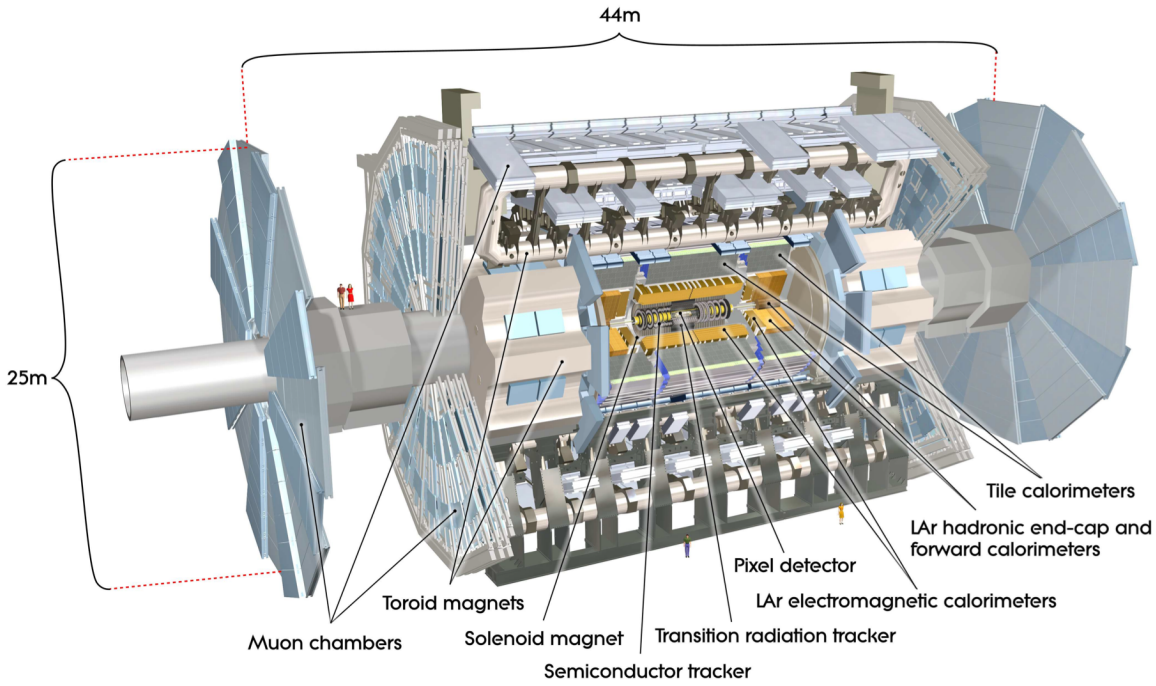

Figure 3.3: Schematic cut-away view of the ATLAS detector [60]. The pixel detector, semiconductor tracker and transition radiation tracker form the Inner Detector which is immersed into a 2 T magnetic field by a thin solenoid magnet. The Calorimeter system surrounds the Inner Detector. It consists of liquid-Argon (LAr) electromagnetic calorimeters in barrel and end-cap, hadronic tile calorimeters as well as LAr hadronic end-cap and forward calorimeters. The large Muon chambers in the barrel and in the end-cap disks in conjunction with the toroid magnets forms the outermost part of the ATLAS detector.

the beampipe. They are made of identical staves inclined with azimuthal angle of 20° in order to avoid dead material. In the end-cap, three disks (diameter of 34 cm) are located perpendicular to the beam pipe and carry 48 modules each.
This design allows a very high spatial resolution of 10 μm in the $R-\phi$ plane and 115 μm in the z-direction as well as 115 μm in R-direction for barrel and end-caps, respectively. Due to the high granularity, the number of readout channels amounts 80.4 million which is about 90 % of the total number of readout channels of the ATLAS detector [60]. Being located so close to the beam pipe, the pixel detector as well as the SCT are exposed to a huge amount of neutron radiation damage. They operate at a temperature of -10°C in order to maintain an adequate noise performance after radiation damage. Despite of the design of the pixel detector being driven by the radiation exposure, it needs to be replaced after roughly three years of operation at design luminosity.

The pixel detector is surrounded by the **semiconductor tracker (SCT)** or silicon microstrip detector. A silicon strip detector is an arrangement of electrode strips placed on a low doped depleted silicon wafer. Two of those sensors being daisy-chained and

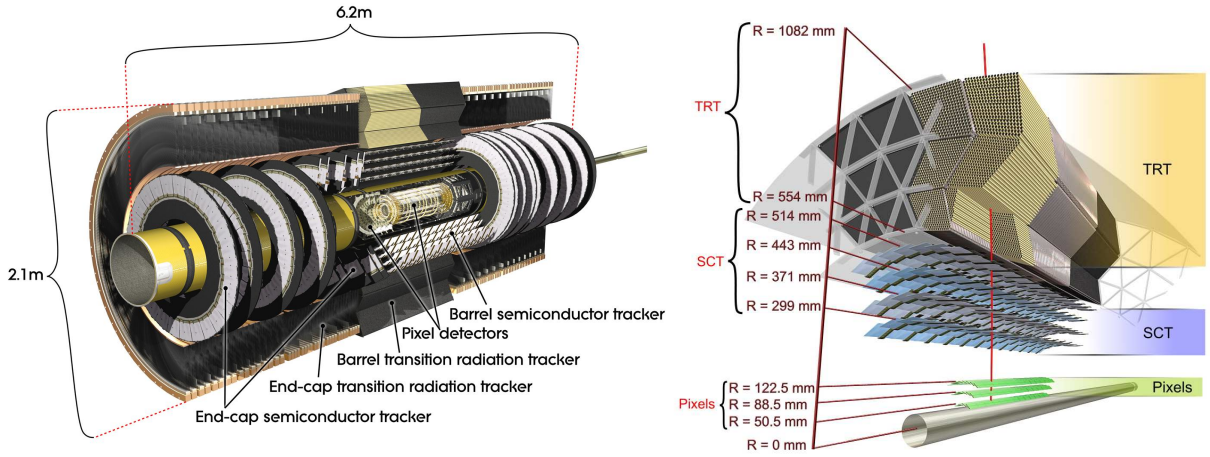

Figure 3.4: The ATLAS Inner Detector [60]. The left figure shows an overview of the transition radiation tracker (TRT) and semicoductor tracker (SCT) in barrel and endcap as well as the pixel detectors. The right figure is a more detailed view of the barrel region of the Inner Detector components, namely Pixels, TRT and SCT.

glued together back-to-back allows for a two-dimensional spatial resolution. The SCT consists of eight strip layers in the barrel region. Each sensor has a size of approximately 6×6 cm^2 and 768 readout strips with a pitch of 80 μm. The end-cap region consists of nine disk layers. The modules cover a total silicon surface area of 63 m^2. At least four spacial precision measurements of a track can be performed with the SCT. The nominal resolution is 17 μm in $R-\phi$ and 580 μm in z or R. Two tracks can be distinguished from each other if they are separated by at least 200 μm [60].

The outermost - and biggest - part of the Inner Detector is the **transition radiation tracker (TRT)** [15], consisting of 3.7×10^5 drift chambers (also called straw-tubes). The straw tubes of the TRT have a diameter of 4 mm and cover a range of $|\eta| \leq 2$. The gas of the drift chamber comprises 70 % xenon, 27 % CO_2 and 3 % oxygen [60]. A tungsten wire plated with a thin layer of gold serves as the anode. The straw tubes provide information on the position in the $R-\phi$ plane with an intrinsic accuracy of 130 μm per straw which is much lower than the accuracy of the silicon detectors. However, the lower precision is compensated by the large number of measurements and longer measured tracks. In the barrel region, the straw tubes are 144 cm long and are parallel to the beam axis. In the end-cap region, the straw tubes are located radially to the z axis and amount a length of 37 cm each. A track passing through the Inner Detector typically hits 36 straw tubes. 4.2×10^5 readout channels provide information about the drift time and thus the distance of the track from the anode [60].

Besides the TRT's ability to detect tracks over a larger distance, it is able to discriminate electrons and charged mesons (especially pions). This separation can be done with the help of transition radiation: The straw tubes are interleaved with polymeric fibres and foils which induce transition radiation, this being an intrinsic property of charged

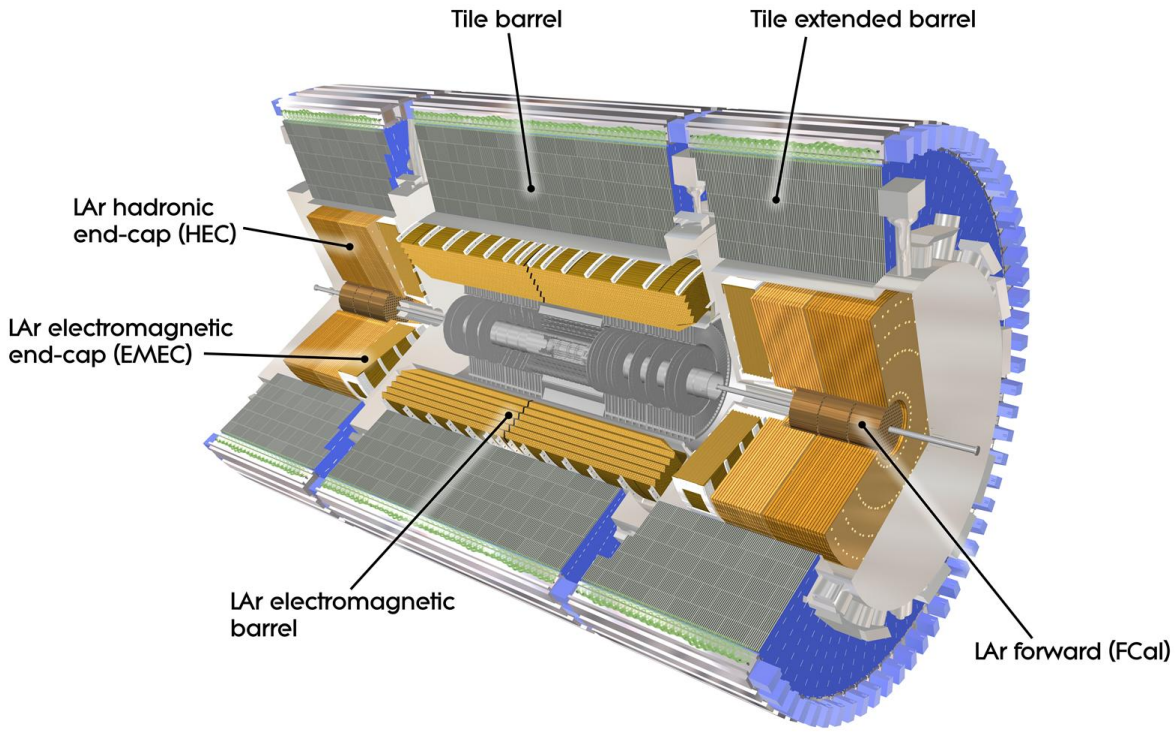

Figure 3.5: The ATLAS calorimeter system [60]. It consists of the electromagnetic calorimeter (ECal)- LAr electromagnetic barrel and EMEC - and the hadronic calorimeter (HCal) - tile barrel and tile extended barrel and HEC. The LAr forward calorimeter (FCal) serves both hadronic and electromagnetic measurements.

relativistic particles which pass two materials with different permittivities. The average number of radiated photons is proportional to the particle's relativistic γ-factor and the intensity is roughly proportional to the particle's energy [62]. Thus, electrons will induce higher-energetic hits in the TRT as charged pions, for instance, so that different thresholds can account for the particle identification.

3.2.4 Calorimeter

The calorimeter system is located around the Inner Detector. There are different calorimeters, hadronic and electromagnetic, in which the energy deposition of the particles is measured. When a particle enters the calorimeter it initiates a shower of further particles which deposit their energy in the calorimeter [15]. ATLAS uses sampling calorimeters where the material producing the shower (absorber) is distinct from the material detecting it (sensing element). The calorimeter system covers the range $|\eta| < 4.9$. The design of the calorimeter system is shown in Fig. 3.5. The two sampling calorimeters used by ATLAS are the electromagnetic calorimeter (ECal) and the hadronic calorimeter (HCal).

The **LAr Electromagnetic calorimeter (ECal)** is divided into a barrel region with

$|\eta| < 1.475$ and two endcaps with $1.375 < |\eta| < 3.2$, each of which is housed in its own cryostat. The barrel calorimeter is separated into two identical half-barrels at $z = 0$. The end-caps are divided into two coaxial wheels. The sensing material for the ECal is liquid argon (LAr) and the absorber material is lead. The electrodes and absorber plates are arranged in an accordion-shaped geometry which provides complete ϕ symmetry without azymuthal cracks (cf. Fig. 3.6). In the region $\eta < 2.5$ (where track information from the Inner Detector is available) the ECal is devoted to precision measurements of electrons and photons and thus has a very fine granularity in η. The rest of the calorimeter has a coarser granulatity which is sufficient for a jet reconstruction and $E_{\mathrm{T}}^{\mathrm{miss}}$ measurement. In depth, it is segmented in three sections. The first segment has a very fine granularity in η which enables a distinction between photons and neutral pions. The second layer has a very high granularity in ϕ and absorbs most of the interacting particle's energy due to its thickness of 16 radiation lengths. The third layer is very thin (two radiation lengths) and serves the purpose of determining the leakage into the hadronic calorimeter [60]. Behind the third layer, trigger towers are located which shall be referred to in more detail in section 3.3.

The **Hadronic calorimeter (HCal)** is separated into the tile calorimeter, the LAr end-cap and the LAr forward calorimeter. The tile calorimeter consists of a large central barrel (tile barrel) and two smaller barrel cylinders on each side (tile extended barrel). The barrel region covers the region $|\eta| < 1.0$ and the extended barrels the region $0.8 < |\eta| < 1.7$ [60]. It uses steel as absorber and plastic scintillator tiles as active material which emit light due to the interaction with the shower. A photomultiplier tube amplifies the number of electrons produced by a photocathode from the photons emitted by the scintillator. An electron from the photocathode is accelerated by a voltage and strikes the first dynode which leads to the emission of several secondary electrons. The usage of several dynodes leads to an exponential multiplication of electrons. The resulting current is then strong enough to be read out [63].

A LAr detector with copper plates as absorbers is used for the hadronic calorimetry in the end-caps. The different design with respect to the barrel region is necessary due to the higher radiation exposure. In addition, there is a LAr forward calorimeter (FCal) which provides both hadronic and electromagnetic energy measurement. It is approximately 10 interaction lengths deep and is separated into three modules. The first module is made of copper and serves for electromagnetic measurements while the other two are made of tungsten and are used for hadronic measurements [60].
By the extended layout of the calorimeter a large part of the pseudo-rapidity range is covered which is especially important for the $E_{\mathrm{T}}^{\mathrm{miss}}$ measurement.

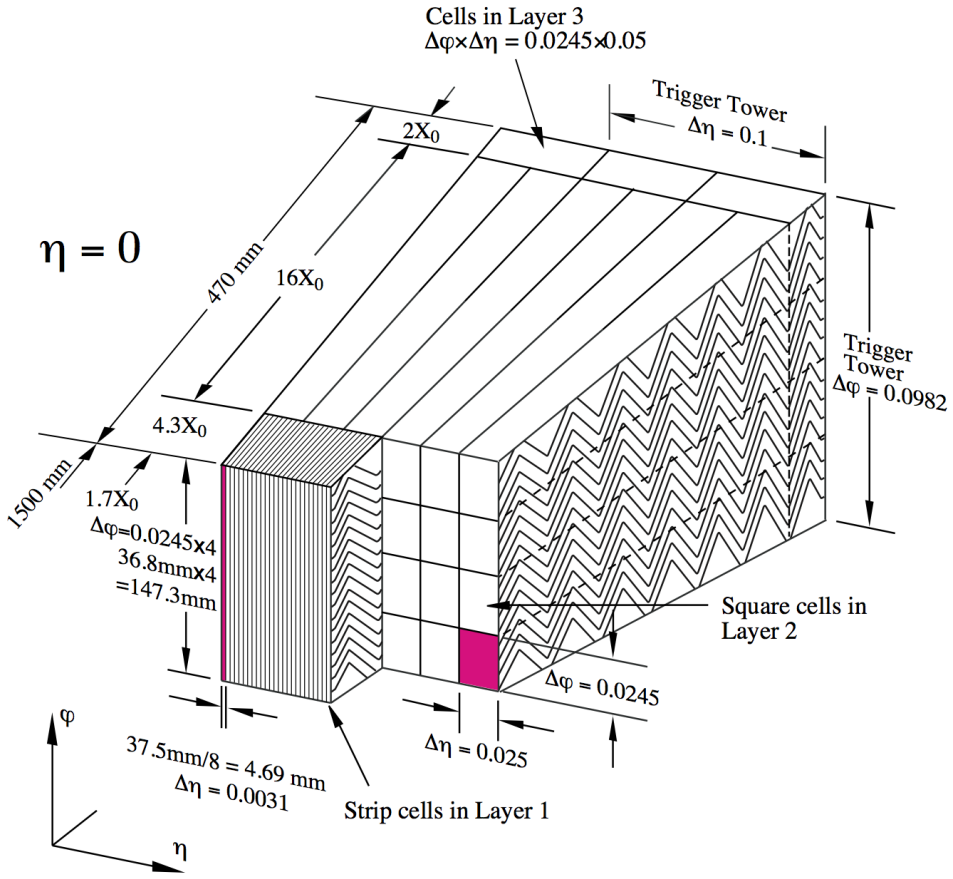

Figure 3.6: Sketch of a barrel module of the electromagnetic calorimeter (ECal) [60]. The arrangement of the electrodes and absorber plates in an accordion-shaped geometry can be seen. The dimensions and resolutions for the three layers are shown. The ECal consists of three layers. The first layer has a very fine granularity in η but does not have a segmentation in ϕ. The second and third layer provides both η and ϕ resolution. The third layer mainly serves for the registration of leakages of the ECal. Behind the third layer, trigger towers are located.

3.2.5 Muon Spectrometer

The large Muon Spectrometer surrounds the calorimeter. The toroidal magnets (one barrel and two end-cap toroids) allow the bending and thus charge identification of the muons. All other detectable particles should be absorbed by the calorimeter system by then. The muon system consists of four different gaseous detector technologies [15]: monitored drift tubes (MDT), cathode strip chambers (CSC), resistive plate chambers (RPC) and thin-gap chambers (TGC). The latter two systems are less precise than the first two, but much faster and thus used as muon trigger chambers which shall be discussed in more detail in Sec. 3.3. Three layers of tracking chambers provide excellent muon momentum resolution. The design of the Muon Spectrometer is shown in Fig. 3.7.

The MDTs, which are used to provide precision measurements of the track coordinates, consist of three to eight layers of drift tubes and cover the range $|\eta| < 2.7$. They measure

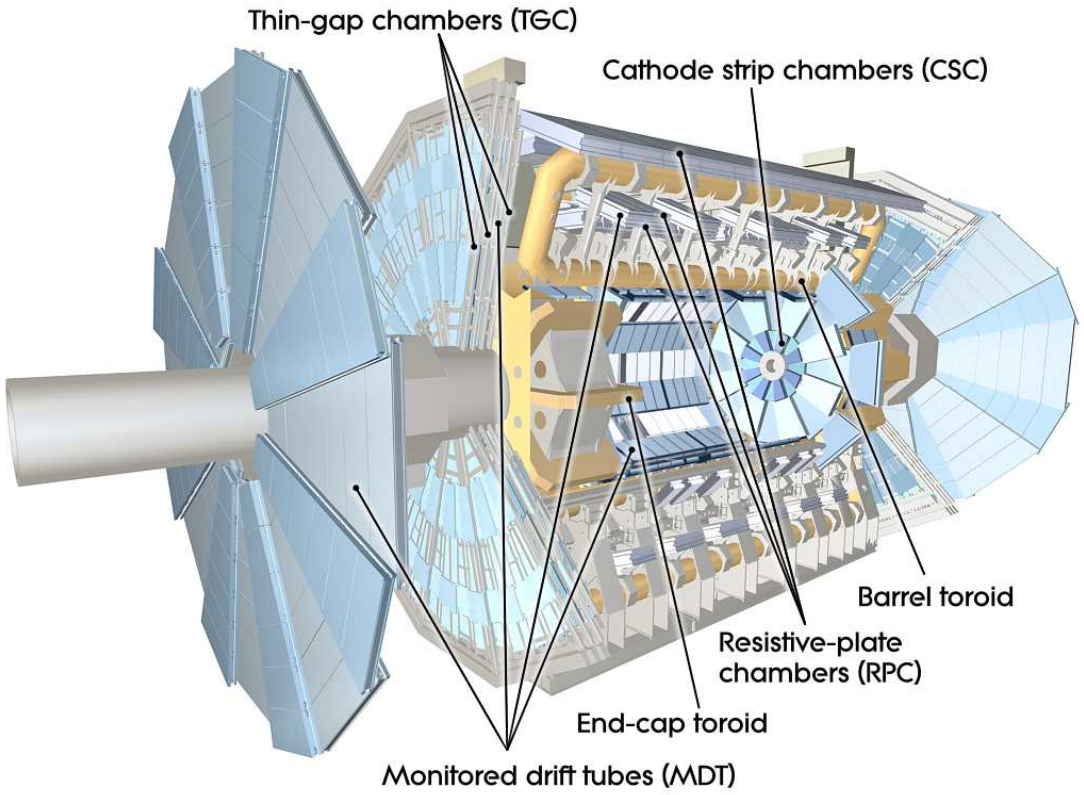

Figure 3.7: Cut-away view of the ATLAS Muon system. The detection system consists of the MDT and the CSC. The trigger system consists of the RPC and the TGC. The toroids bend the muon tracks for better identification [60].

the drift time of electrons that are produced by ionising muons.
The CSCs are multiwire proportional counters with cathode planes segmented into strips. Induced-charge distributions are used to determine the track coordinates. The CSCs are used in the forward region $2.0 < |\eta| < 2.7$ with a resolution of 40 μm in the bending plane and 5 mm in the transverse plane. They have a better time resolution and rate capability compared to the MDTs due to a different gas mixture inside the tubes. The performance goal of 10% resolution for a 1 TeV track is ensured by an optical alignment system which monitors the position of the MDT wires and the CSC strips [60].

Additionally to the high-precision chambers there are additional detector components with a fast readout system which are devoted to the triggering of muons. RPCs with a time resolution of 1.5 ns are used for this purpose in the η region below 1.05. In the end-cap region $1.05 < |\eta| < 2.4$ TGCs with a time resolution of 4 ns are used [60]. The RPCs are gaseous detectors consisting of parallel resistive plates at a distance of 2 mm. An external electric field accelerates the showers towards the anode due to ionisation along the track. Like the CSCs, the TGCs are multiwire proportional counters with a better time resolution due to chambers with smaller radii and a different gas mixture. The increased time resolution is realised at the expense of a reduced spatial resolution. As a complement to the MDT measurement, the TGCs measure both timing and azimuthal coordinate of the muon track. The inner and middle layer of the MDTs are complemented

by two and seven layers of TGCs, respectively.

3.3 The ATLAS Trigger System

The proton collision rate at the LHC amounts ~ 40 MHz for a bunch-spacing of 25 ns. This leads to over 20 pile-up events added at each bunch-crossing on top of the signal event (at nominal luminosity). The resulting interaction rate is ~ 1 GHz. It is impossible to store and process this amount of data. Therefore, the aim of the ATLAS trigger system is to reduce the rate significantly by rejecting 'less interesting' events while keeping all the interesting ones. In fact, the trigger system needs to reduce the interaction rate of ~ 1 GHz down to ~ 200 Hz which can be permanently stored. This is a reduction by seven orders of magnitude. A large fraction of the events are so-called *minimum-bias* events which can be discarded. These denote interactions with small momentum transfer by gluon emission, leading to hadronic final states distributed over the whole detector region. Minimum-bias events have a high cross-section and are the dominant processes at proton-proton collisions. Additionally, a single minimum-bias event creates activity in the whole detector which will 'pile up' and complicate the differentiation of single reactions [64, 65]. On the other hand, the 'interesting' processes of physics beyond the SM have very small cross sections compared to QCD events. For example, the production cross section for b quarks is about a factor of $10^8 - 10^9$ larger than that of typical SUSY processes. Reducing the amount of data by a factor of 10^7 while keeping all the interesting events (Higgs, SUSY, etc.) is a very challenging task. In the following, the building blocks of the ATLAS trigger system are presented.

3.3.1 Overview

The ATLAS trigger system is built up of three stages: *Level 1* (L1), *Level 2* (L2) and *Event Filter* (EF) whereas the latter two form the *High Level Trigger* (HLT). L1 is hardware-based whereas L1 and the EF are software-based. L1 uses reduced-granularity information from a subset of the detectors. It selects detector information which contains high-p_{T} muons, electrons/photons, jets, hadronically decaying tau leptons as well as events with high E_{T} or $E_{\mathrm{T}}^{\mathrm{miss}}$ [60, 66]. The maximum acceptance rate of L1 amounts 75 kHz and a decision whether to keep an event needs to be made within a certain time frame, called the *latency*, which amounts 2.5 μs in this case. L2, which is software-based, is seeded by so-called *Regions of Interest (RoIs)* which are regions of the detector where L1 identifies possible trigger objects. The L2 decisions reduce the event rate to ~ 3.5 kHz at a latency of 40 ms [60]. The L2 decisions are passed to the EF which operates offline. It works on fully-built events and has ~ 4 s to make its decision. It reduces the event rate down to ~ 200 Hz. L2 and EF use the full granularity and precision from the Calorimeter and the Muon Chambers as well as data from the Inner Detector to refine the trigger selections.

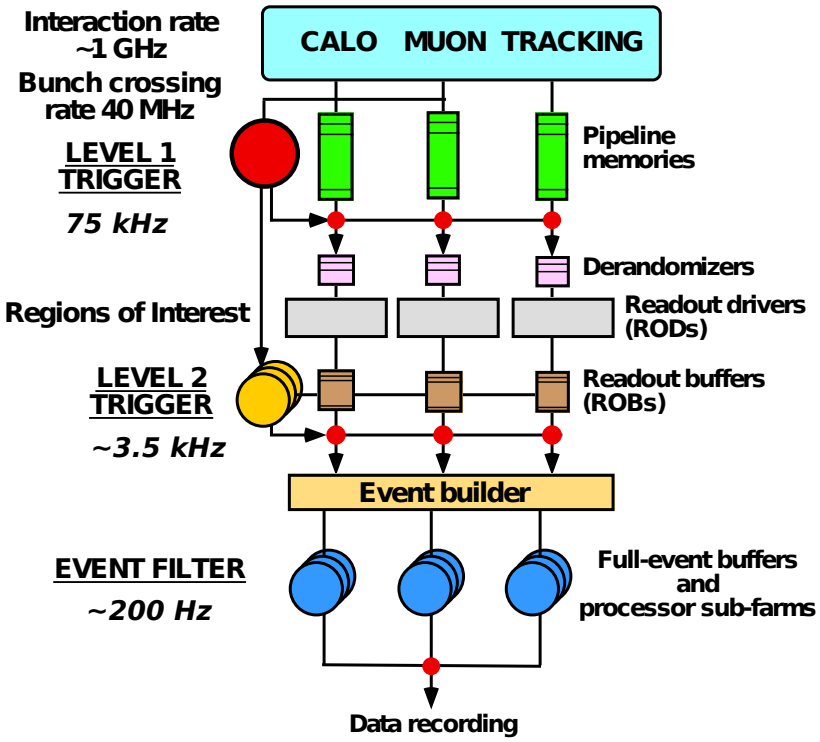

Figure 3.8: The ATLAS Trigger System. The Level 1 Trigger (L1, red) is a hardware trigger based on coarse calorimeter and muon information. It reduces the rate from 1 GHz to 75 kHz within a latency of 2.5 μs. The raw event fragments from the detectors are read out in parallel in pipeline memories. If an event is accepted by L1, the detector information from certain Regions of Interest (RoI) is added to the readout stream via dedicated readout drivers (RODs). Level 2 (L2, yellow) is a software trigger consisting of a farm of 500 processors. It refines the L1 trigger decision by processing the entire detector response at full granularity from the RoIs. The rate is reduced to $\sim$ 3.5 kHz. The Event Filter (EF, blue) reduces the rate further to 200 Hz by a farm of 1600 processors. Moreover, the EF incorporates alignment as well as calibration. The events accepted by the EF are then finally written to mass storage. Modified from [60].

The events which are accepted by the EF are moved to permanent storage. The building blocks of the trigger system are depicted in Fig. 3.8.

3.3.2 Level 1 Trigger

The L1 trigger [67] performs the initial event selection based on coarse information from the Calorimeter and the Muon System. The L1 Calorimeter Trigger (L1Calo) uses all Calorimeter sub-systems by the (analogue) summation of calorimeter cells within so-called *trigger towers*, thus providing Calorimeter information with a reduced granularity of $\Delta\eta \times \Delta\phi = 0.1 \times 0.1$ (cf. Fig. 3.6). It aims at identifying high-energetic objects such as electromagnetic clusters (electrons or photons), jets and hadronic clusters (hadronically decaying tau leptons) as well as events with large transverse energy E_{T} and missing transverse energy $E_{\mathrm{T}}^{\mathrm{miss}}$. A preprocessor digitises the signals from the trigger towers, identifies the corresponding bunch-crossing for each event and determines the total transverse

energy. The latter is realised with the help of look-up tables where the input signal is compared to reference energy values. The digital signal is then forwarded to the cluster processor (CP) and the jet/energy processor (JEP). The CP identifies the number (multiplicity) of electron/photon candidates as well as hadronically decaying tau leptons for eight different p_{T} thresholds. The JEP provides the multiplicities of jet candidates as well as the overall transverse energy for different thresholds. The information from CP and JEP are then sent to the Central Trigger Processor (CTP) [60].

Simultaneously to the L1Calo procession, the L1 Muon trigger system gathers information from the dedicated muon trigger chambers PRC (barrel) and TGC (end-cap). The *Muon-to-central trigger processor interface* (MuCTPI) resolves double-counting of muon candidates and forwards the muon multiplicities of up to 16 so-called Regions of Interest (RoIs) to the CTP as well as to the RoI Builder. The RoI Builder gathers the information from the CTP and the MuCTPI and concatenates the different RoI fragments into one. The available information consists of the η and ϕ regions as well as p_{T}, E_{T} and $E_{\mathrm{T}}^{\mathrm{miss}}$ values for candidate objects.

Information about the geometric location of trigger objects is retained in the trigger processors by the definition of Regions of Interest (RoIs). The overall L1 trigger decision, however, is based only on the multiplicity of trigger objects and is made by the Central Trigger Processor (CTP) which combines the information from different object types. The geometrical information for an accepted event is sent as a RoI to the L2 trigger for further processing. Moreover, the L1 trigger is responsible for the clear identification of the bunch-crossing of interest. The time between two bunch-crossings is 25 ns. The time of flight of a muon through the Muon spectrometer exceeds this time interval. Therefore, pipeline memories need to retain all the relevant detector information until the L1 trigger decision is formed. The latency is required to be less than 2.5 μs[5] [60].

The CTP compares the multiplicities and energies to some conditions and examines items in the trigger menu. Moreover, the CTP applies dead-time and prescale factors. The CTP processes the information containing multiplicities for electrons/photons, hadronically decaying tau leptons, jets, muons and flags indicating which thresholds were passed for total and missing transverse energy or for total jet transverse energy. The CTP uses look-up tables to form trigger conditions from the input signals. These trigger conditions are then combined to form up to 256 *trigger items* where each trigger condition may contribute to each of the trigger items. Furthermore, dead-time and prescale factors are applied. If at least one of the trigger items is fulfilled, the L1 accept signal is send via the *Timing, Trigger and Control* interface (TTC) to the detector front-end. Moreover, information about the trigger decision for all trigger items is sent to the RoI builder and the data acquisition system (ROS). L1 reduces the bunch-crossing rate of 40 MHz to 75 kHz and passes the readout-data to the next step, Level 2. A block diagram of the L1 trigger system is shown in Fig. 3.9.

[5]The delay due to the cable propagation of the signals already accounts for $\sim 1\,\mu$s of this time.

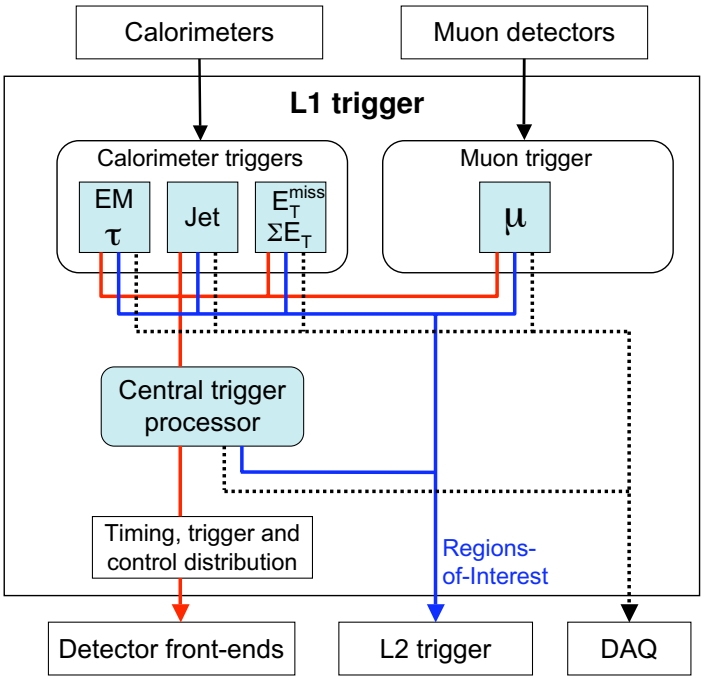

Figure 3.9: Block diagram of the L1 Trigger system [60]. The calorimeter and muon trigger results are passed to the Central Trigger Processor (CTP) which is responsible for the overall L1 accept decision. For a positive decision, the RoIs from the detector subsystems are sent to the L2 trigger (blue line). The trigger decision is sent to the detector front-end and readout system via the Timing, Trigger and Control (TTC) system (red line) as well as to the data acquisition (DAQ) (black dashed line).

3.3.3 High Level Trigger (HLT)

The HLT [68] is composed of the L2 trigger and the Event Filter (EF). The HLT is software-based and makes use of more detailed information from the different detector subsystems, thus refining the L1 trigger decision based on the enhanced available information.

Level 2 Trigger (L2)

The L2 trigger processes only information from the RoIs but, in contrast to L1, with full granularity. The L1 trigger passes the RoIs to L2, i.e., only event data in regions around η and ϕ flagged as 'interesting' regions with electron/photon, tau, jet or muon candidates is unpacked by the HLT. This concept saves time because only 1-4 % of the data volume is unpacked and analysed. The L1 information is transferred to the HLT via so-called *Readout Links* (ROL). The *RoI builder* merges the input from the different L1 sub-systems into one data structure which is passed to the *L2 supervisor* which assigns single events to different L2 trigger processor units. At these units, the processing of single events is performed. The extraction of features of an event is performed in the RoI regions by specialised algorithms that are optimised for the speed constraints and cover all sub-detectors sequentially. Moreover, L2 performs track reconstruction, a process that would be too time-consuming at L1. This is done by including the Inner Detector infor-

mation. A robust and efficient reconstruction of particle trajectories is a prerequisite for triggering of electrons, muons, etc. Moreover, at L2, different detector trigger elements are combined to form trigger objects, e.g., a tau lepton is defined as consisting of a thin jet plus a track. The full data set is only forwarded to the Event Filter (EF) if the RoI has passed the L2 trigger selection which minimises the amount of data transfer for accepted and rejected events [68, 60].

Event Filter (EF)

The final trigger selection is performed by the EF which is seeded by the events accepted by L2. The EF is able to access all detector information, including the Inner Detector and the MDTs and CSCs from the Muon System while reducing the rate to 200 Hz which can be stored permanently. The EF classifies selected events according to a pre-determined set of different event streams. Criteria for selecting events are defined in the *trigger menu* which defines trigger chains, i.e. specifies thresholds and signatures which have to be satisfied. The L2 reconstruction algorithms are specifically designed to meet the strict timing constraints for event processing (40 ms). Since the latency of EF amounts a few seconds, the EF reconstruction algorithms are more accurate. Thus, the EF is able to reduce the L2 rate by roughly a factor of 10 using sophisticated offline algorithms. Moreover, prescale factors can be applied to each trigger object at each stage, that is, only one of n events is accepted. By this, also events with high trigger rates like minimum bias-events can be stored. Besides the p_{T} thresholds, other attributes like isolation requirements (no other object in a certain vicinity of the trigger candidate) can be imposed on the definition of the trigger objects. The accepted events are stored accordingly in different trigger streams, namely `Egamma`, `Muon`, `JetTauEtmiss` and `MinBias` streams [68, 60].

The processing chain of the HLT (both L2 and EF) can be summarised as follows: The L2 supervisor gets the RoIs and sends them to about 500 processors for selection. The processors request the data from the ROS and get the corresponding event fragments. The L2 decision is passes to the Event Builder. The Event Builder builds the full event which is then passed to the Event Filter (EF). The full event, including the EF decision flag is written to the database [69]. This processing chain is shown in Fig. 3.10.

3.3.4 Performance

The trigger performance for a specific run in 2010 data taking is shown in Fig. 3.11. This run had an instantaneous luminosity ranging from 0.85 to 1.8×10^{32} cm^{-2}s^{-1} and an integrated luminosity of 6.4 pb^{-1} [66]. Fig. 3.11 (left) shows the total L1, L2 and EF output rates as a function of the instantaneous luminosity. With rising instantaneous luminosity, the trigger menus need to be adapted in order to counteract the increasing

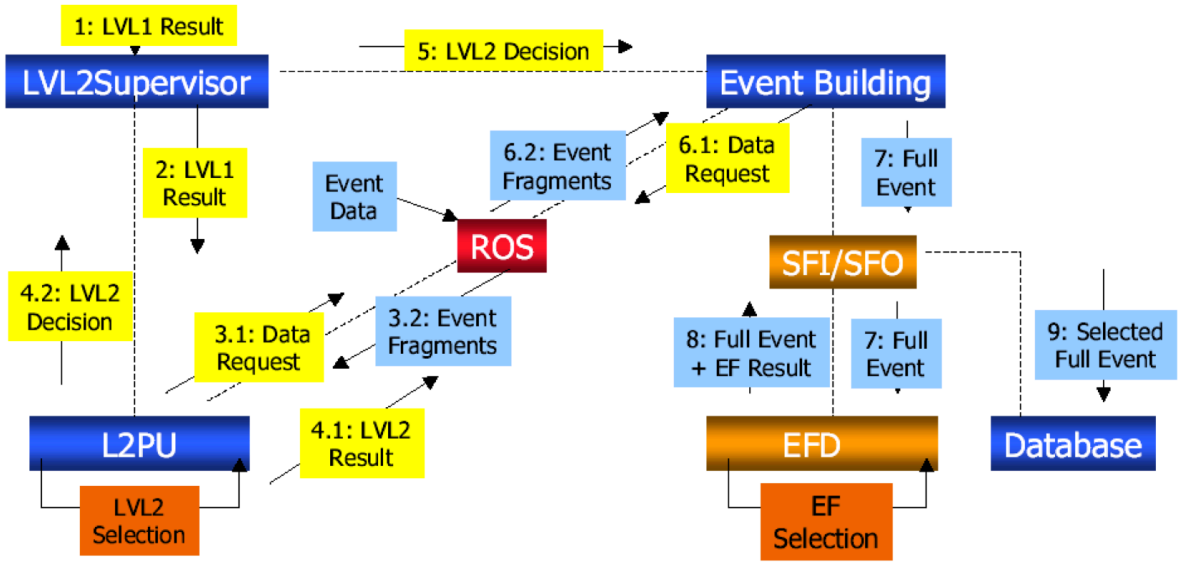

Figure 3.10: Block diagram of the High Level Trigger (HLT) [70]. The L2 supervisor gets the RoIs from L1 and sends them to about 500 processors for selection (L2PU). The processors request the data from the ROS and get the corresponding event fragments. The L2 decision of the processors is sent back to the L2 supervisor which passes it to the Event Builder. The Event Builder requests the data from the ROS and builds the full event which is then passed to the Event Filter (EFD) via the SFI/SFO. The full event, including the EF decision flag, is passed via the SFI/SFO so that the full selected event is written to the database.

bunch-crossing rate. The rates have been kept to $\sim$ 30 kHz (L1), $\sim$ 4 kHz (L2) and $\sim$ 450 Hz (L1) by adjusting the prescale factors [66]. Each discontinuity of the rates shows a change of the prescale factor. The prescale factors for L2 and EF are changed simultaneously while the L1 prescale factors can be changed individually. The total output rates of the different physics streams (`Egamma`, `Muon`, `JetTauEtmiss` and `MinBias`) are shown in Fig. 3.11 (right).

3.3.5 Example Trigger Chain

As an example of the trigger chain, a di-electron event, triggered by a di-electron trigger is regarded. The two electrons could be a possible signature of a SUSY event. Assume that L1 finds two isolated electromagnetic clusters with a p_{T} larger 7 GeV each. At L1, no distinction between photons and electrons is possible. Instead, only the occurrence of an electromagnetic cluster with a certain pre-defined isolation is recognised. From the L1 electromagnetic RoI, the trigger object `L1_2EM7` is formed. Now, by taking into account the cluster shape, electrons can be distinguished from photons, but only at a very preliminary stage. The cluster shapes of both EM clusters are found to be consistent with the electron hypothesis and two electron candidates (`ecand`) are formed. This is shown is step 1 of Fig. 3.12. In the second validation step, L2 includes the Inner Detector responses of the event under study and is able to identify the electron candidates as 'real'

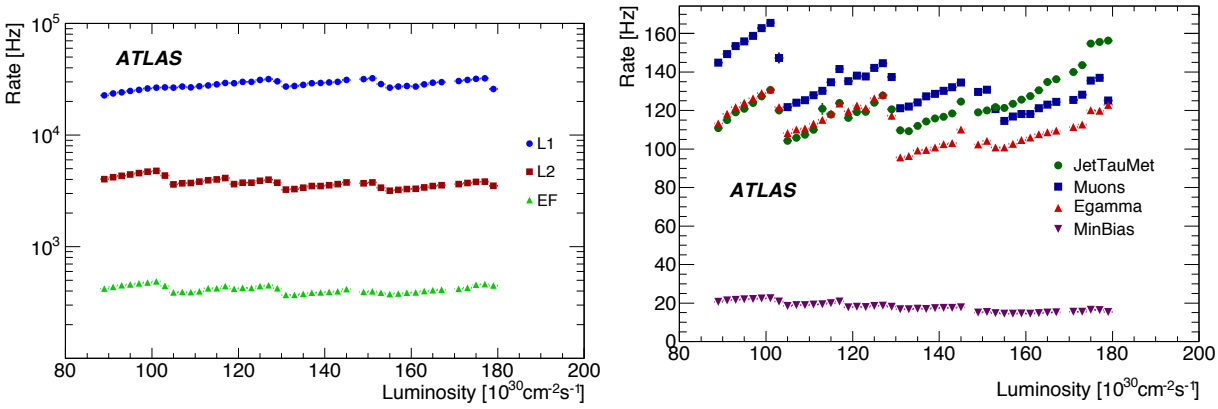

Figure 3.11: Total output trigger rates as a function of instantaneous luminosity in a sample run from period I. Left: Trigger rate for the three trigger levels L1, L2 and EF. Right: Trigger rate for different streams [66].

electrons with the help of track-finding algorithms and the inclusion of the full granularity of the Calorimeter (step 2, intermediate trigger signature '`e+e`'). In the next step, the p_{T} thresholds are refined by the fully available detector response. The electrons reach the 12 GeV threshold but not the threshold above that, so that the attribute '$p_{\mathrm{T}} > 12$ GeV' is connected to the trigger objects (`e12`). After this point, the trigger object `EF_2e12` is formed. In the last step, isolation conditions are checked and the electrons under study are labelled as being isolated (`e12i`). Depending on the type of the electron, the final trigger object is e.g. called `EF_2e12i_medium` (cf. Sec. 4.1). The full event is stored and can be analysed offline. It can be investigated whether the event is a SUSY candidate by including other detector information such as the number of jets and the $E_{\mathrm{T}}^{\mathrm{miss}}$.

The study of different electron triggers for the SUSY dilepton searches forms a major part of this thesis, dealt with in Ch. 7.

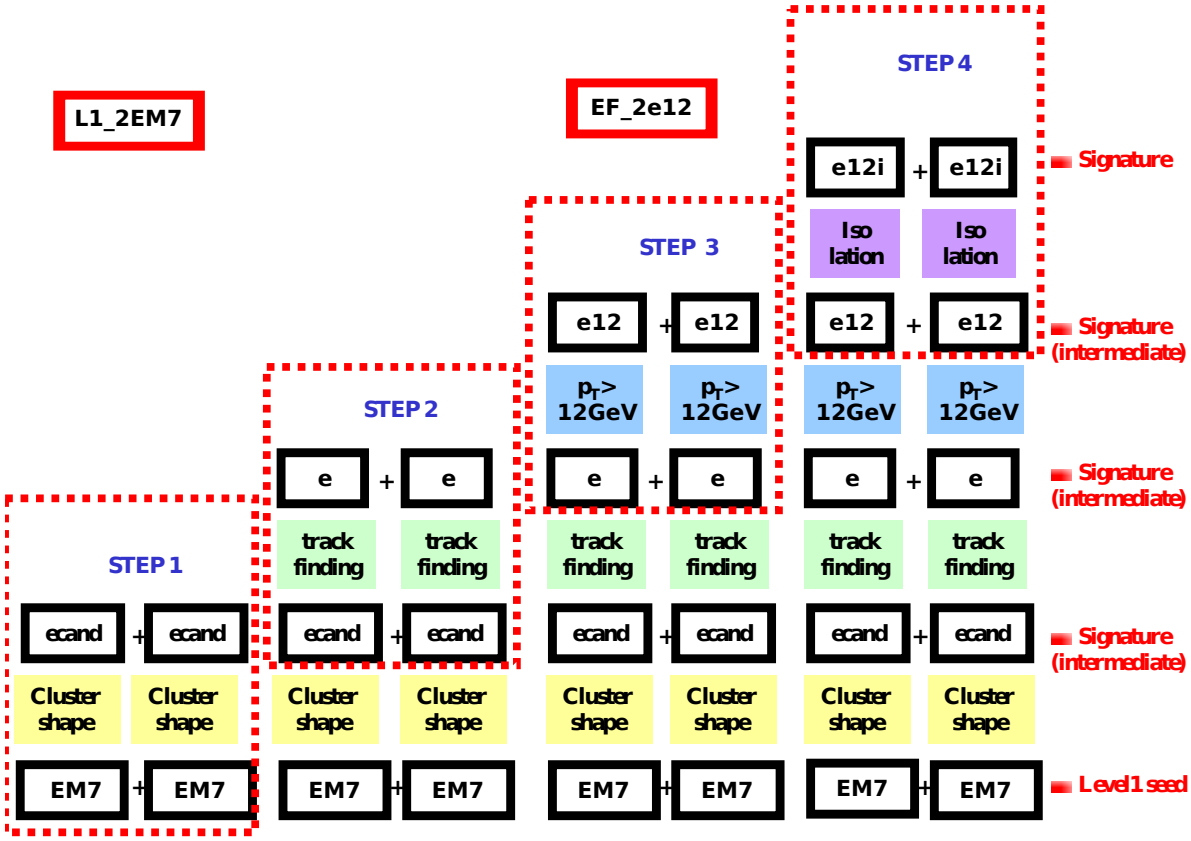

Figure 3.12: Example of the working principle of the HLT selection software for an electron trigger object. The different steps follow each other in time and for each step, the full processing chain preceding it is shown. The names of the intermediate trigger objects are given in the black boxes. The 'final' L1 and EF trigger objects are indicated in the red boxes. The coloured fields symbolise the different HLT trigger algorithms. Modified from [69].

Chapter 4

Data Taking and Event Generation

In this chapter, the offline reconstruction and identification techniques of the particles relevant for this thesis are presented. In addition, this chapter gives a brief introduction to the Monte Carlo generators used for modelling SM and SUSY processes.

4.1 Reconstruction & Identification of Particles

The SUSY signature of this thesis' analysis consists of exactly two leptons (electrons or muons), jets and missing transverse energy in the final state. In this section, a short insight into the reconstruction and identification of these types of particles and the $E_{\mathrm{T}}^{\mathrm{miss}}$ is given.

4.1.1 Electrons

The ratio of the rate of isolated electrons and QCD jets with p_{T} in the range $20-50$ GeV is expected to be $\sim 10^{-5}$ at the LHC, thus an excellent electron identification capability is crucial [71].

Reconstruction

The electron reconstruction algorithms provide electron candidates with high efficiency. Electron reconstruction is seeded from a preliminary set of clusters in the EM calorimeter whose size corresponds to 3×5 cells in $\eta \times \phi$ in the EM middle layer. If the energy deposited in the cluster exceeds an energy of 2.5 GeV and the cluster is found to be within the tracking acceptance of the Inner Detector ($|\eta| < 2.5$), and if the track lies within $\Delta\eta \times \Delta\phi = 0.05 \times 0.1$ of the cluster center, the extrapolated track from the Inner Detector is matched to the energy cluster. A *sliding window* algorithm builds the final cluster with 3×7 cells in the barrel and 5×5 cells in the end-cap [72]. If the allocation of a track to a given cluster is not unique, the track with the smallest $\Delta R = \sqrt{\Delta\eta^2 + \Delta\phi^2}$ is taken.

The cluster energy is measured with high accuracy by computing and summing the energy deposited in the material in front of the EM calorimeter, that deposited in the cluster, that deposited in the calorimeter outside the cluster (lateral leakage) and that deposited beyond the EM calorimeter (longitudinal leakage). Information from the final cluster and the track is used to determine the p_{T} of the electron.

Identification

The electron identification algorithms rely on rectangular cuts using variables which provide good separation between isolated electrons and fake signatures from QCD jets. Three reference cuts are defined, *loose*, *medium* and *tight*. The *loose* selection relies only on hadronic leakage and on shower shapes from the middle EM Calorimeter layer. This set of cuts provides excellent identification efficiency but only low background rejection. The *medium* selection additionally includes EM strip layers, track quality requirements and tracking variables. The medium selection increases the jet rejection by a factor of 3-4 with respect to the loose selection, at the expense of a $\sim 10\%$ reduced identification efficiency. The *tight* selection makes use of several other cuts, amongst them the number of vertexing-layer hits, the number of hits in the TRT and on the ratio of cluster energy to track momentum [71]. The *loose*, *medium* and *tight* electron selections have $Z \rightarrow ee$ signal efficiencies of $\sim 95\%$, $\sim 90\%$ and $\sim 70\%$ at a jet suppression of $\mathcal{O}(10^3)$, $\mathcal{O}(10^4)$ and $\mathcal{O}(10^5)$, respectively [72].

4.1.2 Muons

ATLAS employs different strategies for reconstructing muons. *Standalone* muons are constructed by the use of the Muon Spectrometer only. The tracks found in the MS are then extrapolated to the beamline. *Combined* muons are found by matching the standalone muons with consistent tracks from the Inner Detector. *Tagged* muons are constructed by extrapolating Inner Detector tracks to the MS and searching for nearby hits.

4.1.3 Jets

In general, the jet reconstruction is performed in three steps. The first step is the calorimeter reconstruction in which *calorimeter objects* with p_{T} information are built. This is done by combining the energy depositions of the different calorimeter cells. In the next step, the *jet finder* analyses the calorimeter objects, thus forming *calorimeter jets*. Finally, the calorimeter jets are corrected for the jet energy scale (JES) which reflects the energy and momentum of the original physics objects, unfolded from detector effects.

Being more specific, the calorimeter reconstruction is done by the so-called *topological clustering* which provides three-dimensional calorimeter clusters. The algorithm is seeded

by calorimeter cells with a large signal-to-noise ratio. Then, all neighbouring cells with half the signal-to-noise ratio are added. Finally, all neighbouring cells are added. After the clusters have been produced, the *cluster splitter* searches the topological clusters for a local energy maximum. Such a maximum serves as seed for another iteration of the topological clustering which refines the cluster. Finally, a four-momentum needs to be associated to the topological clusters (needed for the jet finding algorithm). Therefore, the clusters are transformed into massless pseudo-particles, defined by their four-momentum. Its direction points from the center of the coordinate system to the energy-weighted center of the cluster and its energy component is the sum of all cluster cells' energies.

The jet-finding is implemented in the Anti-k_T algorithm [73]. It analyses all pairs (i, j) of four-momentum objects found by the Calorimeter in terms of their relative momenta squared:

$$d_{ij} = \max(k_{T,i}^2, k_{T,j}^2)\frac{R^2}{\Delta R_{ij}^2} \tag{4.1}$$

$$d_i = k_{T,i}^2. \tag{4.2}$$

$k_{T,i}$ is the momentum of the object i, ΔR_{ij}^2 is the relative distance between two objects i and j and R is the fixed cone radius. A narrow jet cone of $R = 0.4$ is used for 'dense' environments like $t\bar{t}$ or SUSY decays. The minimum of the d_i and d_{ij} is chosen and the other one is discarded. If d_{ij} is minimal, the objects i and j are combined to an object k and i and j are discarded. This procedure is repeated until all objects have been removed.

4.1.4 Missing Transverse Energy

The missing transverse energy, $E_{\mathrm{T}}^{\mathrm{miss}}$, is the momentum imbalance in the transverse plane. It is a crucial variable for SUSY searches with R-parity conservation, as the LSP (the lightest neutralino $\tilde{\chi}_1^0$ in the case of mSUGRA) escapes the detector and can only be measured indirectly via the $E_{\mathrm{T}}^{\mathrm{miss}}$. The accurate reconstruction of $E_{\mathrm{T}}^{\mathrm{miss}}$ is difficult because all calorimeter cells as well as the whole muon system in the full $|\eta| < 5$ range have to be considered. Since all final state particles of an event need to be taken into account for the $E_{\mathrm{T}}^{\mathrm{miss}}$ calculation, the statistic and systematic uncertainties of all involved particles propagate into the uncertainty of the $E_{\mathrm{T}}^{\mathrm{miss}}$ determination.

Muon tracks need to be considered separately for the $E_{\mathrm{T}}^{\mathrm{miss}}$ determination since muons do not deposit energy in the Calorimeter. Thus, the determination of the missing transverse energy is composed of the energy deposition in the calorimeters and the measurements from the muon spectrometer,

$$E_{x,y}^{\mathrm{miss}} = E_{x,y}^{\mathrm{miss,calo}} + E_{x,y}^{\mathrm{miss},\mu} \tag{4.3}$$

$$E_{\mathrm{T}}^{\mathrm{miss}} = \sqrt{(E_x^{\mathrm{miss}})^2 + (E_y^{\mathrm{miss}})^2}. \tag{4.4}$$

Due to the large number of calorimeter read-out channels, electronic noise can have a

contribution of up to 13 GeV to the width of the $E_{\mathrm{T}}^{\mathrm{miss}}$ resolution [71]. Noise-suppression is performed by only using calorimeter cells with energies larger than twice the width of the noise distribution of that cell. A *cell-based* algorithm uses the energy depositions in every calorimeter cell that remain after noise suppression. Additional corrections are applied for the muon energy and the energy loss in the cryostats. The muon contribution to the $E_{\mathrm{T}}^{\mathrm{miss}}$ determination is calculated from the measurement of selected muons with $|\eta| < 2.7$.

4.2 Monte Carlo Generators

The simulation of particle collisions and decays as occuring at the LHC are of great importance for the analysis and assessment of the experimental data. Matrix elements (probability amplitudes) can be calculated with the help of Feynman rules and from this, cross sections and kinematics can be deduced which allow the calculation of particle processes. The higher and higher energies that are achieved with colliders lead to events with more and more particles. Analytical tools cannot represent the full complexity detailed enough to compare it with experimental data [74]. Thus, events need to be generated with the help of (pseudo) random number generators. This is realised using Monte Carlo (MC) generators.

The applications of MC generators are versatile. They can be used to study detector requirements so that e.g. trigger chains can be optimised for different hypothetical SUSY models (cf. Ch. 7). Possible background contributions can be simulated and can devise the analysis strategies. MC generators are also crucial to predict SUSY processes and model event rates and decay topologies. This allows the estimation of the feasibility and sensitivity of an analysis in a certain region of the parameter space. An optimisation of signal regions based on MC predictions is performed in Ch. 6. And, most important, the comparison of the data with the MC simulation allows the discovery of SUSY particles or the exclusion of certain regions in the parameter space.

4.2.1 Event Simulation

The MC generator models particles in proton-proton collisions via matrix elements. The generator output are so-called *HepMC* files that contain the final-state particles and their attributes. These files are passed to *GEANT4* which simulates the ATLAS detector response. The output data format of the theoretical prediction is exactly the same as for the experimental data, making it possible to compare directly.

There are different MC generators which differ in the specific calculation of the hard-scattering and hadronisation. The event generation can be divided into several main steps. The primary **hard scattering** is determined by multiplying QCD cross sections, calculated perturbatively, with the parton density function (PDF) of each proton. Dependent

on the generator, either only leading order (tree level) or higher-order (loop corrections) perturbation theory is taken into account. Initial and final state **radiative corrections** via the emission of gluons from initial or final quarks are applied. Moreover, radiation of photons, W or Z bosons are added to the final state. In the next step, **fragmentation** is added; partons need to be fragmented into hadrons which evolve into hadronic showers. The resulting quarks are combined to colour-neutral hadrons. This simulation chain is illustrated in Fig. 4.1. Different MC generators are used in this analysis, `Pythia`, `Herwig`, `Alpgen` and `MC@NLO` which are briefly presented here.

Pythia

`Pythia` [75] is a MC event generator that provides leading-order (LO) calculations for SM and beyond-SM processes. The simulation chain explained above is based on the Pythia implementation, including the string fragmentational model. `Pythia`'s showering and hadronisation calculations can be incorporated in other event generators.

Herwig

The `Herwig` generator [76] is a multi-purpose MC generator with an emphasis on QCD parton shower calculations. QCD jet evolution with soft gluon interferences is included to the calculations via *angular ordering*. `Herwig` provides a cluster model based on non-perturbative gluon-splitting for jet hadronisation and for hadronic events. Many different SUSY processes are included in the framework.

Alpgen

`Alpgen` [77] is particularly designed to model hadronic collisions with an emphasis on multiparton hard processes. Thus, LHC processes can be modelled with high precision. It uses exact calculations for LO parton matrix elements. The evolution of partonic cascades to hadrons are not implemented within the `Alpgen` framework. MC generators like `Pythia` or `Herwig` are used to run the final event generation.

MC@NLO

The `MC@NLO` package [78] uses the Herwig showering and hadronisation calculations but incorporates next-to-leading order (NLO) QCD matrix elements.

4.2.2 Detector Simulation with GEANT4

`GEANT4` (GEometry ANd Tracking) [79] is a program for the simulation of the passage of particles through matter, using Monte Carlo methods. It is used to simulate the response of the ATLAS detector to the MC events. Every component of the ATLAS detector (material composition, location, etc.), including the magnet system is modelled and the

interaction of the MC events with the active and passive detector material is simulated. Every interaction of a generated particle in the simulated detector is recorded and stored as a hit in the corresponding detector cells. The output data has exactly the same format and structure as the experimental data in order to compare both easily. The final offline reconstruction and analysis is performed on real and MC data identically. In addition, the *truth information*, i.e. the original MC final-state particles as well as each intermediate particle is stored. This truth information can be exploited to study, amongst others, trigger or reconstruction efficiencies.

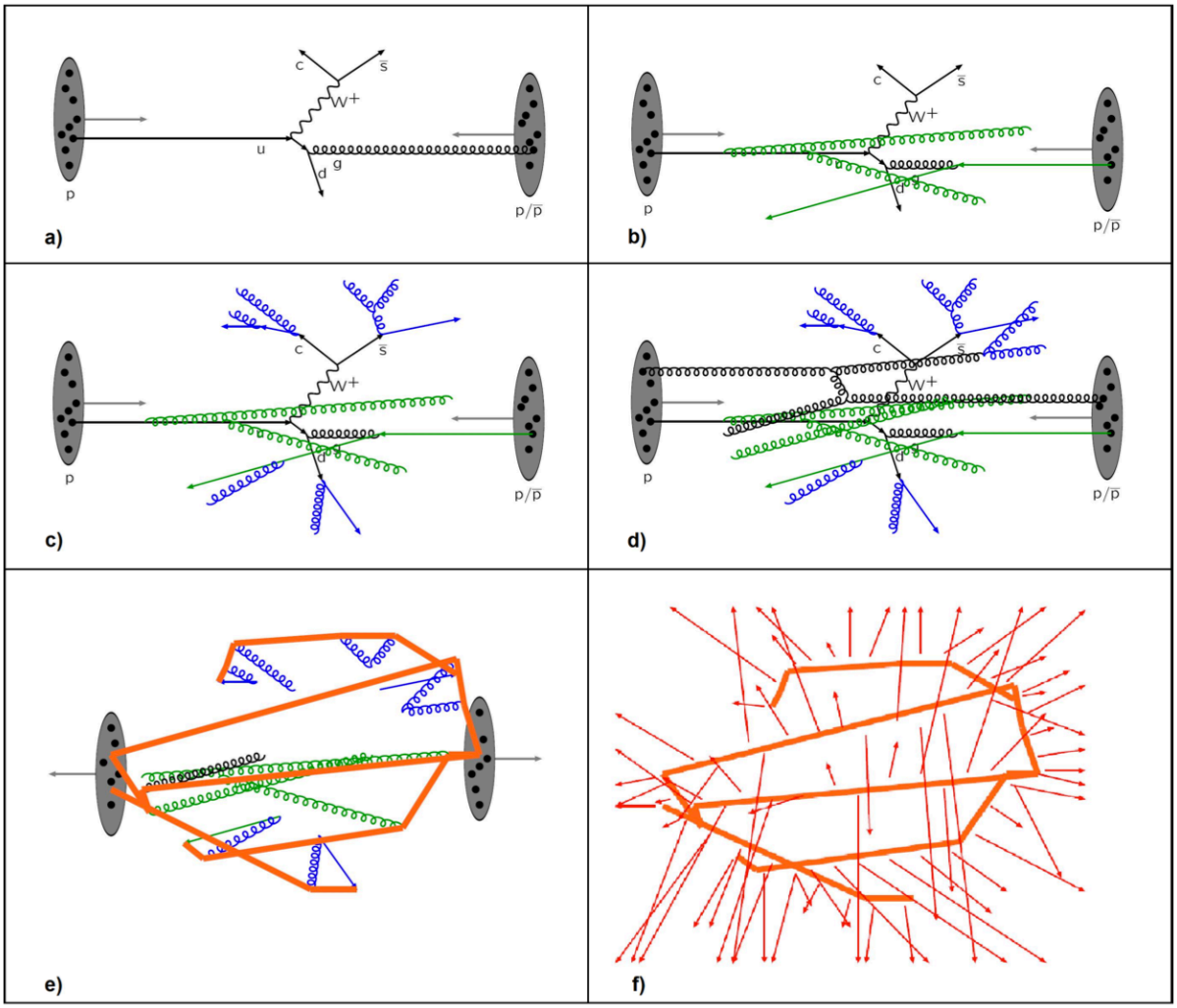

Figure 4.1: Several steps of MC event simulation as it is performed by `Pythia` [75]: **a)** The incoming beams can be described by PDFs. The hard sub-processes are calculated via matrix elements. Furthermore, resonance decays are correlated with the hard sub-processes. **b)** Initial-state radiation is added, here in the form of gluon radiation (green). **c)** Final-state radiation (blue) is added. **d)** As the protons contain multiple partons and more than one parton of a proton can interact, multiple parton-parton interactions need to be taken into account - with its initial- (green) and final-state (blue) radiation. **e)** All beam remnants and other outgoing coloured particles are connected by colour-confining strings (red). **f)** The strings fragmentate to produce primary hadrons. Many of the hadrons are unstable and decay further. These are the particles that hit the detector [74].

Chapter 5

The Underlying Di-Lepton Analysis

5.1 Motivation

In the following studies, di-lepton final states are investigated. Because of its high mass, tau leptons can decay hadronically so that in this analysis the term lepton only refers to electrons and muons, $\ell \in [e, \mu]$. As already pointed out in Sec. 2.2.4, a SUSY decay with two leptons in the final state is phenomenologically interesting because of the resulting clean signal with respect to the QCD background and the potential determination of mass differences through invariant-mass edges.

Depending on the charge and flavour of the leptons, a distinct analysis is required as the background contributions to each channel need to be treated separately. The SUSY di-lepton searches are separated into three sub-channels, the opposite-sign (OS), the same-sign (SS) and the flavour-subtraction analysis. The OS analysis aims at studying events containing exactly two oppositely charged leptons ($e^{\pm}e^{\mp}$, $\mu^{\pm}\mu^{\mp}$ or $e^{\pm}\mu^{\mp}$) while events with exactly two same-sign leptons are covered by the SS analysis. The flavour-subtraction analysis considers the subtraction of opposite-sign different-flavour and opposite-sign same-flavour events (OSDF-OSSF). With this, the excess of same-flavour events over different-flavour events is determined by

$$\mathcal{S} = \frac{N(e^{\pm}e^{\mp})}{\beta(1-(1-\tau_e)^2)} - \frac{N(e^{\pm}\mu^{\mp})}{1-(1-\tau_e)(1-\tau_\mu)} + \frac{\beta N(\mu^{\pm}\mu^{\mp})}{(1-(1-\tau_\mu)^2)} \tag{5.1}$$

where τ_e and τ_μ are electron and muon trigger efficiencies and $\beta = \varepsilon_e/\varepsilon_\mu$ is the ratio of electron and muon reconstruction efficiencies. Flavour-symmetric processes like $t\bar{t}$ can be eliminated efficiently by this method. Furthermore, the advantage of the flavour-subtraction is the reduction of systematic uncertainties such as the jet energy scale and the jet resolution. Besides, the flavour-subtraction analysis is capable of reducing combinatorial SUSY background, thus resulting in cleaner invariant-mass edges compared to the OS mass edges.

This thesis is based on the search for SUSY OS di-lepton final states. The two main topics of this thesis, the optimisation of signal regions and the study of di-lepton triggers serve both the OS as well as the flavour-subtraction analysis. Having regard to the flavour-subtraction analysis, also the optimisation of the OSSF signal region is investigated.

This chapter aims at presenting the data and MC samples used in the analysis as well as the object reconstruction and event selection. Shortly, the main results of the estimation of the SM background and the systematic uncertainties is shown. This chapter closely follows [1][1].

5.2 Trigger, Data Samples, Monte Carlo Samples

The following section names the used Monte Carlo samples and the trigger items as well as the general object reconstruction and event selection. The resulting data and MC samples mark the framework of the subsequent analysis.

Monte Carlo Samples

The different SM contributions are modelled with the following Monte Carlo (MC) event generators (cf. Sec. 4.2): Top-anti-top pairs ($t\bar{t}$) and single top samples are producted with the `MC@NLO` event generator. Samples of W and Z bosons with associated jets are generated with `Alpgen`, diboson (WW, WZ, ZZ) samples with `Herwig`. QCD jets are produced with `Pythia`. The fragmentation and hadronisation for the `Alpgen` and `MC@NLO` samples are performed with `Herwig`, using `Jimmy` [80] for the underlying event. The MC samples are produced using the ATLAS MC10b parameter tune [81] and the `GEANT4` detector simulation. All MC samples are reweighted so that the number of interactions per bunch-crossing agrees with that of the data. Additionally, all processes have different production cross-sections so that they need to be weighted to the same integrated luminosity.

Trigger

Events must either pass the electron trigger `EF_e20_medium` or the muon trigger `EF_mu18`. The triggers reach full efficiency at $p_{\mathrm{T}} > 25$ GeV and $p_{\mathrm{T}} > 20$ GeV, respectively. The selection (trigger) efficiencies for the offline analysis are determined to be $98.74\% \pm 0.01\%$ for electrons and $79.32\% \pm 0.60\%$ for muons [2]. The trigger efficiency curves for electron and muon trigger are shown in Fig. 5.1.

5.2.1 Object Reconstruction

The following criteria need to be fulfilled in order to reconstruct objects and their attributes as precise as possible and to minimise the occurence of misidentified particles.

[1] See also [2] for more details.

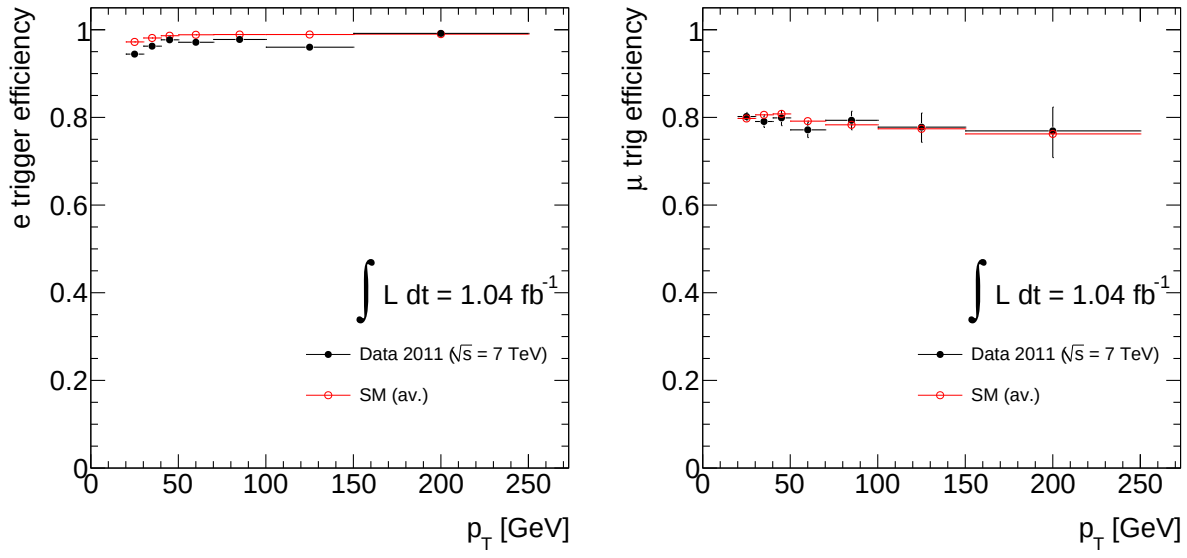

Figure 5.1: Trigger efficiencies for the electron trigger `EF_e20_medium` (left) and the muon trigger `EF_mu18` (right) for an integrated luminosity of $1.04\,\mathrm{fb}^{-1}$. The black points are for data, the red ones for the averaged MC SM simulations [2].

Electrons

Electrons are required to pass the *medium* selection and have $p_{\mathrm{T}} > 20$ GeV and $|\eta| < 2.47$. An overlap removal procedure is applied in order to avoid including misidentified particles (fakes) to the analysis. If an electron e is found in the vicinity of a jet j (within $0.2 < \Delta R_{ej} < 0.4$), the electron is discarded as it is assumed that the electron fakes a jet. If the distance between jet and electron is $\Delta R_{je} < 0.2$, the jet is discarded because this jet is likely to be an electron which has wrongly been identified as a jet. Electrons in the signal regions are required to be *tight*. Moreover, electrons need to be isolated. This means that the p_{T} sum of all tracks above 1 GeV within a cone of $\Delta R < 0.2$ around an electron candidate must be less than 10% of the electron's p_{T}, else the electron is discarded. Finally, if an electron has the highest p_{T} in a lepton pair, its threshold is raised to 25 GeV. This is necessary in order to reach full electron trigger efficiency. Lower p_{T} thresholds would be achievable if di-lepton triggers were used instead of single-lepton triggers (cf. Ch. 7).

Muons

Selected muons must be reconstructed as either *combined* or *tagged* muons (cf. Sec. 4.1.2). Furthermore, muons are required to have a $p_{\mathrm{T}} > 10$ GeV and $|\eta| < 2.4$. If a muon is found within $\Delta R < 0.4$ of a jet, the muon is discarded. Tight cuts are applied to the origin of the muon relative to the primary vertex in order to veto muons resulting from cosmic rays. For a reliable muon reconstruction, muons in the signal region need to be isolated. The momentum sum of tracks within $\Delta R < 0.2$ around the muon candidate must be smaller that 1.8 GeV. If the muon has the highest p_{T} in the lepton pair, its threshold is

raised to 20 GeV. This is necessary in order to reach full muon trigger efficiency.

Jets

Jets are reconstructed using the anti-k_T jet clustering algorithm (Sec. 4.1.3) with a cone radius of $R = 0.4$. Jets are required to have $p_{\mathrm{T}} > 20$ GeV and $|\eta| < 2.8$. In order to remove noise and non-collision backgrounds, events with jets that fail certain quality criteria are rejected.

Missing Energy

The missing transverse energy is determined by calculating the vector sum of the p_{T} of the following objects: jets with $p_{\mathrm{T}} > 20$ GeV, signal leptons, any additional non-isolated muons and calorimeter clusters with $|\eta| < 4.5$ which are not associated with any of the aforementioned objects.

5.2.2 Event Selection

Only events containing exactly two reconstructed tight and isolated leptons (ee, $e\mu$, $\mu\mu$) are selected. Di-electron events need to satisfy the electron trigger, di-muon events the muon trigger. Electron-muon events with the electron having $p_{\mathrm{T}} > 25$ GeV need to satisfy the electron trigger whereas those events with an electron below that threshold must contain a triggered muon with $p_{\mathrm{T}} > 20$ GeV. A cut on the invariant mass of the two leptons ($m_{\ell\ell} > 12$ GeV) is imposed in order to remove low-mass resonances. The primary vertex (the vertex with the highest summed track p_{T}^2) of an event is required to have at least five associated tracks. Due to a damage of the readout system of the LAr calorimeter, a subset of the data needs to be rejected that contains jet with $p_{\mathrm{T}} > 20$ GeV or identified electrons with $-0.1 < \eta < 1.5$ and $-0.9 < \phi < -0.5$.

The events are classified into OS and SS events, according to the lepton's charge. Additionally, both leptons need to satisfy the signal region requirements. Various signal regions are defined, being summarised in Tab. 5.1. Signal regions that introduce requirements on the multiplicity and p_{T} of jets exploit the expected presence of jets in cascade decays from coloured SUSY particle production. They are optimised by considering their potential reach in the mSUGRA parameter space (varying m_0 and $m_{1/2}$, the other free parameters are set to $A_0 = 0$ GeV, $\tan\beta = 10$ and $\mu > 0$). The event selection without applying the signal region cuts is referred to as *general event selection* throughout this thesis. In Table 5.2, a cutflow with the number of observed data events is shown at various stages of event selection.

Table 5.1: Definitions of the three signal regions for the opposite-sign (OS-SRx) analysis, the two signal regions for the same-sign analysis (SS-SRx) and the three signal regions for the flavour-subtraction analysis (FS-SRx) [1]. All units in GeV.

Signal Region	OS-SR1	OS-SR2	OS-SR3	SS-SR1	SS-SR2	FS-SR1	FS-SR2	FS-SR3
$E_{\mathrm{T}}^{\mathrm{miss}}$	250	220	100	100	80	80	80	250
Leading jet p_{T}	-	80	100	-	50	-	-	-
Second jet p_{T}	-	40	70	-	50	-	-	-
Third jet p_{T}	-	40	70	-	-	-	-	-
Fourth jet p_{T}	-	-	70	-	-	-	-	-
# of jets	-	≥ 3	≥ 4	-	≥ 2	-	≥ 2	-
$m_{\ell\ell}$ veto	-	-	-	-	-	80-100	-	-

5.3 SM Backgrounds & Systematic Uncertainties

SM Background Estimation

Fake muons from cosmic rays have an estimated contribution of $< 10^{-3}$ events in each of the signal regions. The fully-leptonic $t\bar{t}$ production is the dominant SM background in the search for opposite-sign (OS) dileptons, making up at least 50% of the total SM event yield. The $t\bar{t}$ background contribution in the signal regions is ascertained by extrapolating the number of $t\bar{t}$ events in a suitable control region into the signal region using the ratio of the number of MC $t\bar{t}$ events in these regions. Smaller contributions arise from Z/γ^*+jets, di-boson and single-top production as well as events containing fake leptons. The contribution from Z/γ^*+jets events is estimated with MC in appropriate control regions. The single top and di-boson contributions are determined with dedicated MC methods. The fake lepton background (mainly coming from W decays and QCD processes) is determined by fully data-driven methods. The tight lepton requirement removes all QCD background, so that a data-driven approach for the estimation of the QCD background is necessary. In all signal regions, Z/γ^*+jets events give the second-highest background contribution. An exception for this is the OS-SR3 where the high jet multiplicity requirement leads to a significant cancellation of this background contribution.

Fig. 5.2 shows the relative size of each SM background contribution for the three OS signal regions. In the upper plot, the $E_{\mathrm{T}}^{\mathrm{miss}}$ distribution for the general event selection can be seen, while the middle and lower plots show the $E_{\mathrm{T}}^{\mathrm{miss}}$ distributions after the three-jet and four-jet requirement, respectively. For low $E_{\mathrm{T}}^{\mathrm{miss}}$, Drell-Yan[2] and Z/γ^*+jets events are the dominant backgrounds. By a cut $E_{\mathrm{T}}^{\mathrm{miss}} > 100$ GeV, the Drell-Yan contribution can be removed entirely and the Z/γ^*+jets significantly. It can be seen that for higher $E_{\mathrm{T}}^{\mathrm{miss}}$, the $t\bar{t}$ decays are the dominant background contribution, followed by Z/γ^*+jets. Including the requirement of three and four high-p_{T} jets lowers the SM background dramatically, at the cost of removing potential rare SUSY events.

[2]Drell-Yan processes denote hadron-hadron scatter processes where a quark and an anti-quark from the hadrons annihilate into a virtual photon or a Z boson which subsequently decay into a pair of oppositely charged leptons.

Table 5.2: Number of observed events in data at various stages of the cutflow for opposite sign events. The following abbreviations are used: GRL: GoodRunLists selection. LArError: Select events with no error from LAr quality assessment. LArHoleVeto: Reject events if an electrons or a jet's eta and phi points to the dead-FEB region of LAr calorimeter. Trig: Selecting events with appropriate trigger requirements. JetClean: Reject events if it has at least one jet failing the jet quality criteria. GoodVertex: Select events where the first primary vertex in the event has at least 5 tracks. CosmicVeto: Reject event that has at least one muon failing the cosmic rejection cuts. Exactly 2lepton+flavor: At this stage select events with exactly two leptons and specific flavors. Sign: Select events according to the sign of the two leptons. mll: Select events with invariant mass of the two leptons to be more than 12 GeV. Signal leptons: Apply isolation criteria to the leptons and apply 'tight' identification to the electrons [2].

Cuts	`Egamma` stream	`Muon` stream	
Total	1.066406e+08	75659176	
GRL	89803544	63933884	
LArError	89795608	63928384	
LArHoleVeto	87779928	63258744	
Trig	58408348	40994184	
JetClean	58165620	40822164	
GoodVertex	57986432	40634840	
	$e^{\pm}e^{\mp}$	$e^{\pm}\mu^{\mp}$	$\mu^{\pm}\mu^{\mp}$
CosmicVeto	57972488	39343888	39343888
Exactly 2lepton+flavor	354391	515014	37994
sign	338803	512106	22750
$m_{ll} > 12$ GeV	336538	464349	16908
signal leptons	237899	444934	5901
$E_{\mathrm{T}}^{\mathrm{miss}}$>80 GeV	522	673	858
OS SR-1 $E_{\mathrm{T}}^{\mathrm{miss}}$>250 GeV	2	3	8
OS SR-2 3jets(80,40,40) GeV	722	1191	332
OS SR-2 3jets +$E_{\mathrm{T}}^{\mathrm{miss}}$>220 GeV	3	5	9
OS SR-3 4jets(100,70,70,70) GeV	20	27	5
OS SR-3 4jets +$E_{\mathrm{T}}^{\mathrm{miss}}$>100 GeV	0	1	1
FS SR-1	344	551	750
FS SR-2	336	567	741
FS SR3	2	3	8

Systematic Uncertainties

The dominant contributions of systematic uncertainties arise from the jet energy scale (JES) and the jet energy resolution (JER). Other sources of systematic uncertainties are theoretical and MC modelling uncertainties as well as uncertainties of the initial- and final-state radiation (ISR/FSR). Furthermore, the limited MC statistics lead to a significant contribution to the uncertainties. Tab. 5.3 summarises the main systematic uncertainties on the $t\bar{t}$ background for the different OS signal regions. Since $t\bar{t}$ dominates the event

yields in these signal regions, these uncertainties make up most of the total systematic uncertainty on the estimated OS background.

Table 5.3: Summary of the dominant systematic uncertainties on the estimates of the fully-leptonic $t\bar{t}$ event yields in each opposite-sign signal region. The uncertainties in each signal region differ due to different control regions [1].

Signal Region	OS-SR1	OS-SR2	OS-SR3
MC & CR statistics	7%	10%	21%
JES	11%	6%	6%
JER	1%	11%	15%
Generator	16%	13%	58%
ISR/FSR	20%	16%	26%
Total	27%	25%	68%

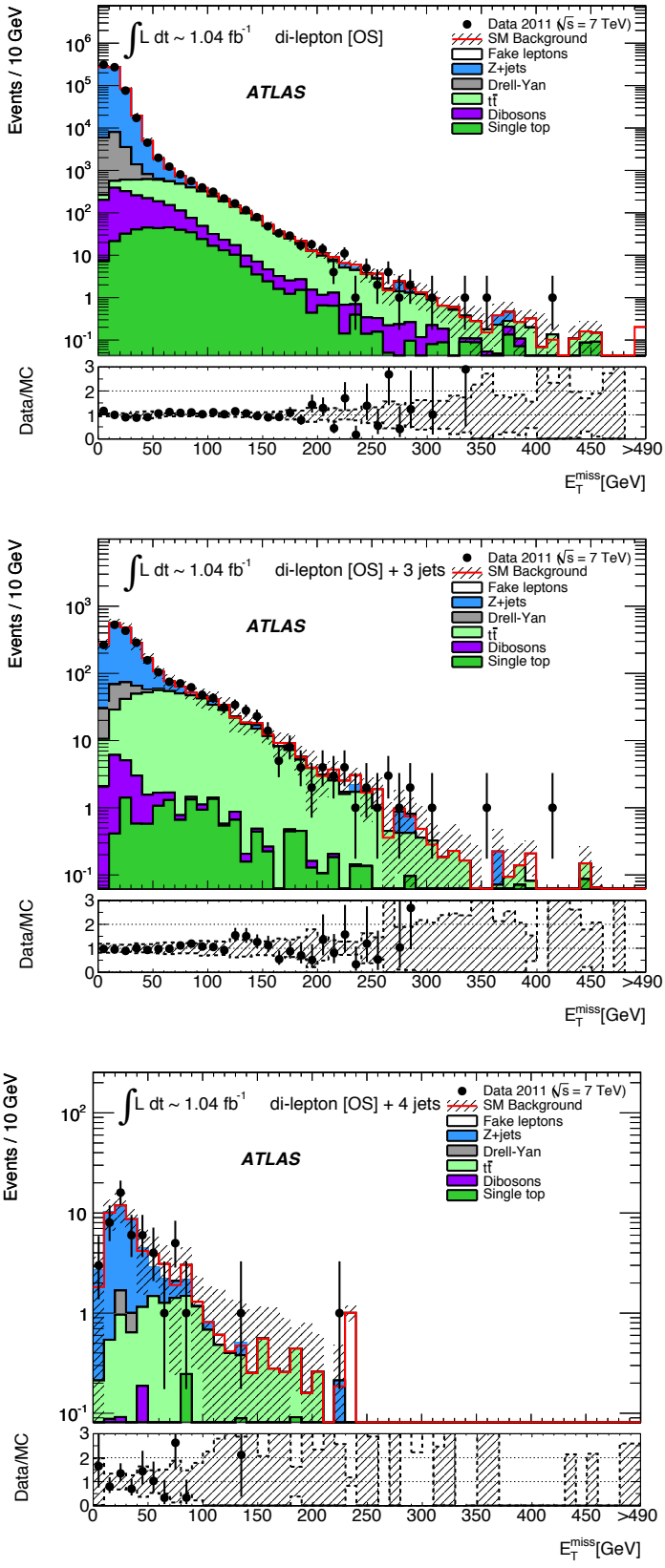

Figure 5.2: Number of opposite-sign dilepton events as a function of the $E_{\mathrm{T}}^{\mathrm{miss}}$ (in bins of 10 GeV) for $\mathcal{L} = 1.04\,\mathrm{fb}^{-1}$, before any jet requirement (a), after requiring 3 high-p_{T} jets (b) and after the 4 jet requirement (c). Errors on data points are statistical, while the error band on the SM background represents the total uncertainty. The lower inserts show the ratio between the data and the SM expectation [1].

Chapter 6

Optimisation of Selection Cuts

In this study, a search channel with two opposite-sign leptons, accompanied by a large amount of $E_{\mathrm{T}}^{\mathrm{miss}}$, due to the LSPs, and possibly jets, is chosen. Such decays typically suffer from very low statistics while background processes with much higher statistics can mimic a SUSY event. For example, consider the decay of a top-antitop pair with the following decay chain:

$$t\bar{t} \rightarrow (W^{+}b)(W^{-}\bar{b}) \rightarrow (\ell^{+}\nu_{\ell}b)(\ell^{-}\bar{\nu}_{\ell}\bar{b}) \tag{6.1}$$

In this process, two jets, missing transverse energy due to the neutrinos as well as two opposite-sign leptons are produced (cf. the Feynman diagrams for the above $t\bar{t}$ decay in Fig. A.6 and a SUSY decay in Fig. A.5). This means that a profound understanding and suppression of the background processes is crucial for the potential discovery of SUSY. This suppression can be achieved by imposing signal region cuts on variables with a good separation power e.g. the number of jets, p_{T} of jets or leptons and the amount of $E_{\mathrm{T}}^{\mathrm{miss}}$. For the 2010 SUSY di-lepton analysis, one signal region, defined by the cut $E_{\mathrm{T}}^{\mathrm{miss}} > 100$ GeV was chosen. It is expected that the ratio of signal and background can be increased significantly if one takes the kinematics of SUSY decays into account. For example, jets are expected to have a higher multiplicity and higher p_{T} than those from SM background processes like $t\bar{t}$ decays. In this study an optimisation of such cut values is performed, aiming at separating supersymmetric signal signatures from SM background in the best possible way. That is, to achieve a maximal signal efficiency together with a maximal background suppression (minimal background efficiency). The optimisation is performed by dint of the toolkit *TMVA* [82]. In the following section, some basic statistical methods and optimisation tools necessary for the subsequent analysis are presented. The cut optimisation is first performed on the mSUGRA benchmark point SU4 (Sec. 6.2.1), followed by an optimisation on different regions in the mSUGRA parameter space (Sec. 6.2.2). Distinct studies for opposite-sign (OS) and opposite-sign-same-flavour (OSSF) events are presented. In Sec. 6.2.3, the obtained cuts are applied to another mSUGRA grid ($\tan\beta = 10$) and compared to other signal regions.

6.1 Optimisation Techniques

Statistical Tests & Machine Learning

In order to be able to discover SUSY, one needs to separate the potential SUSY signal from SM background. It is desired to have rules which decide on statistically justified grounds whether a given event should be treated as signal (S) or background (B). For this to be possible, two *hypotheses* need to be formulated, a null hypothesis H_0 for signal and a complement background hypothesis H_1. A *statistical test* provides a rule for accepting or rejecting the hypothesis depending of the outcome of a measurement x. Accepting the hypothesis H_0 even though it is wrong, i.e. classifying an background event as signal is called a *Type-I error*. The probability for such a Type-I error to occur is the *significance level* α,

$$\alpha = \int P(x|B)\ \mathrm{d}x \tag{6.2}$$

and corresponds to the background selection efficiency. Type-I errors lead to a loss of purity in the selection of signal events. Rejecting the hypothesis H_0 even though it is true, i.e. , failing to identify a signal event as such is called a *Type-II error*. The probability for this to occur,

$$\beta = \int P(x|S)\ \mathrm{d}x \tag{6.3}$$

depends on the alternative (true) hypothesis H_1. $1-\beta$ is called the *power* of the test to reject H_1 and corresponds to the signal selection efficiency. Type-II errors lead to a loss of efficiency in selecting signal events [83].

As a selection criterion, the *likelihood ratio*

$$\lambda(x) = \frac{f(x|H_0)}{f(x|H_1)} \equiv \frac{P(x|S)}{P(x|B)} \tag{6.4}$$

can be used. The maximum of $\lambda(x)$ gives the best possible background rejection for each selection efficiency. The *Neyman-Pearson lemma* [84] states that Eq. (6.4) represents the test statistic with which one may obtain the highest purity sample for a given signal efficiency. The background rejection as a function of the signal efficiency is called *Receiver Operation Characteristics* (ROC) curve. Fig. 6.1 shows different ROC curves with different capabilities to separate signal from background. The 'best' possible ROC curve is given by the maximum likelihood ratio [85]. In practice, however, the true probability density functions are typically unknown so that the Neyman-Pearson lemma is not applicable. Instead, a set of known (already classified) 'events' is generated with MC. These *training* events are used to find a discriminating function $\lambda(x)$ and a corresponding decision boundary that optimally separates signal from background. This procedure is called *supervised (machine) learning* and can be realised with multivariate techniques. In a training phase, the training, testing and evaluation of classifiers using data samples

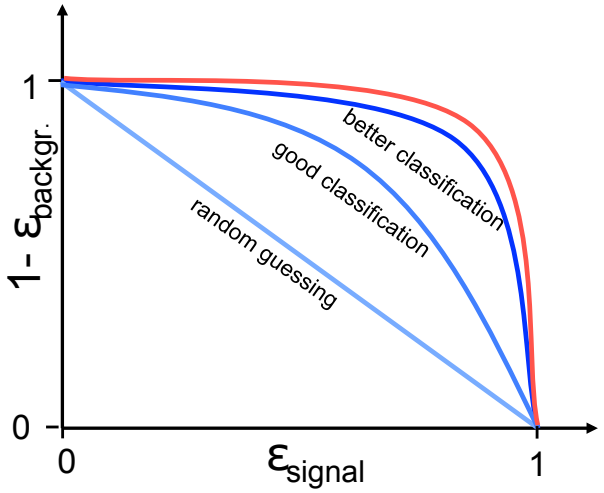

Figure 6.1: The background rejection $1 - \varepsilon_{\text{backgr.}}$ as a function of the signal efficiency $\varepsilon_{\text{signal}}$ [85]. The curves are called *Receiver Operation Characteristics* (ROC) curves. The blue linear function is the result of random guessing while the other blue curves represent a 'good' and 'better' classification. The outermost (red) function symbolises the 'best' possible ROC curve and corresponds to the maximum likelihood ratio according to the Neyman-Pearson lemma.

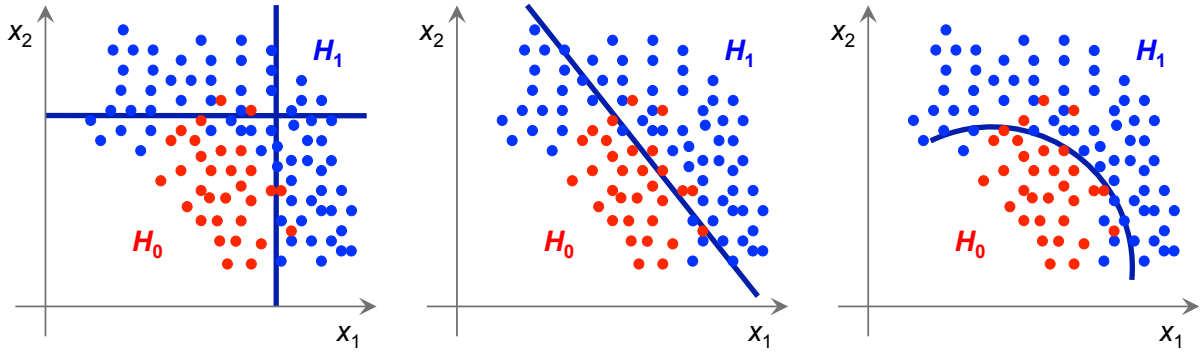

Figure 6.2: Distributions of the background sample H_1 (blue points) and the signal sample H_0 (red points) as functions of two discriminating variables x_1 and x_2 [85]. Three different types of decision boundaries for signal classification are shown. In the left example, the signal region is defined by a rectangular cut, in the middle and right picture, linear and non-linear functions discriminate signal from background.

with known signal and background composition is performed. Then, the selected trained classifiers can be used to classify unknown data samples.

There exist three types of decision boundaries that can be realised, namely rectangular, linear and non-linear boundaries (see Fig. 6.2). The rectangular boundary leads to a set of independent cut values. For linear and non-linear boundaries, a discriminating function of the discriminating variables classifies each event as either signal or background.

Significance and p-value

New physics, i.e. physics beyond the SM is discovered if one can reject the hypothesis that the observed data contains only SM background. The compatibility (or lack thereof)

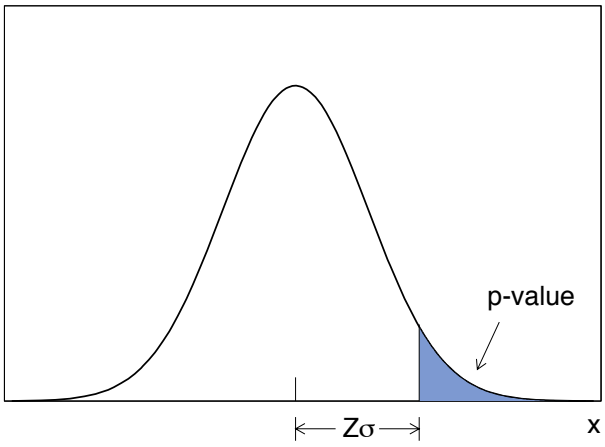

Figure 6.3: Illustration of the correspondence between p-value and significance. The significance Z is related to the p-value by $Z = \Phi^{-1}(1-p)$ where Φ is the cumulative distribution from the standard Gaussian. σ is the standard deviation of the Gaussian distribution [86].

between data and a given hypothesis is quantified by the p-value. The p-value is the probability, under the assumption of a given hypothesis, of obtaining data with equal or less compatibility compared to the level found with the observed data [86]. The *significance* is the number of standard deviations Z at which a Gaussian random variable of zero mean would give a one-sided tail area equal to the p-value. The significance Z is related to the p-value by

$$Z = \Phi^{-1}(1-p) \tag{6.5}$$

where Φ is the cumulative distribution from the standard (zero mean, unit variance) Gaussian. This correspondence is illustrated in Fig. 6.3. Usually, a significance of $Z \geq 3$ is regarded as 'evidence' and $Z \geq 5$ as 'discovery'.

The significance is also used as an optimising selection criterion. TMVA maximises the significance as a function of the signal efficiency for a given background rejection. By default, TMVA defines the significance as $Z_{SSB} = S/\sqrt{S+B}$ where S and B being the number of signal and background events, respectively. For small signal contributions, $Z_{SB} = S/\sqrt{B}$ is a better approximation for the significance, though [87]. Moreover, the yield of the optimisation in this chapter is quantified by comparing the significance Z_{SB} after the application of the optimised cuts with the significance from a reference cut. The quantity Z_{SB} is the expected (median) significance in the limit $S \ll B$ [86, 88]. For quantifying the yield of the optimisation, this assumption is unjustified. After the application of the optimised cuts, S is in fact larger than B. However, this significance definition is assumed to be sufficiently accurate for the purpose of determining the optimisation yield qualitatively and Z_{SB} is chosen because of its simplicity.

TMVA

The optimisation is performed with the help of the toolkit TMVA (Toolkit for Multivariate Analysis) [82] which is integrated into the object-oriented data analysis framework ROOT [89]. It hosts a large variety of multivariate classification algorithms.
An analysis with TMVA is typically performed in three steps. In the *training phase* Monte Carlo samples for signal (S) and background (B), i.e., a set of already classified events is examined. From these samples, a discrimination function and corresponding cut values are found which render an optimal separation between signal and background. This is called supervised (machine) learning and is performed by a variety of algorithms. In the *testing phase* the goodness of the trained classification is evaluated using a statistically independent sample. In the *application phase* the classification is applied to real data.

Genetic Algorithm

In this study, the simplest and most intuitive technique for signal-background separation is chosen, the `CutsGA` algorithm which is not a multivariate algorithm but a sequence of univariate ones. With the help of a genetic algorithm (GA) a rectangular volume is cut from the parameter space, thus ideally separating signal from background. A genetic algorithm finds solutions of optimisation problems for which no or no efficienct solution can be obtained analytically, using techniques inspired by natural evolution.

The problem is modeled by a group (*population*) of abstract representations (*genoms*) of possible solutions (*individuals*). The individuals develop towards an optimal solution. For this, a *fitness* function as a measure for the goodness of an individual is necessary. *Inheritance*, *mutation* and *crossing* are performed in the course of the optimisation. The individuals are kept or discarded corresponding to their fitness. Surviving individuals are copied, mutated and crossed until the initial population size is reached. This process is continued until an individuum reaches a predefined maximal fitness and the best individual is taken to be the solution of the problem [90].

CutsGA

With this algorithm the signal efficiency ε_S is scanned and for each value of ε_S the background suppression is maximised. The fitness function is defined by good background suppression and high signal efficiency. In the first step, all parameters of all individuals are chosen randomly. Then, the individuals are evaluated with regard to their background suppression and signal efficiency. Mutation leads to a random variation (following a Gaussian distribution) of some randomly chosen variables. The output of the program is a significance curve as a function of the signal efficiency whose maximum corresponds to a set of optimal cut values. Thus, the optimal cuts maximise the signal efficiency at given background efficiency.

6.2 Cut Optimisation

In the first part of the analysis only events with two leptons originating from the same decay chain, thus having opposite sign and same flavour (OSSF, $e^{\pm}e^{\mp}$ and $\mu^{\pm}\mu^{\mp}$), are chosen. This is realised by selecting events based on truth information of the SUSY decay chain. Thus, a typical signature of such events contains a large amount of missing transverse energy due to the LSPs, jets and exactly two OSSF leptons. Even though this reduces the number of expected signal events, it has the advantage of a very clear mass edge extraction, once SUSY is found. The major motivation for this optimisation is to assess the benefit of different signal regions for the flavour subtraction analysis.

First, the optimisation is performed on the benchmark point SU4 and the cut values are applied to the whole available subset of the mSUGRA grid. Then, the optimisation is performed on different regions in the parameter space and a thorough comparison of the resulting significances in different regions of the parameter space is carried out.

6.2.1 Optimisation on SU4

SU4 is a benchmark point in the mSUGRA parameter space with $m_0 = 200$ GeV, $m_{1/2} = 160$ GeV, $A_0 = -400$ GeV, $\tan\beta = 10$ and $\mu > 0$. This point was mainly chosen due to its closeness to the TeVatron bound. First, an optimisation of cut values is performed on this point. Then, the resultant cuts are applied to the mSUGRA grid in order to see if and in which regions of the parameter space these cuts can improve the significance with respect to the reference cut. In the following, reference cut refers to the signal region defined by $E_{\mathrm{T}}^{\mathrm{miss}} > 100$ GeV which was incorporated by the 2010 analysis of the SUSY di-lepton working group.

First of all, only the $t\bar{t}$ background is considered as it has by far the most significant contribution to the SM background. Various variables with potential separation power are assessed by comparing their signal and background distributions. For the given number of training events, the `CutsGA` algorithm does only converge if the number of input variables does not exceed four. Therefore, the four variables with the highest separation power between SU4 signal and $t\bar{t}$ background are chosen. These are the missing transverse energy $E_{\mathrm{T}}^{\mathrm{miss}}$, the transverse momentum of the first two leading jets p_{T}^{j1}, p_{T}^{j2} as well as the opening angle between the two leptons, $\Delta R_{\ell\ell}$ with $\Delta R = \sqrt{\Delta\eta^2 + \Delta\phi^2}$. The distributions of these variables can be seen in Fig. 6.4.

The fact that the two leptons originate from the same leg has an impact on their kinematics and can be exploited by considering the $\Delta R_{\ell\ell}$ distribution, displayed in Fig. 6.5 (blue area). The data points in the figure show the distribution for two leptons from SUSY events without the same-leg requirement. The comparison shows that, by only considering OSSF lepton pairs, $\Delta R_{\ell\ell}$ becomes a variable with good separation power with respect to both the SM as well as SUSY background.

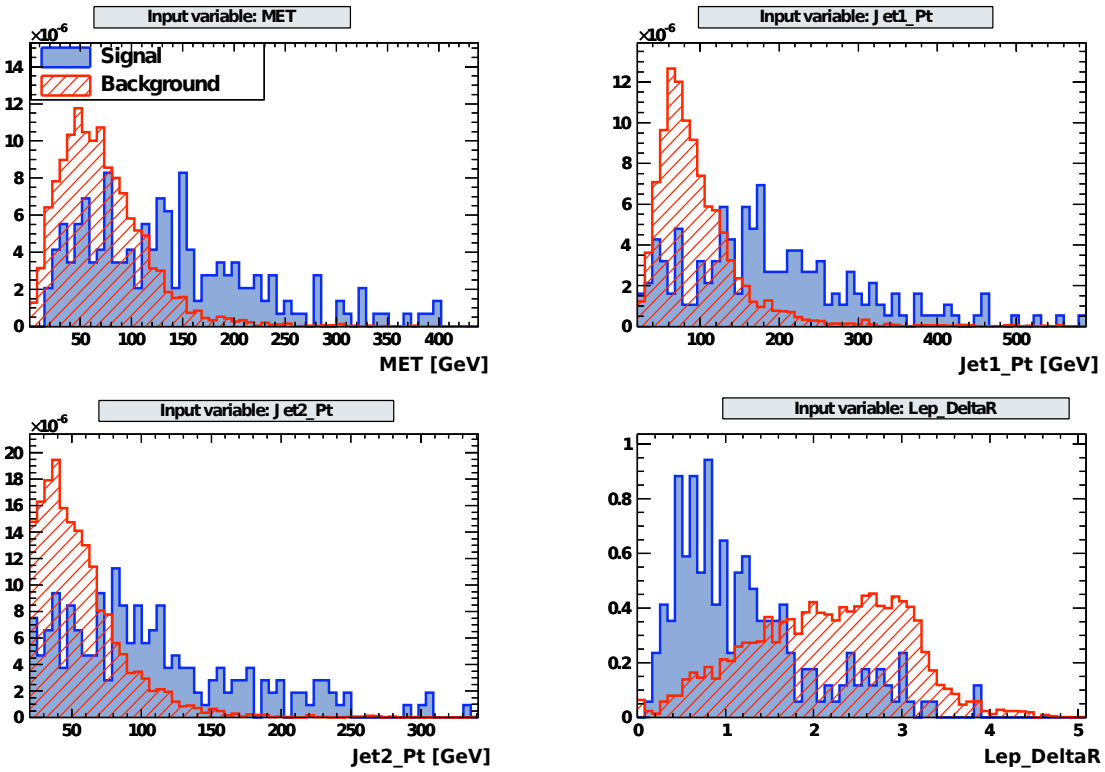

Figure 6.4: Distributions of $E_{\mathrm{T}}^{\mathrm{miss}}$ (MET), p_{T} of leading and subleading jet (Jet1_Pt and Jet2_Pt) and ΔR of the two leptons for signal (SU4) (solid blue) and background ($t\bar{t}$) (red, dashed) for $\mathcal{L} = 34\ \mathrm{pb}^{-1}$. The signal and background distributions are weighted to the total number of signal and background events, respectively which enables the direct comparison of their shapes.

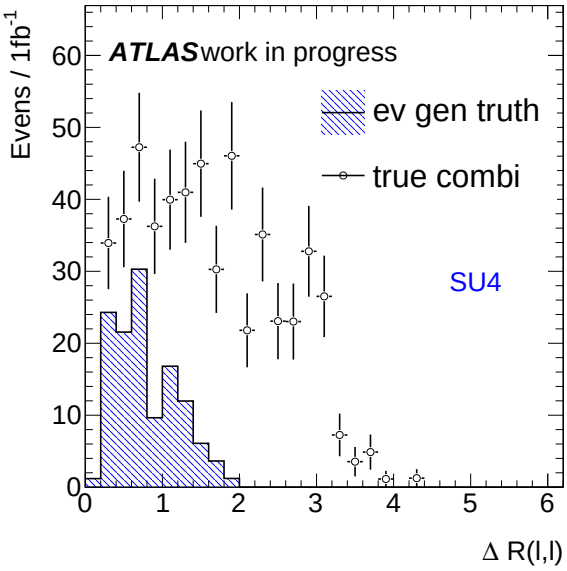

Figure 6.5: $\Delta R_{\ell\ell}$ distribution for events with both leptons originating from one leg (blue) and general di-lepton events (data points) for SU4, weighted to $\mathcal{L} = 1\,\mathrm{fb}^{-1}$.

Fig. 6.6 shows, together with other control curves, the significance $Z_{SSB} = S/\sqrt{S+B}$ whose maximum determines the optimal signal efficiency. From this, the optimal cut values can be determined. The blatant large statistical fluctuations are the limitating

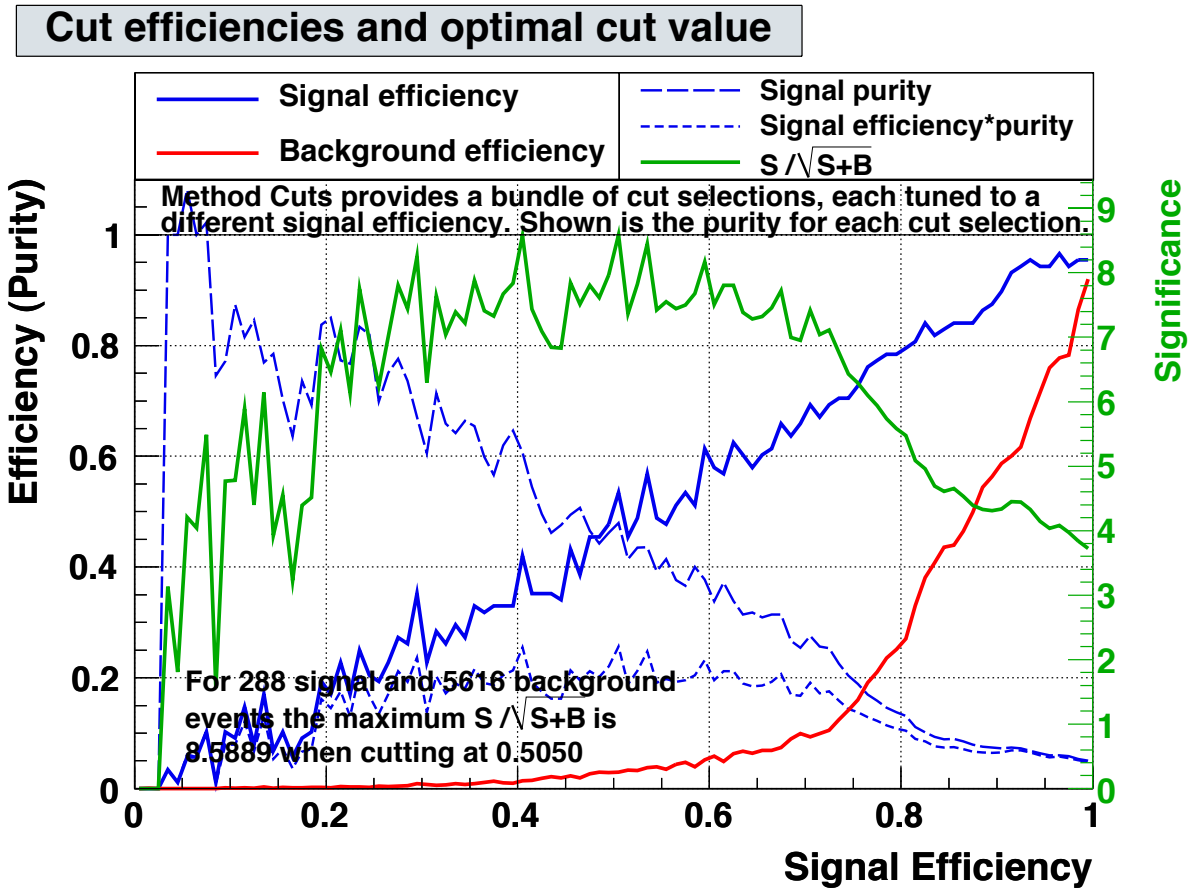

Figure 6.6: Cut efficiencies and optimal cut value for the method `CutsGA`. The optimisation is performed on the SU4 signal and the $t\bar{t}$ background sample for 288 signal and 5616 background events. All curves are plottet as a function of the signal efficiency. The green curve and the corresponding y-axis on the right-hand-side show the significance $S/\sqrt{S+B}$. The maximum of the significance gives the optimal signal efficiency cut. The solid blue and red curves show the signal and background efficiency, respectively. The signal efficiency curve deviates from a perfect straight line due to large statistical fluctuations. The blue dotted lines show the signal purity and the signal efficiency multiplied with the purity. All curves depend on the number of signal and background events.

factor of the optimisation.

For $\sim$ 300 signal and $\sim$ 5600 background events the optimisation yields a signal efficiency of 0.5 at a background efficiency of $\sim$ 0.03. The corresponding cut values are found to be $E_{\mathrm{T}}^{\mathrm{miss}} > 55$ GeV, $p_{\mathrm{T}}^{\mathrm{Jet\ 1}} > 110$ GeV, $p_{\mathrm{T}}^{\mathrm{Jet\ 2}} > 40$ GeV and $\Delta R_{\ell\ell} < 1.65$. Note that all given cut values are generously rounded because of the statistical fluctuations due to the small number of signal events. The number of signal and background events after the application of these cuts and the comparison to the number of events in case of the reference cut are listed in Tab. 6.1 for the different channels ee, $e\mu$ and $\mu\mu$. The background can be suppressed by a factor of $\sim 5-9$ with respect to the reference cut whereas the signal is only reduced by a factor of $\sim$ 1.5. Moreover, the signal $e\mu$ pairs, that are not supposed to survive the OSSF event selection, are drastically reduced. The

efficient reduction of these $e\mu$ events is the result of the $\Delta R_{\ell\ell}$ cut.

Table 6.1: Number of OS $t\bar{t}$ and SU4 events after the application of the optimised cuts and after the reference cut ($E_{\mathrm{T}}^{\mathrm{miss}} > 100$ GeV), respectively for an integrated luminosity of $\mathcal{L} = 1\,\mathrm{fb}^{-1}$. Events are selected according to the general event selection described in Sec. 5.2.2.

	Background ($t\bar{t}$)		Signal (SU4)	
	$E_{\mathrm{T}}^{\mathrm{miss}} > 100$ GeV	Optimised cuts	$E_{\mathrm{T}}^{\mathrm{miss}} > 100$ GeV	Optimised cuts
ee	2.89	0.59	3.32	2.25
$e\mu$	5.11	0.87	5.94	1.47
$\mu\mu$	7.54	0.86	5.80	3.33

Application of the SU4 cuts to the mSUGRA grid

As it is not feasible to perform a cut optimisation on each grid point in the mSUGRA m_0-$m_{1/2}$ plane, a set of cut values needs to be applicable to many points in the parameter space. Therefore, the optimised SU4 cuts are applied to other grid points in the mSUGRA plane and the impact on each point is studied. For each grid point in the mSUGRA $m_0 - m_{1/2}$ plane, approximately 10 000 events are simulated with `Herwig`. The cross section drops rapidly for increasing m_0 and $m_{1/2}$ as can be seen in Fig. 6.7.

Fig. 6.8 shows the number of $e^{\pm}e^{\mp}$ events after the application of the SU4 cuts, superimposed with a logarithmic colour plot. For large m_0 and $m_{1/2}$ the number of OS ee events drops dramatically due to the smaller production cross sections at these points. For the points in the upper right of the figure (blue grid points), about $50\,\mathrm{fb}^{-1}$ would be needed for one $e^{\pm}e^{\mp}$ event to survive the event selection and cuts. In order to quantify the improvement of the SU4 cuts with respect to the reference cut, the ratio of the significances $S/\sqrt{B}$ is determined for the OS di-electron channel[1]. Fig. 6.9 shows that the SU4 cut's significance is greater than that of the reference cut for nearly every point in the mSUGRA plane. Even though the kinematics of the decays differ for varying m_0 and $m_{1/2}$, the application of the SU4 cuts leads to an improvement of a factor $2-3$ for nearly all grid points.

Whether these results can be further improved by implementing different sets of cuts for different regions in the mSUGRA parameter space is investigated in the following.

6.2.2 Optimisation on the mSUGRA grid

For this study, not only the $t\bar{t}$ but all SM background samples are used for the optimisation.

[1] From here on, all results refer to the ee channel. The $\mu\mu$ channel performs very similarly.

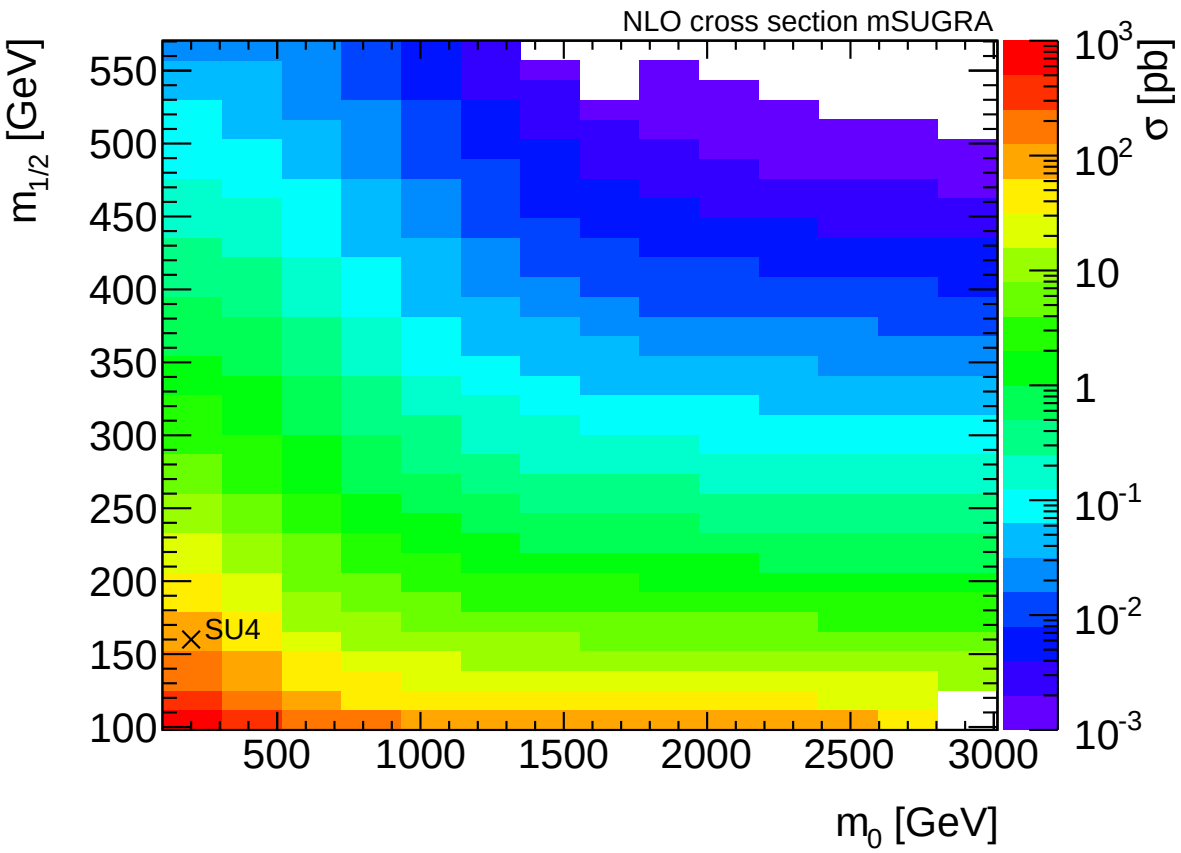

Figure 6.7: Next-to-leading order (NLO) cross sections σ in the mSUGRA parameter space as a function of m_0 and $m_{1/2}$. The cross section drops steeply for higher mass parameters. The remaining free parameters are fixed to $\tan\beta = 10$, $A_0 = 0$ GeV and $\mu > 0$. The cross indicates the SU4 benchmark point (for which $A_0 = -400$ GeV) [91].

2-body vs. 3-body decays

The $m_0 - m_{1/2}$ plane can be divided into two regions depending on the mass difference between squarks and gluinos. If the mass of the gluino is larger than that of the squark ($m_{\tilde{g}} > m_{\tilde{q}}$), 2-body decays via a real squark take place. For $m_{\tilde{g}} < m_{\tilde{q}}$, the two-body decay is kinematically forbidden, so that the gluino decays via a virtual squark (3-body decay) (cf. Sec. 2.2.4). Fig. 6.10 shows the mass difference between the gluino and the lightest squark in the mSUGRA $m_0 - m_{1/2}$ plane. The black line roughly corresponds to $m_{\tilde{g}} = m_{\tilde{q}}$ and thus divides the $m_0 - m_{1/2}$ plane into a 2-body and a 3-body region. Fig. 6.11 illustrates the mass hierarchy for two points in the mSUGRA parameter space for 2-body (left) and 3-body (right) decays, respectively. Taking into account the branching ratios of the different decays as well, it turns out that in 2-body decays, typically less and softer jets are produced than in 3-body decays. This leads to higher values of $E_{\mathrm{T}}^{\mathrm{miss}}$ in the 2-body region.

In fact, there is no strict distinction between 2-body and 3-body decays in the $m_0 - m_{1/2}$ plane, though, as there exists a transition region containing both squarks of heavier and

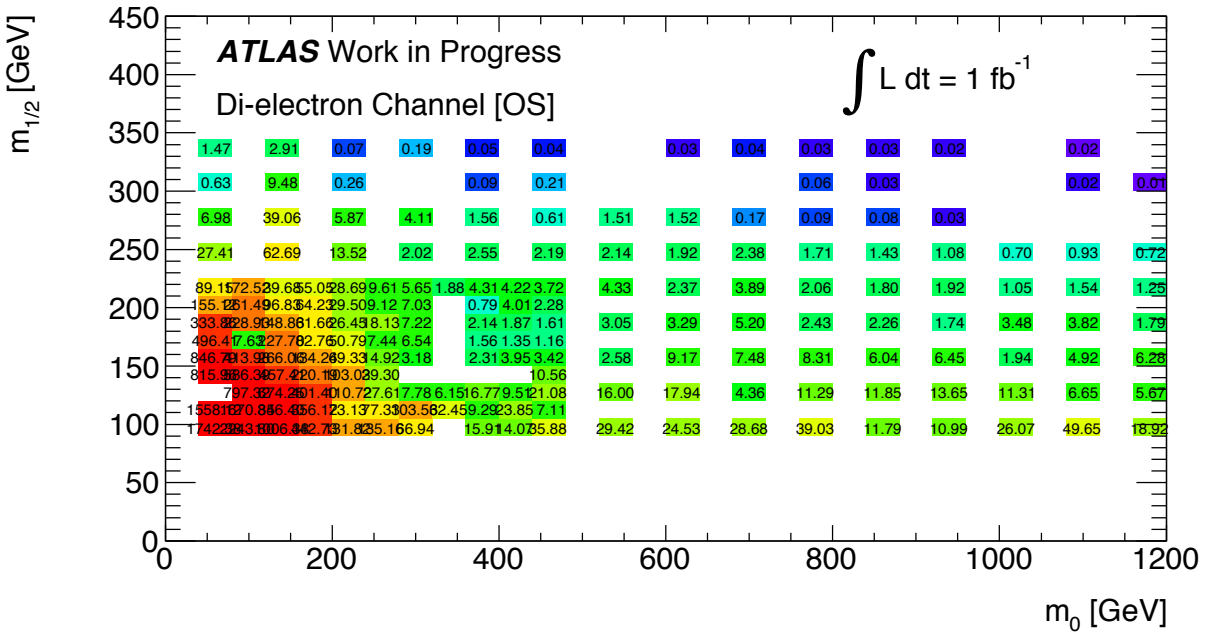

Figure 6.8: Number of $e^{\pm}e^{\mp}$ events after the application of the SU4 cuts in the mSUGRA $m_0 - m_{1/2}$ plane, overlaid with a logarithmic colour plot. The MC events are weighted to an integrated luminosity of 1fb^{-1}.

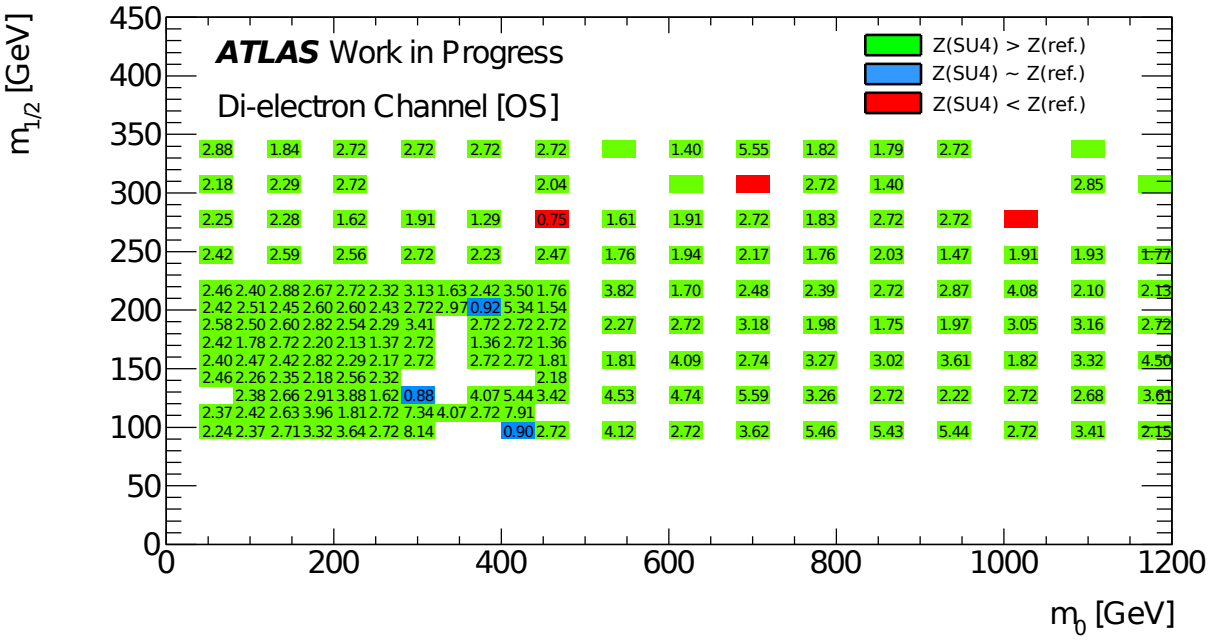

Figure 6.9: Ratio of the significances for the SU4 cuts and the reference cut ($E_{\mathrm{T}}^{\mathrm{miss}} > 100$ GeV) for the $e^{\pm}e^{\mp}$ channel. If the new cut's significance is greater than that of the reference cut, the corresponding grid point is underlaid greenly, else redly. If the deviation of the significances lies within 20%, the corresponding grid point is underlaid in blue.

lighter mass than that of the gluino. Consequently, both decays can take place in this region. This mass hierarchy can be seen e.g. in Fig. 2.11 for SU4. The kinematic differences between 2-body and 3-body decays can be exploited by designing different signal regions for them. It is analysed whether this distinction in the mSUGRA plane

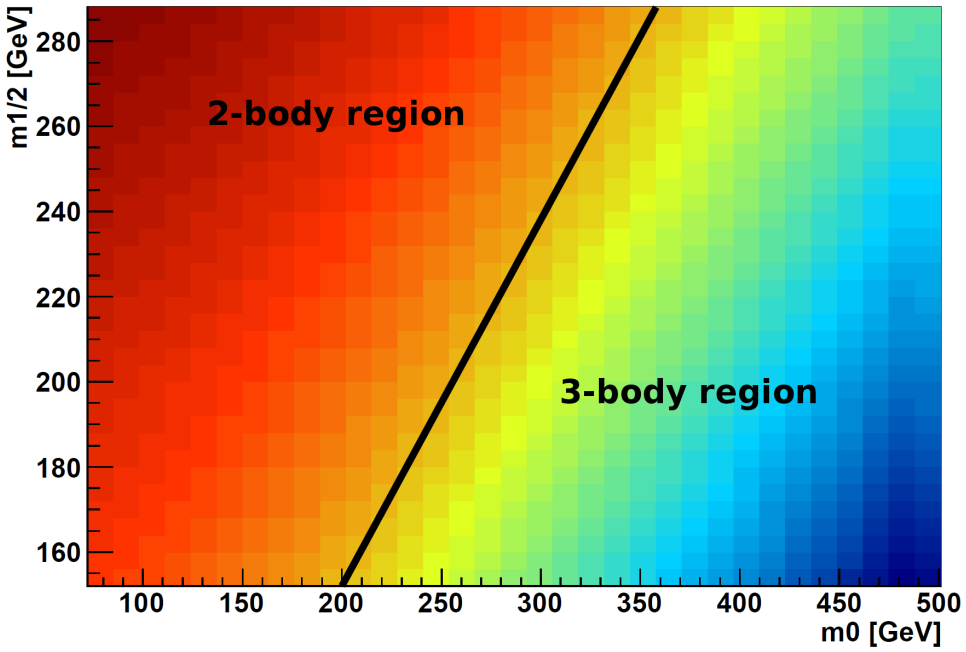

Figure 6.10: Mass difference between the gluino and the lightest squark in the mSUGRA plane. The colour code depicts the mass difference, starting at negative mass differences ($m_{\tilde{g}} < m_{\tilde{q}}$) in blue. The black line corresponds to $m_{\tilde{g}} \approx m_{\tilde{q}}$ and thus divides the $m_0 - m_{1/2}$ plane into a 2-body and a 3-body region [2].

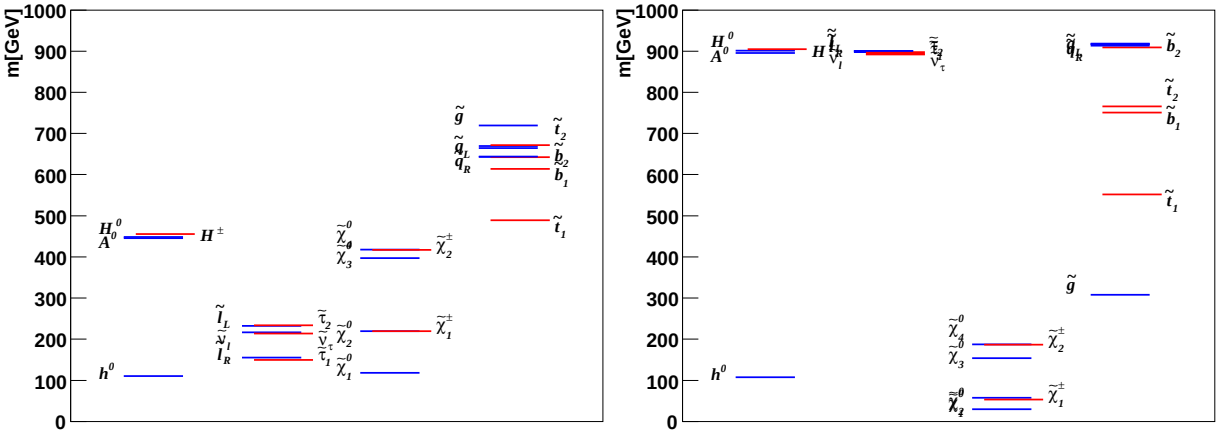

Figure 6.11: Mass spectrum for one mSUGRA point in the 2-body region (left) and one in the 3-body region (right). The spectra correspond to the following set of parameters: 2-body: $m_{1/2} = 300$ GeV, $m_0 = 100$ GeV, $\tan(\beta) = 10$, $A_0 = 0$ GeV and $\mu > 0$, 3-body: $m_{1/2} = 100$ GeV, $m_0 = 900$ GeV, $\tan(\beta) = 10$, $A_0 = 0$ GeV and $\mu > 0$. On the right hand side of each plot the gluino and squark masses are shown.

leads to an improvement of significance with respect to a single global signal region. For this optimisation, two different regions in the mSUGRA plane, one for large m_0 and small $m_{1/2}$ and one for small m_0 and large $m_{1/2}$ are chosen. For this analysis both the OS as well as the OSSF channels are investigated.

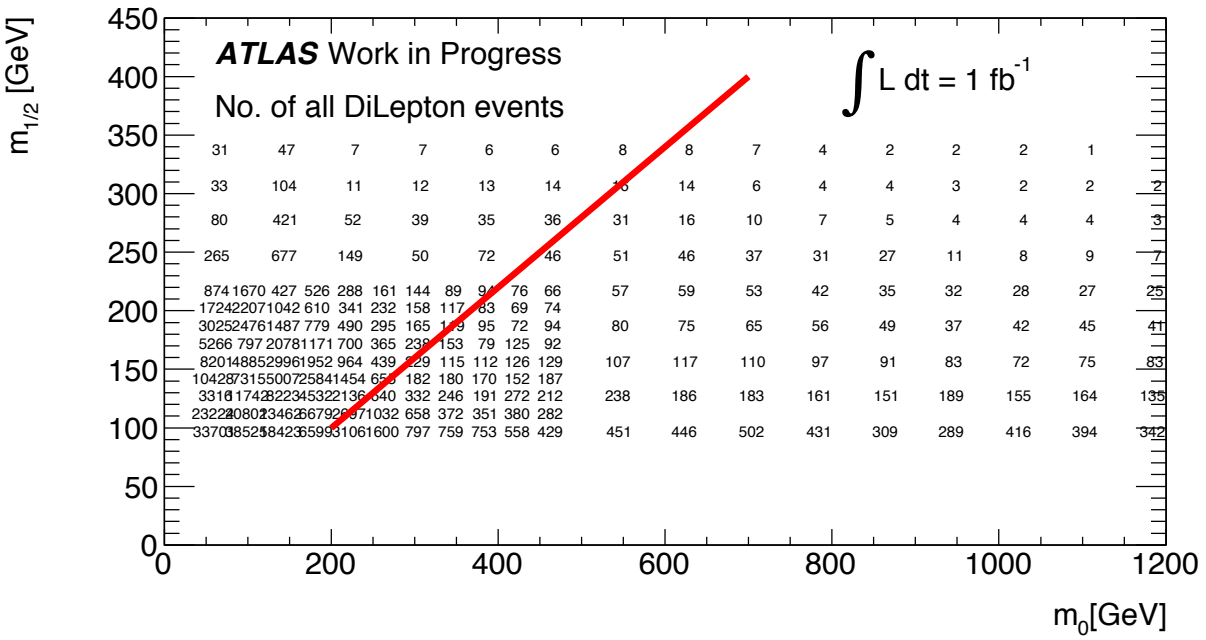

Figure 6.12: Number of all OS di-lepton events after the general event selection for 1 fb^{-1}. The red line indicates the separation between 2-body and 3-body region.

OS study

Fig. 6.12 shows the number of OS di-lepton events after the general event selection (the event selection described in Ch. 5 excluding the signal region cuts). The red line indicates the separation between 2-body and 3-body region. As stated above, two different regions in the mSUGRA plane, one for small m_0 and large $m_{1/2}$ (defined as *Region1*) and one for large m_0 and small $m_{1/2}$ (defined as *Region2*) (and thus one for the 2-body and one for the 3-body region) are chosen. The grid points inside these regions are merged in order to gain more statistics. On these combined grid points the optimisation is performed.

For the optimisation on these two regions, the missing transverse energy and the p_{T} of the two leading jets are used as separating variables. The distributions of these variables for the 2-body and 3-body region are shown in Fig. 6.13 and 6.14, respectively. The signal distributions in the 3-body region have a more distinct maximum than those of the 2-body region.

Significance & systematic uncertainties

By default, TMVA defines the significance as $Z_{SSB} = S/\sqrt{S+B}$ where S and B being the number of signal and background events, respectively. However, for small signal contributions, $Z_{SB} = S/\sqrt{B}$ is a better means for the significance [87, 92]. This quantity is the expected (median) significance in the limit $S \ll B$ [86, 88].
For these two definitions of significance the optimisation is performed independently in order to see the impact of this change on the resulting cuts. Fig. 6.15 shows the significance (in green) as a function of the signal efficiency for both significance definitions. The

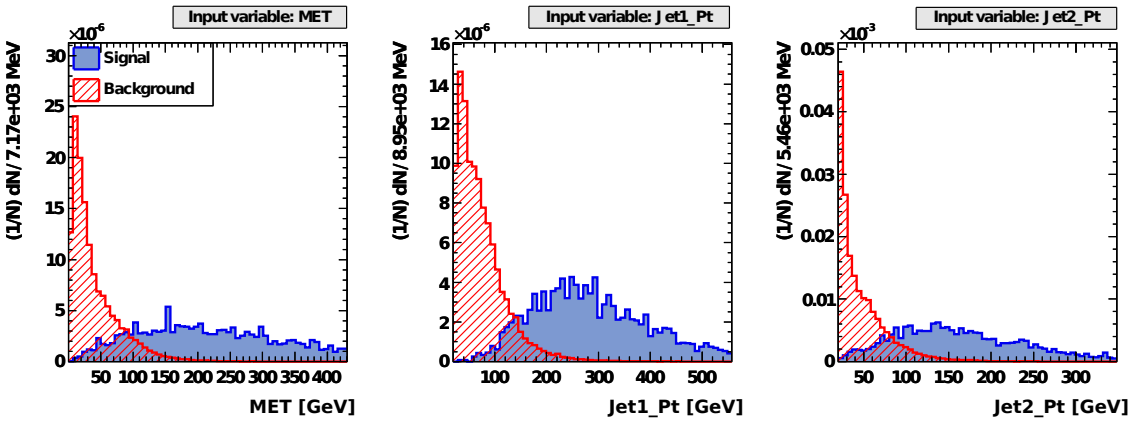

Figure 6.13: Distributions of the three variables which are used for the optimisation of 2-body decays. The signal and background distributions are weighted to the total number of signal and background events, respectively which enables the direct comparison of their shapes.

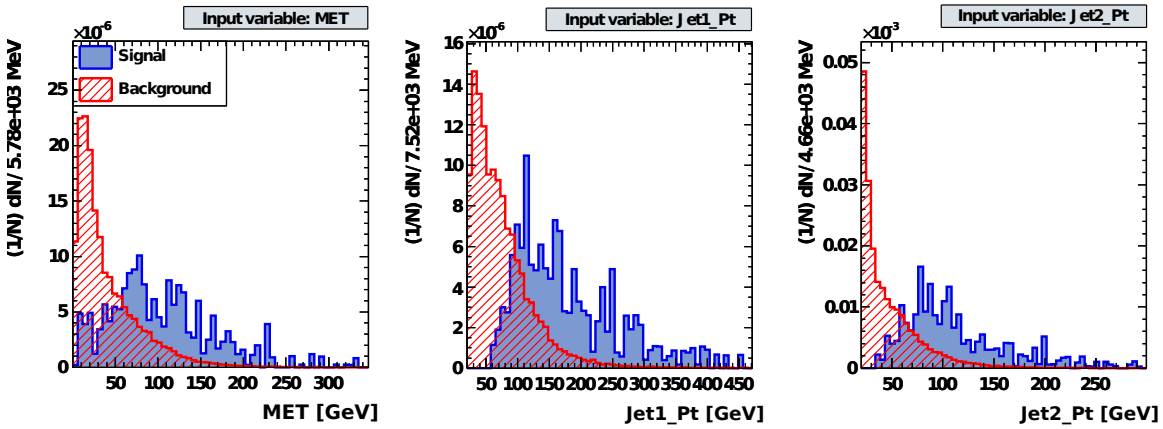

Figure 6.14: Distributions of the three variables which are used for the optimisation of 3-body decays. The signal and background distributions are weighted to the total number of signal and background events, respectively which enables the direct comparison of their shapes.

increased number of signal events with respect to the SU4 optimisation leads to much smoother distributions[2]. Both methods produce consistent results within the scope of statistical uncertainties as they both peak at approximately the same signal efficiency and thus leading to approximately the same cut values. Thus, the cuts are robust against the definition of the significance.

Moreover, the impact of systematic uncertainties on the resulting cut values is investigated. For this, a systematic uncertainty of 20% on the number of background events is assumed. With the substitution $B \to B + \delta B$ with $\delta = 0.2$ it is attempted to incorporate

[2]Moreover, the bin-width is enlarged to smooth the distributions.

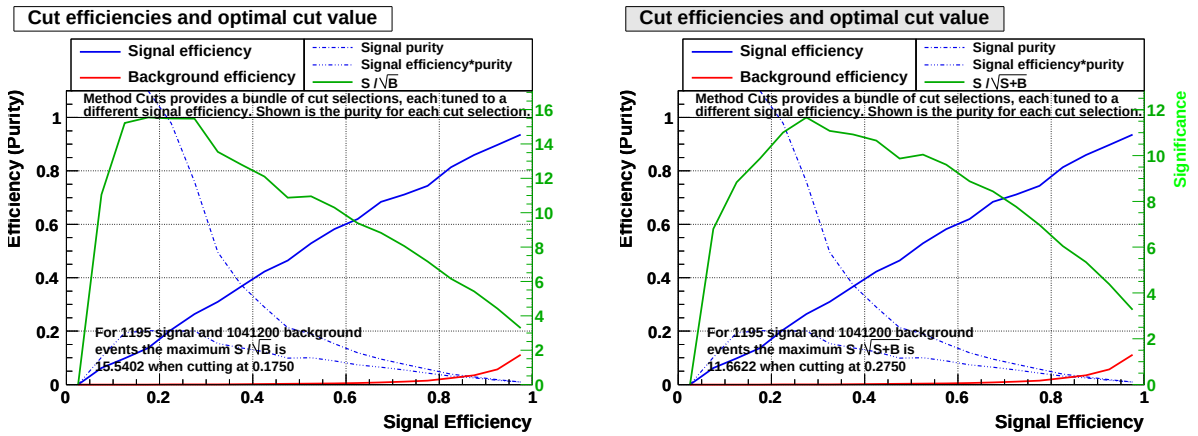

Figure 6.15: These plots show the significance (green), the signal efficiency (red), the background efficiency (blue) as well as signal purity and signal purity*efficiency as a function of the signal efficiency. In the left plot the significance is defined as $S/\sqrt{B}$ and in the right plot as $S/\sqrt{S+B}$.

the uncertainty in B [92]:

$$Z_{SB,\text{sys.}} = \frac{S}{\sqrt{B + (\delta B)^2}}. \tag{6.6}$$

The curves for this modified significance are shown in the appendix in Fig. A.7. One can see, very roughly and again bearing in mind the large statistical uncertainties, that the incorporation of systematic uncertainty on the number of background events does not lead to substantial changes in the significance curve. This approach is very conservative and clearly needs to be studied further with more elaborate methods. But it leads to the preliminary conclusion that the resulting cut values of this optimisation are relatively robust against systematic uncertainties. Note that this statement may need to be revised if the statistical uncertainty can be reduced.

The cut values are determined with the same optimisation technique as in the previous section. The resulting cut values are listed in Tab. 6.2. Note that the cuts for the low m_0-high $m_{1/2}$ region are much tighter than in the other region. The comparison of these

Table 6.2: Overview of the OS cuts for the two optimisation regions. *Region1* corresponds to the low m_0 and large $m_{1/2}$ region and *Region2* refers to the one with large m_0 and small $m_{1/2}$.

	Region1	*Region2*
$E_{\text{T}}^{\text{miss}}$	120 GeV	65 GeV
p_{T}^{j1}	195 GeV	90 GeV
p_{T}^{j2}	75 GeV	70 GeV

cuts with the reference cut is shown in Fig. 6.16 and 6.17. These figures show the ratio of the new cut's significance and the reference cut's significance(with Z_{SB} being used). The *Region2* cuts are able to improve the significance by a factor of ~ 2 over the whole grid

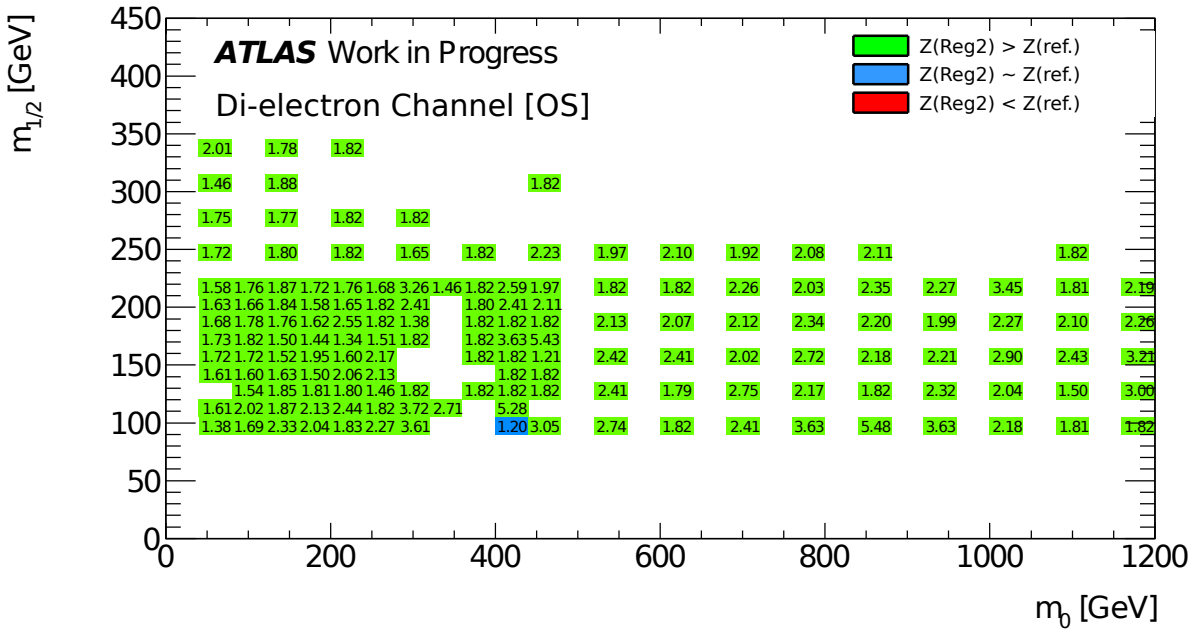

Figure 6.16: Ratio of the significances for the *Region2* cuts and the reference cut ($E_{\mathrm{T}}^{\mathrm{miss}} > 100$ GeV) for the $e^{\pm}e^{\mp}$ channel. If the new cut's significance is greater than that of the reference cut, the corresponding grid point is underlaid greenly, else redly. If the deviation of the significances lies within 20%, the corresponding grid point is underlaid in blue.

region. The *Region1* cuts improve the significance by a factor of $\sim 3-5$ over the whole grid region with the exception of some low $m_{1/2}$ points. Due to the tighter cuts of *Region2*, the number of background events is reduced significantly which leads to numerical problems in the calculation of Z_{SB}. This is why several points in the significance-ratio plot are missing.

It suggests itself to assign the *Region1* cuts to all grid points in the 2-body region and the *Region2* cuts to those in the 3-body region. In order to scrutiny this, the ratio of the significances for the two sets of cuts is calculated. One could expect that the *Region1* cuts suit best for 2-body decays while the *Region2* cuts suit best for the 3-body decay region. But as one can see from Fig. 6.18 this is not the case. Instead, it seems that the *Region1* cuts perform better for $m_{1/2} \gtrsim 170$ GeV and the *Region2* cuts lead to higher significances for $m_{1/2} \lesssim 170$ GeV. So, a possibility would be to apply the *Region1* signal region to all points with $m_{1/2} \geq 170$ GeV and the *Region2* signal region to all points with $m_{1/2} < 170$ GeV.

OSSF Study

In this study, in contrast to the previous one, only events containing two leptons originating from the same decay leg are considered, that is events with exactly two oppositely charged leptons of the same flavour (OSSF: $e^{\pm}e^{\mp}$, $\mu^{\pm}\mu^{\mp}$). The number of OSSF events in the mSUGRA $m_0 - m_{1/2}$ plane is shown in Fig. 6.19.

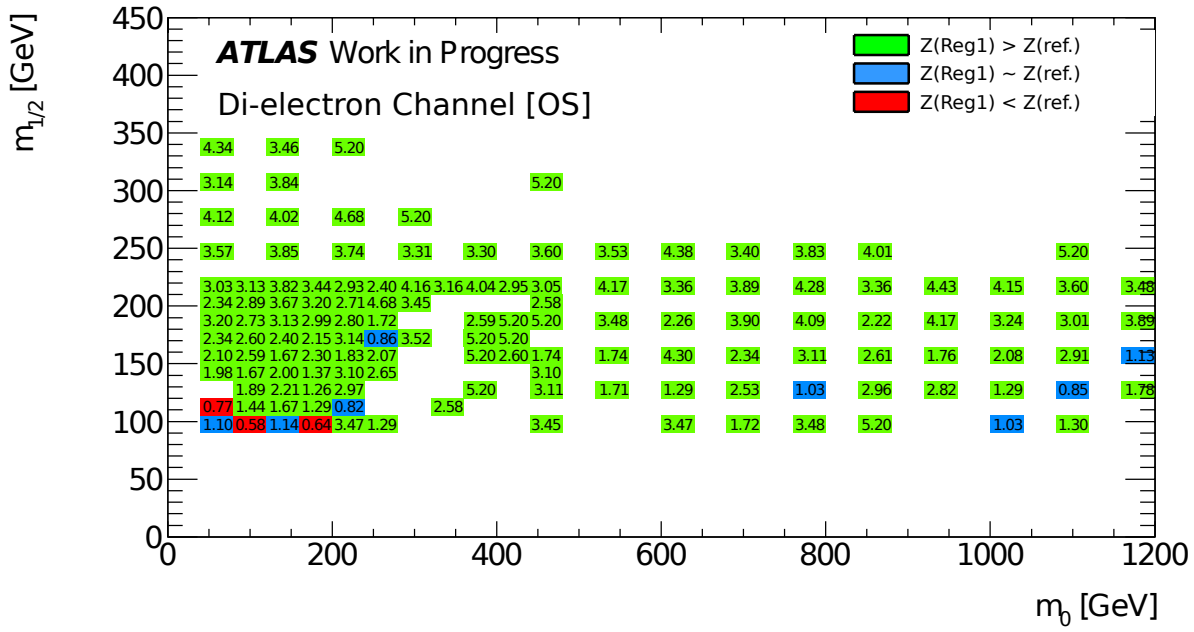

Figure 6.17: OS: Ratio of the significances for the *Region1* cuts and the reference cut ($E_{\mathrm{T}}^{\mathrm{miss}} > 100$ GeV) for the $e^{\pm}e^{\mp}$ channel. If the new cut's significance is greater than that of the reference cut, the corresponding grid point is underlaid greenly, else redly. If the deviation of the significances lies within 20%, the corresponding grid point is underlaid in blue.

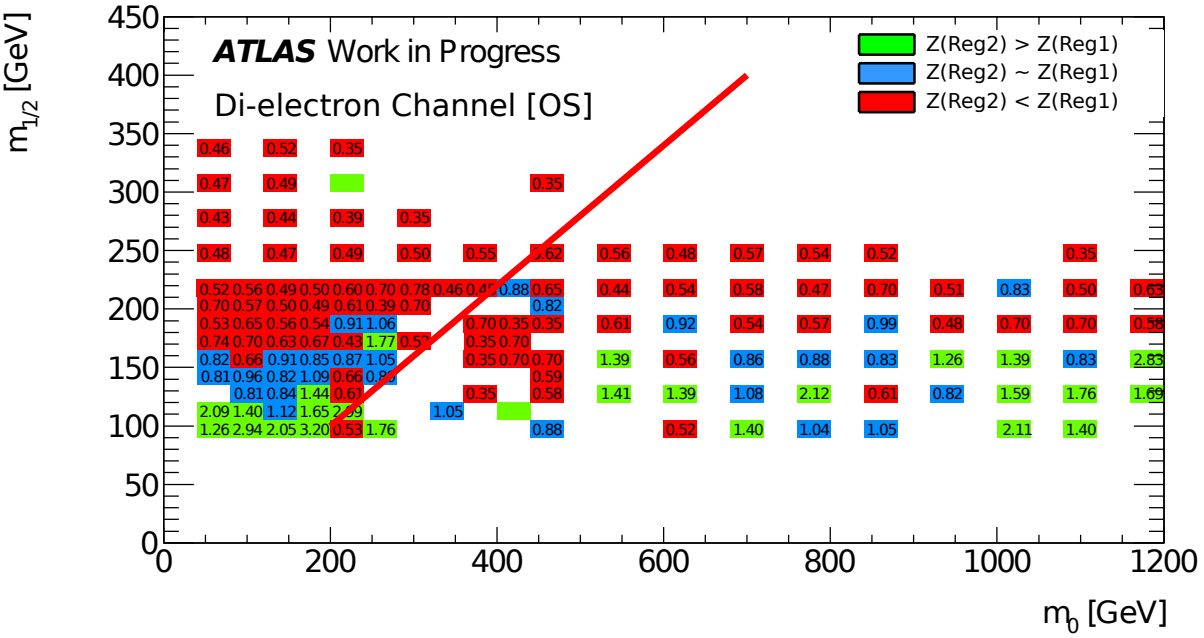

Figure 6.18: OS: Ratio of the significances for the *Region1* cuts and the *Region2* cuts for the $e^{\pm}e^{\mp}$ channel. If the significance of *Region1* is greater than that of *Region2*, the corresponding grid point is underlaid greenly, else redly. If the deviation of the significances lies within 20%, the corresponding grid point is underlaid in blue.

The separating variables used for this optimisation are the ones which were also used for the optimisation of the OSSF SU4 signal region (cf. Sec. 6.2.1). i.e. the $E_{\mathrm{T}}^{\mathrm{miss}}$, the p_{T} of the first two leading jets as well as the ΔR between the two leptons whose distributions

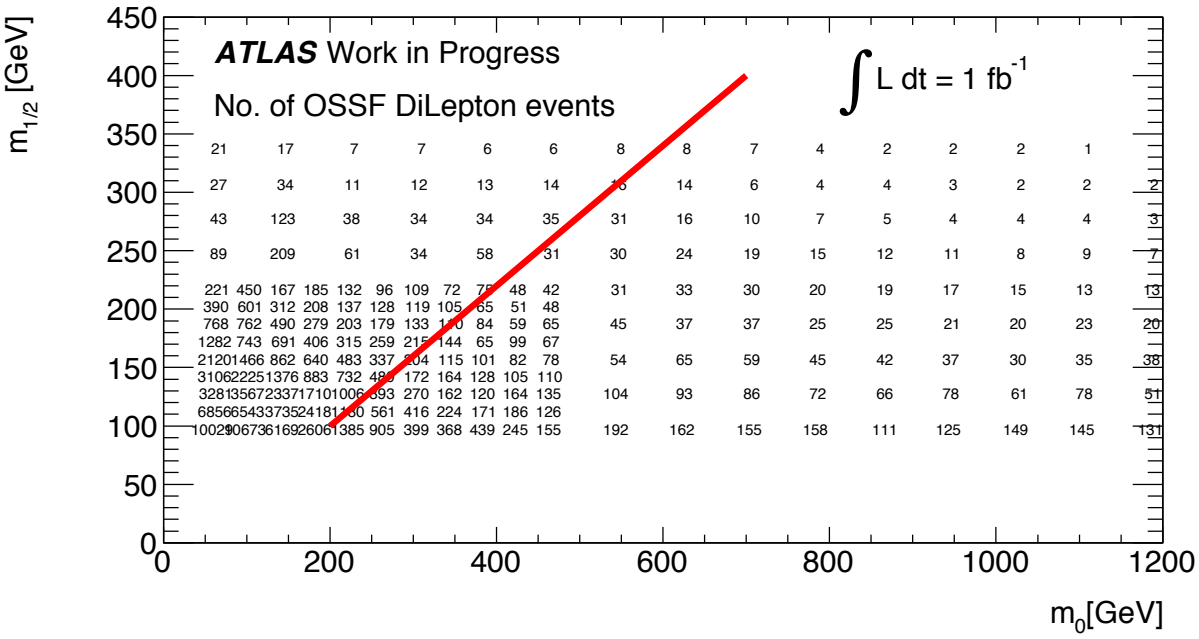

Figure 6.19: Number of all OSSF di-lepton events after the general event selection for $1\,\mathrm{fb}^{-1}$. The red line indicates the separation between 2-body and 3-body decays.

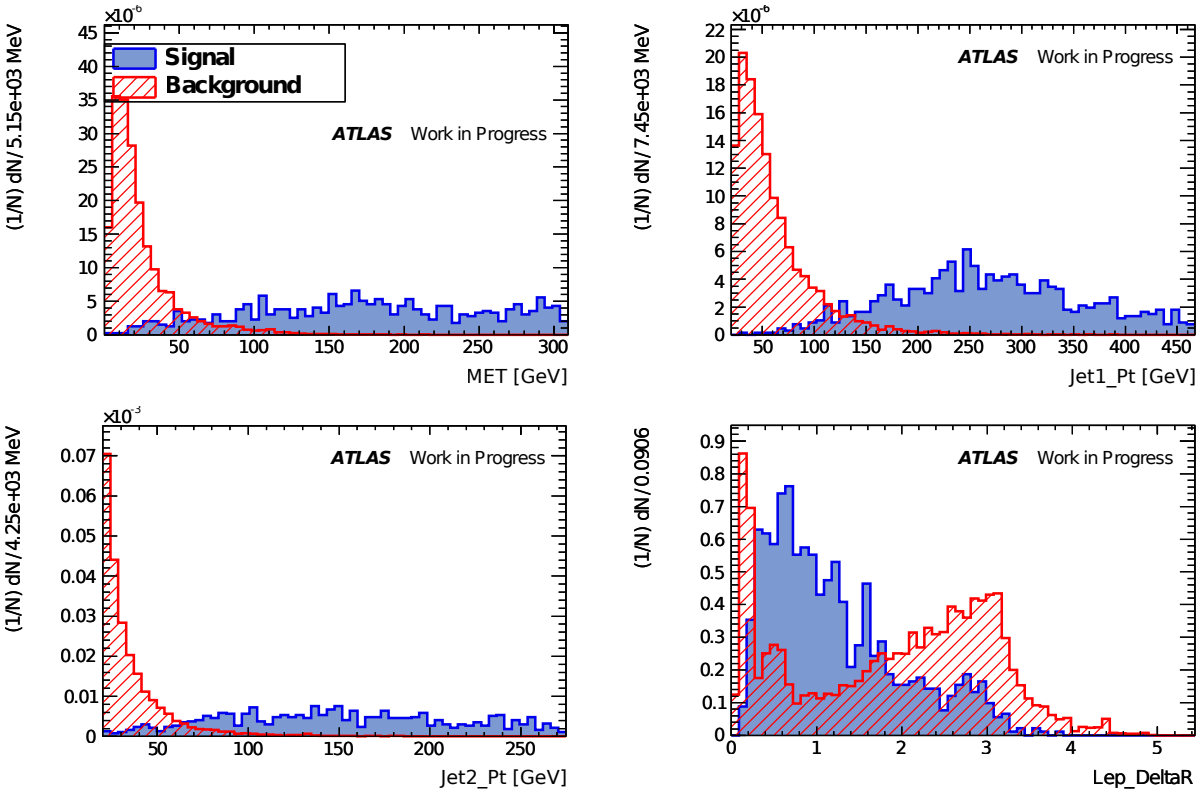

Figure 6.20: Distribution of the variables for the OSSF cut optimisation for $\mathcal{L} = 34\ \mathrm{pb}^{-1}$. The signal and background distributions are weighted to the total number of signal and background events, respectively which enables the direct comparison of their shapes.

are shown in Fig. 6.20.

The optimisation of *Region1* leads to tighter cuts with respect to *Region2*, just as in

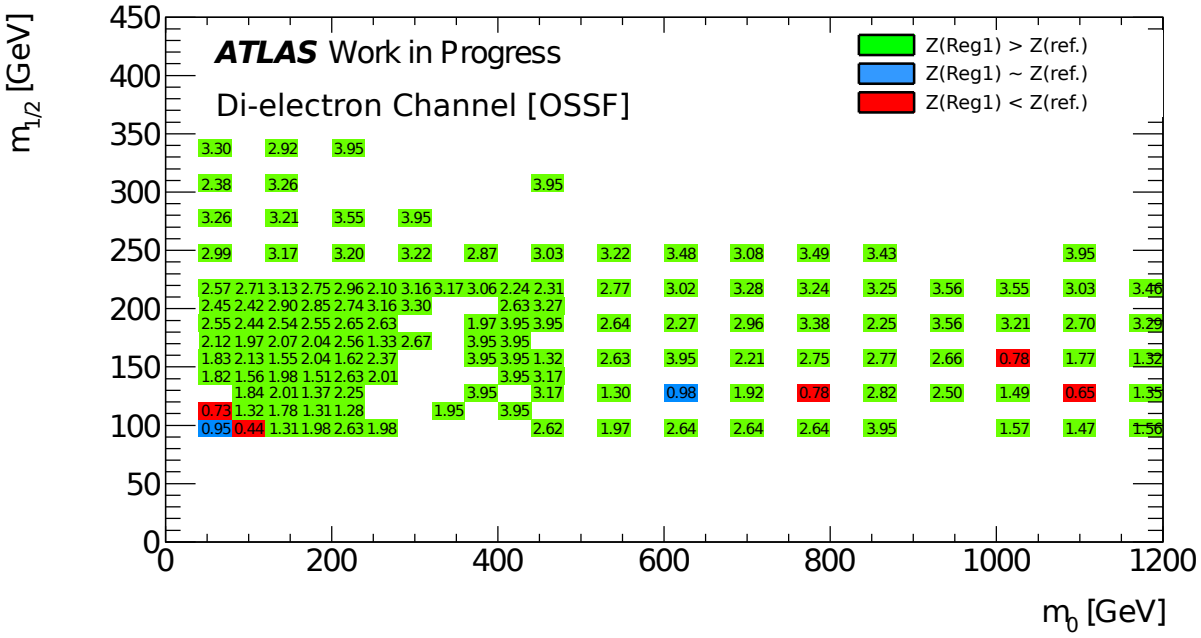

Figure 6.21: OSSF: Ratio of the significances for *Region1* cuts and that of the reference cut for the $e^{\pm}e^{\mp}$ channel. If the new cut's significance is greater than that of the reference cut, the corresponding grid point is underlaid greenly, else redly. If the deviation of the significances lies within 20%, the corresponding grid point is underlaid in blue.

the OS case. The resulting cut values are listed in Tab. 6.3.

Table 6.3: Overview of the OSSF cuts for the two optimisation regions. *Region1* corresponds to the low m_0 and large $m_{1/2}$ region and *Region2* refers to the one with large m_0 and small $m_{1/2}$.

	Region1	*Region2*
$E_{\mathrm{T}}^{\mathrm{miss}}$	110 GeV	85 GeV
p_{T}^{j1}	170 GeV	70 GeV
p_{T}^{j2}	80 GeV	55 GeV
$\Delta R_{\ell\ell}$	$0.3 < \Delta R_{\ell\ell} < 2$	$0.3 < \Delta R_{\ell\ell} < 2$

The application of these cuts to the mSUGRA grid is shown in Fig. 6.21 for *Region1* and in Fig. 6.22 for *Region2*. Again, the ratio of the optimised cut's significance and the reference cut's significance is determined for each point in the mSUGRA grid. With the help of the *Region1* cuts, an improvement of significance by a factor of ~ 2 over the whole region of the parameter space is achieved. The application of the *Region2* cuts leads to an improvement of a factor $2-3$ with the exception of some few points.

Analogously to the OS case, the ratio of the significances for the two sets of cut values is calculated (Fig. 6.23). Again, no correlation between the 2-body/ 3-body regions and the *Region1* /*Region2* cuts can be observed. Instead, one can - again - very roughly draw a horizontal line at about $m_{1/2} = 170$ GeV and define the two signal regions accordingly.

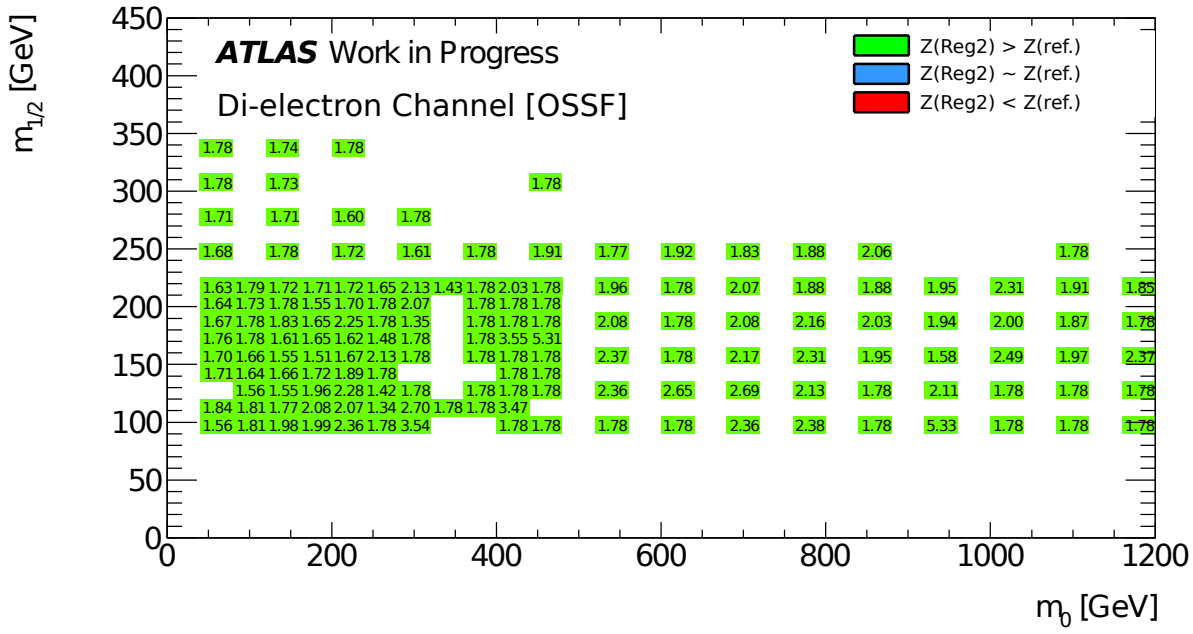

Figure 6.22: OSSF: Ratio of the significances for the *Region2* cuts and that of the reference cut for the $e^{\pm}e^{\mp}$ channel. If the new cut's significance is greater than that of the reference cut, the corresponding grid point is underlaid greenly, else redly. If the deviation of the significances lies within 20%, the corresponding grid point is underlaid in blue.

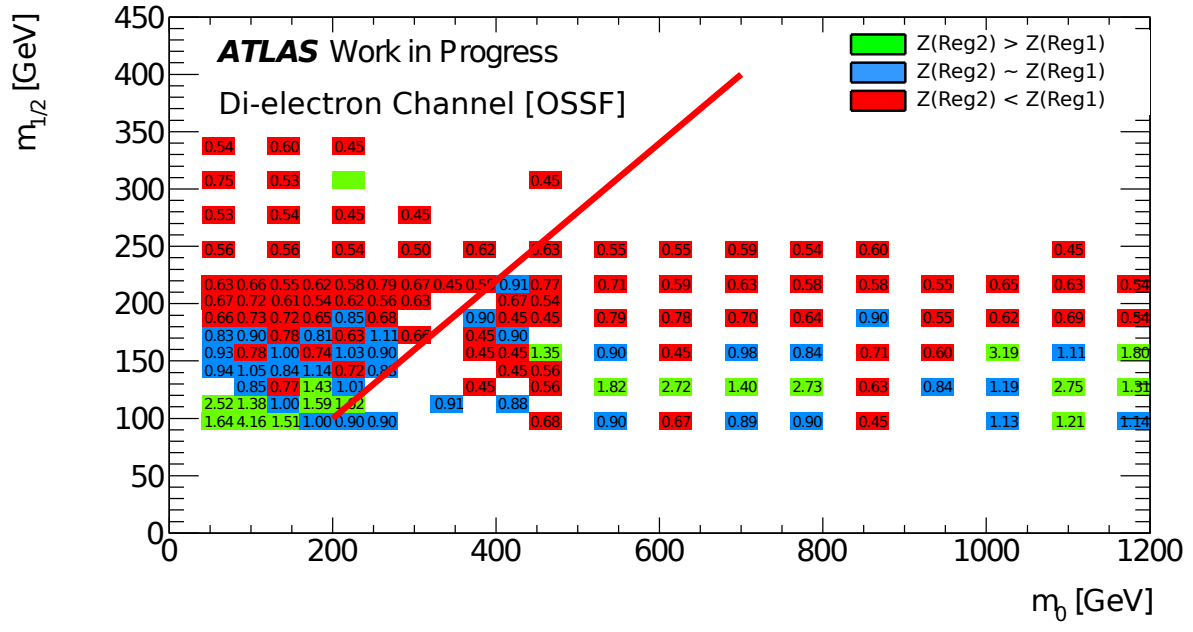

Figure 6.23: OSSF: Ratio of the significances for the *Region2* cuts and that of the *Region1* cuts for the $e^{\pm}e^{\mp}$ channel. If the significance of *Region2* is greater than that of *Region1*, the corresponding grid point is underlaid greenly, else redly. If the deviation of the significances lies within 20%, the corresponding grid point is underlaid in blue.

6.2.3 Comparison to other Signal Regions

Another cut optimisation is performed by running the optimisation on all merged grid points below and above $m_{1/2} = 170$ GeV (denoted as *Region3* and *Region4*, respectively). The motivation is to gain more reliable cuts due to an enhanced number of training and testing events. Moreover, this optimisation is performed on a different mSUGRA grid with $\tan\beta = 10$ (the studies above were performed on a grid with $\tan\beta = 3$) in order to be able to assess the applicability of the signal regions to other mSUGRA models. The higher value of $\tan\beta$ is expected to affect especially the 2-body region. The resulting cut values for these two regions are listed in Tab. 6.4.

Table 6.4: Overview of the cut values obtained from the rectangular cut optimisation on *Region3* and *Region4*.

	Region3 ($m_{1/2} < 170$ GeV)	*Region4* ($m_{1/2} > 170$ GeV)
$E_{\mathrm{T}}^{\mathrm{miss}}$	120 GeV	140 GeV
p_{T}^{j1}	120 GeV	170 GeV
p_{T}^{j2}	100 GeV	130 GeV

These new sets of cuts is compared to the *Region1* and *Region2* cuts as well as to the reference $E_{\mathrm{T}}^{\mathrm{miss}} > 100$ GeV cut. Moreover, they are compared to the signal regions OS-SR2 and OS-SR3 presented in Sec. 5. The different signal regions and the corresponding number of background events are listed in Tab. 6.5.

Table 6.5: Number of background events in the OS ee channel in different signal regions for $\mathcal{L} = 1\,\mathrm{fb}^{-1}$.

No.	Comment	Cuts	No. of B events
1	reference cut	$E_{\mathrm{T}}^{\mathrm{miss}} > 100$	201
3	*Region1* cuts	$E_{\mathrm{T}}^{\mathrm{miss}} > 120$ GeV, 2 jets $> 195, 75$ GeV	10
2	*Region2* cuts	$E_{\mathrm{T}}^{\mathrm{miss}} > 65$ GeV, 2 jets $> 90, 70$ GeV	122
4	*Region3* cuts	$E_{\mathrm{T}}^{\mathrm{miss}} > 120$ GeV, 2 jets $> 120, 100$ GeV	4
5	*Region4* cuts	$E_{\mathrm{T}}^{\mathrm{miss}} > 140$ GeV, 2 jets $> 170, 130$ GeV	11
6	OS-SR2	$E_{\mathrm{T}}^{\mathrm{miss}} > 220$ GeV, 3 jets $> 80, 40, 40$ GeV	5
7	OS-SR3	$E_{\mathrm{T}}^{\mathrm{miss}} > 100$ GeV, 4 jets $> 100, 70, 70, 70$ GeV	1

Fig. 6.24 shows the $m_0 - m_{1/2}$ plane of the mSUGRA $\tan\beta = 10$ grid. The number and the corresponding colour code depicts the signal region with the highest significance for each grid point. The results are shown exemplarily for the $e^{\pm}e^{\mp}$ channel. The best performance for most of the grid is cut 7 (OS-SR3). On several points in the 2-body region, however, the *Region3* cuts have the best separation power, followed closely by cut 6 (OS-SR2). Fig. 6.25 shows which signal region leads to the second-highest significance. Fig. 6.26 and Fig. 6.27 show the corresponding significances for the best and the second-best signal regions, respectively. It can be seen that for the points with low m_0 and $m_{1/2}$,

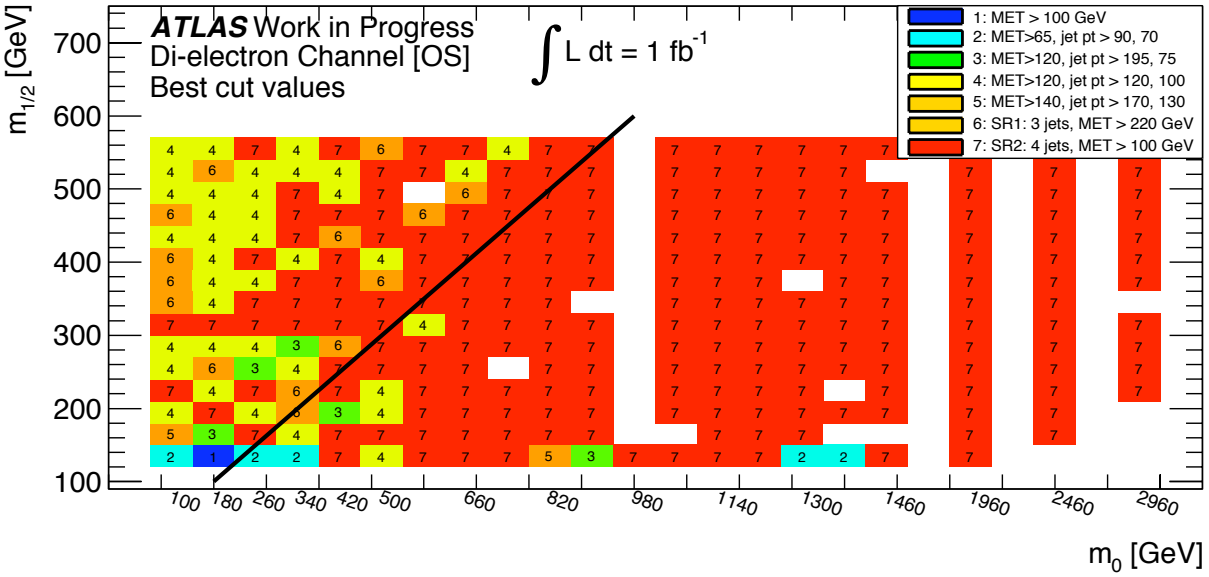

Figure 6.24: Comparison of different cut values in the mSUGRA $\tan\beta = 10$ grid for the OS ee channel. The number and the colour indicate the signal region which gives the highest value of $S/\sqrt{B}$. The $e\mu$ and $\mu\mu$ channel behave very similarly.

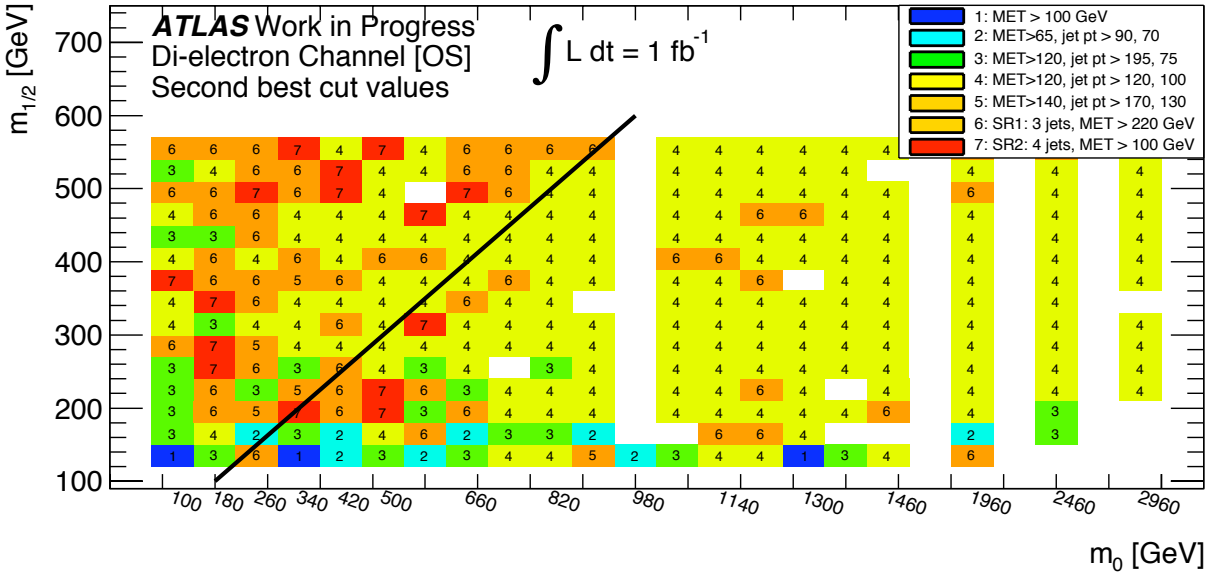

Figure 6.25: Comparison of different cut values in the mSUGRA $\tan\beta = 10$ grid for the OS ee channel. The number and the colour indicate the signal region which gives the second-highest value of $S/\sqrt{B}$. The $e\mu$ and $\mu\mu$ channel behave very similarly.

a very high significance ($Z > 5$) can be achieved. Thus, at these points in the parameter space, SUSY would have been observed if it existed in this region of the parameter space. The non-observation can be translated into exclusion regions in the parameter space. The high m_0 and $m_{1/2}$ region cannot be excluded due to the low SUSY production cross sections.

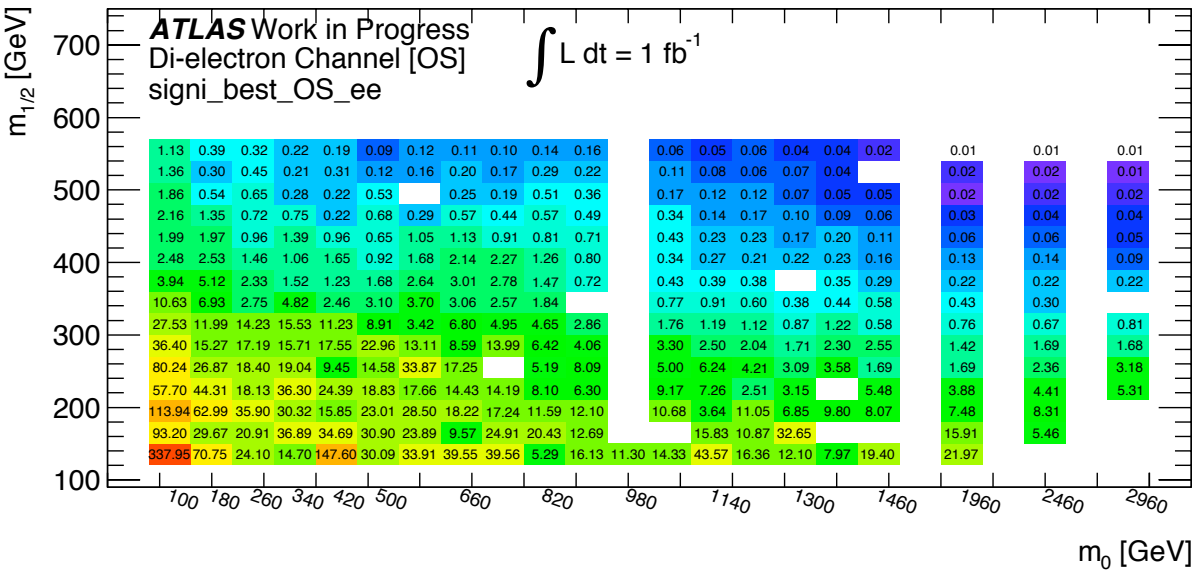

Figure 6.26: Significance of the signal region with the highest value of $S/\sqrt{B}$ in the $m_0 - m_{1/2}$ plane for the OS ee channel for $\mathcal{L} = 1\,\mathrm{fb}^{-1}$.

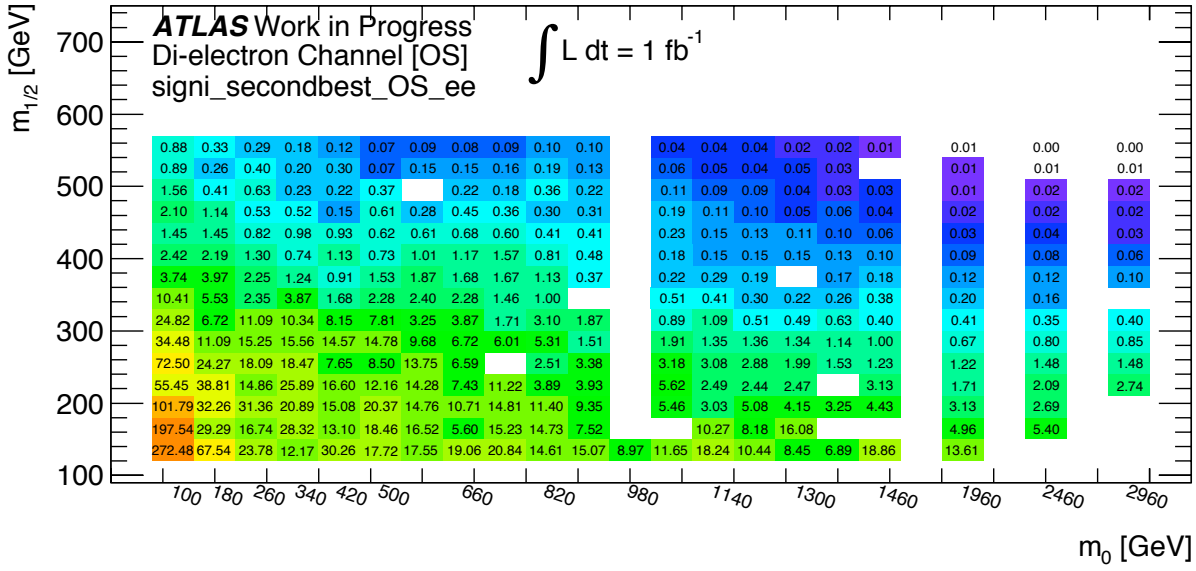

Figure 6.27: Significance of the signal region with the second-highest value of $S/\sqrt{B}$ in the $m_0 - m_{1/2}$ plane for the OS ee channel for $\mathcal{L} = 1\,\mathrm{fb}^{-1}$.

6.3 Summary & Outlook

Tab. 6.6 lists the cut values for both the OS and the OSSF analysis. As one can see, the cuts are very close to each other for OS and OSSF (except for the additional ΔR cut for OSSF). Thus, for simplification, it would be possible to define the same signal regions for OS and OSSF, only adding the ΔR cut for OSSF.

As the optimisation's accuracy suffers from low signal statistics, these cut values are to be taken with a grain of salt. However, it was found that these cuts can improve the significance of at least a factor of two throughout the entire mSUGRA $m_0 - m_{1/2}$ plane.

Table 6.6: Overview of the cut values obtained from the rectangular cut optimisation for both OS and OSSF

	OS		OSSF	
	For $m_{1/2} < 170$ GeV	For $m_{1/2} > 170$ GeV	For $m_{1/2} < 170$ GeV	For $m_{1/2} > 170$ GeV
$E_{\mathrm{T}}^{\mathrm{miss}}$	65	120	85	110
p_{T}^{j1}	90	195	70	170
p_{T}^{j2}	70	75	55	80
$\Delta R_{\ell\ell}$	–	–	$0.3 < \Delta R_{\ell\ell} < 2$	$0.3 < \Delta R_{\ell\ell} < 2$

Moreover, these cuts are relatively robust concerning different significance definitions as well as systematic uncertainty on the number of background events.

As already pointed out in Ch. 5, the signal regions with three and four jets (OS-SR2 and OS-SR3) for 2-body and 3-body decays, respectively have been established for the 2011 SUSY OS di-lepton analysis. Requiring such a high jet multiplicity may be problematic. First of all, jets are the objects with the largest systematic uncertainty (JES & JER). Thus, incorporating a high number of jets leads to a loss of accuracy in the reconstruction of SUSY events. Moreover, these signal regions explicitly exploit the kinematics of the mSUGRA model which is just one out of a huge number of possible SUSY scenarios. For example, the DirectGaugino model, a simplified model with strong production, exhibits short decay chains and therefore typically less jets. That is, requiring three or four jets includes a strong model dependence. On the other hand, the OS-SR2 signal region leads to the highest significance for most of the mSUGRA $\tan\beta = 10$ parameter space.

The signal regions which were suggested in this analysis aim at finding an agreement between good performance in the mSUGRA parameter space on the one hand and universality with respect to different SUSY scenarios on the other hand. It was shown that the suggested signal regions perform similarly well as the four-jet signal region (OS-SR2).

The optimisation of cut values with the help of the rectangular cuts algorithm (`CutsGA`) is a simple technique to define signal regions. However, much fine-tuning of the algorithm's parameters is necessary in order to find the best possible set of cuts. The main drawback of this optimisation turned out to be the lack of MC signal statistics. Larger MC SUSY samples would enable a more accurate and thorough study. Besides, the usage of multivariate optimisation tools such as neural networks, support vector machines or boosted decision trees could possibly enhance the yield of such an optimisation. Moreover, the application of the signal regions to other SUSY models would be important to cross-check the model-dependence of these cuts, combined with an independent cut optimisation on such grids.

Chapter 7

Study of Di-Lepton Triggers

With the constant increase of the instantaneous luminosity and the constraints on the throughputs of the ATLAS trigger system ($\sim$ 75 kHz at L1, $\sim$ 3.5 kHz at L2 and $\sim$ 200 Hz at EF), the trigger selections need to be tightened to keep the rates below the limits. So far, the triggering of events with leptons in the final state is employed with single lepton triggers. In order to keep the rates of single lepton triggers at a level compatible with the constraints of the trigger system, several approaches at the different trigger levels are possible. At L1, higher p_{T} thresholds can be required (e.g. `L1_EM14` $\rightarrow$ `L1_EM16`, cf. Sec. 3.3.5). Moreover, variable threshold values and hadronic core isolation can be adopted (e.g. `L1_EM16` $\rightarrow$ `L1_EM16VH`). `V` denotes the η-dependent threshold while `H` is the hadronic core isolation. For lepton triggers, the L1 rate is the bottleneck. The L2 rate can be reduced e.g. by optimising the isolation requirement for the medium/tight electron selection. By this, the fake electron rejection can be increased by a factor of $\sim$ 3. At EF level, the rate can be reduced by raising the p_{T} thresholds (e.g. `EF_e20_medium` $\rightarrow$ `EF_e22_medium`) or by tightening the electron identification (e.g. `EF_e22_medium` $\rightarrow$ `EF_e22_medium1`)[1]. Moreover, trigger chains with a high rate can be prescaled (cf. Sec. 3.3) which is, however, no option for rare processes.

Raising the p_{T} thresholds of the triggers is very problematic as this reduces the number of events in the signal region. Some SUSY scenarios favour low-p_{T} leptons so that with an increased threshold many potential SUSY events are discarded. Alternatively, for analyses that search for decays with more than one lepton in the final state, di-lepton triggers can be introduced. Di-lepton triggers have the advantage of lower p_{T} thresholds without the need of prescaling, as the rate of di-lepton events is much lower than that of single-lepton events.

This chapter presents the study of di-lepton triggers for the SUSY di-lepton analysis. First, the yield of di-lepton triggers and thus lower thresholds with respect to single lepton triggers is examined on different SUSY models. The inclusion of a $E_{\mathrm{T}}^{\mathrm{miss}}$ cut to the di-

[1] The `medium1` selection corresponds to the `medium` selection with additional requirements such as tighter shower shapes for $|\eta| > 2.01$, tighter $\Delta\eta$ track-cluster matching ($|\Delta\eta| < 0.005$) and stricter b-layer and Pixel hit requirements.

lepton triggers is studied as well. In the second part of the analysis, trigger efficiencies are determined both on MC and data and compared to each other.

7.1 Emulation of New Triggers

Several di-lepton triggers are emulated offline and the yield with respect to the current baseline is determined for different SUSY grids. The studied grids are the mSUGRA $\tan\beta = 10$ grid, three different DirectGaugino (DGemt) simplified models as well as the phenomenological model PhenoGrid PG11. The DirectGaugino model is studied for three different values of M_1 (cf. Sec. 2.2.4). In these grids, $\tan\beta = 6$ is used. In the PG11 grid under study, the LSP mass is set to 100 GeV (*light-LSP mode*).

In the following, reconstructed electrons are denoted as *offline* electrons while the electrons seen by the trigger are referred to as *online* electrons. Especially asymmetric di-lepton triggers as well as di-lepton triggers in combination with a $E_{\mathrm{T}}^{\mathrm{miss}}$ trigger, which could allow even lower p_T leptons, are studied.

New trigger lines are emulated by setting an offline cut at the lepton's p_{T}. The expected performance of triggers that do not (yet) exist in the trigger menu can be studied by emulation. The rule of thumb is that for electrons and muons the plateau of the p_{T} dependent trigger efficiency curve is reached 5 GeV and 2 GeV above the trigger threshold, respectively (cf. Fig. 5.1). For example, the electron trigger `EF_e20_medium` would require an offline cut at 25 GeV in order to be on the plateau. The same assumptions are made for the di-lepton triggers, i.e., for the trigger `EF_2e12_medium` the p_{T} of both electrons is required to be larger than 17 GeV offline. The investigated events are SUSY di-lepton events at reconstruction level (reconstructed events after the detector simulation). The event selection is described in Sec. 5.2.2 with the exception that all di-lepton events with the lepton's p_T above 5 GeV are accepted and the restriction of a m_{ll} cut of 12 GeV for all channels.

For different emulated di-lepton triggers the yield is studied on different grid points. The yield is calculated by

$$\varepsilon = \frac{n_{T\mathtt{or}B}}{n_B} \tag{7.1}$$

where $n_{T\mathtt{or}B}$ is the number of events that were either triggered or selected by the baseline requirement and n_B is the number of baseline events. This means that the yield is defined as the ratio of events that are triggered or fulfil the baseline requirements and the number of events fulfilling the baseline requirements. By this definition, only an improvement of the trigger relative to the baseline can be seen. *Baseline* refers to the general trigger selection presented in Sec. 5.2.2. This selection requires the trigger `EF_e20_medium` as well as offline p_{T} cuts of 25 GeV and 10 GeV for the leading and subleading electron, respectively. For the offline p_{T} cuts, the following notation is used: $p_{\mathrm{T}}^{ee} > (25, 10)$ GeV refers to the lepton pair's transverse momentum, the first number to the leading lepton's

p_{T} and the second number to the sub-leading p_{T}. The di-muon baseline requires `EF_mu18` and $p_{\mathrm{T}}^{\mu\mu} > (20, 8)$ GeV offline. The baseline for electron-muon events is $p_{\mathrm{T}}^{e\mu} > (25, 8)$ GeV if the electron triggers the event or $p_{\mathrm{T}}^{e\mu} > (20, 10)$ GeV if the muon triggers the event. The number of events that pass the new emulated trigger is compared to the corresponding baseline.

There are some di-lepton triggers which are already implemented in the trigger menu, namely `EF_2e12_medium`, `EF_2e15_loose`, `EF_2mu10`, `EF_e10_medium_mu10` and `EF_e10_medium_mu6`. These existing triggers are tested along with the emulated di-lepton triggers.

In total, 39 different triggers are emulated and tested, i.e., compared to the baseline or to each other and are listed in Tab. A.1. The most promising emulated triggers with the highest yield are presented in this chapter exemplarily for the ee channel. The plots for the $e\mu$ and $\mu\mu$ triggers can be found in the appendix (Fig. A.8 - A.11). For the di-lepton triggers, each figure shows the yield of the emulated trigger with respect to the baseline for the mSUGRA, DGemt and PG11 grids. Multiple di-lepton triggers with symmetric and asymmetric p_{T} cuts are emulated and compared to each other. For the hybrid di-lepton-$E_{\mathrm{T}}^{\mathrm{miss}}$ triggers, the yield is determined with respect to the (baseline `and` $E_{\mathrm{T}}^{\mathrm{miss}}$ cut). Three different offline $E_{\mathrm{T}}^{\mathrm{miss}}$ cuts are implemented, $E_{\mathrm{T}}^{\mathrm{miss}} > 80$, 100, 150 GeV, accompanied by several symmetric and asymmetric lepton p_{T} cuts.

A general tendency for the different grids can be observed:
PG11: For the ee and $e\mu$ channels the additional yield of the new triggers on the PG11 grid is negligible, being between $1-3\%$. The reason for the poor results is that this model produces by construction hard leptons (cf. Tab. 2.6) so that lower p_{T} thresholds hardly have any significant impact. Furthermore, the LSP mass is set to 100 GeV so that an additional $E_{\mathrm{T}}^{\mathrm{miss}}$ cut does not have a significant ramification, either.
DGemt: As stated above, there are three DGemt grids. The grids with $M_1 = 100$ GeV and $M_1 = 140$ GeV show very similar results so that only one of those is included in the subsequent plots (Fig. 7.1-7.3). The trigger on the $M_1 = 250$ GeV grid perform slightly worse than on the other two DGemt grids. The emulated di-lepton and di-lepton+$E_{\mathrm{T}}^{\mathrm{miss}}$ triggers have the largest impact on the DGemt grids compared to the other models.
mSUGRA: For most of the emulated triggers, only a significant effect is visible for thin bands at $m_{1/2} \approx 100$ GeV and $m_{1/2} \approx 350$ GeV while leaving all other points nearly unchanged. The low $m_{1/2}$ points at which the highest yield is achieved share a common mass hierarchy. The charginos and neutralinos are relatively light and almost degenerate while the sleptons are very heavy (cf. right plot in Fig. 6.11). By this, the decays from neutralinos via a virtual slepton are highly suppressed, giving rise to decays like $\tilde{\chi}_i^{\pm} \rightarrow \ell^{\pm}\nu\tilde{\chi}_j^0$ (via a charged current). The latter ones produce light leptons due to the low mass difference between the charginos and neutralinos.

ee Channel

On the DGemt grids the `EF_2e12_medium` trigger leads to an average improvement of $10-30\%$ with respect to the current baseline. On the mSUGRA grid, this trigger only has an effect on grid points with $m_{1/2} \approx 100$ GeV and $m_{1/2} \approx 350$ GeV while leaving all other points nearly unchanged. The yield of `EF_2e12_medium` with an offline cut of $p_{\mathrm{T}}^{ee} > (17, 17)$ GeV with respect to the baseline can be seen in Fig. 7.1 for three different SUSY models. Asymmetric triggers, i.e., di-lepton triggers with different thresholds for the two leptons turn out to be very useful. Raising the offline threshold of the leading lepton from 17 GeV to 20 GeV while lowering that of the second lepton to 10 GeV could lead to a yield of 15 to over 100% and thus performs much better than a symmetric trigger. This can be seen in Fig. 7.2.

Adding the missing transverse energy $E_{\mathrm{T}}^{\mathrm{miss}}$ to the trigger requirements has the advantage that the p_{T} threshold of the leptons can be reduced significantly. Therefore, a trigger which consists of some low lepton p_{T} trigger and a cut on the missing transverse energy was emulated for all channels. Three cuts on the $E_{\mathrm{T}}^{\mathrm{miss}}$ were chosen, 80, 100 and 150 GeV offline, accompanied with different low lepton p_{T} thresholds. The $E_{\mathrm{T}}^{\mathrm{miss}} > 80$ GeV cut was chosen as this corresponds to one of the flavour subtraction signal regions. With a trigger requiring $p_{\mathrm{T}}^{ee} > (7, 7)$ GeV as well as $E_{\mathrm{T}}^{\mathrm{miss}} > 80$ GeV, an improvement of up to 300% can be achieved on the DGemt grid. For mSUGRA this holds only for the low $m_{1/2}$ region, for higher $m_{1/2}$ no improvement can be observed (see Fig. 7.3). Increasing the $E_{\mathrm{T}}^{\mathrm{miss}}$ threshold to 100 GeV and even to 150 GeV decreases the yield only slightly but is disfavoured because such a trigger would cut away some of the signal region for the flavour subtraction analysis. When increasing the lepton thresholds to $p_{\mathrm{T}} > 15$ GeV for the $E_{\mathrm{T}}^{\mathrm{miss}} > 100$ GeV threshold, hardly any improvement with respect to the baseline is achieved.

$\mu\mu$ and $e\mu$ Channels

For the $\mu\mu$ channel the same tendency as for the ee channel can be observed. The `EF_2mu10` trigger with offline cuts at 12 GeV and also the one with 14 GeV offline lead to no significant improvement for most of the considered parameter space. The low $p_{\mathrm{T}} + E_{\mathrm{T}}^{\mathrm{miss}}$ triggers perform extremely well for the muon channel (Fig. A.8). Here, the same holds as for the ee channel. Concerning the asymmetric triggers, especially the emulated triggers with $p_{\mathrm{T}}^{\mu\mu} > (15, 8)$ GeV (Fig. A.9) and $p_{\mathrm{T}}^{\mu\mu} > (15, 10)$ GeV (Fig. A.10) show very good performance.

An electron-muon trigger with $p_{\mathrm{T}}^{e\mu} > (15, 8)$ GeV (Fig. A.11) shows the highest yield with respect to the baseline. The low $p_{\mathrm{T}} + E_{\mathrm{T}}^{\mathrm{miss}}$ triggers show worse results than for the ee and the $\mu\mu$ channel.

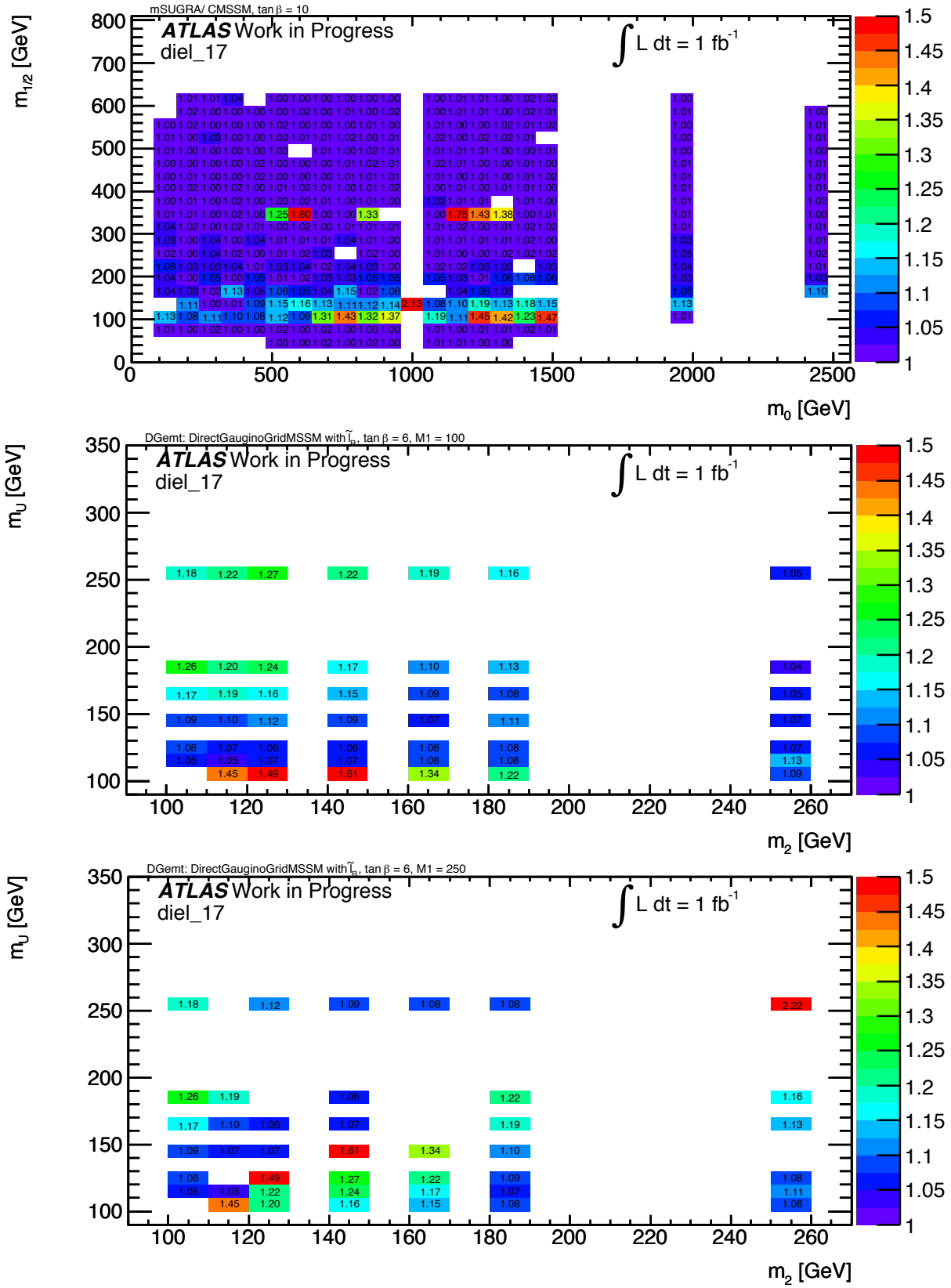

Figure 7.1: Yield of the trigger `EF_2e12_medium` with respect to the baseline for the ee channel on different SUSY models. Additionally to the trigger, a cut on $p_{\mathrm{T}}^{ee} > (17, 17)$ GeV for the offline electrons is required in order to reach the efficiency plateau. The upper plot shows the yield in the mSUGRA $\tan\beta = 10$ $m_0 - m_{1/2}$ plane. The middle and lower plots show the yield on the DGemt grid with $M_1 = 100$ GeV and $M_1 = 250$ GeV in the $m_2 - \mu$ plane, respectively.

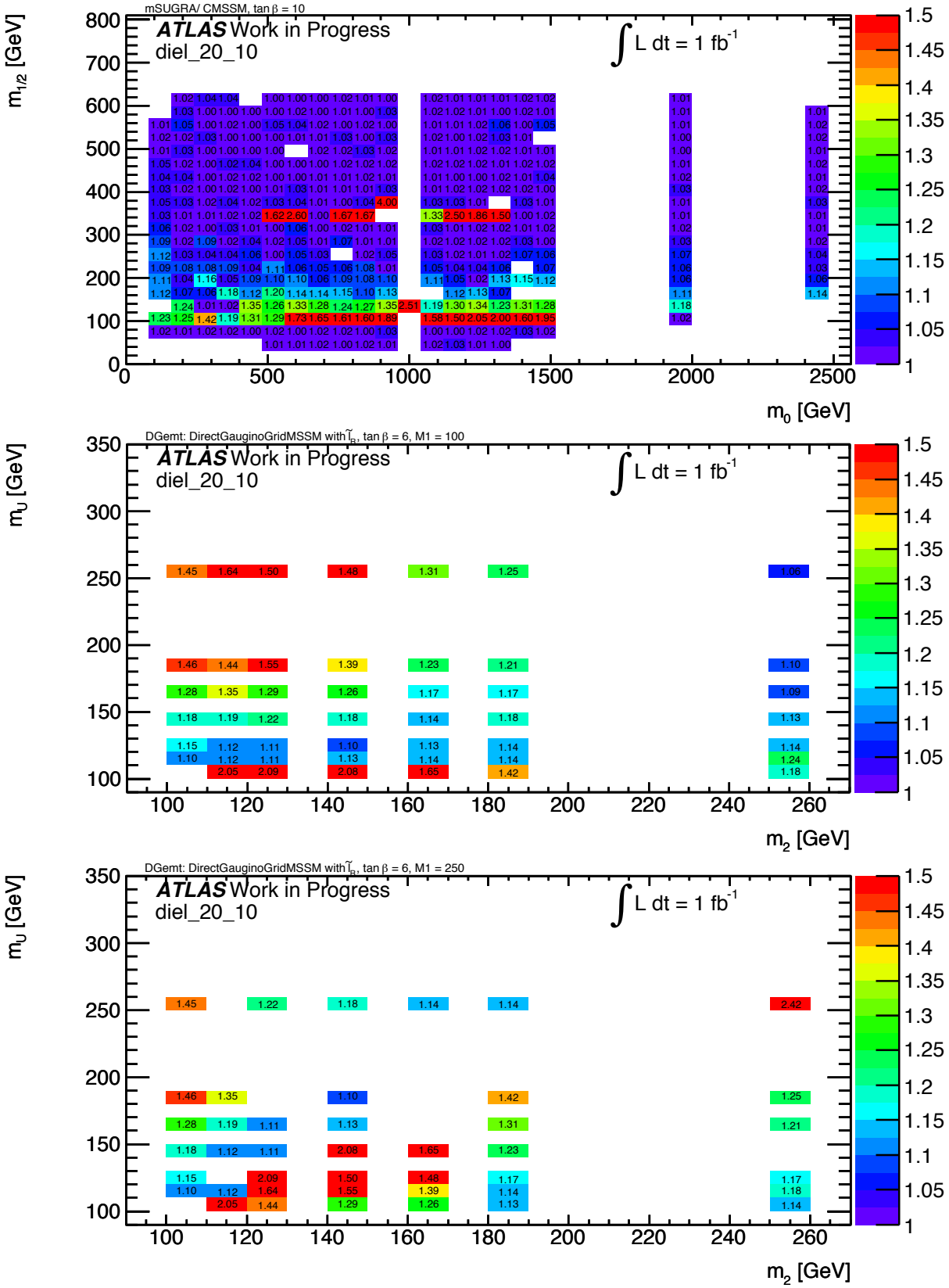

Figure 7.2: Yield of an emulated trigger with a cut on $p_{\mathrm{T}}^{ee} > (20, 10)$ GeV offline with respect to the baseline on different SUSY models. The upper plot shows the yield in the mSUGRA $\tan\beta = 10$ $m_0 - m_{1/2}$ plane. The middle and lower plots show the yield on the DGemt grid with $M_1 = 100$ GeV and $M_1 = 250$ GeV, respectively.

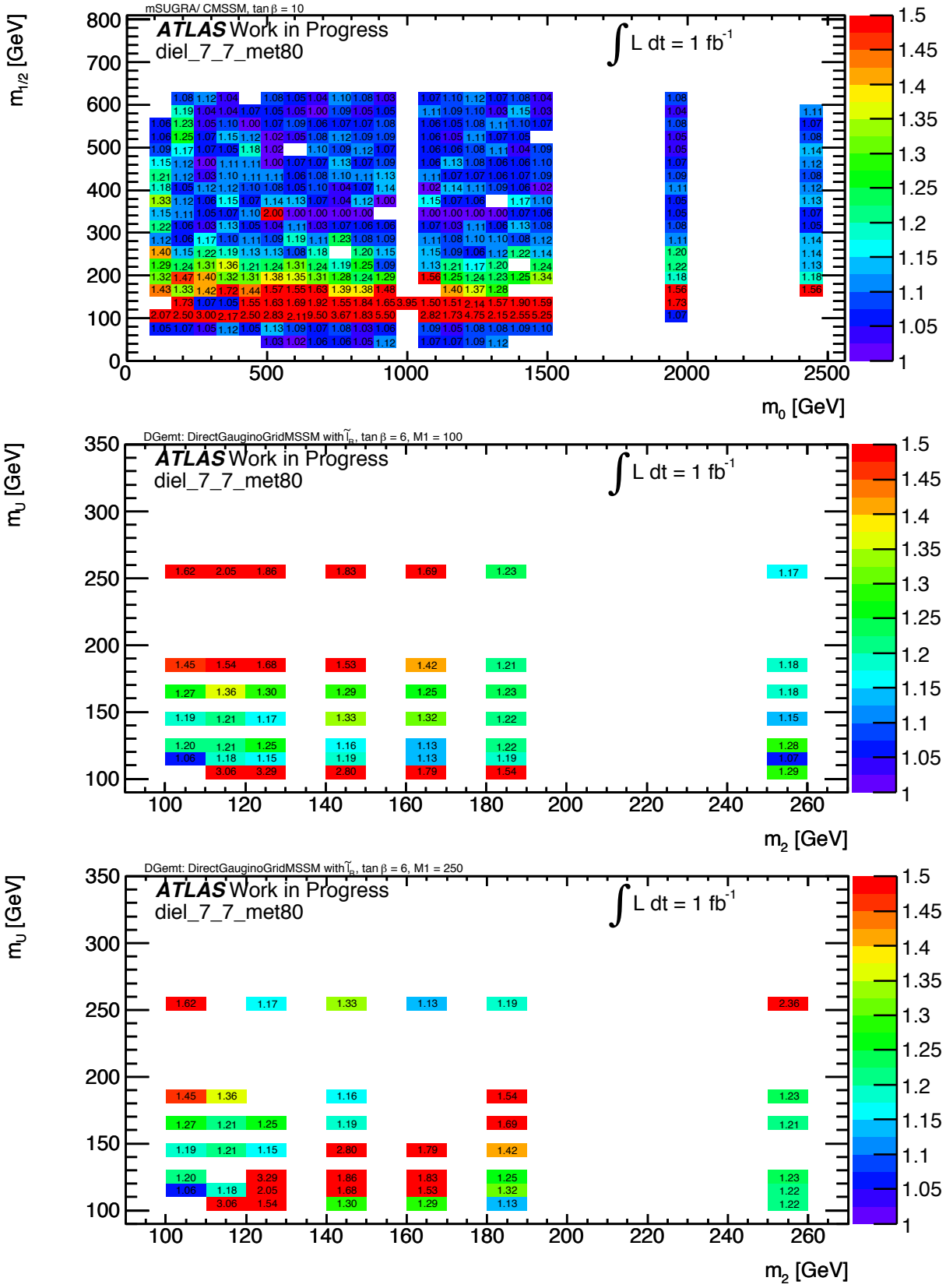

Figure 7.3: Yield of an emulated trigger with a cut on $p_{\mathrm{T}}^{ee} > (7, 7)$ GeV offline and $E_{\mathrm{T}}^{\mathrm{miss}} > 80$ GeV offline with respect to the baseline on different SUSY models. The upper plot shows the yield in the mSUGRA $\tan\beta = 10$ $m_0 - m_{1/2}$ plane. The middle and lower plots show the yield on the DGemt grid with $M_1 = 100$ GeV and $M_1 = 250$ GeV, respectively.

7.2 Trigger Efficiency Determination

This section presents the study of electron trigger efficiencies that were obtained from both MC[2] and data. Similar studies on muon trigger efficiencies have been performed, e.g. in [94, 95, 96]. The studied di-lepton trigger chains are `EF_2e12_medium` and `EF_2e12T_medium`, where `T` stands for a tighter L1 threshold. The latter needs to be emulated as it does not exist in MC yet. Furthermore, it is analysed how precisely di-electron trigger efficiencies can be estimated from the corresponding single-electron trigger.

The trigger efficiency is a function of several quantities, most prominently the p_{T} as well as η and ϕ of the triggered object. In this analysis, the determination of the p_{T} dependence of the trigger efficiencies is appraised. The efficiency is thus projected onto the $p_{\mathrm{T},i}$ axis while the other dimensions ($p_{\mathrm{T},j}$, η, ϕ, etc.) are integrated out. The precise determination of the trigger efficiency is crucial due to several reasons. Trigger efficiencies have a characteristic p_{T} *turn-on curve*. Electron triggers for instance only reach full efficiency at about 5 GeV above the p_{T} threshold of the trigger. Therefore, it is important for every analysis to know at which p_{T} threshold the trigger reaches the full plateau efficiency. In the flavour subtraction analysis, the electron and muon trigger efficiencies are vital for the calculation of the yield of same-flavour over opposite-flavour events (cf. Eq. (5.1)). Furthermore, the knowledge of trigger efficiencies is mandatory for the determination of a cross section or the setting of limits on the cross section. The cross section is given by

$$\sigma = \frac{N}{\varepsilon_{\mathrm{T}} \cdot \varepsilon_{\mathrm{reco}} \cdot L} \tag{7.2}$$

where N is the number of observed events, L the instantaneous luminosity and ε_{T} and $\varepsilon_{\mathrm{reco}}$ the trigger and reconstruction efficiency, respectively.

On MC samples, the efficiency of a certain trigger can be determined via the division of the number of selected events passing the trigger and the number of selected events. However, this is not possible on data because the non-triggered events are generally not stored. There exist several data-driven methods for the determination of trigger efficiencies. The most common ones are the *Tag & Probe* method, pass-through methods, the *Bootstrap* method as well as methods relying on orthogonal trigger streams. Here, an orthogonal stream is used to study electron trigger efficiencies. By requiring an orthogonal stream, the trigger decision under study is decoupled from the event selection, so that the efficiency can be determined by counting, just like for MC as described above. The `muon` stream is chosen for the determination of electron trigger efficiencies. It only contains events selected by a muon trigger. It is assumed that the number of electrons per event is independent of the number of muons. So it is possible to use the `muon` stream as the

[2] The MC studies were developed in collaboration with Maciej Misiura, University of Warsaw, who worked as a summer student at the DESY ATLAS group in August 2011 [93].

reference sample, containing both triggered and non-triggered electrons. The advantage of this method is its simplicity in comparison to other methods such as the bootstrap method and that it is in principle unbiased with respect to the trigger under study. However, it is limited due to a lack of statistics because only events triggered by one of the muon triggers are available.

7.2.1 Frequentist vs. Bayesian Trigger Efficiency Determination

In this subsection, some statistical knowledge important for the determination of trigger efficiencies and its uncertainties is reviewed.

When talking about probability, one needs to distinguish between *Frequentist* and *Bayesian statistics*. The Frequentist ansatz considers the subsets of the sample space A as outcomes of a repeatable experiment. The probability $P(A)$ is then equal to the limiting frequency of occurrence of A. So, the Frequentist statistics gives the objective outcome of an experiment. The Frequentist solution is usually expressed as a *confidence interval*. For example, after carrying out the same experiment a large number of times, a 95% confidence interval is expected to contain the true (unknown) value of some parameter for at least 95% of the repeated experiments. For the Bayesian probability, the subsets of the sample space are interpreted as hypotheses, i.e., statements that are either true or false. Then, $P(A)$ is interpreted as the degree of belief that the hypothesis A is true. The Bayesian point of view allows to input the degree of belief about the parameter's values before carrying out the experiment. The prior degree of belief is updated by the experimental data [83]. The trigger efficiency in this thesis is determined with the help of both, Frequentist and Bayesian methods.

By the trigger selection, a subset of the input data is rejected. The trigger efficiency is the probability that an event from a sample A passes the trigger selection T and is a function of the reference quantity x which is denoted by $\varepsilon_T(x; A)$. It is emphasised that an absolute trigger efficiency does not exist; each efficiency can only be determined relative to a sample A. In this thesis, when referring to the absolute trigger efficiency, this is always meant as the efficiency relative to the preselection. For instance, the efficiency of a single-lepton trigger is determined with respect to a sample containing all events with one lepton in the final state (plus some other event selection criteria). Thus, the trigger efficiency is the conditional probability

$$\varepsilon_T(x; A) = P(T|A). \tag{7.3}$$

In the Frequentist interpretation, the trigger efficiency ε is a constant but unknown quantity which does not fluctuate so that no probability distribution can be associated to it. Instead, the uncertainty of ε quantifies the frequency for the true value of ε to be contained

by the confidence interval. In the Bayesian interpretation, probabilities can be associated to ε, allowing to give the probability that the credible interval contains the true value of ε [97]. In Frequentist statistics, the expectation value of the number of passed events k is given by the product of the true efficiency and the total number of events n. The efficiency is estimated by replacing the expected number of passed events by the observed number of passed events,

$$E(\varepsilon) \approx \hat{\varepsilon} = \frac{k}{n}. \tag{7.4}$$

In practice, the ratio of triggered and non-triggered events is calculated in bins of the object's p_{T}. This quantity converges in probability to the true (unknown) efficiency for $n \to \infty$ by the law of large numbers [83].

Usually, the statistical uncertainty of the efficiency is approximated by regarding the triggering of events as a Bernoulli process which leads to a binomial probability distribution. The maximum-likelihood estimator (MLE) for a Bernoulli process is exactly the observed relative frequency $\hat{\varepsilon} = f = k/n$. The variance is then estimated by

$$V(\varepsilon) = \frac{\varepsilon(1-\varepsilon)}{n} \approx \frac{k(n-k)}{n^3}. \tag{7.5}$$

This approximation fails for $\varepsilon \to 1$ and $\varepsilon \to 0$ (or $k = n$ and $k = 0$). In both cases the uncertainty is zero, independent of the number of total events n.

Therefore, other approaches for estimating the uncertainty are established. The ROOT `TEfficiency` class is used for the calculation of the efficiency and its uncertainty [98] and hosts several Frequentist and Bayesian methods. The confidence interval for the Frequentist efficiency can be estimated by the Clopper-Pearson method. It is recommended by the PDG [15] and is the default method of the `TEfficiency` class. However, it is often too conservative and the resulting errors on the efficiency might be too large. Another approach is to determine the efficiency and its credible intervals with Bayesian methods, using the *Jeffrey's prior* [99]. In Bayesian statistics, a likelihood-function and a prior probability are used to determine a posterior probability. *Bayes' theorem* states that the conditional probability of A given B is

$$P(A|B) = \frac{P(B|A)P(A)}{P(B)}. \tag{7.6}$$

The desired quantity $P(A|B)$ is called the *posterior* probability. $P(B|A)$ is denoted as the *likelihood* which states how probable it is to obtain the observed data assuming a true efficiency. $P(A)$ is the *prior* and gives the probability that a certain true efficiency is actually realised. Thus, the probability distribution for the true efficiency ε given n_i and k_i is given by

$$P(\varepsilon_i|k_i, n_i) \propto P(k_i|\varepsilon_i, n_i)P(\varepsilon_i, n_i). \tag{7.7}$$

n_i and k_i are known (measured) and the process is assumend to be a Bernoulli process so that $P(k_i|\varepsilon_i, n_i)$ is given by the binomial distribution $\mathrm{Bi}(k_i|\varepsilon_i, n_i)$. The prior should be independent of the sample size, $P(\varepsilon_i|n_i) = P(\varepsilon_i)$, hence, the probability for the true efficiency in bin i to lie between ε_i and $\varepsilon_i + \delta\varepsilon_i$ is given by

$$P(\varepsilon_i|k_i, n_i) \propto \mathrm{Bi}(k_i|\varepsilon_i, n_i)P(\varepsilon_i). \tag{7.8}$$

The prior encodes the state of knowledge before the measurement is carried out. It is reasonable to model the lack of knowledge or the ignorance thereof with a prior PDF which is called the *beta* function. The beta function has two free parameters, α and β. The recommended prior is *Jeffrey's prior*, a beta function with $\alpha = \beta = 1/2$ [99]. With this, the estimator for the efficiency is given by the following expectation value of the posterior distribution:

$$E(\varepsilon) = \frac{k + 1/2}{n + 1} \tag{7.9}$$

The uncertainty of the trigger efficiency is taken to be the variance of the posterior,

$$V(\varepsilon) = \frac{(k + 1/2)(n - k + 1/2)}{(n + 1)^2(n + 2)}. \tag{7.10}$$

The trigger efficiencies on MC are determined with the default Frequentist Clopper-Pearson method while the trigger efficiencies on data are ascertained with both methods allowing a comparison.

7.2.2 Single-Electron Trigger Efficiencies

Before treating di-electron triggers, some single-electron triggers are presented on which basic tests such as the trigger matching are performed.

Fig. 7.4 shows the p_{T} distributions of electrons from events with at least one or at least two electrons on data. These p_{T} distributions are utilised as 'denominators' for the trigger efficiency determination. Tab. 7.1 lists some of the primary electron triggers and their rates at L1 and EF.

Table 7.1: List of some of the primary electron triggers, their L1 seed and the corresponding rates for an instantaneous luminosity of $L = 3 \times 10^{33}$ cm^{-2} s^{-1}.

Trigger	L1 seed	L1 rate (kHz)	EF rate (Hz)
`EF_e22vh_medium1`	`EM16VH`	10	60
`EF_e45_medium1`	`EM30`	2.5	8
`EF_2e12T_medium`	`2EM10VH`	2	3
`e10_medium_mu6`	`EM5_MU6`	4	15

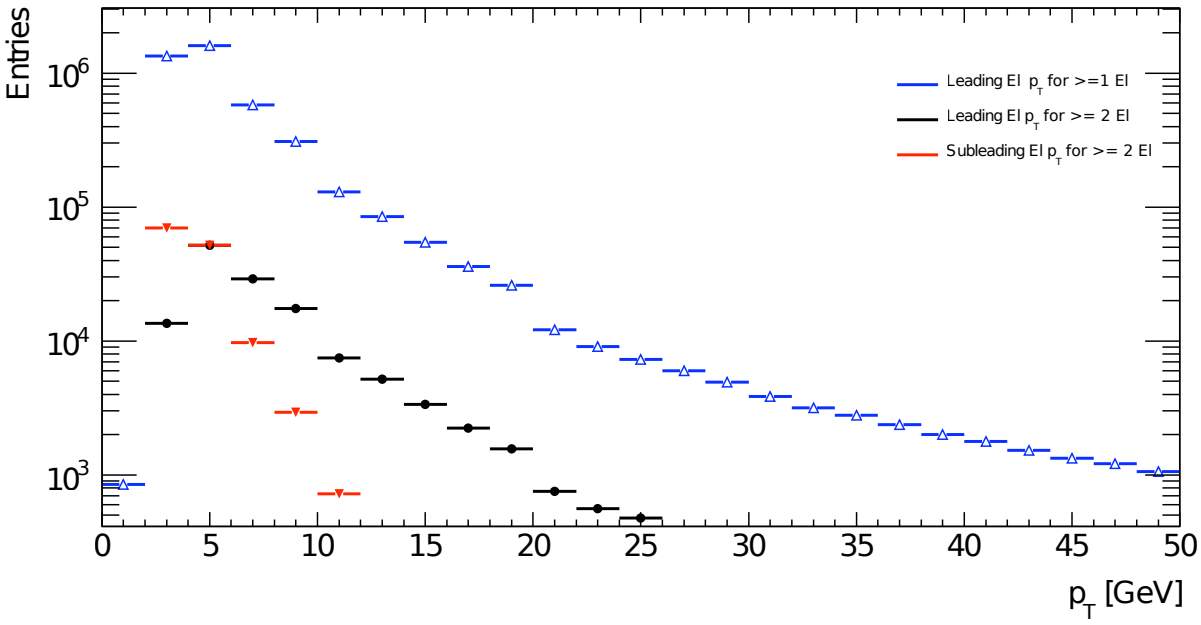

Figure 7.4: Electron p_{T} distributions in data events (periods B,D-J). The blue data points show the p_{T} distribution of the leading electron from a sample with at least one selected electron. The black and red points refer to the p_{T} of the leading and subleading electron, respectively, from a sample with at least two selected electrons. The discontinuities in the distributions at 10 GeV and 20 GeV may originate from different trigger skimming cuts for different data periods.

Data and MC Samples

For the MC studies, a $Z \rightarrow ee$ sample as well as a mSUGRA sample is used. For the SUSY sample, all grid points of the mSUGRA $\tan\beta = 10$ grid are merged in order to obtain higher statistics. For the electron trigger efficiency determination on data, the `muon` stream for different 2011 run periods is considered. The different trigger studies use different data samples because not all trigger items are available in each run period. The numbers of events for different triggers, separated by run period are listed in Tab. A.2.

Trigger Matching

The Event Filter (EF) and the offline reconstruction employ different algorithms for the reconstruction of particles. For a precise trigger efficiency determination, the concurrence of the triggered objects (the objects reconstructed by the trigger system) and the offline reconstructed objetcs needs to be assured. The online and offline objects can be matched by minimising their distance ΔR. An offline electron is regarded as being identical (matched) to a given online electron if $\Delta R < 0.01$. If more than one offline electron fulfils this condition, the electron with the smallest ΔR is selected. The $\Delta R < 0.01$ cut is justified and leads to a negligible amount of acceptance loss as presented in Fig. 7.5. The effect of the trigger matching is illustrated in Fig. A.13 which shows the p_{T} distribution for events triggered by `EF_e20_medium1` with and without trigger matching applied.

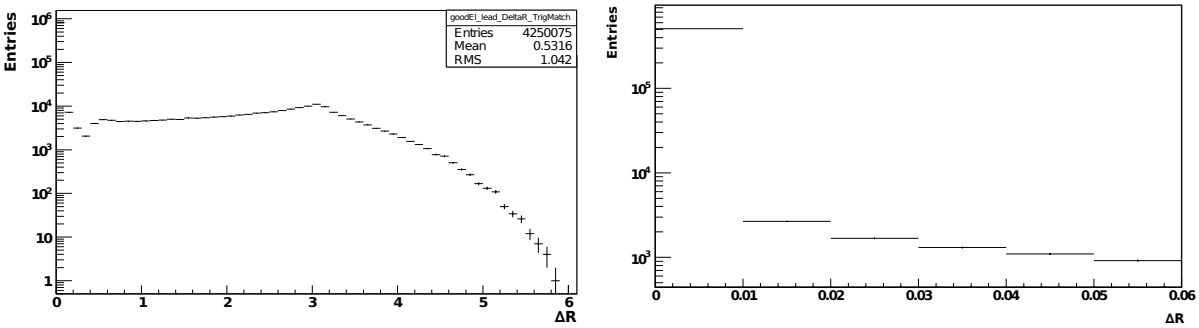

Figure 7.5: Distribution of ΔR between the online and the offline electron in data events (periods B,D-J). Left plot: Distribution over the whole range $[0, 2\pi]$. The peak at $\Delta R \approx \pi$ originates from two electrons from a $Z \to ee$ decay, flying in diametrally opposite directions. The boost of the Z boson leads to a shift to $\Delta R < \pi$. There is a sharp peak at very small ΔR which can be seen in the right plot which is a zoom into the low-ΔR region.

This is also depicted in Fig. 7.6 which shows the effect of the trigger matching on the trigger efficiency of `EF_e20_medium` on a MC $Z \to ee$ sample. The plateau efficiencies for `EF_e20_medium` amout 0.993 ± 0.005 without trigger matching and 0.992 ± 0.005 with trigger matching. Evidently, the trigger matching significantly reduces low-p_{T} artifacts due to fake electrons. Above the trigger threshold, the distributions are equal within the statistical uncertainty.

Single-Electron Trigger Efficiencies

In Fig. 7.7, the efficiency curves for `EF_e10_medium` and `EF_e20_medium` are displayed, showing the characteristic turn-on curve. The plateau efficiency is reached at about 5 GeV above the trigger threshold for both triggers. The plateau efficiencies are determined by a constant fit of the efficiency curves in the plateau region. They are calculated to be 0.992 ± 0.005 for `EF_e20_medium` and 0.994 ± 0.003 for `EF_e10_medium`. `EF_e10_medium` will be important again for the estimation of di-electron trigger efficiencies from single-electron triggers. As an example of a prescaled trigger, Fig. 7.8 exhibits the efficiency curve of `EF_e20_medium1` which has a tighter selection with respect to `EF_e20_medium`. The plateau efficiency is computed to be 0.532 ± 0.003 with both the Frequentist and the Bayesian method. One can see that for efficiencies not close to one, the two methods produce nearly the same results.

7.2.3 Di-Electron Trigger Efficiencies

Single-lepton trigger efficiencies can be determined easily via the *Tag & Probe* method which is the standard method for electron and muon trigger efficiencies. This method uses e.g. a data sample with decays of Z bosons to electron-positron pairs. One of the electrons is used as a *tag* which provides an unbiased sample while the other electron is used as

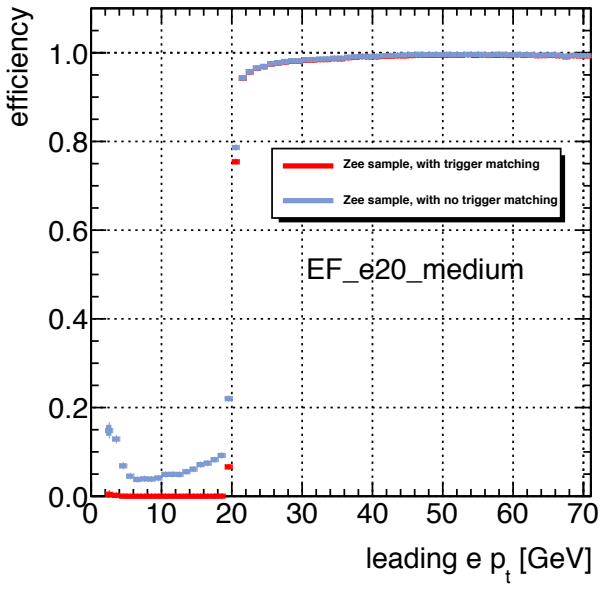

Figure 7.6: Trigger efficiency curve as a function of the leading electron p_{T} for the trigger `EF_e20_medium` for a MC Zee sample. The blue and red curves are the efficiencies without and with the application of trigger matching, respectively.

probe for which the single-electron trigger efficiency can be determined. This technique is not applicable to di-lepton triggers. This is why the di-electron trigger efficiencies are determined with the help of the orthogonal-stream method.

For the study of di-electron triggers on data, the sample A is required to consist of events with at least two *medium* electrons. The fact that at least two and not exactly two electrons are required accounts for both the higher statistics achievable as well as the applicability to the multi-lepton SUSY searches. However, this approach might introduce ambiguities on events with more than two electrons with p_{T} above the trigger threshold. It is possible that the electrons that trigger the event are not the two leading electrons. The probability for this to occur is assumed negligible and the trigger efficiencies are determined as a function of the leading and subleading electron p_{T}. For the MC studies, at least two *tight* electrons are requested. The expected difference between medium and tight electrons is sufficiently small to allow a direct comparison between the data and MC studies. The di-electron event is regarded to be triggered if both offline electrons have matching online electrons according to the trigger matching definition.

The di-electron triggers under study are `EF_2e12_medium` and `EF_2e12T_medium`. These triggers differ in their L1 seed; the first one is seeded by `L1_2EM7` the latter one by `L1_2EM10`. In the MC samples, `EF_2e12T_medium` is not available. Since the only difference between this trigger and `EF_2e12_medium` is the tighter L1 seed, it is examined whether `EF_2e12T_medium` can be emulated by requiring `EF_2e12_medium && L1_2EM10`.

Fig. 7.9 shows the absolute efficiency of `EF_2e12_medium` as a function of the leading (left) and subleading (right) electron p_{T}. There is a significant difference between the $Z \rightarrow ee$ and the SUSY sample for the leading electron. A possible explanation for this is

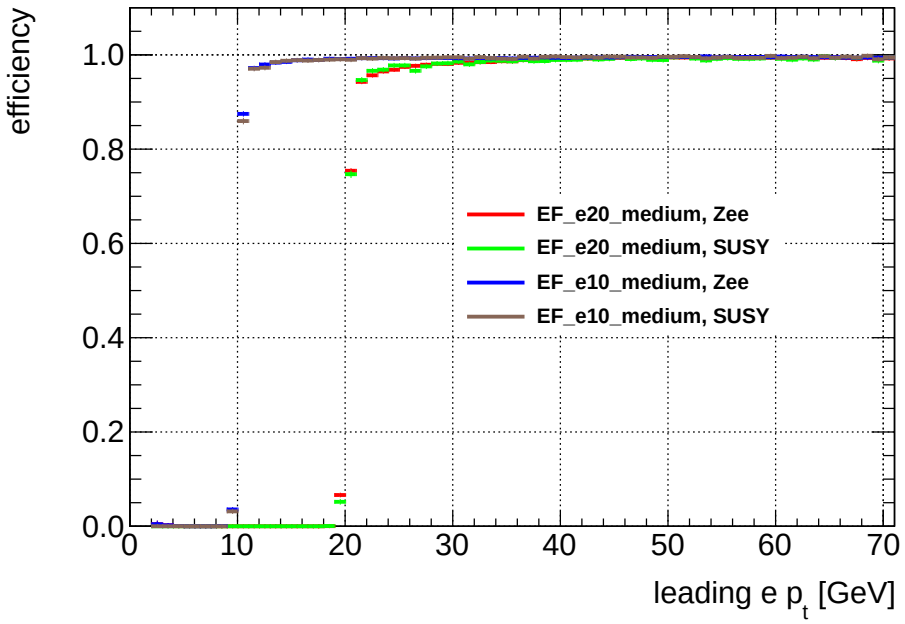

Figure 7.7: Trigger efficiency curve as a function of the leading electron p_{T} for the triggers `EF_e10_medium` and `EF_e20_medium` for both Zee and SUSY MC samples. The efficiency is calculated with respect to the sample of events with at least one tight electron.

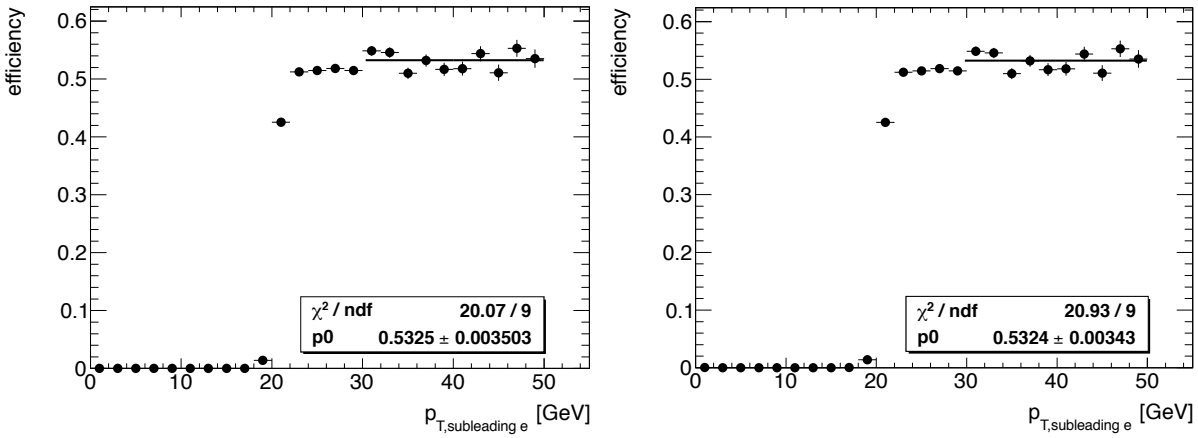

Figure 7.8: Trigger efficiency curve of the prescaled trigger `EF_e20_medium1` as a function of the p_{T} of the subleading electron. The left curve is determined with the frequentist Copper-Pearson method while the right curve uses Bayesian methods with Jeffrey's prior. $p0$ gives the fit value of the plateau efficiency and its (symmetric) uncertainty. Used data periods: B, D-J.

that the di-electron trigger efficiency is a function of both leading and subleading electron p_{T}. In order to obtain the di-electron trigger efficiency as a function of the leading electron it is integrated over the subleading electron,

$$\varepsilon_{2e}(p_{\mathrm{T},1}) = \int \varepsilon_{2e}(p_{\mathrm{T},1}, p_{\mathrm{T},2}) \cdot f(p_{\mathrm{T},2}; p_{\mathrm{T},1}) \mathrm{d}p_{\mathrm{T},2}. \tag{7.11}$$

ε_{2e} symbolises the di-electron trigger efficiency and $f(p_{\mathrm{T},2}; p_{\mathrm{T},1})$ is the probability density

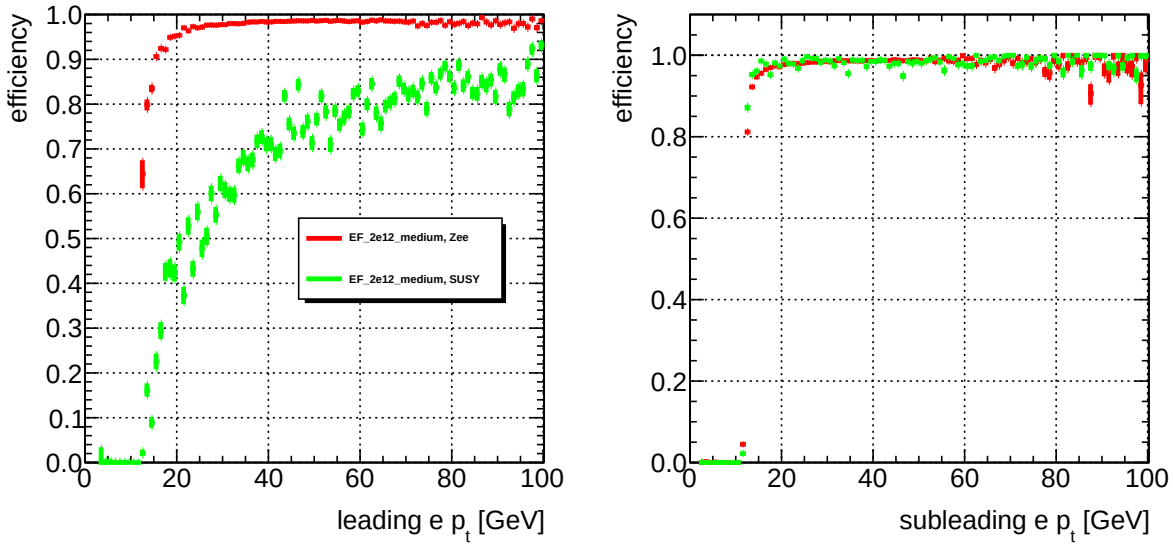

Figure 7.9: Trigger efficiency curve as a function of the leading (left) and subleading (right) electron p_{T} for the `EF_2e12_medium` for Zee (red) and SUSY (green) MC samples.

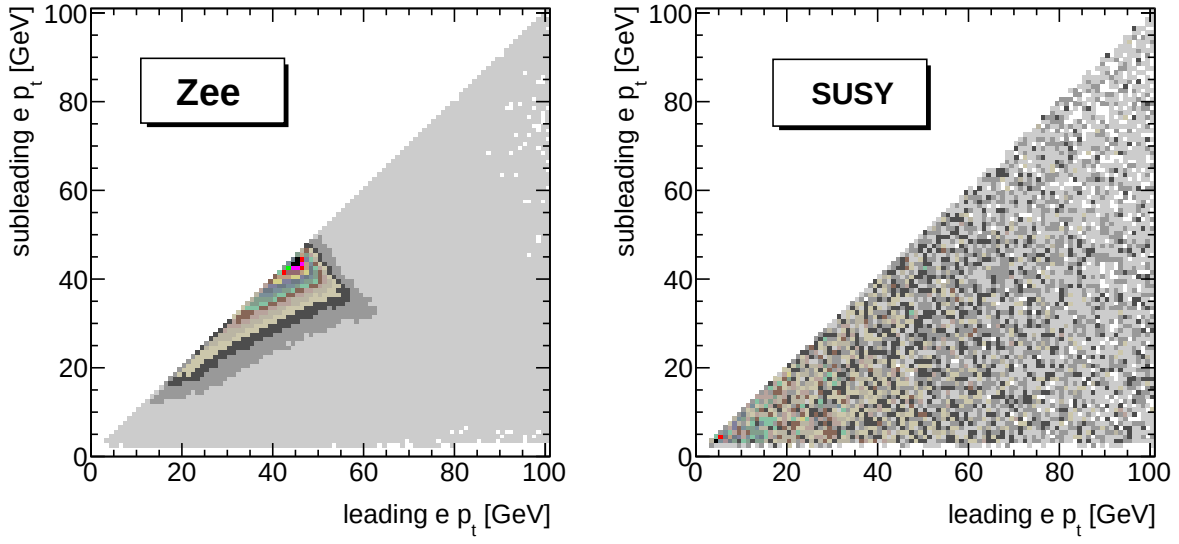

Figure 7.10: Scatter plot of leading and subleading electron p_{T} for the $Z \to ee$ (left) and the SUSY (right) MC samples.

function for a subleading electron with $p_{\mathrm{T},2}$ for a given $p_{\mathrm{T},1}$. The p_{T} distribution of the subleading electron $f(p_{\mathrm{T},2}; p_{\mathrm{T},1})$ is in general different for the $Z \to ee$ and SUSY MC samples. The scatter plot of leading and subleading electron p_{T} for the $Z \to ee$ and the SUSY MC samples is depicted in Fig. 7.10. The $Z \to ee$ sample exhibits a peak at half the Z boson's mass while the p_{T} distributions for the SUSY sample does not have this feature. Thus, the differing trigger efficiency curves of the leading lepton p_{T} for $Z \to ee$ and SUSY can be explained with the correlation between the leading and subleading electron p_{T}. For $Z \to ee$ decays, the subleading electron is likely to have a p_{T} close to the leading one whereas the $p_{\mathrm{T},2}$ for the SUSY sample is evenly distributed for a given $p_{\mathrm{T},1}$. So, for the

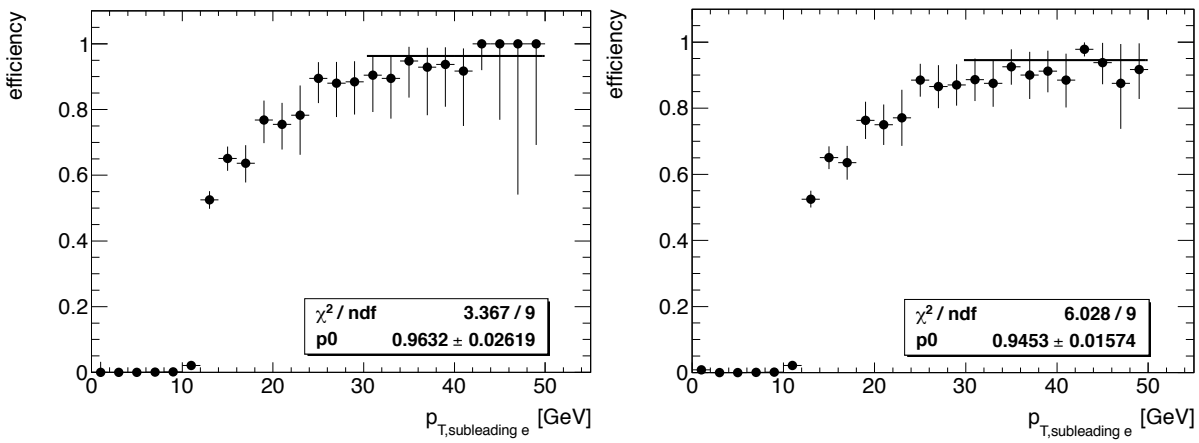

Figure 7.11: Trigger efficiency curve of `EF_2e12_medium` as a function of the p_T of the subleading electron. The left curve is determined with the frequentist Copper-Pearson method while the right curve uses Bayesian methods with Jeffrey's prior. $p0$ gives the fit value of the plateau efficiency and its (symmetric) uncertainty. Used data periods: B, D-J.

SUSY sample it is more likely that the subleading electron has not reached the efficiency plateau yet.

The trigger efficiency curve of `EF_2e12_medium` as determined from data is shown in Fig. 7.11. The left plot is created with the Frequentist Clopper-Pearson method while the right curve is determined with a Bayesian method using Jeffrey's prior. The plateau efficiency is determined to 0.963 ± 0.026 and 0.945 ± 0.016 for the two different methods, respectively. For the efficiencies close to one, the two methods produce significantly different mean values and uncertainties.

With an increasing instantaneous luminosity, the `EF_2e12_medium` trigger needs to be tightened in order to keep the rates low enough. As L1 is the bottleneck, it is reasonable to tighten the L1 seed of `EF_2e12_medium` which is seeded by `L1_2EM7`. By pushing the L1 threshold to 10 GeV (`L1_2EM7` $\rightarrow$ `L1_2EM10`), the EF trigger name changes to `EF_2e12T_medium`. As this trigger is not available in MC, it needs to be emulated. This is done by approximating `EF_2e12T_medium` $\sim$ `EF_2e12_medium && L1_2EM10`. Fig. A.14, which shows the ratio of these two, justifies the assumption; the deviation between the two amounts $\sim 0.2\%$. The p_T dependant efficiency curve of `EF_2e12_medium && L1_2EM10` using data is shown in Fig. 7.12. It can be seen that the orthogonal-stream method is strongly limited by a lack of statistics. Besides, the turn-on of these efficiency curves is very slow; the efficiency plateau is not reached 5 GeV above the online p_T cut. This may be due to the lack of statistics for this method.

The relative efficiency of `EF_2e12T_medium` with respect to `EF_2e12_medium` can be seen for both MC and data in Fig. 7.13. In this case, the studies on data are performed on the `Egamma` stream which is possible because a relative trigger efficiency is determined. The difference of the L1 trigger has an impact on the low-p_T region. The results for $Z \rightarrow ee$ MC and data are consistent within the statistical uncertainties. The relative efficiency

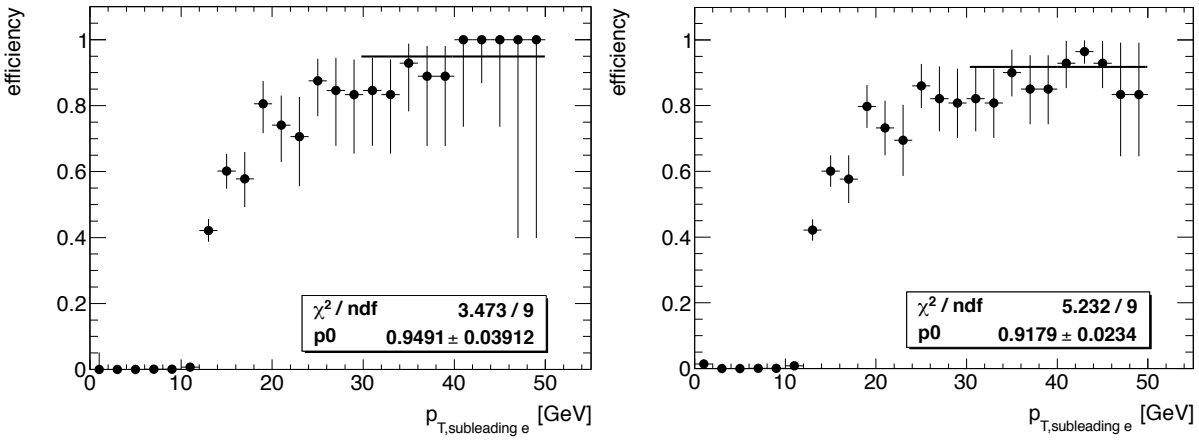

Figure 7.12: Trigger efficiency curve of `EF_2e12T_medium` emulated by `EF_2e12_medium && L1_2EM10` as a function of the p_{T} of the subleading electron. The left curve is determined with the frequentist Copper-Pearson method while the right curve uses Bayesian methods with Jeffrey's prior. $p0$ gives the fit value of the plateau efficiency and its (symmetric) uncertainty. Used data periods: B,D,E,I,J.

determined with events from the `muon` stream is shown in Fig. 7.14. The relative efficiency curves for the `Egamma` and `muon` stream differ significantly in the low-p_{T} region.

7.2.4 Estimation of Di-Electron Trigger Efficiency from Single-Electron Triggers

As discussed above, estimating the trigger efficiency for a di-electron trigger is difficult. The *Tag & Probe* method is not applicable and the orthogonal-stream method is limited by the lack of statistics.

It would be very useful if it were possible to estimate the efficiency of a di-lepton trigger with a single-lepton trigger with the same p_{T} threshold. The single-lepton trigger efficiency of a given threshold is determined easily via the *Tag & Probe* method. It may then be used to determine the efficiency of a di-electron trigger with the same p_{T} threshold by multiplying the single-electron trigger efficiencies for leading and subleading electron p_{T}. This is in principle possible as the algorithms for single- and di-electron triggers are almost identical with the exception that the di-electron trigger requires two instead of one electron over a given online p_{T} threshold [94]. This study is based on the single-electron trigger `EF_e10_medium` and the corresponding di-electron trigger `EF_2e10_medium` using MC. First, it was examined whether the product of the single-electron trigger efficiencies for leading and subleading electron p_{T} approximates the di-electron trigger efficiency with satisfying accuracy. Correlations between the electrons are not taken into account as they are expected to be negligible. The difference between this product and the true di-lepton trigger efficiency for leading and subleading electron,

$$\xi_1 \equiv \varepsilon_{1e}(p_{\mathrm{T},1}) \cdot \varepsilon_{1e}(p_{\mathrm{T},2}) - \varepsilon_{2e}(p_{\mathrm{T},1}) \tag{7.12}$$

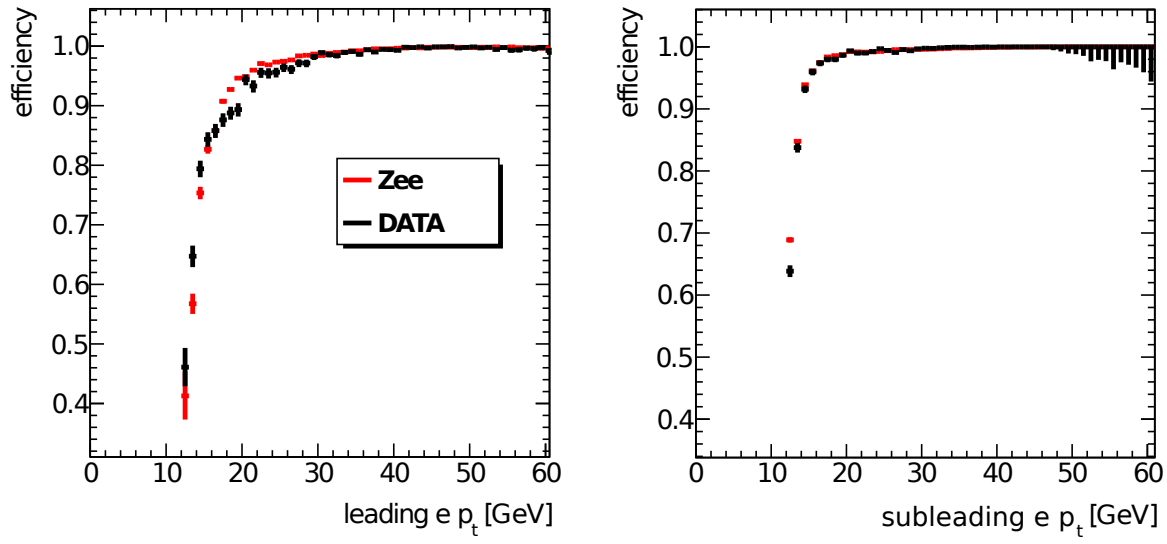

Figure 7.13: Relative trigger efficiency of `EF_2e12T_medium` with respect to `EF_2e12_medium` as a function of leading (left) and subleading (right) electron p_{T} for data (black) and MC Zee (red). The used data sample consists of data from runs 185761 and 185823 from period I2.

and

$$\xi_2 \equiv \varepsilon_{1e}(p_{\mathrm{T},1}) \cdot \varepsilon_{1e}(p_{\mathrm{T},2}) - \varepsilon_{2e}(p_{\mathrm{T},2}) \tag{7.13}$$

should be narrow distributions, centered at zero. From a MC $Z \rightarrow ee$ sample with at least two electrons, the efficiencies of `EF_e10_medium` and `EF_2e10_medium` are determined analogously to the previous section. The distributions for ξ_1 and ξ_2 are shown in Fig. 7.15. Especially the ξ_1 distribution is relatively wide, featuring a full width at half maximum (FWHM) of $\sim 8\%$. The distribution of ξ_2 is with a FWHM of $\sim 4\%$ narrower than that of ξ_1. Both distributions are biased as they exhibit a shift towards positive values, thus the approximation over-estimates the di-electron trigger efficiency.

Another approach is to take into account the integrated p_{T} distribution of the subleading electron for the determination of the leading electron's di-electron trigger efficiency by estimating the di-electron trigger efficiency with

$$\varepsilon_{2e}(p_{\mathrm{T},1}) \approx \varepsilon_{1e}(p_{\mathrm{T},1}) \cdot \int \varepsilon_{1e}(p_{\mathrm{T},2}) \cdot f(p_{\mathrm{T},2}; p_{\mathrm{T},1}) \mathrm{d}p_{\mathrm{T},2} \tag{7.14}$$

where $f(p_{\mathrm{T},2}; p_{\mathrm{T},1})$ is the distribution of $p_{\mathrm{T},2}$ for a given $p_{\mathrm{T},1}$. With this approach, the di-electron trigger efficiency as a function of the leading electron p_{T} is estimated by the single-electron trigger efficiency multiplied with the integrated single-electron trigger efficiency as a function of the subleading electron p_{T}, folded with the subleading p_{T} distribution. $f(p_{\mathrm{T},2}; p_{\mathrm{T},1})$ strongly depends on the kinematics of the process under study, as was shown in the previous section. However, it can be easily determined from MC and data. The integral can be regarded as a correction factor which accounts for the p_{T} distribution and trigger efficiency of the subleading electron. The correction factor is determined

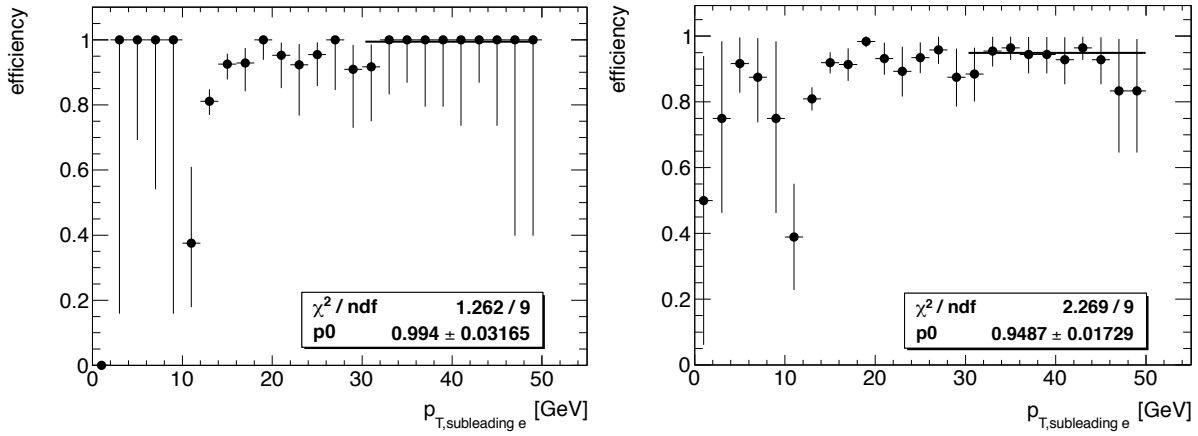

Figure 7.14: Relative trigger efficiency of (`EF_2e12_medium and L1_2EM10`) with respect to `EF_2e12_medium` as a function of the subleading electron p_{T} for data (periods B,D,E,I,J). The left curve is determined with the frequentist Copper-Pearson method while the right curve uses Bayesian methods with Jeffrey's prior. $p0$ gives the fit value of the plateau efficiency and its (symmetric) uncertainty.

using the `TProfile` class of ROOT, which returns the bin-wise mean of $\varepsilon_{1e}(p_{\mathrm{T},2})$. This quantity is multiplied bin by bin with $\varepsilon_{1e}(p_{\mathrm{T},1})$ to give the estimated di-electron trigger efficiency curve. Analogously, the di-lepton trigger efficiency for the subleading electron is determined by

$$\varepsilon_{2e}(p_{\mathrm{T},2}) \approx \varepsilon_{1e}(p_{\mathrm{T},2}) \cdot \int \varepsilon_{1e}(p_{\mathrm{T},1}) \cdot f(p_{\mathrm{T},1}; p_{\mathrm{T},2}) \mathrm{d}p_{\mathrm{T},1}. \tag{7.15}$$

The comparison of this approximation with the true efficiency curve is shown in Fig. 7.16 for both leading and subleading electron. Aside from some outliers and differences in the uncertainties, the two curves are in good agreement, thus allowing to estimate di-electron triggers with the help of single-electron triggers. This method would benefit from a more careful treatment of the uncertainties. A cross-check on data is not possible since the triggers used for this study are not available on data, nor are other triggers which have the same p_{T} threshold.

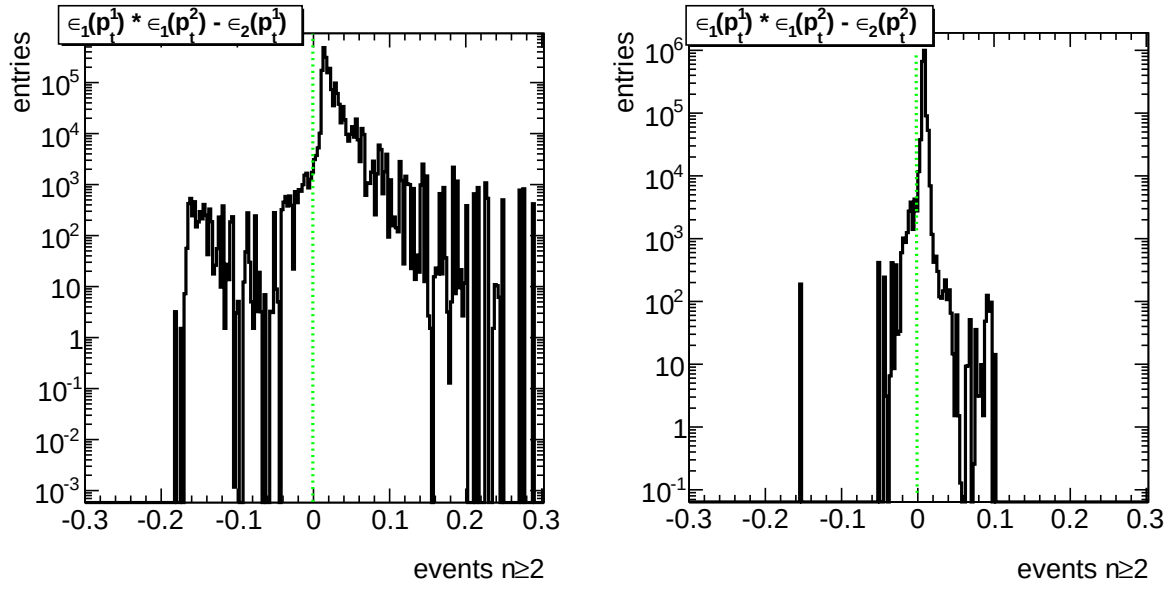

Figure 7.15: Distributions of ξ_1 an ξ_2, the difference between the estimated and the true di-electron trigger efficiency for MC $Z \rightarrow ee$ events with at least two tight electrons.

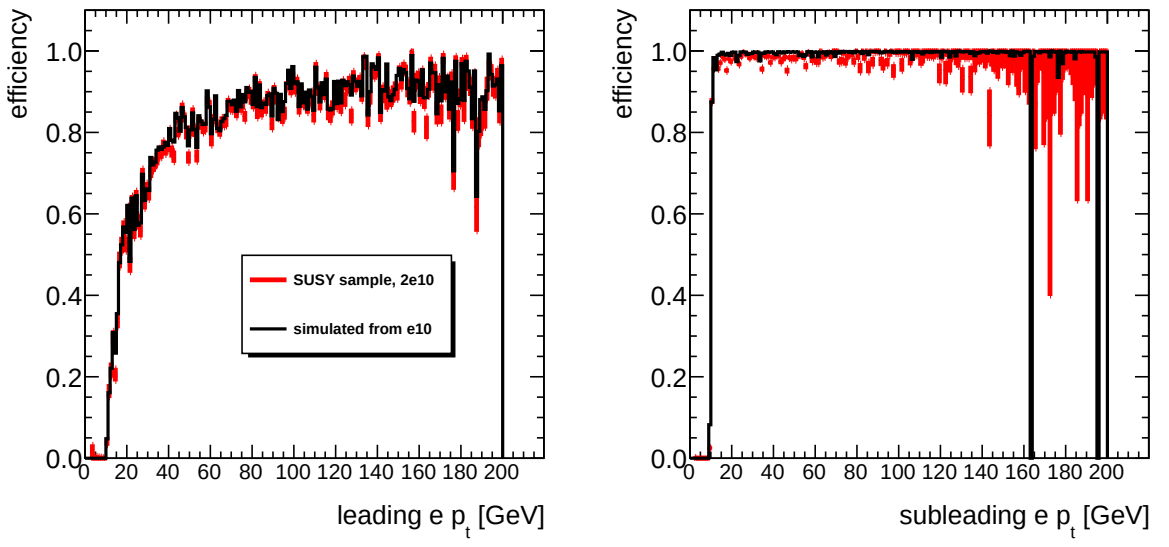

Figure 7.16: Trigger efficiency curves as a function of leading (left) and subleading (right) electron p_{T} for the di-electron trigger `EF_2e10_medium` (red) and for the simulation using the single-electron trigger `EF_e10_medium` (black), using the SUSY MC sample.

7.3 Summary & Outlook

In this chapter, the impact of di-lepton triggers on the event yield of SUSY searches was examined. The event yields are maximal on the DGemt grid, whereas in the mSUGRA plane, only for low $m_{1/2}$ an improvement can be achieved. The PhenoGrid in the light LSP mode is, by construction, relatively insensitive to the inclusion of di-lepton triggers. It was shown that di-lepton triggers, especially asymmetric ones, are able to lead to significant improvements relative to the currently used single-lepton triggers. The inclusion of missing transverse energy to the di-lepton trigger allows to lower the p_{T} thresholds of the leptons significantly. These triggers turned out to lead to a significant improvement as well. In short, di-lepton triggers do not only allow to keep the trigger rates at an acceptable level, the performance can be even improved with respect to the current baseline.

The efficiencies for the di-electron triggers `EF_2e12_medium` and `EF_2e12T_medium` were studied in some detail. Both triggers exhibit the same efficiency in the plateau region but differ in their turn-on region. The plateau efficiencies of these triggers were determined with both data and Monte Carlo. The determination of the electron trigger efficiency curves on data was performed with the help of the orthogonal `muon` stream for a Frequentist and a Bayesian method. Especially for efficiencies close to one, the two methods differ significantly. For the Frequentist method, severe approximations were assumed, leading to large uncertainties. The incorporated Bayesian method on the other hand uses a rather arbitrary tuning of the prior in order to (artificially) reduce the uncertainties. It was revealed that the orthogonal-stream method is limited by a lack of statistics. The turn-on curves are much slower than those determined from MC. In order to verify the results obtained from data, a cross-check of the trigger efficiencies with the help of the bootstrap method needs to be performed.

Finally, two different approaches for the estimation of di-lepton trigger efficiencies from single-lepton triggers were established. The squared single-electron trigger efficiency turned out to over-estimate the di-electron trigger efficiency. The other approach was to take into account the integrated subleading p_{T} distribution for the determination of the di-electron trigger efficiency as a function of the leading electron's p_{T}. This approach models the di-electron trigger efficiency quite accurately.

Chapter 8

Conclusion

In this thesis, two distinct studies have been performed that aim at enhancing the capabilities to find SUSY in searches using final states with two leptons and missing transverse energy. On the one hand, an optimisation of signal regions with the help of sophisticated algorithms has been performed. On the other hand, di-lepton triggers have been suggested to account for the need of lower trigger thresholds.

The optimisation of cut values has been performed on different regions of the mSUGRA $m_0 - m_{1/2}$ plane for both opposite-sign and opposite-sign same-flavour events. It turned out that the variables which exhibit the best separation power between SUSY and SM background are the $E_{\mathrm{T}}^{\mathrm{miss}}$ and the p_{T} of the two leading jets. It was found that the optimised cuts can improve the significance of at least a factor of two throughout the entire mSUGRA $m_0 - m_{1/2}$ parameter space with regard to the reference cuts. Moreover, these cuts are relatively robust concerning different significance definitions as well as systematic uncertainties on the number of background events. Requiring three and four jets for two-body and three-body decays, respectively instead of two jets leads to slightly higher significances. However, incorporating a high number of jets results in a loss of accuracy in the reconstruction of SUSY events because of systematic uncertainties on the jet-energy scale and the jet-energy resolution. Furthermore, these signal regions explicitly exploit the kinematics of the mSUGRA model. Other models may feature decay chains with less jets. This is especially true for the *DirectGaugino* model. That is, requiring three or four jets includes a strong model dependence. The signal regions suggested in this analysis aim at finding an agreement between good performance in the mSUGRA parameter space on one hand and model independence on the other. The optimisation of the OSSF signal region for the flavour subtraction analysis unveiled that the distance ΔR between the two leptons exhibits a strong separation power.

The optimisation of cut values with the help of the rectangular cuts algorithm is a simple technique to define signal regions. Still, much fine-tuning of the algorithm's parameters is necessary in order to find the best possible set of cuts. The main drawback of this optimisation transpired to be the lack of MC signal statistics. It is important to

cross-check the model-dependence of these cuts by applying the signal regions to other SUSY models, combined with an independent cut optimisation on such grids. Besides, the signal regions would probably benefit from the application of multivariate techniques such as Support Vector Machines.

In the second part of the analysis, the impact of di-lepton triggers on the event yield of SUSY searches was examined. The event yields are maximal on the *DirectGaugino* grid, whereas in the mSUGRA plane, only for low $m_{1/2}$ an improvement can be achieved. The PhenoGrid in the light LSP mode is relatively insensitive to the inclusion of di-lepton triggers due to the hard leading lepton p_{T}. It was shown that di-lepton triggers, especially asymmetric ones, lead to a significant improvement with respect to the currently used single-lepton triggers. The inclusion of missing transverse energy to the di-lepton trigger allows to lower the p_{T} thresholds of the leptons even more and turned out to lead to a significant improvement as well. Di-lepton triggers do not only allow to keep the trigger rates at an acceptable level, the performance can even be improved with respect to the current baseline. The efficiencies for the di-electron triggers `EF_2e12_medium` and `EF_2e12T_medium` were studied in some detail. Both triggers exhibit the same efficiency in the plateau region but differ in their turn-on region. The plateau efficiencies of these triggers were determined on both data and Monte Carlo. The determination of the electron trigger efficiency curves on data was performed with the help of the orthogonal `muon` stream for a Frequentist and a Bayesian method. It was shown that especially for efficiencies close to one, the two methods differ significantly. This orthogonal-stream method is limited by a lack of statistics and should be compared to other data-driven techniques such as the bootstrap method. Finally, two different approaches for the estimation of di-lepton trigger efficiencies from single-lepton triggers were established and tested. It was shown that the squared single-electron trigger efficiency over-estimates the di-electron trigger efficiency. Another approach was taking into account the integrated subleading p_{T} distribution for the determination of the di-electron trigger efficiency as a function of the leading electron's p_{T}. This approach emerged to model the di-electron trigger efficiency quite accurately for SUSY MC samples. This p_{T} distribution, however, depends on the kinematics of the process under study.

The studies on the signal region optimisation performed in this thesis are included in the 2011 di-lepton support note [2]. The di-lepton trigger analyses have contributed to the incorporation of such triggers into the 2011 and 2012 ATLAS trigger menu. A support note including the di-lepton trigger studies of this thesis is in preparation.

These studies contributed to the direct searches for Supersymmetry in decays involving exactly two leptons. With an integrated luminosity of more than $5\,\mathrm{fb}^{-1}$ recorded in 2011, the LHC and the ATLAS detector perform extremely well. However, neither this search channel nor any other could provide an indication of the existence of SUSY particles yet. Instead, regions in parameter spaces of dedicated constrained models such as mSUGRA have been excluded. The available SUSY parameter space is too large to be ruled out

completely in the near future. Still, it is possible to exclude most MSSM scenario indirectly by the Higgs searches. The exclusion of a light Higgs boson would automatically preclude many constrained SUSY models. Recent results of ATLAS and CMS present a strong hint on the existence of the Higgs boson with a mass of $m_H \approx 125$ GeV. It is expected that by the end of 2012, the existence of the Higgs boson can be either proven or excluded. If no sign of SUSY appears, one would be forced to think about new models of the particle world from scratch as it seems very likely that new physics emerges in the 16 orders of magnitude in energy between the presently explored territory and the Planck scale. In either case, it remains exciting.

Bibliography

[1] The ATLAS Collaboration. Searches for supersymmetry with the ATLAS detector using final states with two leptons and missing transverse momentum in $\sqrt{s} = 7$ TeV proton-proton collisions. *arXiv:hep-ex/1110.6189v1*, 2011.

[2] A Alonso, S Brazzale, P Bechtle, M Bianco, M Boehler, A Castaneda, C Clement, W Ehrenfeld, J Firmino da Costa, S Franchino, ST French, G Gaudio, C Giuliani, B Kile Gjelsten, E Gorini, E Gramstad, D Harper, T Lari, F Legger, CG Lester, J Lundberg, M Lungwitz, B Meirose, F Meloni, T Mueller, H Okawa, F Ould-Saada, N Panikashvili, M Pedersen, G Polesello, J Poveda, M Primavera, T Sarangi, I Serenkova, R Soualah, A Taffard, B Toggerson, C Troncon, M Tylmad, M Uslenghi, A Ventura, P Wagner, HH Williams, S Williams, S Wu, Z Yang, and M Zvolsky. Searching for Supersymmetry with two leptons and missing transverse momentum at $\sqrt{s} = 7$ TeV. Technical Report ATL-COM-PHYS-2011-649, CERN, Geneva, Jun 2011.

[3] C. N. Yang. *Selected Papers*. Freeman, 1983.

[4] I. Aitchison and A. Hey. *Gauge Theories in Particle Physics*. Taylor & Francis Group, 2003.

[5] J. Schwinger. On Quantum-Electrodynamics and the Magnetic Moment of the Electron. *Phys. Rev., 73, 416*, 1948.

[6] R. P. Feynman. Space-Time Approach to Quantum Electrodynamics. *Phys. Rev., 76, 769*, 1949.

[7] R. P. Feynman. Mathematical Formulation of the Quantum Theory of Electromagnetic Interaction. *Phys. Rev., 80, 440*, 1950.

[8] M. Peskin and D. Schröder. *An Introduction to Quantum Field Theory*. Addison Wesley, 1997.

[9] D. Griffiths. *Introduction to Elementary Particles*. Wiley-VCH, 2008.

[10] T. Hahn and P. Lang. FeynEdit - a tool for drawing Feynman diagrams. *Comput.Phys.Commun.179:931-935*, 2008.

[11] H. Fritzsch, M. Gell-Mann, and H. Leutwyler. Advantages of the Color Octet Gluon Picture. *Phys. Lett. B 47, 365*, 1973.

[12] Mark-J Collaboration, D.P. Barber, et al. Discovery of Three-Jet Events and a Test of Quantum Chromodynamics at PETRA. *Phys.Rev.Lett. 43, 830*, 1979.

[13] David J. Gross and Frank Wilczek. Ultraviolet behavior of non-abelian gauge theories. *Phys. Rev. Lett.*, 30:1343–1346, Jun 1973.

[14] S. Bethke. The 2009 world average of α_s. *arXiv:0908.1135v2 [hep-ph]*, 2009.

[15] K. Nakamura et al. Review of particle physics. *JPG 37, 075021 (http://pdg.lbl.gov)*, 2010.

[16] S.L. Glashow. Partial-symmetries of weak interactions. *Nucl. Phys. 22, 579*, 1961.

[17] S.L. Glashow, J. Iliopoulos, and L. Maiani. Weak interactions with lepton-hadron symmetry. *Physical Review, D2, 1585*, 1970.

[18] S. Weinberg. A model of leptons. *Phys. Rev. Lett. 19, 1264*, 1967.

[19] P. Schmüser. *Feynman-Graphen und Eichtheorien für Experimentalphysiker.* Springer, 1995.

[20] F. J. Hasert et al. Observation of neutrino-like interactions without muon or electron in the Gargamelle neutrino experiment. *Phys. Lett. 46B 121*, 1973.

[21] The UA1 Collaboration. Experimental observation of lepton pairs of invariant mass around 95 GeV/c^2 at the CERN SPS collider. *Phys. Lett. B*, 126:398, 1985.

[22] The UA1 Collaboration. Experimental observation of isolated large transverse energy electrons with associated missing energy at $\sqrt{s} = 540$ GeV. *Phys. Lett. B*, 122:103, 1983.

[23] The UA2 Collaboration. Evidence for $Z^0 \rightarrow e^+e^-$ at the CERN $\bar{p}p$ collider. *Phys. Lett. B, 129, 130*, 1983.

[24] The UA2 Collaboration. Observation of single isolated electrons of high transverse momentum in events with missing transverse energy at the CERN $\bar{p}p$ collider. *Phys. Lett. B, 122, 476*, 1983.

[25] The ATLAS Collaboration. Combined Standard Model Higgs boson searches with up to 2.3 fb^{-1} of pp collision data at $\sqrt{s} = 7$ TeV at the LHC. *ATLAS-CONF-2011-157*, 2011.

[26] G. Abbiendi et al. Search for the Standard Model Higgs Boson at LEP. *Phys. Lett. B 565, 61*, 2003.

[27] Combination of Higgs Boson Searches with up to $4.9\,\mathrm{fb}^{-1}$ of pp Collisions Data Taken at a center-of-mass energy of 7 TeV with the ATLAS Experiment at the LHC. Technical Report ATLAS-CONF-2011-163, CERN, Geneva, Dec 2011.

[28] K2K Collaboration, M. H. Ahn, et al. Measurement of neutrino oscillation by the K2K experiment. *arXiv:hep-ex/0606032v3*, 2006.

[29] T Morii, C.S. Lim, and S.N. Mukherjee. *The Physics Of The Standard Model and Beyond*. World Scientific, 2004.

[30] M.J.G. Veltman and G. 't Hooft. Regularization and renormalization of gauge fields. *Nuclear Physics B44*, 1972.

[31] U. Amaldi, W. de Boer, and H. Fürstenau. Comparison of Grand Unified Theories with electroweak and strong coupling constants measured at LEP. *Physics Letters Bd. 260*, 1991.

[32] D. I. Kazakov. Beyond the standard model (in search of supersymmetry). *arXiv:hep-ph/0012288v2*, 2001.

[33] P. Langacker and M. Luo. Implications of precision electroweak experiments for m_t, ρ_0, $\sin^2\theta_W$ and grand unification. *Phys. Rev. D 44, 817*, 1991.

[34] Nobelprize.org. The nobel prize in physics 2011 - scientific background. `http://www.nobelprize.org/nobel_prizes/physics/laureates/2011/sci.html`, 15 Oct 2011.

[35] I. Aitchison. *Supersymmetry in Particle Physics*. Cambridge University Press, 2007.

[36] S. Martin. A supersymmetry primer. *arXiv:hep-ph/9709356v5*, 2008.

[37] A. Chamseddine, R. Arnowitt, and P. Nath. Locally Supersymmetric Grand Unification. *Physical Review Letters. 49, 970*, 1982.

[38] B. de Wit. Supergravity. *arXiv:hep-th/0212245*, 2002.

[39] J. Wess and B. Zumino. Supergauge transformations in four dimensions. *Nucl. Phys. B 70, 39*, 1974.

[40] J. Wess and B. Zumino. A Lagrangian model invariant under supergauge transformations. *Phys. Lett. B 49, 52*, 1974.

[41] G. L. Kane, C. Kolda, and J. D. Wells. Calculable Upper Limit on the Mass of the Lightest Higgs Boson in Any Perturbatively Valid Supersymmetric Theory. *arXiv:hep-ph/9210242*, 1992.

[42] J. R. Espinosa and M. Quiros. Upper Bounds on the Lightest Higgs Boson Mass in General Supersymmetric Standard Models. *arXiv:hep-ph/9212305*, 1992.

[43] J. Rosiek. Complete set of Feynman rules for the MSSM - ERRATUM. *arXiv:hep-ph/9511250*, 1995.

[44] The Super-Kamiokande Collaboration: H. Nishino and S. Clark. Search for Proton Decay via $p \to e^+\pi^0$ and $p \to \mu^+\pi^0$ in a Large Water Cherenkov Detector, 2009.

[45] D. Dimopoulos and D. Sutter. The supersymmetric flavor problem. *arXiv:hep-ph/9504415v1*, 1995.

[46] H. Baer, F. Paige, S. Protopopescu, and X. Tata. Simulating Supersymmetry with ISAJET 7.0/ ISASUSY 1.0. *arXiv:hep-ph/9305342*, 1993.

[47] The ATLAS Collaboration. Searches for supersymmetry using final states with two-leptons and missing transverse momentum with the ATLAS detector in sqrt(s) = 7 TeV proton-proton collisions. *CERN-PH-EP-2011-165*, 2011.

[48] P. Bechtle, K. Desch, H. K. Dreiner, M. Krämer, B. O'Leary, C. Robens, B. Sarrazin, and P. Wienemann. Present and possible future implications for mSUGRA of the non-discovery of SUSY at the LHC. *arXiv:hep-ph/1105.5398*, 2011.

[49] P. Bechtle, K. Desch, H. K. Dreiner, M. Krämer, B. O'Leary, C. Robens, B. Sarrazin, and P. Wienemann. What if the LHC does not find supersymmetry in the sqrt(s)=7 TeV run? *arXiv:hep-ph/1102.4693*, 2011.

[50] The ATLAS Collaboration. SUSY searches with dileptons and high missing transverse momentum. Technical Report ATL-PHYS-INT-2011-030, CERN, Geneva, Apr 2011.

[51] The ATLAS collaboration. Phenogrid2. `https://twiki.cern.ch/twiki/bin/viewauth/AtlasProtected/PhenoGrid2`, 17 Oct 2011.

[52] R. P. Feynman. *The Character of Physical Law*. Modern Library, 1965.

[53] O. S. Brüning, P. Collier, P. Lebrun, S. Myers, R. Ostojic, J. Poole, and P. Proudlock. *LHC Design Report*. CERN, Geneva, 2004.

[54] L. Evans and P. Bryant. The CERN Large Hadron Collider: Accelerator and Experiments: LHC machine. *JINST 3 S08001*, 2008.

[55] LHC at home. `http://lhcathome.web.cern.ch/LHCathome/`, 23 Oct 2011.

[56] A. Acquafredda et al. The OPERA experiment in the CERN to Gran Sasso neutrino beam. *JINST 4 P04018 doi:10.1088/1748-0221/4/04/P04018*, 2009.

[57] J. Roßbach and P. Schmüser. Basic course on accelerator optics. CERN Accelerator School 1992, DESY M-93-02, 1992.

[58] F. Hinterberger. *Physik der Teilchenbeschleuniger und Ionenoptik.* Springer, 2008.

[59] The ATLAS collaboration. Luminosity public results. `https://twiki.cern.ch/twiki/bin/view/AtlasPublic/LuminosityPublicResults#Luminosity_versus_day`, 14 Sept 2011.

[60] G. Aad et al. The ATLAS Collaboration. The ATLAS experiment at the CERN Large Hadron Collider. *JINST 3 S08003*, 2008.

[61] J. Collins. Light-cone Variables, Rapidity and all that. *arXiv:hep-ph/9705393*, 1997.

[62] T. Ferbel (ed.). *Experimental Techniques in Nuclear and Particle Physics.* World Scientific, 1991.

[63] G. F. Knoll. *Radiation detection and measurement.* John Wiley & Sons, 2000.

[64] A. Moraes, C. Buttar, and I. Dawson. Prediction for minimum bias and the underlying event at LHC energies. *SN-ATLAS-2006-057*, 2008.

[65] D. Kar. Minimum Bias and Early QCD at ATLAS. *ATL-PHYS-PROC-2010-082*, 2010.

[66] The ATLAS Collaboration. Performance of the ATLAS Trigger System in 2010. *arXiv:hep-ex/1110.1530v1*, 2011.

[67] *ATLAS Level-1 trigger.* Technical Design Report ATLAS. CERN, Geneva, 1998.

[68] P. Jenni, M. Nessi, M. Nordberg, and K. Smith. *ATLAS high-level trigger, data-acquisition and controls.* Technical Design Report ATLAS. CERN, Geneva, 2003.

[69] S. Armstrong et al. Architecture of the ATLAS High Level Trigger Event Selection Software. *Nucl. Instrum. Meth. A 518, 537*, 2004.

[70] S. Prasad. The ATLAS Trigger System. Harward ATLAS weekly meeting, April 04 2007, `http://www.hepl.harvard.edu/atlas/group/Trigger_Overview_Srivas.pdf`, 01 Nov. 2011.

[71] The ATLAS Collaboration. *Expected performance of the ATLAS experiment: detector, trigger and physics.* CERN, Geneva, 2009.

[72] D. Banfi. Electron and Photon reconstruction and identification with the ATLAS detector and performance with $\pi^0 \to \gamma\gamma$ and $\eta \to \gamma\gamma$ with $\sqrt{s} = 900$ GeV data. *Journal of Physics: Conference Series 293, 012063*, 2011.

[73] M. Cacciari, G. P. Salam, and G. Soyez. The anti-k_t jet clustering algorithm. *JHEP*, 04:063, 2008.

[74] T. Sjöstrand. Monte Carlo generators for the LHC. In *Academic Training Lectures*, page Streaming video ; transparencies ; 4 DVD video, 2005. CERN, Geneva, 4 - 7 Apr 2005.

[75] T. Sjöstrand, S. Mrenna, and P. Z. Skands. PYTHIA 6.4 Physics and Manual. *JHEP*, 0605:026, 2006.

[76] G. Corcella, I. G. Knowles, G. Marchesini, S. Moretti, K. Odagiri, P. Richardson, M. H. Seymour, and B. R. Webber. HERWIG 6.5: an event generator for Hadron Emission Reactions With Interfering Gluons (including supersymmetric processes). *JHEP 0101:010*, 2001.

[77] M. L. Mangano, M. Moretti, F. Piccinini, R. Pittau, and A. D. Polosa. ALPGEN, a generator for hard multiparton processes in hadronic collisions. *JHEP 0307, 001*, 2003.

[78] S. Frixione and B. R. Webber. Matching NLO QCD computations and parton shower simulations. *JHEP 0206, 029*, 2002.

[79] S. Agostinelli et al. GEANT4: A simulation toolkit. *Nucl. Instrum. Meth.*, A506:250–303, 2003.

[80] J. Butterworth, J. Forshaw, and M. Seymour. Multiparton Interactions in Photoproduction at HERA. *Z. Phys. C72, 637*, 1996.

[81] The ATLAS Collaboration. First tuning of HERWIG/JIMMY to ATLAS data. Technical Report ATL-PHYS-PUB-2010-014, CERN, Geneva, Oct 2010.

[82] A. Hoecker, P. Speckmayer, J. Stelzer, J. Therhaag, E. von Toerne, and H. Voss. TMVA - Toolkit for Multivariate Data Analysis. *arXiv:physics/0703039*, 2007.

[83] R. J. Barlow. *Statistics: A Guide to the Use of Statistical Methods in the Physical Sciences.* John Wiley & Sons, 1989.

[84] J. Neyman and E. S. Pearson. On the Problem of the Most Efficient Tests of Statistical Hypotheses. *Phil. Trans. R. Soc. Lond. A 231, 289*, 1933.

[85] A. Hoecker. TMVA Workshop - Introduction. `http://indico.cern.ch/getFile.py/access?contribId=0&resId=2&materialId=slides&confId=112879`, 2011.

[86] G. Cowan and E. Gross. Discussion and Guidelines on Significance. ATLAS Statistics Forum, 2009.

[87] G. Cowan and E. Gross. Discovery significance with statistical uncertainty in the background estimate. ATLAS Statistics Forum, 2008.

[88] R. D. Cousins, J. T. Linnemann, and J. Tucker. Evaluation of three methods for calculating statistical significance when incorporating a systematic uncertainty into a test of the background-only hypothesis for a Poisson process. *Nucl. Inst. Meth. A 595, 480*, 2008.

[89] R. Brun and F. Rademakers. ROOT - An Object Oriented Data Analysis Framework. *Nucl. Inst. Meth. A 389, 81*, 1997.

[90] R. O. Duda, P. E. Hart, and D. G. Stork. *Pattern Classification.* John Wiley & Sons, 2000.

[91] Private Communication with M. Boehler.

[92] J. T. Linnemann. Measures of Significance in HEP and Astrophysics. *arXiv:physics/0312059*, 2003.

[93] M. Misiura. Studies of single and double electron triggers at the ATLAS experiment. Summer Student Report, `http://www.desy.de/f/students/2011/reports/misiura.pdf`, Dec. 2011.

[94] C. Hensel, M. Hamer, and J. Hofestädt. Trigger Efficiency Measurement for Di-Muon Triggers. Technical Report ATL-COM-DAQ-2011-131, CERN, Geneva, Nov 2011.

[95] C. Hensel, F. Kohn, M. Hamer, and A. Quadt. Muon Trigger Efficiencies with a combined Tag & Probe and Bootstrap Method. Technical Report ATL-COM-PHYS-2010-916, CERN, Geneva, Nov 2010.

[96] M. Hamer, C. Hensel, F. Kohn, and A. Quadt. Measurement of Trigger Efficiencies from Data and their Application in Physics Analyses. Technical Report ATL-COM-DAQ-2011-083, CERN, Geneva, Sep 2011.

[97] D. Casadei. Estimating the Trigger Efficiency. A Tutorial. *ATLAS Statistics Forum*, 2010.

[98] ROOT: Class TEfficiency. `http://root.cern.ch/root/html/TEfficiency.html`, 20 Nov 2011.

[99] D. Casadei. Efficiency Measurement: A Bayesian Approach. *arXiv:0908.0130v5*, 2010.

[100] The ATLAS Collaboration. Search for squarks and gluinos using final states with jets and missing transverse momentum with the ATLAS detector in $\sqrt{s} = 7$ TeV proton-proton collisions. Technical Report arXiv:1109.6572. CERN-PH-EP-2011-145, CERN, Geneva, Sep 2011.

List of Figures

List of Tables

Appendix A

Miscellaneous Material

A.1 Theory

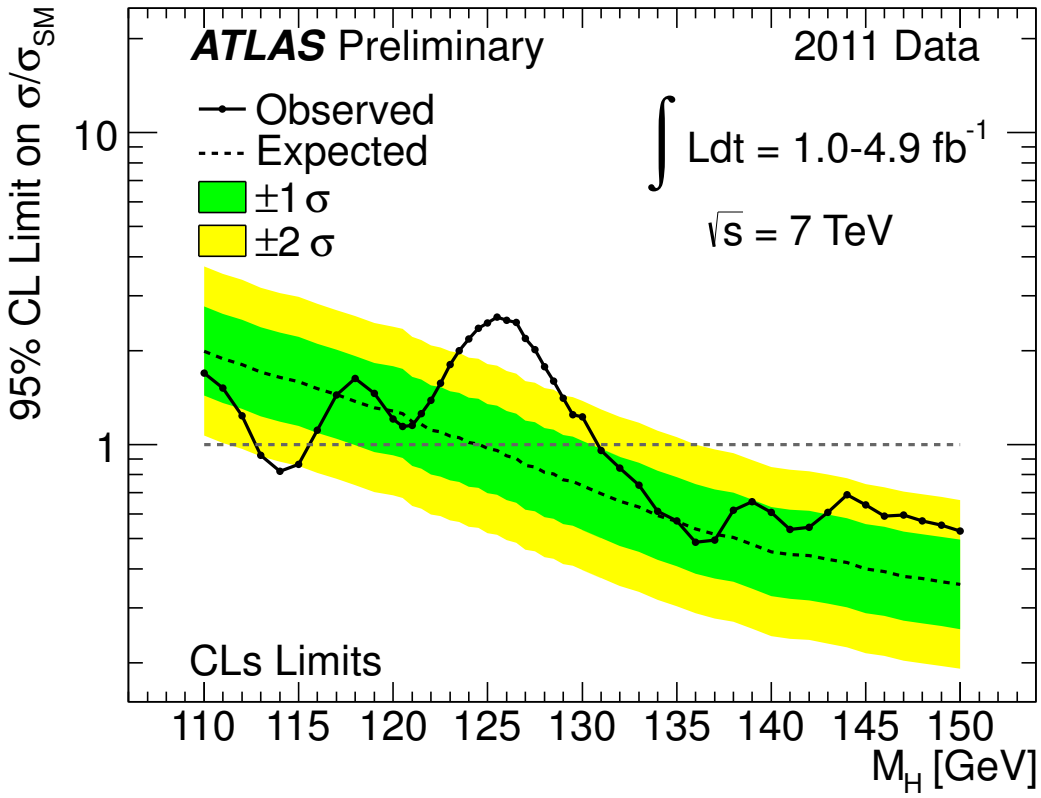

Figure A.1: The combined upper limit on the Standard Model Higgs boson production cross section divided by the Standard Model expectation as a function of m_H is indicated by the solid line. This is a 95% CL limit using the CLs method in the low mass range between 110 and 150 GeV. The dotted line shows the median expected limit in the absence of a signal and the green and yellow bands reflect the corresponding 68% and 95% expected regions. An excess of events is observed for a Higgs boson mass hypothesis close to $m_H = 126$ GeV [27].

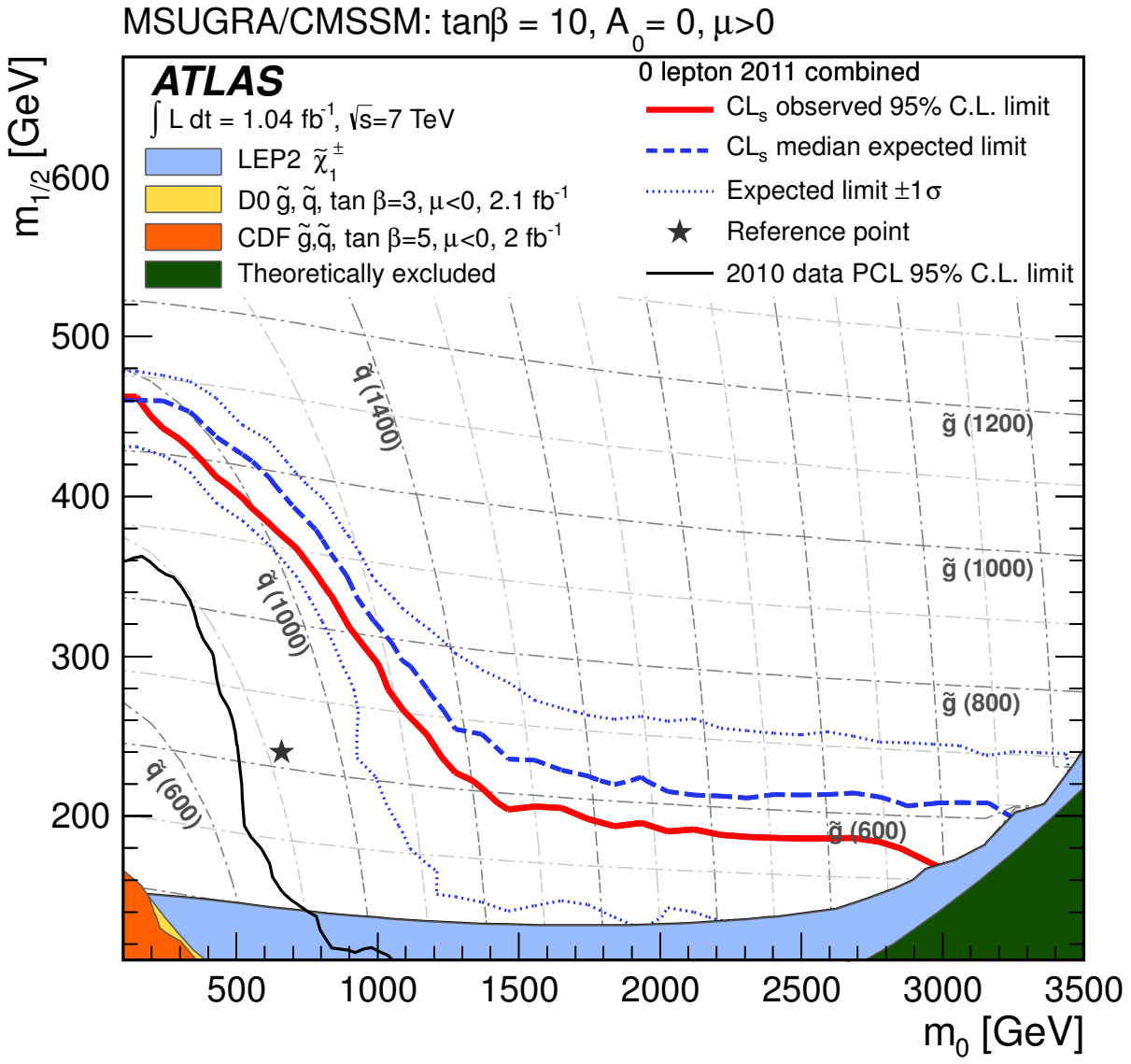

Figure A.2: Expected (dashed line) and observed (solid line) exclusion limits for mSUGRA in the $m_0 - m_{1/2}$ plane. The limit is obtained using the CL_s method in the 0-lepton analysis for an integrated luminosity of $1.04\,\text{fb}^{-1}$. The combined limits are obtained by using the signal region which generates the best expected limit at each point in the parameter plane. The dashed-blue line corresponds to the median expected 95% C.L. limit and the red line corresponds to the observed limit at 95% C.L. The dotted blue lines correspond to the $\pm 1\sigma$ variation in the expected limits. The coloured areas depict the limits from LEP and the Tevatron (some of these limits were generated with different models or parameter choices, c.f. legends) as well as the area which is theoretically excluded. The previous published ATLAS limits from this analysis are also shown. The dashed grey curves exhibit the "isobars" of constant gluino and squark mass [100].

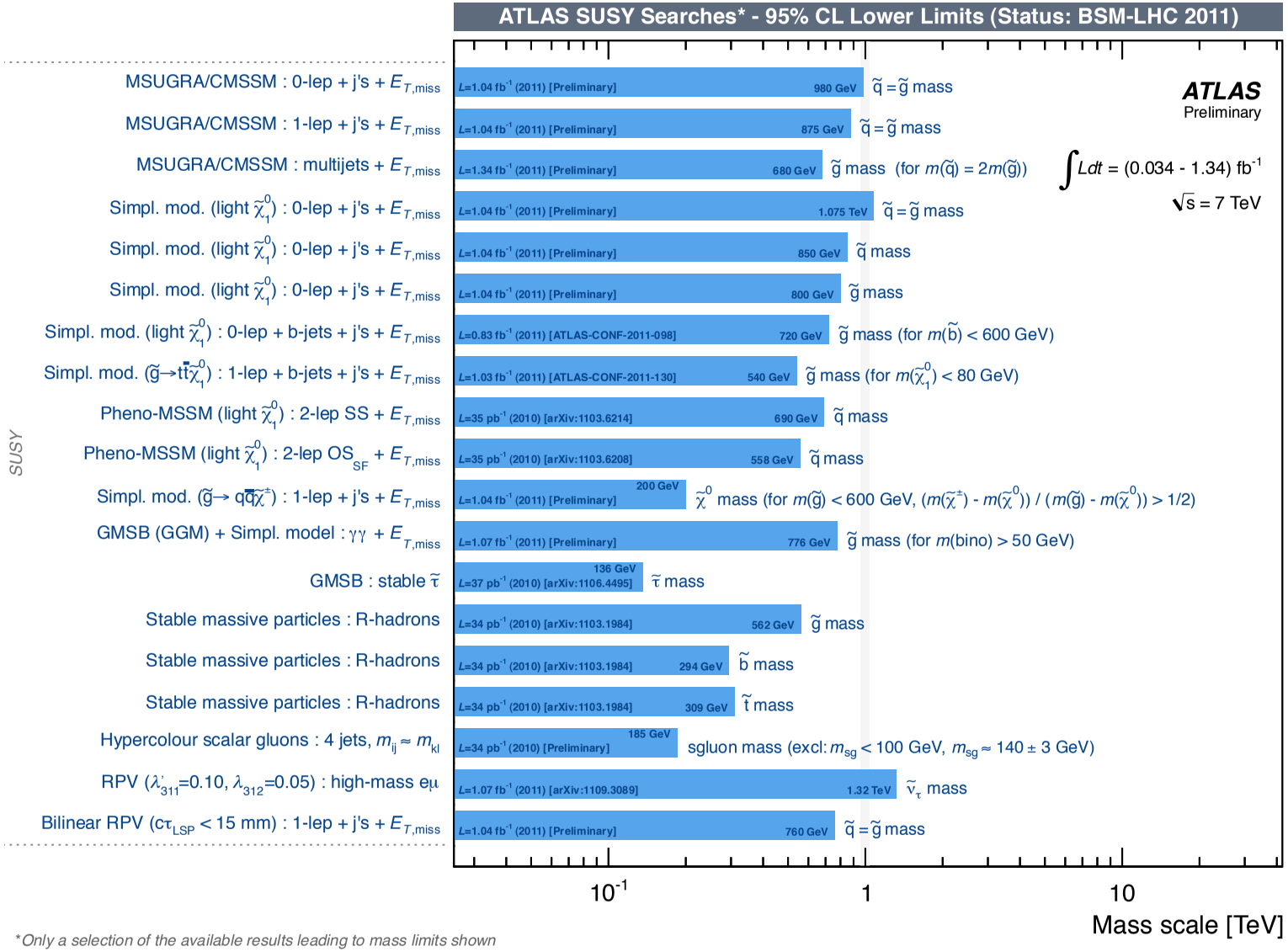

Figure A.3: Mass reach of ATLAS searches for SUSY. The left row states the model and the search channel from which the corresponding limit is obtained. The blue bands depict the 95 % CL lower limits on the masses of several sparticle masses for different integrated luminosities.

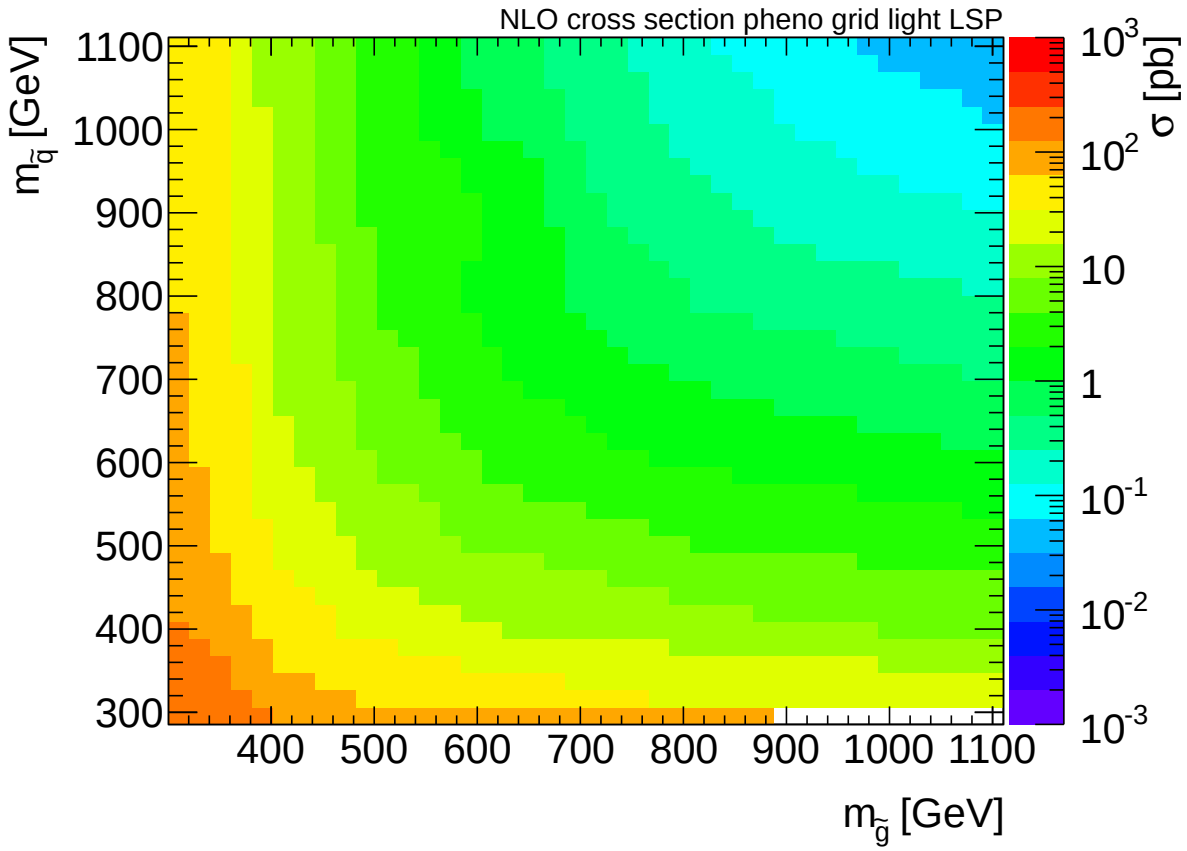

Figure A.4: Next-to-leading order (NLO) cross sections σ in the PhenoGrid parameter space as a function of $m_{\tilde{g}}$ and $m_{\tilde{q}}$). $m_{\tilde{q}}$ corresponds to the mass of the squarks of the first and second generation which are degenerate. The squarks of the third generation are set to 3 TeV. The mass of the LSP is set to $m_{\tilde{\chi}_1^0} = 100$ GeV (*Light LSP mode*) [91].

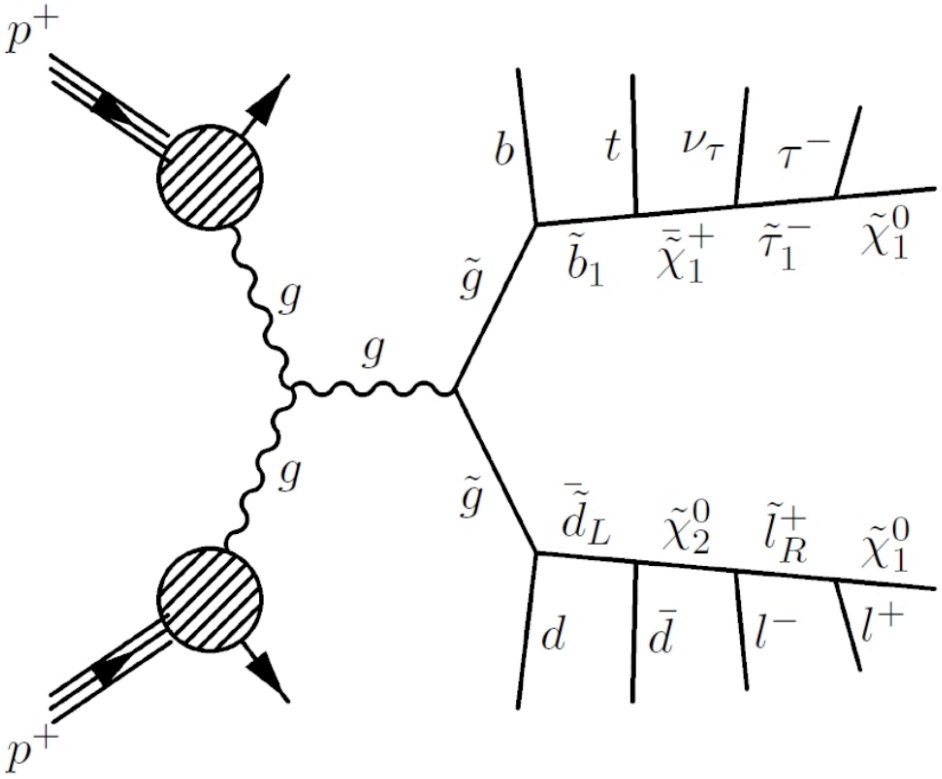

Figure A.5: Feynman diagram for a typical SUSY production and decay chain that results in two OSSF leptons, jets, $E_{\mathrm{T}}^{\mathrm{miss}}$ as well as other decay products.

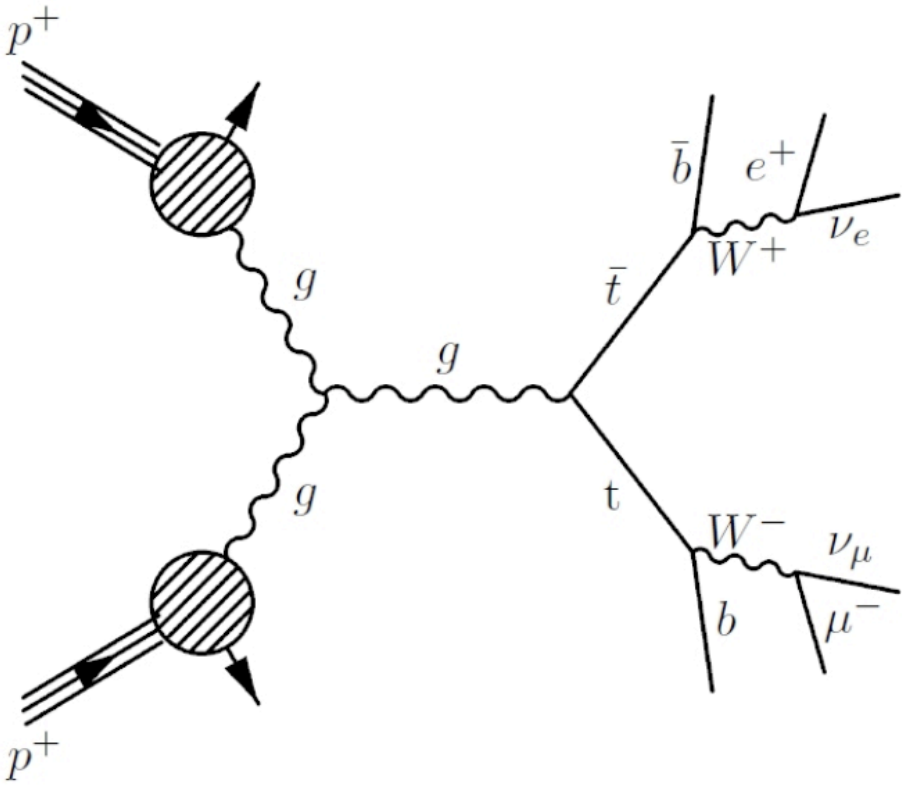

Figure A.6: Feynman diagram for a typical $t\bar{t}$ production and decay chain according to $t\bar{t} \rightarrow (W^+b)(W^-\bar{b}) \rightarrow (e^+\nu_e b)(\mu^-\bar{\nu}_\mu\bar{b})$.

A.2 Cut Optimisation

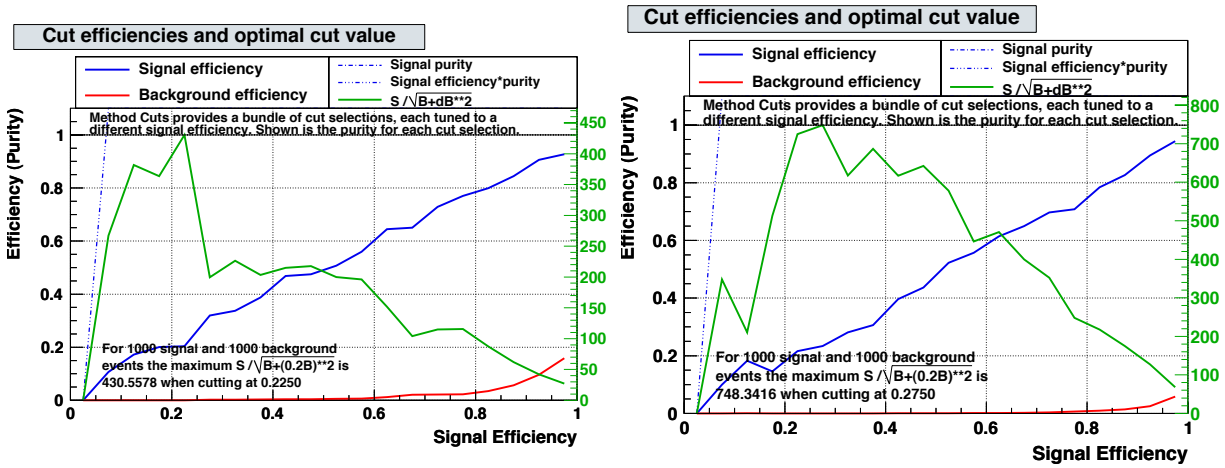

Figure A.7: These plots show the significance (green), the signal efficiency (red), the background efficiency (blue) as well as signal purity and signal purity*efficiency as a function of the signal efficiency. A systematic uncertainty on the number of background events of ±20% was included. The left plot shows the results for the optimisation on the low $m_{1/2}$ region, the right one refers to the high $m_{1/2}$ region.

A.3 Trigger Optimisation

Table A.1: Implemented dilepton triggers. The pair of numbers in the brackets refer to the offline p_{T} cut of the leading and subleading lepton. The triggers for ee, emu, mumu mean: (trigger line `or` baseline) so that the corresponding trigger divided by the baseline gives a number ≥ 1.

	Trigger
	ee baseline: `EF_e20_medium and` (25,10) offline mumu baseline: `EF_mu18 and` (20,8) offline emu baseline: (25,8) if e triggered or (20,10) if mu triggered
ee	
	2e12_medium `and` (17,17) 2e15_loose `and` (20,20) (15,15) (20,10) `or` (15,15) (20,10) (20,15) (baseline `and` MET80) `or` ((7,7) `and` MET80) (baseline `and` MET80) `or` ((10,7) `and` MET80) (baseline `and` MET80) `or` ((12,10) `and` MET80) (baseline `and` MET100) `or` ((7,7) `and` MET100) (baseline `and` MET150) `or` ((7,7) `and` MET150) (baseline `and` MET100) `or` ((15,15) `and` MET100) (17,17) (20,10) `or` (17,17) (20,10) `or` (20,20) `or` (25,10) (20,20) `or` (25,10)
$\mu\mu$	
	2mu10 `and` (12,12) 2mu10 `and` (14,14) mu18 `and` (20,15) (15,8) (15,10) (baseline `and` MET80) `or` ((7,7) `and` MET80) (baseline `and` MET80) `or` ((10,7) `and` MET80) (baseline `and` MET80) `or` ((12,10) `and` MET80) (baseline `and` MET100) `or` ((7,7) `and` MET100) (baseline `and` MET150) `or` ((7,7) `and` MET150) (baseline `and` MET100) `or` ((15,15) `and` MET100)
$e\mu$	
	e10_medium_mu6 `and` (15,12) e10_medium_mu6 `and`(15,8) e10_medium_mu6 `and` (15,10) e10_medium_mu6 `and` (20,8) (baseline `and` MET80) `or` ((7,7) `and` MET80) (baseline `and` MET80) `or` ((10,7) `and` MET80) (baseline `and` MET80) `or` ((12,10) `and` MET80) (baseline `and` MET100) `or` ((7,7) `and` MET100) (baseline `and` MET150) `or` ((7,7) `and` MET150) (baseline `and` MET100) `or` ((15,15) `and` MET100) (15,10) `or` (15,12)

Table A.2: Number of events with good electrons and certain triggers in muon stream, separated by period. The single electron triggers require at least one good electron, the dielectron triggers require at least two. "gEl" means "good electrons" which refers to the medium electron selection.

Period	≥ 1 gEl	≥ 2 gEl	L1_2EM10	EF_2e12_medium	EF_2e12_medium && L1_2EM10
B	$2.65e+04$	$9.18e+02$	$1.02e+02$	$3.00e+00$	$2.00e+00$
D	$3.69e+05$	$1.24e+04$	$1.49e+03$	$7.80e+01$	$7.30e+01$
E	$1.04e+05$	$3.50e+03$	$2.54e+02$	$2.00e+01$	$1.00e+01$
F	$3.04e+05$	$1.02e+04$	0	$6.40e+01$	0
G	$1.07e+06$	$3.54e+04$	0	$2.28e+02$	0
H	$2.80e+05$	$8.62e+03$	0	$4.60e+01$	0
I	$1.25e+06$	$3.88e+04$	$3.88e+03$	$2.10e+02$	$1.99e+02$
J	$8.46e+05$	$2.67e+04$	$2.77e+03$	$1.54e+02$	$1.39e+02$
Total	$4.25e+06$	$1.36e+05$	$8.50e+03$	$8.03e+02$	$4.23e+02$

Period	EF_e10_medium	EF_e20_medium	EF_e20_medium1	EF_2e12T_medium
B	$1.40e+01$	0	$3.07e+02$	$7.00e+00$
D	$7.90e+01$	0	$5.06e+03$	$1.19e+02$
E	$1.60e+01$	$5.02e+04$	$1.40e+03$	$1.60e+01$
F	$5.10e+01$	0	$2.94e+03$	0
G	$2.20e+01$	0	$1.05e+04$	0
H	$7.00e+00$	$2.01e+05$	$1.99e+03$	0
I	$2.60e+01$	0	$9.37e+03$	0
J	$1.50e+01$	0	$6.54e+03$	0
Total	$2.30e+02$	$2.51e+05$	$3.81e+04$	$1.42e+02$

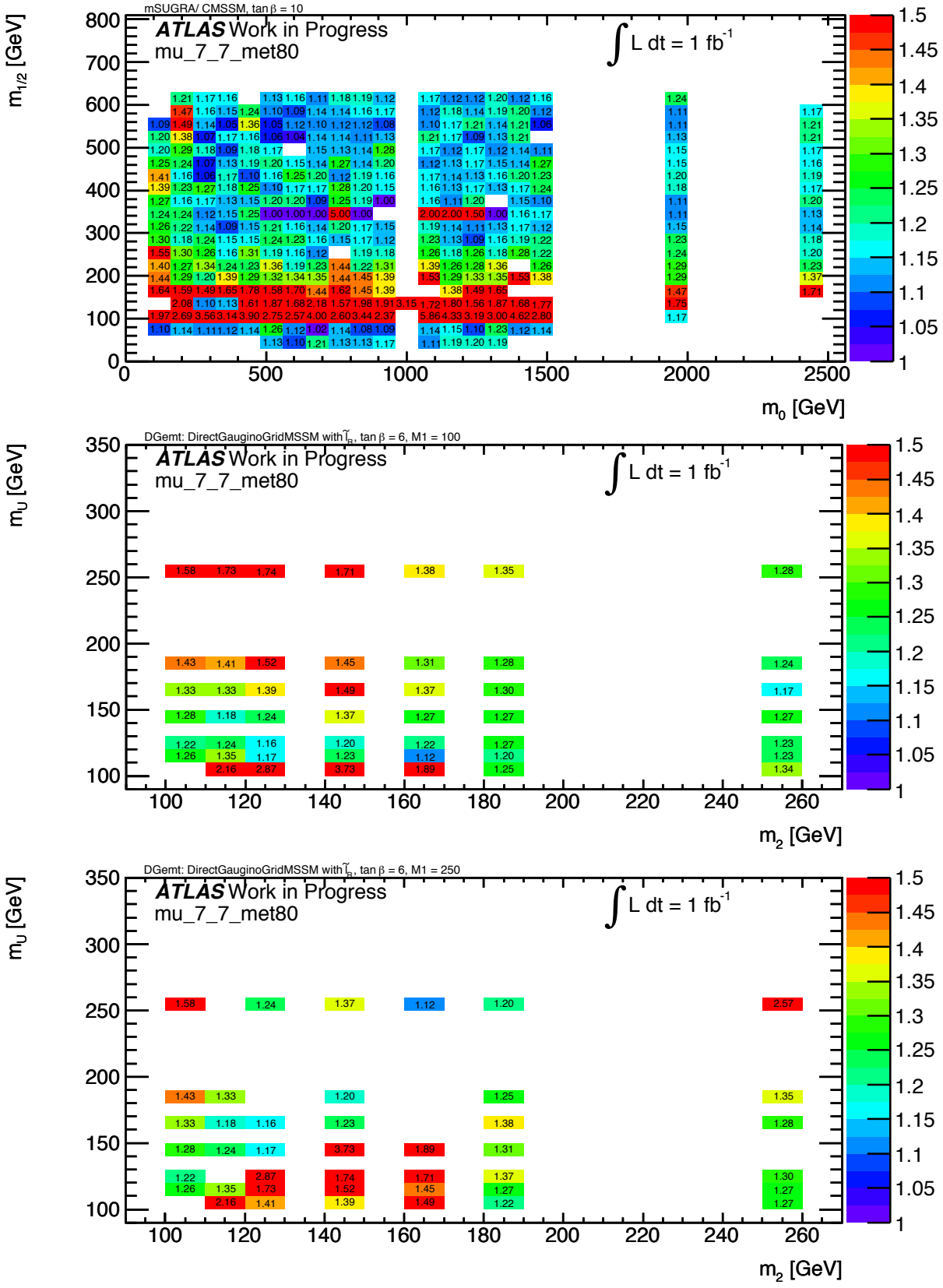

Figure A.8: $\mu\mu$ channel: Yield of an emulated trigger with $p_{\mathrm{T}}^{\mu\mu} > (7,7)$ GeV + $E_{\mathrm{T}}^{\mathrm{miss}} > 80$ GeV offline with respect to ($\mu\mu$ baseline & & $E_{\mathrm{T}}^{\mathrm{miss}} = 80$ GeV) on different SUSY models. The upper plot shows the yield in the mSUGRA $\tan\beta = 10$ $m_0 - m_{1/2}$ plane. The middle and lower plots show the yield on the DGemt grid with $M_1 = 100$ GeV and $M_1 = 250$ GeV, respectively.

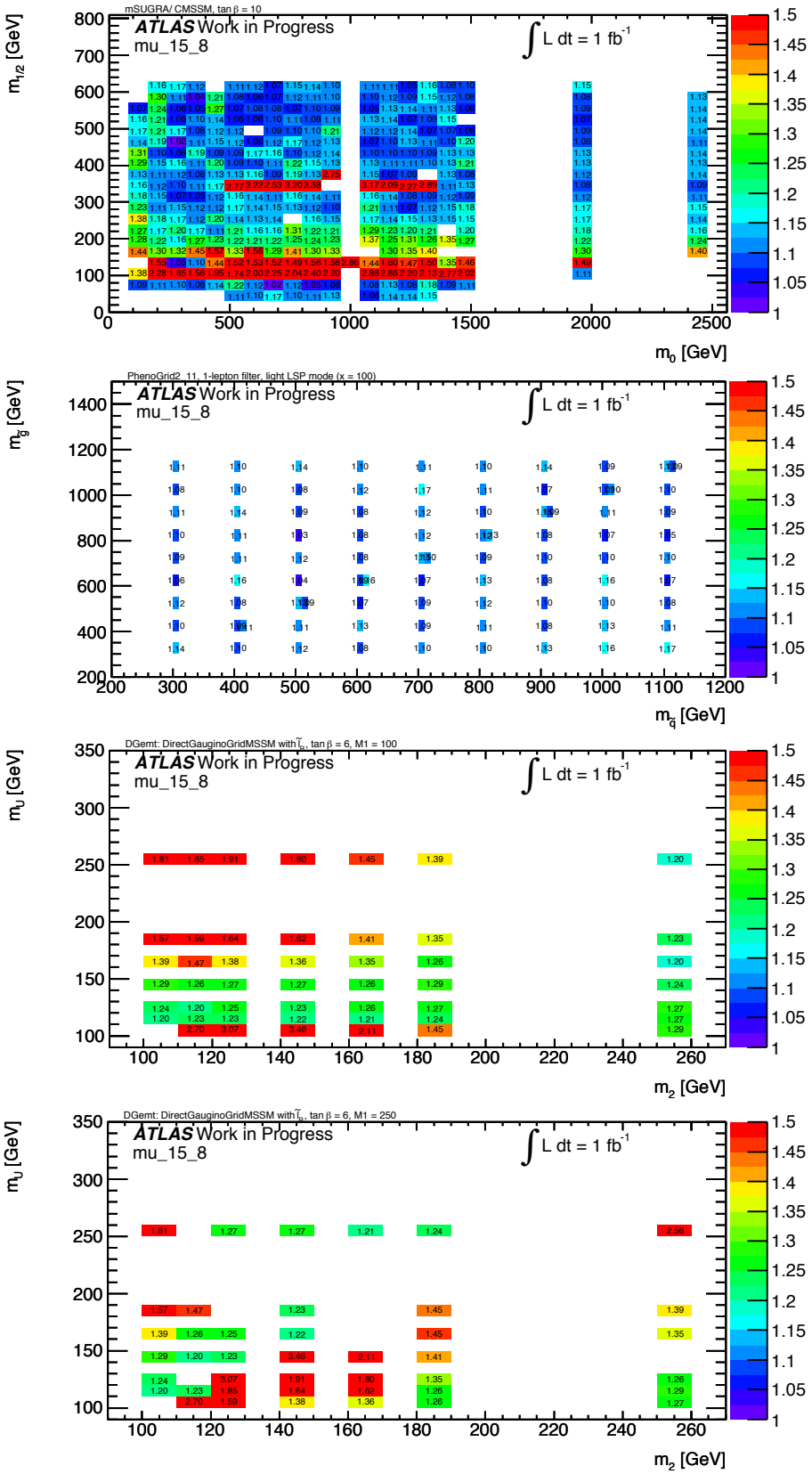

Figure A.9: $\mu\mu$ channel: Yield of an emulated trigger with $p_{\mathrm{T}}^{\mu\mu} > (15, 8)$ GeV offline with respect to the $\mu\mu$ baseline on different SUSY models. The upper plot shows the yield in the mSUGRA $\tan\beta = 10$ $m_0 - m_{1/2}$ plane. The second plot shows the yield on the PhenoGrid2 (PG11 with 1-lepton filter and light LSP mode). The lower two plots show the yield on the DGemt grid with $M_1 = 100$ GeV and $M_1 = 250$ GeV, respectively.

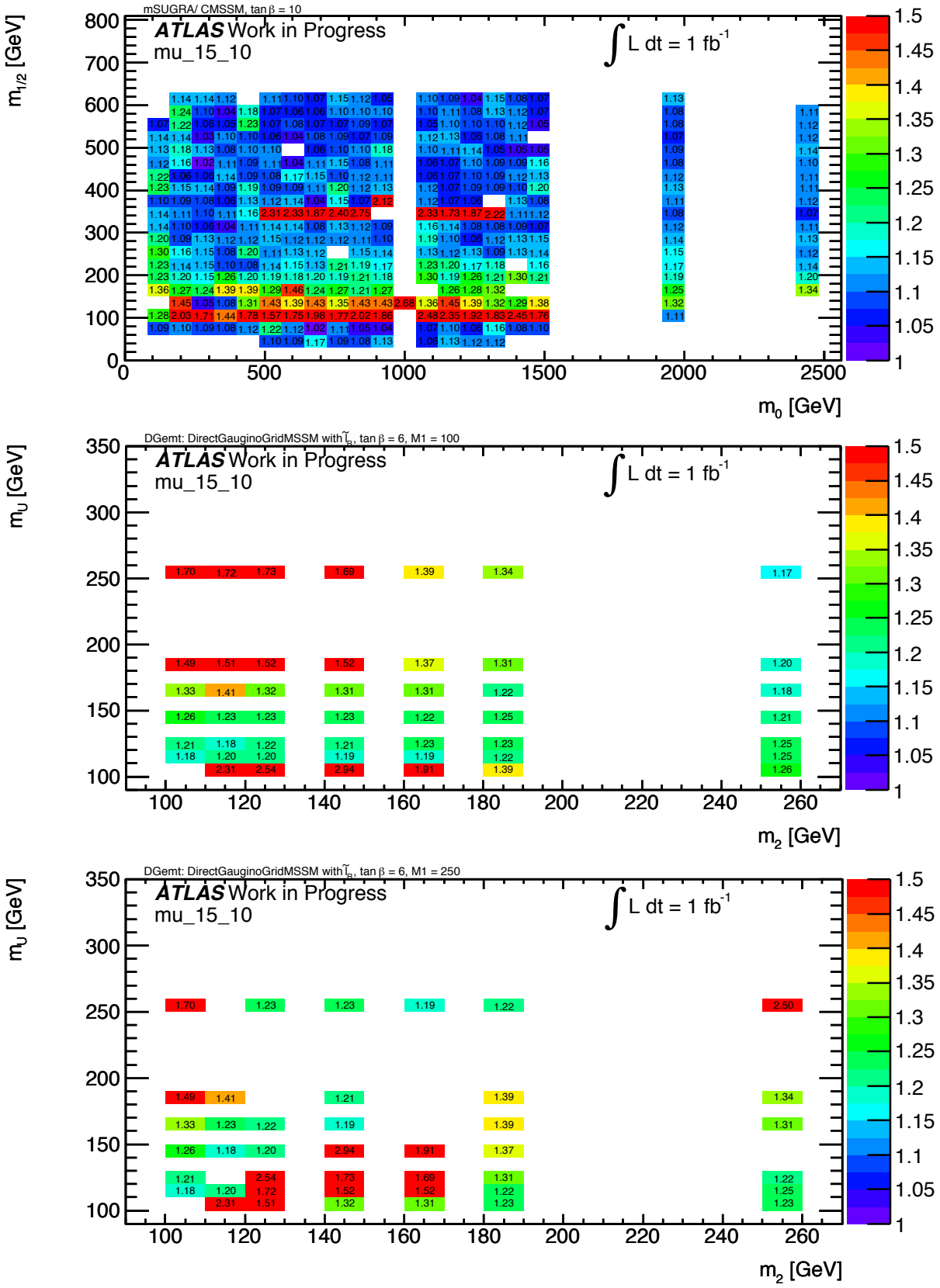

Figure A.10: $\mu\mu$ channel: Yield of an emulated trigger with $p_{\mathrm{T}}^{\mu\mu} > (15, 10)$ GeV offline with respect to the $\mu\mu$ baseline on different SUSY models. The upper plot shows the yield in the mSUGRA $\tan\beta = 10$ $m_0 - m_{1/2}$ plane. The middle and lower plots show the yield on the DGemt grid with $M_1 = 100$ GeV and $M_1 = 250$ GeV, respectively.

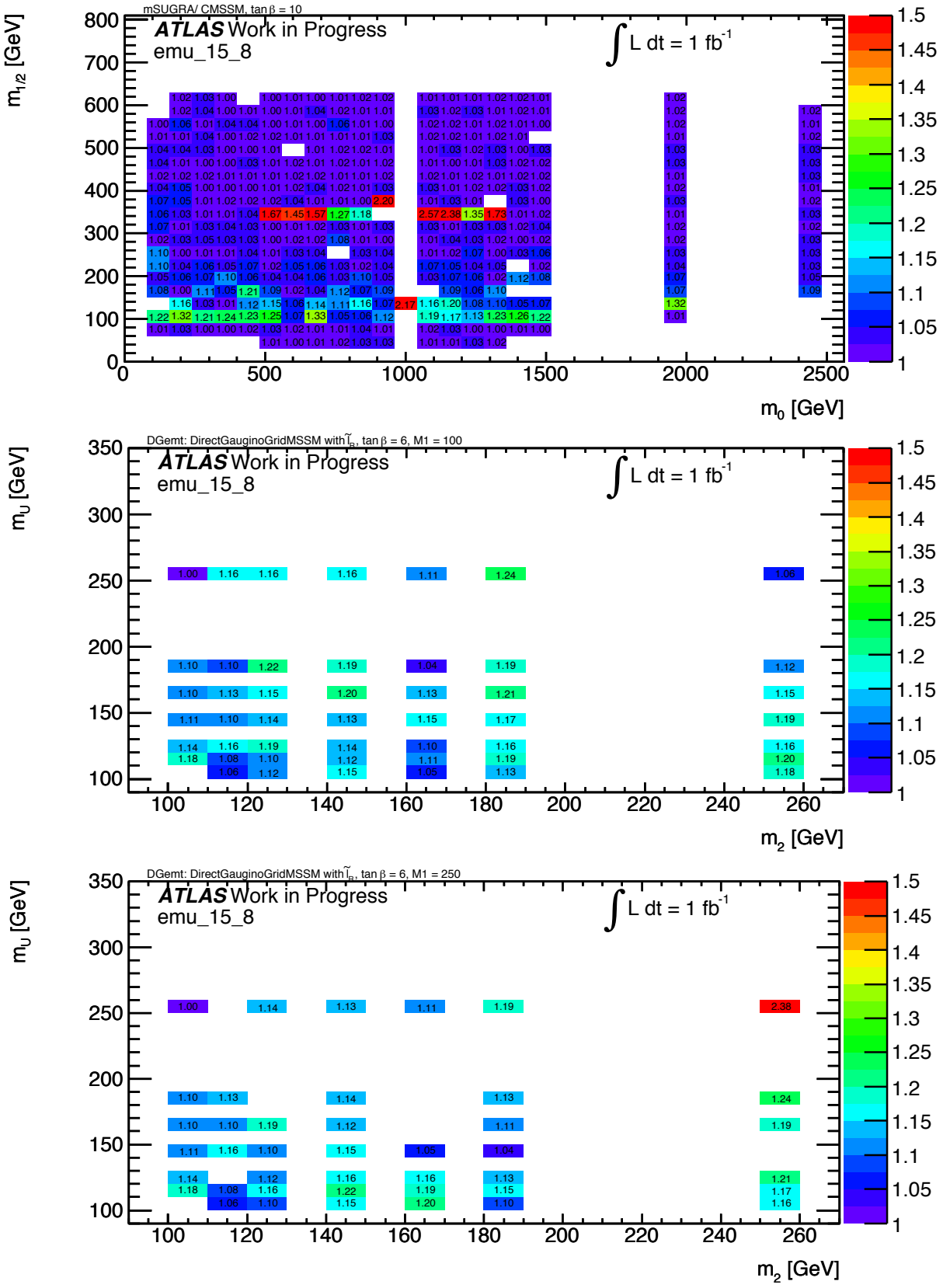

Figure A.11: $e\mu$ channel: Yield of an emulated trigger with $p_{\mathrm{T}}^{e\mu} > (15, 8)$ GeV offline with respect to the $e\mu$ baseline on different SUSY models. The upper plot shows the yield in the mSUGRA $\tan\beta = 10$ $m_0 - m_{1/2}$ plane. The middle and lower plots show the yield on the DGemt grid with $M_1 = 100$ GeV and $M_1 = 250$ GeV, respectively.

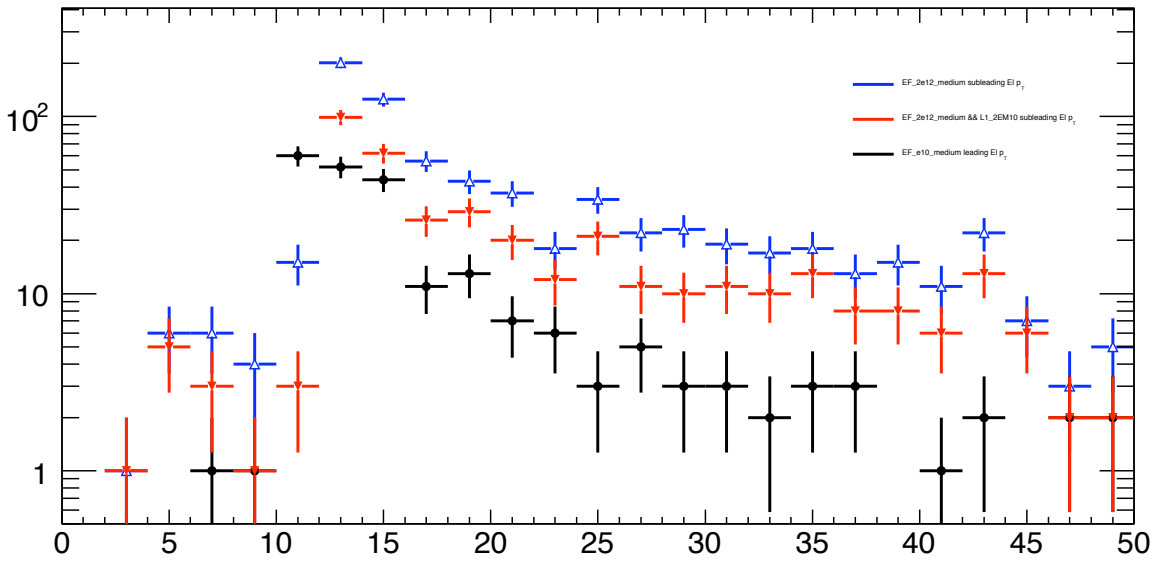

Figure A.12: Electron p_{T} distributions of different triggers in the muon stream. Blue: subleading p_{T} of `EF_2e12_medium`. Red: subleading p_{T} of `EF_2e12_medium && L1_2EM10`. Black: leading p_{T} of `EF_e10_medium`. Used data periods: B,D-J.

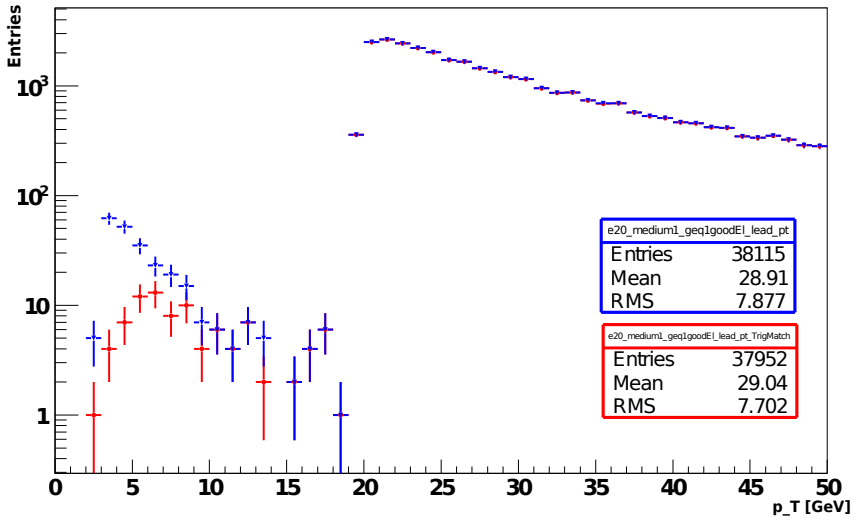

Figure A.13: p_{T} distribution of the leading electron for events triggered by `EF_e20_medium1` with (red) and without (blue) trigger matching being applied. The preselection requires at least one medium electron.

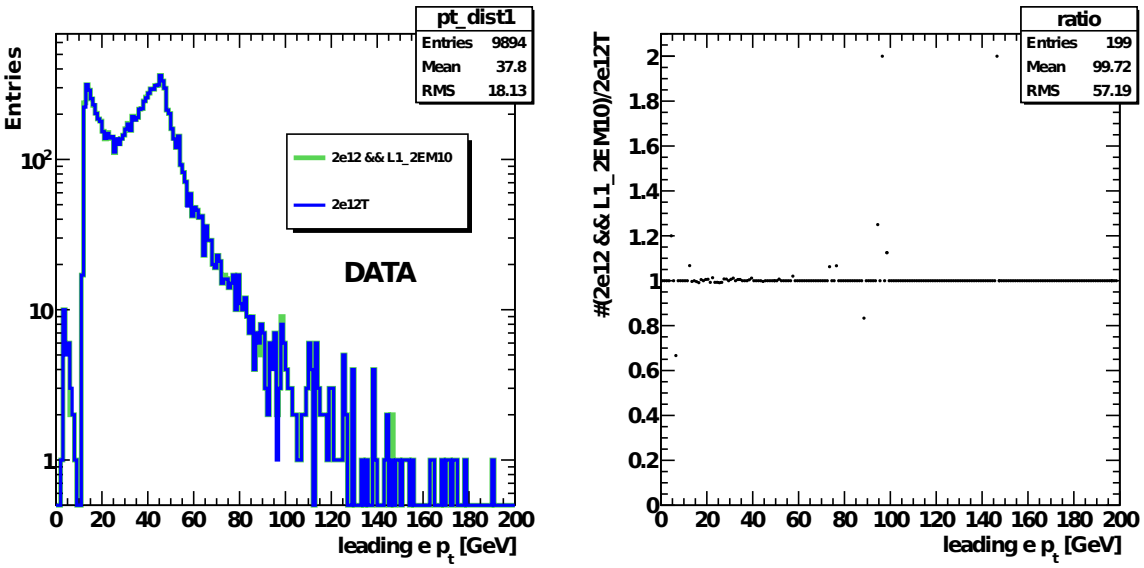

Figure A.14: Left: Leading electron p_{T} distribution of the emulation of `EF_2e12T_medium` as `EF_2e12_medium && L1_2EM10` (green) and `EF_2e12T_medium` (black) on data (two runs from period I2). Right: Ratio of both [93].

Acknowledgement

First of all, I express my gratitude to Dr. Philip Bechtle for giving me the opportunity to write my master thesis in his group. By his support it was possible to for me to participate in many workshops and conferences at which I gained valuable experiences.
I also would like to thank my second referee Prof. Dr. Peter Schleper for his co-review.
Special thanks go to Dr. João Firmino da Costa, Dr. Wolfgang Ehrenfeld and Michael Böhler for their supervision, their patient support day and night, the very enlightening discussions and the proofreading. Especially Michael was of great help with the infinite number of minor and major problems (24 hours...). I would also like to thank my 'lectors' Theresa Brümmer, Robert Büchner, Jörgen Samsung and Paul Gwozdz for their thorough proofreading. I am especially grateful to Theresa, who read every single word of my thesis in-depth despite being probably totally bored. Thank you for forgiving me my affair with Susy.
Credit also goes to Maciej Misiura, University of Warsaw, in collaboration with whom the studies of the trigger efficiencies on MC were performed.
Besides, I thank all members of the DESY ATLAS group for the pleasant working atmosphere.